HIGH RESOLUTION LASER EXCITATION AND DISPERSED FLUORESCENCE SPECTROSCOPY OF THE ALKALINE EARTH MONOHYDROXIDES: THE LOW-LYING ELECTRONIC STATES OF THE CaOH/CaOD AND SrOH RADICALS.

by

PAUL IVAN PRESUNKA

Submitted in partial fulfillment of
the requirements for the degree of
DOCTOR OF PHILOSOPHY
at
Dalhousie University
Halifax, Nova Scotia, Canada
May 1994

ISBN 0-612-05170-6

Name Paul Presnaka

Dissertation Abstracts International is arranged by broad, general subject categories Please select the one subject which most nearly describes the content of your dissertation Enter the corresponding four-digit code in the spaces provided

Physical Chemistry
SUBJECT TERM

C494
SUBJECT CODE

U·M·I

Subject Categories

THE HUMANITIES AND SOCIAL SCIENCES

COMMUNICATIONS AND THE ARTS

Architecture	0729
Art History	0377
Cinema	0900
Dance	0378
Fine Arts	0357
Information Science	0723
Journalism	0391
Library Science	0399
Mass Communications	0708
Music	0413
Speech Communication	0459
Theater	0465

EDUCATION

General	0515
Administration	0514
Adult and Continuing	0516
Agricultural	0517
Art	0273
Bilingual and Multicultural	0282
Business	0688
Community College	0275
Curriculum and Instruction	0727
Early Childhood	0518
Elementary	0524
Finance	0277
Guidance and Counseling	0519
Health	0680
Higher	0745
History of	0520
Home Economics	0278
Industrial	0521
Language and Literature	0279
Mathematics	0280
Music	0522
Philosophy of	0998
Physical	0523
Psychology	0525
Reading	0535
Religious	0527
Sciences	0714
Secondary	0533
Social Sciences	0534
Sociology of	0340
Special	0529
Teacher Training	0530
Technology	0710
Tests and Measurements	0288
Vocational	0747

LANGUAGE, LITERATURE AND LINGUISTICS

Language	
General	0679
Ancient	0289
Linguistics	0290
Modern	0291
Literature	
General	0401
Classical	0294
Comparative	0295
Medieval	0297
Modern	0298
African	0316
American	0591
Asian	0305
Canadian (English)	0352
Canadian (French)	0355
English	0593
Germanic	0311
Latin American	0312
Middle Eastern	0315
Romance	0313
Slavic and East European	0314

PHILOSOPHY, RELIGION AND THEOLOGY

Philosophy	0422
Religion	
General	0318
Biblical Studies	0321
Clergy	0319
History of	0320
Philosophy of	0322
Theology	0469

SOCIAL SCIENCES

American Studies	0323
Anthropology	
Archaeology	0324
Cultural	0326
Physical	0327
Business Administration	
General	0310
Accounting	0272
Banking	0770
Management	0454
Marketing	0338
Canadian Studies	0385
Economics	
General	0501
Agricultural	0503
Commerce Business	0505
Finance	0508
History	0509
Labor	0510
Theory	0511
Folklore	0358
Geography	0366
Gerontology	0351
History	
General	0578
Ancient	0579
Medieval	0581
Modern	0582
Black	0328
African	0331
Asia, Australia and Oceania	0332
Canadian	0334
European	0335
Latin American	0336
Middle Eastern	0333
United States	0337
History of Science	0585
Law	0398
Political Science	
General	0615
International Law and Relations	0616
Public Administration	0617
Recreation	0814
Social Work	0452
Sociology	
General	0626
Criminology and Penology	0627
Demography	0938
Ethnic and Racial Studies	0631
Individual and Family Studies	0628
Industrial and Labor Relations	0629
Public and Social Welfare	0630
Social Structure and Development	0700
Theory and Methods	0344
Transportation	0709
Urban and Regional Planning	0999
Women's Studies	0453

THE SCIENCES AND ENGINEERING

BIOLOGICAL SCIENCES

Agriculture	
General	0473
Agronomy	0285
Animal Culture and Nutrition	0475
Animal Pathology	0476
Food Science and Technology	0359
Forestry and Wildlife	0478
Plant Culture	0479
Plant Pathology	0480
Plant Physiology	0817
Range Management	0777
Wood Technology	0746
Biology	
General	0306
Anatomy	0287
Biostatistics	0308
Botany	0309
Cell	0379
Ecology	0329
Entomology	0353
Genetics	0369
Limnology	0793
Microbiology	0410
Molecular	0307
Neuroscience	0317
Oceanography	0416
Physiology	0433
Radiation	0821
Veterinary Science	0778
Zoology	0472
Biophysics	
General	0786
Medical	0760

EARTH SCIENCES

Biogeochemistry	0425
Geochemistry	0996
Geodesy	0370
Geology	0372
Geophysics	0373
Hydrology	0388
Mineralogy	0411
Paleobotany	0345
Paleoecology	0426
Paleontology	0418
Paleozoology	0985
Palynology	0427
Physical Geography	0368
Physical Oceanography	0415

HEALTH AND ENVIRONMENTAL SCIENCES

Environmental Sciences	0768
Health Sciences	
General	0566
Audiology	0300
Chemotherapy	0992
Dentistry	0567
Education	0350
Hospital Management	0769
Human Development	0758
Immunology	0982
Medicine and Surgery	0564
Mental Health	0347
Nursing	0569
Nutrition	0570
Obstetrics and Gynecology	0380
Occupational Health and Therapy	0354
Ophthalmology	0381
Pathology	0571
Pharmacology	0419
Pharmacy	0572
Physical Therapy	0382
Public Health	0573
Radiology	0574
Recreation	0575
Speech Pathology	0460
Toxicology	0383
Home Economics	0386

PHYSICAL SCIENCES

Pure Sciences

Chemistry	
General	0485
Agricultural	0749
Analytical	0486
Biochemistry	0487
Inorganic	0488
Nuclear	0738
Organic	0490
Pharmaceutical	0491
Physical	0494
Polymer	0495
Radiation	0754
Mathematics	0405
Physics	
General	0605
Acoustics	0986
Astronomy and Astrophysics	0606
Atmospheric Science	0608
Atomic	0748
Electronics and Electricity	0607
Elementary Particles and High Energy	0798
Fluid and Plasma	0759
Molecular	0609
Nuclear	0610
Optics	0752
Radiation	0756
Solid State	0611
Statistics	0463

Applied Sciences

Applied Mechanics	0346
Computer Science	0984
Engineering	
General	0537
Aerospace	0538
Agricultural	0539
Automotive	0540
Biomedical	0541
Chemical	0542
Civil	0543
Electronics and Electrical	0544
Heat and Thermodynamics	0348
Hydraulic	0545
Industrial	0546
Marine	0547
Materials Science	0794
Mechanical	0548
Metallurgy	0743
Mining	0551
Nuclear	0552
Packaging	0549
Petroleum	0765
Sanitary and Municipal	0554
System Science	0790
Geotechnology	0428
Operations Research	0796
Plastics Technology	0795
Textile Technology	0994

PSYCHOLOGY

General	0621
Behavioral	0384
Clinical	0622
Developmental	0620
Experimental	0623
Industrial	0624
Personality	0625
Physiological	0989
Psychobiology	0349
Psychometrics	0632
Social	0451

DALHOUSIE UNIVERSITY

FACULTY OF GRADUATE STUDIES

The undersigned hereby certify that they have read and recommend to the Faculty of Graduate Studies for acceptance a thesis entitled "High Resolution Laser Excitation and Dispersed Fluorescence Spectroscopy of the Alkaline Earth Monohydroxides: The Low-Lying Electronic States of the CaOH/CaOD and SrOH Radicals"

by Paul Presunka

in partial fulfillment of the requirements for the degree of Doctor of Philosophy.

Dated June 24, 1994

External Examiner

Research Supervisor

Examining Committee

DALHOUSIE UNIVERSITY

DATE: June 30/94

AUTHOR: Paul Presunka

TITLE: "High Resolution Laser Excitation and Dispersed Fluorescence Spectroscopy of the Alkaline Earth Monohydroxides: The Low-Lying Electronic States of the CaOH/CaOD and SrOH Radicals"

DEPARTMENT OR SCHOOL: Department of Chemistry

DEGREE: Ph.D. CONVOCATION: Fall YEAR: 1994

Permission is herewith granted to Dalhousie University to circulate and to have copied for non-commercial purposes, at its discretion, the above title upon the request of individuals or institutions.

Signature of Author

This thesis is dedicated to the memory of my father,
the late Mr. P. Presunka, B. Eng., B.A. (U. Tor.).

TABLE OF CONTENTS

LIST OF FIGURES

LIST OF TABLES

ABSTRACT

Dispersed laser-induced fluorescence from the $\tilde{A}^2\Pi$ state of CaOH and CaOD has been utilized to observe the fine structure associated with the excited vibrational levels (v_1,0,0) with $v_1 \leq 4$ of the ground $\tilde{X}^2\Sigma^+$ state. In addition, the $\tilde{A}^2\Pi(100) \sim \tilde{A}^2\Pi(020)$ Fermi resonance interaction has been exploited to provide access to both the $\ell = 0$ and $\ell = 2$ components of the $\tilde{X}^2\Sigma^+(020)$ vibrational level via a perturbation-facilitated approach. This work provides the first detailed spectroscopic constants for excited vibrational levels in the $\tilde{X}^2\Sigma^+$ states of CaOH and CaOD.

The $\tilde{B}^2\Sigma^+ - \tilde{X}^2\Sigma^+$ system of SrOH has been investigated using Doppler-limited laser excitation and dispersed fluorescence. Bending vibrational levels with $v_2 \leq 2$ of both electronic states have been rotationally analyzed. The effects of a weak ℓ-type resonance between the Σ and Δ components of the $v_2 = 2$ vibrational level were observed and the off-diagonal matrix elements were evaluated in a case (b) basis.

Sub-Doppler intermodulated fluorescence and Doppler-limited excitation spectra of the 2_0^1 and 2_1^1 bands in the $\tilde{A}^2\Pi - \tilde{X}^2\Sigma^+$ system of SrOH have enabled the observation of all Renner-Teller components associated with the $\tilde{A}^2\Pi(010)$ level. A strong perturbation due to a K-resonance crossing of the $\mu^2\Sigma^{(+)}$ and $^2\Delta_{3/2}$ vibronic components is observed. All measured line positions have been included in a complete deperturbation analysis of the $v_2 = 1$ moiety that takes account explicitly of Renner-Teller, spin-orbit, Λ-type doubling and ℓ-type doubling interactions. The results include the first reliable estimate of the Renner-Teller parameter for SrOH ($\epsilon = -0.0791$). In addition, a high resolution investigation of the $\tilde{A}^2\Pi(100) \leftarrow \tilde{X}^2\Sigma^+(000)$ band combined with rotationally resolved dispersed fluorescence spectra of the 1_1^1, 1_2^1, 2_1^1, 2_2^1, and 2_3^1 bands provides accurate rotational and vibrational constants for the $\tilde{A}^2\Pi$ and $\tilde{X}^2\Sigma^+$ states of SrOH.

LIST OF ABBREVIATIONS AND SYMBOLS

α	Amplitude factor in drum wavelength correction function
α_i	Vibration-rotation interaction constant
$(\alpha_2)_{h1}$	Coriolis contribution to α_2
$(\alpha_2)_{h2}$	Pseudo-anharmonic contribution to α_2
$(\alpha_2)_{anh}$	Anharmonic contribution to α_2
A	Spin-orbit coupling constant
A_D	Centrifugal distortion correction to the spin-orbit coupling constant
A_{eff}	Effective spin-orbit coupling constant
Å	Ångström unit (1×10^{-10} m)
a	Least-squares parameter in drum wavelength correction function
β	phase factor in drum wavelength correction function
B_v	Rotational constant for vibrational level v
B_e	Equilibrium rotational constant
b	Least-squares parameter in drum wavelength function
c	Speed of light (2.99792458×10^8 ms^{-1})
c	Least-squares parameter in drum wavelength function
ΔT^{Δ}	Vibronic energy parameter; $\Delta T^{\Delta} = G(\Sigma) - G(\Delta)$
D	Debeye unit
D_v	Centrifugal distortion constant; coefficient of $[J(J + 1)]^2$
D_0	Dissociation energy (from lowest vibrational level)
d_i	Degeneracy of vibrational mode v_i
dc	Direct current
ϵ	Renner-Teller parameter
ϵ_1	Dipolar (HT) contribution to ϵ
ϵ_2	Quadrupolar (RT) contribution to ϵ
e	Rotation-independent parity label

eV	Electronvolt unit
ζ_{ij}	Coriolis coupling constant between vibrational modes ν_i and ν_j
f	Rotation-independent parity label
f_n	Chopping frequency
F	Rotational energy
FWHM	Full width at half maximum
γ_v	Spin-rotation constant for vibrational level v
γ_v^D	Centrifugal distortion correction to γ_v
γ_2	Vibration-rotation interaction constant; coefficient of $(v_2 + 1)^2$
γ_{ll}	Vibration-rotation interaction constant; coefficient of ℓ^2
γ	Quasi-linear parameter
γ_0	Reduced quasi-linear parameter
G_v	Vibrational energy of vibrational level v
$\boldsymbol{G}$	Vibrational angular momentum operator
G_0	Vibrational energy with respect to lowest vibrational level
g_{22}	Vibrational anharmonicity constant; coefficient of ℓ^2
g_K	Second-order correction to the vibronic energy
HT	Herzberg-Teller
H_v	Centrifugal distortion constant; coefficient of $[J(J + 1)]^3$
$\boldsymbol{H}$	Hamiltonian operator
h	Planck's constant (6.626 075 5(40) $\times$ 10^{-34} Js)
$\hbar$	$\hbar = h/2\pi$
$I^{(z)}$	Moment of inertia about z axis
IMF	Intermodulated fluorescence
$\boldsymbol{J}$	Total angular momentum operator (exclusive of nuclear spin)
J	Total angular momentum quantum number (exclusive of nuclear spin)
κ	Vibronic state label for highest energy component

K	Vibronic angular momentum quantum number
$k^{\pm}$	Force constants for $V^{\pm}$ bending potential functions
Λ	Projection of orbital angular momentum on z-axis
$\boldsymbol{L}$	Orbital angular momentum operator
L	Orbital angular momentum quantum number
ℓ	Vibrational angular momentum quantum number
λ_{d}	Drum wavelength
LIF	Laser-induced fluorescence
μ	Vibronic state label for lowest energy component
M	Metal atom
MODR	Microwave-optical double resonance
ν	Azimuthal angle describing the orientation of electron with respect to an arbitrary reference plane
ν_i	Vibrational mode
$\tilde{\nu}$	wavenumber
$\boldsymbol{N}$	Total angular momentum operator (excluding spin)
N	Total angular momentum quantum number (excluding spin)
π	Fundamental constant pi
p_v^{e}	Lambda-doubling parameter for vibrational level v
P	Vibronic angular momentum quantum number including electron spin
PMT	Photomultiplier tube
p	Effective spin-rotation constant
ρ	Bending coordinate
ρ_v^{v}	Higher order ℓ-type doubling parameter of vibrational level v
q_v^{v}	ℓ-type doubling constant for vibrational level v
q_{eff}	Effective ℓ-type doubling constant
q_v^{e}	Lambda-doubling parameter for vibrational level v

Q_v	Effective lambda-doubling constant
$q_{\pm}$	Bending coordinate ladder operator
RT	Renner-Teller
$\boldsymbol{R}$	Nuclear rotational angular momentum operator
S/N	Signal-to-noise ratio
$\boldsymbol{S}$	Total electron spin angular momentum operator
S	Total electron spin angular momentum quantum number
$U_K^{\pm}(\rho)$	Potential energy of Born-Oppenheimer potentials
v_i	Vibrational quantum number of vibrational mode ν_i
V	Volt unit
VET	Vernier etalon
$V^{\pm}$	Potential energy of Born-Oppenheimer potentials
$V_0(\rho)$	Potential energy of the mean of $V^{\pm}$ potentials
χ	Azimuthal coordinate describing the orientation of the plane containing the nuclei with respect to an arbitrary reference plane
Ψ	Eigenfunction
ω_i	Vibrational frequency of i^{th} vibrational mode
W_{20}	Perturbation element
x_{ik}	Vibrational anharmonicity constant; coeff. of $(v_i + d_i/2)(v_k + d_k/2)$

ACKNOWLEDGEMENTS

I wish to express my gratitude to Professor John Coxon for his untiring encouragement and support. Under his liberal direction, I was challenged to pursue this research to the height of my abilities. My experience at Dalhousie has been enriched considerably by his friendship over the past few years.

I would also like to thank Mr. Mingguang Li with whom I have enjoyed many fruitful collaborations. It has been a privilege to work with a scientist of his high calibre.

Mr. M. Murphy, whose friendship and companionship at numerous fishing holes and drinking establishments across Nova Scotia was greatly appreciated, is acknowledged as is the entire Murphy family for their kind support over many years. Mr. and Mrs. F. Hickey are also thanked for their generous hospitality on many weekend excursions to Cape Breton Island.

The camaraderie among members of the Department of Chemistry have made my time here an enjoyable one. Special thanks are extended to Master Glassblower Jurgen Mueller and Dr. I. Mclennan for many protracted discussions which helped keep everything in perspective.

Dalhousie University and the W. C. Sumner Foundation are thanked for financial support in the form of graduate scholarships.

Most of all, I would like to thank my mother (Mrs. M. Presunka), uncle (Mr. S. Presunka) and one other very special person (Ms. C. Hickey) whose love and support during this thesis work has meant more than I can say.

Chapter I

General Introduction

In recent decades, the proliferation of a variety of new laser techniques in high resolution spectroscopy has contributed to the vast amount of empirical data that now exists for a large number of polyatomic species. Despite this, the overwhelming majority of linear triatomic molecules that have been studied to date, for example NCO, N_3 and CCN, are composed of lighter elements. Notwithstanding the many subtle complexities exhibited in these systems, such molecules are generally characterized by small spin-orbit splittings and well separated electronic states in contrast to their heavier analogs. Accordingly, this bias is reflected in much of our understanding of linear triatomic molecules, which is based upon approximations that are valid for lighter species, yet may break down for molecules containing heavier elements.

Comparatively few linear triatomic molecules containing a fourth or fifth row atom have been the subject of high resolution investigations. A notable exception to this trend is found in the alkaline earth monohydroxides, for which a large body of experimental data is rapidly accumulating. This interesting class of molecules presents a number of ideal candidates for optical studies since several of the low-lying electronic states are located in a very convenient region for dye laser excitation and their spectra exhibit many interesting phenomena which are poorly understood.

Spectroscopic investigations of the gas phase alkaline earth monohydroxides have provided a wealth of information on the lowest vibrational level of several valence electronic states; however, there is a paucity of data for excited vibrational levels. In large part this is due to the enhanced

complexity and spectral congestion frequently associated with the higher vibrational levels. Rather than being a mere exercise in tenacity, detailed analysis of the excited vibrational levels can yield a wealth of important molecular data. Gas phase spectroscopic investigations of this kind involving more than one isotopomer often provide the only reliable determinations of bond angles and bond distances for many molecules. Even in cases where other experimental data are available, the gas phase structural information is usually the most accurate and is free of many interactions common to condensed phases. More importantly, the observation of excited vibrational energy levels enables the determination of an accurate potential energy surface, which, ultimately is essential to a detailed understanding of the intramolecular dynamics. More subtle effects such as Born-Oppenheimer breakdown through the Renner-Teller effect, angular momentum couplings, vibration-rotation interactions and the like may also be ascertained through such investigations. In situations where perturbations occur in the excited vibrational levels, a successful deperturbation analysis may provide physical insight into the nature of subtle interaction mechanisms.

The visible spectra of the alkaline earth monohydroxides CaOH and SrOH, as well as their related deuterides, involve transitions from the ground $\tilde{X}^2\Sigma^+$ state to three low-lying electronic states namely the $\tilde{A}^2\Pi$, $\tilde{B}^2\Sigma^+$, and $\tilde{C}^2\Delta$ states. The subject matter of the present thesis involves the high resolution spectroscopic investigation of numerous bands associated with the $\tilde{A}^2\Pi$ - $\tilde{X}^2\Sigma^+$ systems of CaOH/CaOD and SrOH as well as the $\tilde{B}^2\Sigma^+$ - $\tilde{X}^2\Sigma^+$ system of SrOH. The primary objective of this work has been to initiate a systematic investigation of excited vibrational levels in the $\tilde{A}^2\Pi$, $\tilde{B}^2\Sigma^+$ and $\tilde{X}^2\Sigma^+$ states of SrOH, however, progress in this respect has been considerably slower than anticipated owing to extensive perturbations observed in vibrationally excited

levels of the $\tilde{A}^2\Pi$ and $\tilde{B}^2\Sigma^+$ states. Despite these difficulties, significant progress has been made particularly with respect to the $\tilde{A}^2\Pi$ and $\tilde{X}^2\Sigma^+$ states.

A more complete introduction to the research of this thesis is presented in the following chapter. In particular, the relevance of this work is discussed in a broader scientific context. A brief review of previous work on SrOH, CaOH and their deuterated analogs is presented along with a summary of the known properties of the low-lying electronic states.

The third chapter provides details concerning the experimental apparatus and techniques used to acquire the spectra, and includes a description of the modified Broida type oven used to produce the gas phase radicals observed in this work. The use of a computer-interfaced digitally scanning monochromator to obtain rotationally resolved dispersed fluorescence spectra is described. A detailed account of the Doppler-limited laser excitation and sub-Doppler intermodulated fluorescence experiments used to investigate the $\tilde{A}^2\Pi$ - $\tilde{X}^2\Sigma^+$ and $\tilde{B}^2\Sigma^+$ - $\tilde{X}^2\Sigma^+$ systems of SrOH is also given.

As a preamble to the experimental work presented in this thesis, chapter 4 contains a review of some relevant empirical formulae that are used to represent the quantized energy levels in linear triatomic molecules. The discussion extends beyond a mere presentation of energy level formulae, particularly with respect to such relevant topics as the Renner-Teller effect and ℓ-type doubling, in an attempt to provide a physical insight which is used to interpret the data presented in chapters 5 to 7.

Chapter 5 concerns the investigation of excited vibrational levels in the $\tilde{X}^2\Sigma^+$ state of CaOH and CaOD by resolved fluorescence spectroscopy. Dispersed laser induced fluorescence (LIF) from selectively populated rotational levels of $\tilde{A}^2\Pi(100)$ is used to access the vibrational levels $(v_1 00)$ with $v_1 \leq 3$ of the ground state for both molecules and the (400) level for CaOH only. The strong

(100) ~ (020) Fermi resonance in the $\tilde{A}^2\Pi$ state is exploited to access the $v_2 = 2$ vibrational level of the $\tilde{X}^2\Sigma^+$ state via a perturbation facilitated approach. The $\tilde{X}(020)$ level is split into Δ ($\ell = 2$) and Σ ($\ell = 0$) components with spacings of 24.369 and 17.183 cm^{-1} for CaOH and CaOD respectively. Vibrational and rotational constants are determined for all the observed levels.

A rotational analysis of the excited bending vibrations with $v_2 \leq 2$ of the $\tilde{B}^2\Sigma^+$ and $\tilde{X}^2\Sigma^+$ states of SrOH is presented in chapter 6. All data are included in a global least-squares fit in which the effects of a weak ℓ-type resonance between the $\ell = 0$ and $\ell = 2$ components of the (020) level of both states are observed and analyzed in a Hund's case (b) basis.

The results of a deperturbation analysis of *K*-resonance in the $v_2 = 1$ moiety of the $\tilde{A}^2\Pi$ state of SrOH are discussed in chapter seven. A level crossing of the Σ and Δ vibronic components of the lower spin-orbit members is observed and provides an excellent example of a *K*-resonance crossing. This phenomenon has been observed previously in only one other case, the $\tilde{A}^2\Pi_u$ state of BO_2. The extensive and highly accurate data provide for the determination of a complete set of deperturbed molecular constants; in addition, they serve as a means of assessing the applicability of the current matrix model to a linear triatomic molecule involving a relatively heavy atom. In order to further address the deficiency of $\tilde{A}^2\Pi$ state vibrational data, an analysis of the $\tilde{A}^2\Pi(100) - \tilde{X}^2\Sigma^+(000)$ band is also included in this chapter. In addition, data from dispersed fluorescence spectra of the 1_1^1 , 1_2^1 and 2_3^1 bands of the $\tilde{A}^2\Pi - \tilde{X}^2\Sigma^+$ system are presented and provide information that complements the ground state data presented in chapter 6.

Chapter II

Background

2.1 Introduction

In addition to the objectives stated in chapter 1, the present spectroscopic study of the group IIA monohydroxides is warranted for a number of reasons. This particular class of free radicals is of considerable interest in such diverse areas as astrophysics and atmospheric chemistry. Tsuji[1] has predicted that the hydroxyl compounds of the alkaline earth metals are important species in stellar atmospheres. Although there has been a tentative assignment of a CaOH spectrum in late M-type dwarf stars[2], a microwave search[3] has failed to detect interstellar CaOH. Significant quantities of alkaline earth metal hydroxides are also expected to be found in the terrestrial atmosphere. The group IIA metals are believed to be deposited in the lower mesosphere and stratosphere primarily by two mechanisms: meteoric ablation[4,5] and unintentional release from high flying aircraft[4]. Under ambient conditions present in the upper atmosphere, the dominant gas phase species of the group IIA metals is expected to be the monohydroxide[5].

Spectroscopic data often provide a benchmark for quantum mechanical calculations. Theorists are provided with a good reference point by which they can assess the quality and accuracy of their calculations. Poor agreement between theory and experiment may highlight deficiencies in a model, paving the way for development of an improved understanding. For the M-X molecules (M = alkaline earth, X = OH^-), two semi-empirical models, namely the modified Rittner model[6] and ligand-field model[7], have been used to predict the properties of the low-lying electronic states. Frequently, molecular constants obtained from gas phase work are also used as input parameters in

calculations, thereby minimizing the number of adjustable parameters and increasing the accuracy of the result. In the work of Mestdagh and Visticot[8], for instance, the experimentally determined bond lengths and M-OH stretching frequencies were employed as input parameters.

Information on the excited vibrational levels of the group IIA monohydroxides is of particular interest to workers studying the dynamics of the chemiluminescent reactions of the alkaline earth metals with H_2O and H_2O_2. The nature of the reaction mechanism may be elucidated through the nascent product state distributions which, in principle, can be ascertained from the resulting chemiluminescence. The reliable extraction of the nascent population distributions, however, requires precise spectroscopic data for the electronic states involved. For the specific reactions of H_2O_2 with Ca and Sr, the chemiluminescence is produced via the following reactions[9]:

$$M + H_2O_2 \longrightarrow MOH\ (\tilde{A}^2\Pi,\ \tilde{B}^2\Sigma^+) + OH \qquad (2.1)$$

$$M + H_2O_2 \longrightarrow MO\ (\tilde{A}^1\Sigma^+,\ \tilde{A}'^1\Pi) + H_2O \qquad (2.2)$$

Using computer simulations of the chemiluminescent spectra, Cheong and Parsons[9] have provided convincing evidence that reaction (2.2) proceeds via insertion of the metal atom into an O-H bond. The same authors were unable to carry out a similar analysis of the monohydroxide forming reaction owing to the lack of spectroscopic data for the excited vibrational levels.

Gas phase spectroscopic investigations of the monovalent hydroxide derivatives of the group IIA metals are of interest to chemists from another perspective. Previous knowledge of metal ligand chemistry is obtained primarily from condensed phase studies. Under these conditions solution and/or matrix effects may introduce sizable interactions. Gas phase work provides a unique opportunity to study the isolated metal-ligand system and has been

increasingly applied[10] in recent years.

2.2 History of CaOH and SrOH

The visible emission spectra of flames containing alkaline earth metals were described as early as 1823 by Herschel[11]. These emissions, which were later widely employed as a means of testing for the presence of the alkaline earth metals[12], were produced by the addition of metal containing salts to an alcohol flame. Despite the rather early observation of these flame spectra and their use in elemental analysis, the nature of the carrier was erroneously assigned for many years. In 1955 James and Sugden[12] provided convincing evidence that the observed bands were due to the alkaline earth monohydroxide radicals. This contention was based largely on similarities to the isoelectronic alkaline earth halide emission spectra. Confirmation of this assignment for the SrOH bands was provided by isotopic substitutions in which D_2O was substituted for H_2O in flames[13,14] and arcs[14,15]. Subsequent low resolution optical investigations of the Ca[16,17] and Sr[18] flame spectra were carried out, however, as a result of the complexity and spectral congestion in the high temperature sources used in these studies, very little progress was made. The first spectroscopic investigation of the visible bands of SrOH and CaOH using tunable dye laser excitation was carried out in 1978 by Weeks *et al.*[19] Owing to the high temperature of the flame source and relatively large bandwidth of the dye laser, the laser excitation spectrum was virtually identical to the flame emission bands.

The spectroscopy of the group IIA monohydroxides has attracted considerably more attention in the last decade. In large part, this renewed interest was stimulated by the work of Wormsbecher *et al.*[20] which demonstrated that the flowing metal vapor reaction system,[21] previously used

only for production of diatomic molecules, was also capable of producing large number densities of polyatomic species. This type of source became known as a "Broida oven", and represented a substantial improvement over previous flame sources: typically, alkaline earth monohydroxides produced in a Broida oven are characterized by a much lower state of thermal excitation ($T \approx 700$ K) in comparison to the earlier flame sources ($T \approx 2000$ K). Combined with narrow bandwidth tunable dye laser excitation, this new molecular source enabled the first rotational analyses to be carried out. Nakagawa *et al.*[22] observed several $\Delta v = 0$ sequence bands in the $\tilde{B}^2\Sigma^+ - \tilde{X}^2\Sigma^+$ system of SrOH and SrOD at high resolution. Almost concurrently, Hilborn and co-workers[23] investigated the (000)-(000) band of the $\tilde{A}^2\Pi - \tilde{X}^2\Sigma^+$ transition of CaOH and CaOD. The rotational structure observed in these early studies was well described by models in which the radicals have linear structures for the ground and excited states. Subsequently, a number of high resolution optical LIF studies on the $\tilde{A}^2\Pi - \tilde{X}^2\Sigma^+$ and $\tilde{B}^2\Sigma^+ - \tilde{X}^2\Sigma^+$ systems of CaOH[24-31], CaOD[28,29,31,32] and SrOH[33,34] have appeared in the literature. Recently, the low-lying $\tilde{C}^2\Delta$ electronic state in CaOH/CaOD was observed Jarman and Bernath[35] via the electronically forbidden $\tilde{C}^2\Delta - \tilde{X}^2\Sigma^+$ transition. Despite this increased level of scrutiny, data for the excited vibrational levels of the alkaline earth monohydroxide radicals remains limited, with the majority of such information having been obtained in this laboratory.

The microwave spectra of the ground states of the CaOH[36] and SrOH/SrOD[37] radicals have been observed in direct absorption spectroscopy. While this work has provided highly accurate rotational constants for the $\tilde{X}^2\Sigma^+$ states, the resolution was inadequate to resolve the small hyperfine splittings.

More recent advances in experimental techniques have been applied to the

spectroscopic investigation of the alkaline earth monohydroxides. Whitman *et al.*[38] demonstrated that the technique of laser ablation/supersonic expansion could be used to produce sufficient quantities of gas phase CaOH in very low states of thermal excitation (T_{VIB} and $T_{ROT} \leq 50$ K). This method of production was subsequently employed by Steimle and co-workers[3] who measured the permanent electric dipole moments of CaOH and SrOH in the $\tilde{A}^2\Pi$, $\tilde{B}^2\Sigma^+$ and $\tilde{X}^2\Sigma^+$ states. The low internal temperatures achieved in the laser ablation/supersonic expansion source were further utilized in pump/probe microwave optical double resonance experiments on SrOH[39] and CaOH[40]. The extremely narrow linewidths observed in this work ($\leq$ 80 kHz) enabled the first determination of hyperfine parameters for the ground states of both radicals.

SrOH and CaOH have also been the object of a number of theoretical investigations. Bauschlicher and Partridge[41] carried out calculations on the dissociation energies of CaOH. An expanded and more detailed *ab initio* study of the structure and energetics of the alkali and alkaline earth monohydroxides by the same group was published in 1986[42]. In accord with all experimental data obtained for CaOH and SrOH to date, this study concluded that the ground state equilibrium structures are linear. Very recently, a ligand field approach[43] has been used to calculate the transition energies, molecular wavefunctions and dipole moments of the low-lying electronic states of the Ca, Sr and Ba monohydroxides. CaOH has been the subject of further theoretical investigations: electron propagator calculations have been carried out by Ortiz[44] and the permanent electric dipole moment in the $\tilde{A}^2\Pi$, $\tilde{B}^2\Sigma^+$ and $\tilde{X}^2\Sigma^+$ states has been calculated by Bauschlicher *et al.*[45] In addition, an electrostatic polarization model of the alkaline earth monohydroxides has been used by Mestdagh and Visticot[8] to determine dissociation energies and term energies of the low-lying states. Jakubek and Field[46] have also performed

ligand field calculations on CaOH in which atomic spin-orbit parameters were employed to calculate the molecular spin-orbit coupling constant for the $\tilde{C}^2\Delta$ state of CaOH.

2.3 Properties of the Low-lying Electronic States of the CaOH and SrOH

The visible spectrum of CaOH consists of a series of complex and congested band systems in the red (600 - 630 nm), yellow-green (540 - 570 nm), and blue (450 - 464 nm). For the SrOH radical, these systems are shifted to the red, where the known visible systems are centered at 660 and 640 nm. The electronic structure of these radicals is well described in terms of a simple ionic model, in which the chemical bonding is viewed as arising from closed shell M^{2+} and OH^- ions having a single unpaired electron on a molecular orbital localized on the metal atom. The $\tilde{A}^2\Pi$ and $\tilde{B}^2\Sigma^+$ states arise from the promotion of this non-bonding electron from a $nsnp_\sigma$ orbital ($\tilde{X}^2\Sigma^+$) to a metal $np_\pi(n - 1)d_\pi$ ($\tilde{A}^2\Pi$) or $np_\sigma(n - 1)d_\sigma$ ($\tilde{B}^2\Sigma^+$) hybrid orbital. Since the transitions are localized on the metal atom and are associated with the promotion of a non-bonding electron, the potential energy surfaces are very similar. The Franck-Condon factors thus strongly favor $\Delta v_n = 0$ sequences, which, owing to the similarity of the vibrational frequencies in these low-lying valence electronic states, are severely overlapped. Consequently at low resolution, the optical spectra of SrOH and CaOH appear virtually featureless.

The equilibrium structures of the alkaline earth monohydroxides are largely dependent on the nature (i.e. covalent versus ionic) of the chemical bonding. This has been thoroughly investigated by Bauschlicher *et al.*[42] for the ground $\tilde{X}^2\Sigma^+$states. If the bonding is primarily ionic and dominated by electrostatic forces, a linear structure is more energetically favorable. With

an increasing degree of covalency, the bending potential becomes flatter and eventually a bent equilibrium geometry is observed. For the lightest group IIA monohydroxide BeOH, the ionization potential of the metal atom is quite high and the electrostatic stabilization gained through formation of the hydroxide is insufficient to completely ionize the metal. Consequently there is a significant covalent character in BeOH and the bent structure is energetically favored[42,47]. For MgOH, a linear structure with a predominantly quartic potential is predicted,[42,47] and is consistent with experimental observations[48]. The analogous systems of the heavier alkaline earth atoms have an even greater ionic character associated with the chemical bonding and thus are linear[42].

In accord with earlier high resolution spectroscopic investigations[22,23] of the alkaline earth monohydroxides, the vibrational levels referred to herein are designated (v_1,v_2,v_3) where v_1 corresponds to the M-O stretch, v_2 the doubly degenerate bending mode and v_3 the O-H stretch. The lowest frequency vibration is that of the degenerate bend (with fundamental vibrational frequencies of $\approx$ 364 and $\approx$ 353 cm^{-1} for the ground states of SrOH and CaOH, respectively) which is also characterized by a large amplitude. The relatively low frequency of metal-oxygen stretch, 609 cm^{-1} for CaOH and 527 cm^{-1} for SrOH, is such that numerous accidental degeneracies of excited vibrational levels are observed. The O-H stretching frequency is a matter of some uncertainty. Jarman and Bernath[35] have published values of 3847(10) cm^{-1} for CaOH and 3766(10) cm^{-1} for SrOH, however, these estimates are considerably larger than the free ion value of 3555.6 cm^{-1}[49].

There are numerous experimental determinations of the ground state dissociation energy, D_0, of Ca-OH[50-53] and Sr-OH[51,53-55]. These measurements are generally in reasonable agreement with the values of 4.18 and

4.19 eV for CaOH and SrOH, respectively, calculated by Bauschlicher, Langhoff and Partridge[42]. The comparatively large magnitude of D_0 for these hydroxides attests to the ability of the low-lying electronic states to support a large manifold of excited vibrational levels.

The permanent electric dipole moments of the ground states of CaOH and SrOH have been determined[3] as 1.465(61) and 1.900(14) *D*, respectively. While these values may seem unexpectedly small for such predominantly ionic species, the observed values can be explained in terms of the large polarizabilities associated with the M^+ and OH^- ions which have the effect of decreasing the charge separation. In contrast to the ground state, the experimental determinations for the excited state dipole moments[3] are in poor agreement with the theoretical calculations[8,43,45]. The source of this discrepancy is uncertain, although vibronic interactions off-diagonal in Λ have been implicated[3].

Although the radiative lifetimes of the excited states of CaOH and SrOH have not been determined, Dagdigian *et al.*[56] have measured the corresponding quantities for the isoelectronic species CaF and SrF. While it is reasonable to expect that the radiative lifetimes for these isoelectronic species are of a comparable magnitude, it is conceivable that the lifetimes of the $\tilde{A}^2\Pi$ and $\tilde{B}^2\Sigma^+$ states of the monohydroxides may be significantly longer than the 20 to 30 ns range observed in CaF and SrF on account of vibronic mixing with the $\tilde{C}^2\Delta$ state through the degenerate bending mode. This type of interaction has no analogy in diatomic molecules.

Bond lengths associated with the equilibrium structure of the CaOH/CaOD and SrOH/SrOD radicals have been estimated by using high resolution gas phase data. Since not all of the vibration-rotation interaction constants α_i are known, vibrational corrections to the r_0 structure can only be estimated. The

ground state equilibrium O-H bond length of the Ca and Sr monohydroxides have been estimated at 0.930(7) Å[23] and 0.945 Å,[22] respectively, which, given the approximation involved, is reasonably close to the r_e value of the free ion (0.964 Å) given in ref. 49. Metal-oxygen bond lengths (r_e) for the $\tilde{X}^2\Sigma^+$ state are 1.976 Å[23] for CaOH and 2.102 Å[22] for SrOH. The latter value is considerably shorter than the bond length in either RbOH (2.301 Å[57]) or CsOH (2.391 Å[58]). Although accurate M-O stretch force constants are not yet available for the alkaline earth monohydroxides CaOH and SrOH, it is of some interest to to compare the fundamental vibrational frequencies as corrected for reduced mass. For example, using a simple approach analogous to that for diatomic species, the ratio of the force constants $k_{M\text{-}O}$(SrOH)/$k_{M\text{-}O}$(CsOH) is approximately 2.19, where the M-O stretching frequencies of ref. 22 are used. The larger force constants for the alkaline earth monohydroxides reflects the greater ionic attraction of the M^{2+} - O^- versus M^+ - O^- bond.

Chapter III

Experimental

3.1 Production of Gas Phase Radicals

Traditionally, gas phase spectroscopic investigations of molecules containing refractory element(s) have proven to be a formidable challenge to the experimentalist. A major impediment has been the difficulty associated with the gas phase production of such molecules. Only a handful of methods have been successful in producing sufficient number densities to permit spectroscopic observation. The more commonly used sources include laser ablation[59], oven methods[21,60,61], sputter sources[62] and microwave discharges[63]. These sources, however, generally exhibit a deficiency of some sort whether by virtue of a lack of generality, inability to produce molecules in a low state of thermal excitation or by prohibitive requirements in terms of the equipment needed.

For the work presented in this thesis, the gas phase radicals were produced in a flow-metal-reaction system,[21] more commonly referred to as a Broida-type oven. In contrast to earlier oven methods such as the heat pipe oven[60] or King furnace,[61] which typically produce molecules at thermal energies corresponding to 1000-1500 K, the inert gas bath used in the Broida oven method results in a substantial cooling of the product molecules. Under the conditions used in our experiments, the rotational and vibrational temperature of the radicals was estimated to be approximately 700 K.

The Broida oven used in this work is based on the design of West and co-workers[21] and is illustrated in figure 3.1. The metal sample is contained in a small alumina crucible (1" diameter) that is resistively heated by a preformed, commercially available tungsten wire basket (R. D. Mathis Co.,

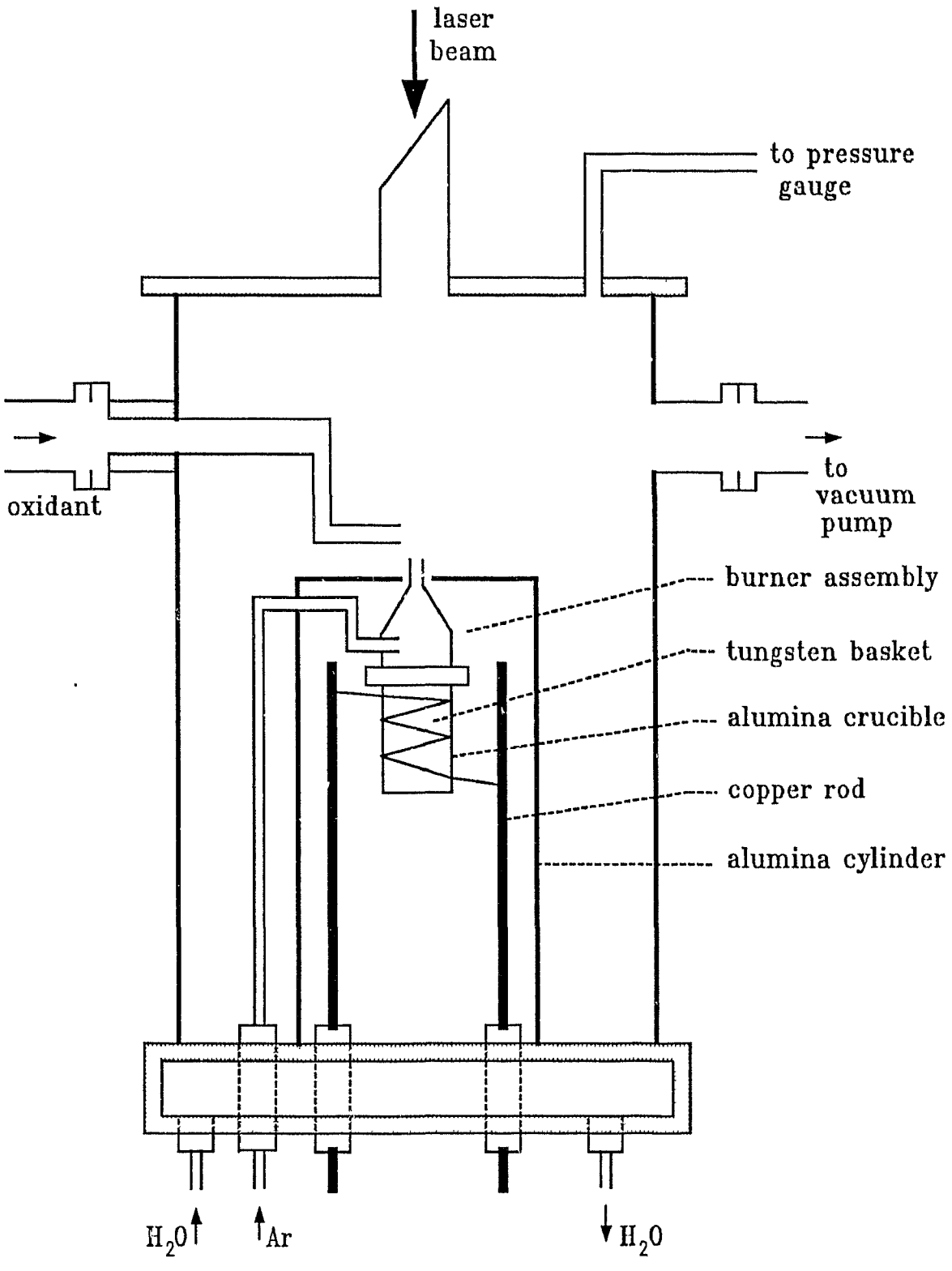

Figure 3.1: Broida oven.

B10 - 4 X .030W). A stainless steel burner in the shape of an inverted funnel is placed above the crucible. The burner and crucible are separated by a stainless steel ring to minimize direct heating of the burner by the tungsten wire basket. A crescent shaped section of 1/16" diameter stainless steel with a series of small holes (0.02") placed inside the stainless ring is used to introduce the carrier gas. Metal vapor entrained in the inert carrier is swept up through the burner into the reaction zone where it is reacted with a suitable oxidant.

The tungsten wire and crucible are supported by two copper rods that serve as electrical leads. These supports, along with the crucible/burner assembly, are contained in a 2.5" diameter alumina cylinder to minimize heat loss due to gas conduction, which is the primary mechanism of heat loss at reduced pressures and at temperatures below 2000 K[21]. The burner nozzle protrudes through a ¼" aperture in an alumina disc that encloses the upper end of the alumina cylinder. In later experiments, the heating efficiency was considerably enhanced by the addition of asbestos mat insulation around the exterior surfaces of the alumina cylinder. The entire assembly was housed in a 8" segment of 4" copper pipe. Several turns of copper tubing soldered to the outside of the housing allowed for water cooling. Brass end plates with flanged O-ring mounts enable the system to maintain reduced pressures of a few mtorr. The lower end plate was water cooled and contained four vacuum feedthroughs: two electrical feedthroughs for the copper electrodes, one for the carrier gas and a fourth surplus feedthrough.

The Broida oven is pumped through a 1" flanged mount opening located in either the upper end plate or the upper portion of the oven housing. Several different pumping speeds were tested; however, there appeared to be little correlation between the strength of the LIF signal and the pumping speed.

Ultimately a small vacuum pump (Leybold Heraeus D4A) was selected. The operating pressure inside the oven was continuously monitored through a ¼" opening in the upper end plate using a capacitance manometer (Vacuum General, CM-21).

The oxidant used for the present work, which was either H_2O, D_2O or H_2O_2, was contained in a Pyrex sidearm tube. It was found that the vapor pressure was sufficiently high such that adequate amounts of the oxidant could be obtained simply by pumping off the liquid at room temperature. A needle flow valve on the Pyrex sidearm provided control over the oxidant partial pressure. For the work on the $\tilde{A}^2\Pi$ - $\tilde{X}^2\Sigma^+$ system of CaOH and CaOD, a microwave discharge cavity was placed over the quartz tube carrying the oxidant gas to the reaction zone. A 2450 MHz microwave discharge (typically run at 50 - 75 W) was found to enhance the dispersed LIF signal considerably.

The presence of multiple flanged ports on the Broida oven enabled the reaction zone to be probed by the laser beam in either the horizontal or vertical directions. In either configuration, LIF could be viewed orthogonal to the laser beam through two separate optical windows. For the Doppler-limited excitation and resolved fluorescence experiments, the reaction zone was intersected by the laser beam in the vertical direction. In this configuration the burner assembly served as a convenient beam dump which greatly limited scattered laser light. The experimental configuration was modified for the IMF experiments by the addition of two Brewster mounted optical windows on opposite sides of the Broida oven. In these experiments, the two counterpropagating beams defined a horizontal plane through the oven.

The power requirements of the Broida oven were supplied by two transformers (Hammond, 165X5) connected in parallel. Typically, the Ca metal was vaporized using a current of approximately 35 A at 4 V. The lower melting

point of Sr enabled slightly lower settings to be used. Precise control of the heating was achieved using a variable transformer (Powerstat, 116B) to vary the primary voltage supplied to the transformers.

Of critical importance to the strength of the LIF signal was the condition and surface area of the metal to be vaporized. For the work on CaOH/CaOD, calcium shot (Aldrich, 99%) was used. Sr metal, however, which is much more prone to rapid oxidation upon even brief exposure to the atmosphere, was more difficult to deal with. Immediately prior to each experiment, the oxidized surface of a segment of Sr rod (Johnson Matthey Catalog Co., 98%) was scraped off and the segment was broken into small pieces ($\leq$ 2.0 cm diameter). With as little delay as possible, the metal charge was loaded into the Broida oven; after pumping down the oven for two hours, the metal was slightly heated in an atmosphere of $\approx$ 0.15 torr Ar (Linde prepurified, 99.998%). By slowly increasing the primary voltage to the heating element, the temperature of the metal charge was gradually increased. For the first three increments the sample was given a minimum of 30 min. to allow for thermal equilibriation; subsequent delays were limited to 5-10 min. During experiments, the metal sample was brought to just below the melting point (1112 K for Ca and 1041 K for Sr). If the melting point was exceeded, the efficient and stable operation of the metal charge over extended periods of time was considerably reduced. Under ideal conditions, operation of the Broida oven was limited to a maximum of about 5 hours, after which time the metal surface was damaged and/or the burner aperture was eclipsed by condensed metal vapor.

Optimum conditions in the Broida oven were attained in a metal rich environment with partial pressures of 5-6 torr Ar and a few mtorr of oxidant. Under these conditions, a strong visible chemiluminescence was observed. It was found that the intensity of this chemiluminescence was strongly correlated

to that of the LIF. Accordingly, the visible chemiluminescent emissions served as a useful means of optimizing the flame environment for the strongest LIF signal.

3.2 Dispersed Fluorescence

The resolved fluorescence experiments were carried out using a digitally interfaced scanning monochromator. Dispersed fluorescence was obtained from excitation of rotationally resolved features of the $\tilde{A}^2\Pi \leftarrow \tilde{X}^2\Sigma^+$ and $\tilde{B}^2\Sigma^+ \leftarrow \tilde{X}^2\Sigma^+$ systems. These experiments yielded complementary data to the laser excitation work, providing access to excited vibrational levels of the ground electronic state that might otherwise be experimentally difficult to observe. In principle, this technique may be used to observe vibrational levels up to the dissociation limit[64]; in practice, however, this is rarely possible. The Franck-Condon factors associated with the $\tilde{A}^2\Pi$ - $\tilde{X}^2\Sigma^+$ and $\tilde{B}^2\Sigma^+$ - $\tilde{X}^2\Sigma^+$ systems in the alkaline earth monohydroxides are such that $\Delta v_n = 0$ sequences are strongly favored. Consequently, the intensity of progressions observed in fluorescence decreases rapidly with increasing Δv_n, the effect of which, imposes limitations on our ability to observe bands characterized by large changes in the vibrational quantum number.

An important aspect of the present work was the ability to record high accuracy ($\leq$ 0.05 cm^{-1}) rotationally resolved fluorescence spectra using a unique laboratory built computer controlled spectrometer coupled with highly sensitive photon counting detection. The system was originally developed under the supervision of Coxon[65] to record the spectra of weak chemiluminescent emissions of diatomic cations. This apparatus was adapted in the present work to record dispersed LIF spectra of the CaOH/CaOD[29,31]and SrOH[34,66,67] radicals. In essence, the system consists of a scanning monochromator and

photon counting detector interfaced to a dedicated computer. The primary advantages in this experimental scheme include: (i) direct computer control of the experiment, (ii) simultaneous recording of experimental and calibration spectra, thereby eliminating time dependent errors associated with the drum wavelength calibration and (iii) electronic data acquisition.

A block schematic diagram of the experimental arrangement used in the resolved fluorescence work is given in figure 3.2. The LIF was dispersed by a 1.26 m f/9 Czenzy-Turner type scanning monochromator (Spex Industries, model 1269) fitted with a 2400 groove/mm grating (Bausch and Lomb) blazed at 5000 Å. The monochromator was controlled by a Spex compudrive with a scanning resolution capability of 0.001 Å per step in the first order. The LIF signal was detected photoelectrically with a selected GaAs photomultiplier (RCA C31034A-02) cooled to -20 ^{o}C in a RF shielded housing (PRI, model TE-192-RF). The photomultiplier signal was fed into a PAR 1120 amplifier/discriminator and PAR 1105 photon counter. Depending on the intensity of the LIF, the slit width was varied from 40 to 55 μm. Typically, the dark count was less than 10 counts s^{-1}, although the background noise level from the chemiluminescent reaction was usually in the vicinity of 100 counts s^{-1}. The experimental resolution of our dispersed fluorescence spectra was in the range of 0.2 to 0.3 cm^{-1}.

The calibration signal for the drum wavelengths was provided by a U/Ar hollow cathode discharge lamp running continuously at a current of 15 to 20 mA. When properly aligned, an adequate number of sufficiently intense U atomic lines were found in the 12000-14000 cm^{-1} region of interest. An electronically controlled shutter (Optikon model 21412AOT5B) positioned between the Broida oven and U lamp enabled discrimination of the calibration and experimental signals.

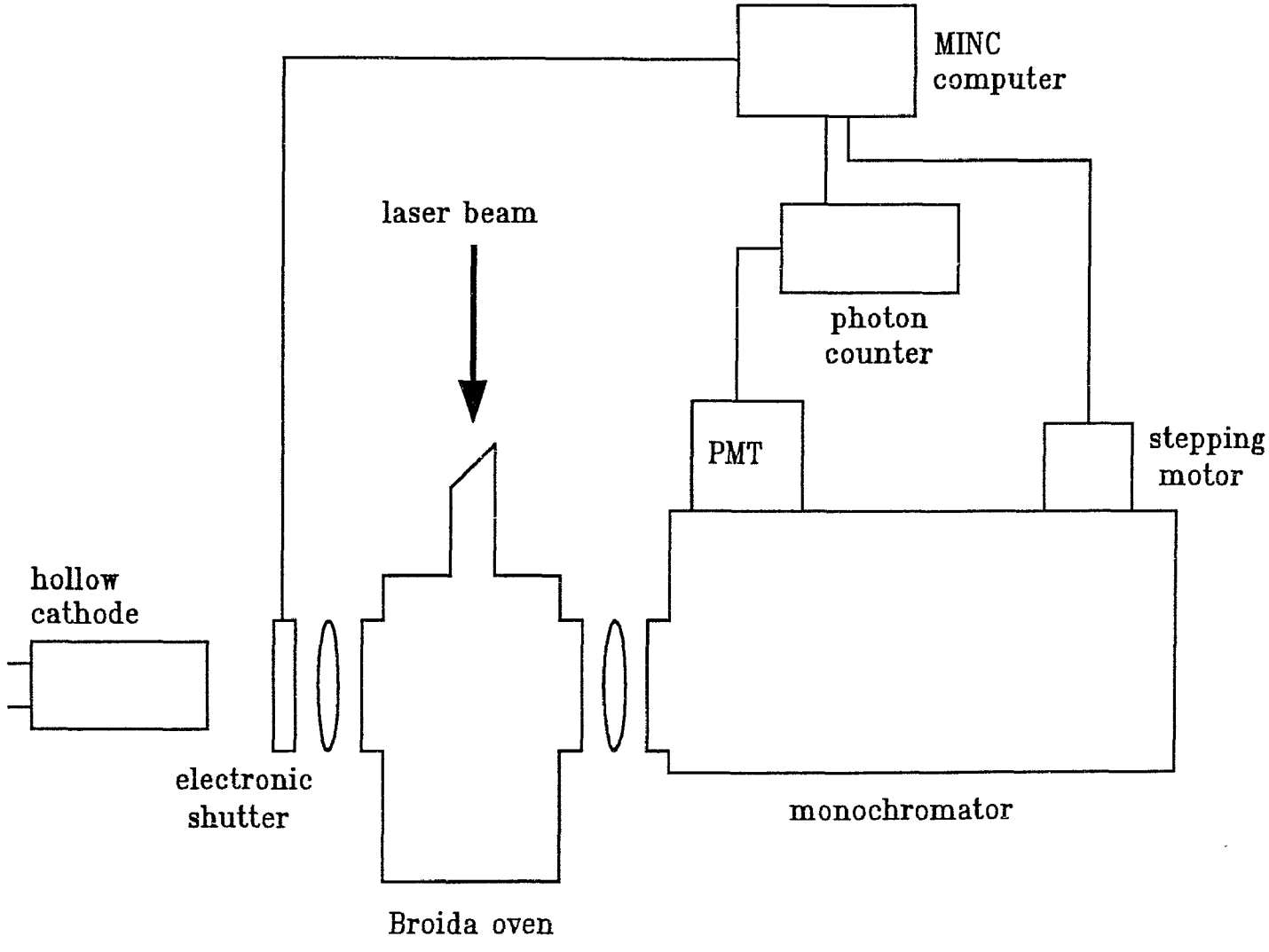

Figure 3.2: Schematic diagram of resolved fluorescence experiment.

The spectrometer, photon counting system and electronic shutter are interfaced to a MINC MNCII-AA computer (Digital Equipment Corporation) with model VT105 graphics terminal. Since the details of the interface construction and description of the software have been given elsewhere[65,68], only a brief summary of the operational details of the automated scanning monochromator will be given here.

The scan program that executes the automated scan sequence requires as input a calibration data file and three variables: the scan range, count time and resolution interval. In practice, the scan range was first determined by a low resolution dispersed fluorescence spectrum which would tentatively locate the unknown vibrational level. The length of the resolved fluorescence scans was generally limited to some 15-30 Å, just being sufficient to observe the *P* and *R* lines and, where appropriate, *Q* lines and satellite lines. The count time refers to the duration in seconds over which the signal is accumulated for each wavelength increment of the monochromator. Count times were varied from 0.1 to 1.0 s depending on the strength of the LIF signal. The resolution interval specifies the step size in Å by which the monochromator is incremented. The criterion for selecting an appropriate resolution interval depended on the the experimentally determined linewidths which, in turn, were a function of the slit width. For the 40 to 55 μm slit widths used in this work, the full width at half maximum (FWHM) of isolated rotational lines in the dispersed fluorescence spectra varied from approximately 0.1 to 0.2 cm^{-1}. The resolution interval used in the experiments represented a compromise between expediency and measurement accuracy. At one extreme, a small resolution interval resulted in a large number of points defining each line position and was experimentally time consuming. Conversely, if too few points were obtained to define a line, the measurement accuracy suffers. In the end,

a resolution interval in the range of 0.015 to 0.025 Å was chosen such that each line position was determined by 8 to 10 points.

For each band system observed in the dispersed fluorescence work, a separate input calibration file was created. This calibration file contained the drum wavelengths of between 8 and 15 atomic uranium lines spanning the wavelength region of interest. The uranium lines were selected from a previous scan of a U/Ar hollow cathode lamp: only the well isolated and more intense lines were used in the drum wavelength calibration procedure. Typically, the calibration data file contained two uranium lines before the start of the scan range and at least one beyond.

The sequence of events for the resolved fluorescence experiments is as follows. The variable input parameters, including the calibration data file name, are entered into the scan program. The laser frequency is set to correspond to that of a particular rotational transition obtained from the excitation spectrum. The drum wavelength of the monochromator is then manually set to the appropriate starting wavelength and the automated scan is initiated. For the U lines that are recorded at wavelengths before the start of the scan range, the monochromator rapidly slews to a wavelength of $\approx$ 0.2 Å before the calibration line wavelength and begins acquiring calibration data. Data is accumulated until the monochromator has scanned $\approx$ 0.2 Å beyond the calibration line at which point the monochromator is rapidly slewed to the next calibration line. After these initial calibration lines have been recorded the monochromator slews to the beginning of the scan range. During the scan, the interface accumulates counts for the specified count time at each wavelength increment. When the drum wavelength reaches the vicinity of a calibration line in the experimental scanning region, counts are accumulated at each increment with the shutter open and closed so that, in effect, a

separate spectrum of the dispersed LIF and calibration lines can be obtained. Upon reaching the end of the scan region, at least one other calibration line is recorded in a similar fashion as that for the initial calibration lines recorded before the start of the experimental scan.

The duration of a single dispersed LIF scan depended on several factors, namely the length of the scan, the resolution interval, the count time and the number of calibration lines. In most cases, each scan required approximately 15 to 25 minutes to complete. During this time, it was essential that the laser frequency remain fixed within the envelope of the Doppler broadened excitation profile. Stability of this kind in the single mode operation of the 699-29 ring dye laser could only be achieved after a precise optical alignment procedure was completed. As a precautionary measure, however, the laser frequency was continuously monitored for all the resolved fluorescence scans by measuring the output of the VET sensor on the 699-29 wavemeter. If the laser frequency drifted or suddenly jumped, a noticeable change in the VET sensor voltage was observed. On the few occasions when this occurred, the scan was immediately terminated and repeated when stable single mode laser oscillation was restored.

It is emphasized that the unique procedure used in these experiments enables the complete differentiation between the dispersed LIF and calibration signals even though the two are recorded virtually simultaneously. Without this ability many weaker calibration lines could be masked by the dispersed LIF and even strong lines could be distorted as a result of blending. Alternatively, strong calibration lines may prohibit the observation of weaker portions of the dispersed fluorescence spectrum. The use of a computer controlled shutter permits the separation of experimental and calibration spectra without the effects of any mutual contamination.

Table 3.1: Test of the accuracy of dispersed LIF measurements; values are given in cm^{-1}.

Laser Frequency ($\bar{\nu}_{laser}$)	Frequency As Determined By Monochromator ($\bar{\nu}_{mon.}$)	$\Delta\bar{\nu} = \bar{\nu}_{laser} - \bar{\nu}_{mon.}$
16437.0002	16436.986	0.0142
16446.9992	16447.003	-0.0038
16456.9999	16456.987	0.0129
16445.0015	16444.993	0.0085
16449.9992	16449.960	0.0392
16435.0013	16434.977	0.0243
16436.9994	16436.964	0.0354
16440.9994	16440.980	0.0194
16443.0001	16442.969	0.0311

The drum wavelength of the monochromator was calibrated for each resolved fluorescence scan by the U line positions that were recorded simultaneously with the dispersed LIF spectrum. A non-linear least-squares fit of the difference $\Delta\lambda$ between the drum wavelength λ_d and the interferometric U line measurements of Palmer et al.[69] was performed. The following five parameter function was used:

$$\Delta\lambda = a + b\lambda_d + c\lambda_d^2 + \alpha \sin\left[\frac{2\pi(\lambda_d - \beta)}{50}\right]. \qquad (3.1)$$

The inclusion of the sine function takes account of the periodic error of the lead screw which had been established by previous work in this laboratory[70]. With the present grating in the SPEX 1269 monochromator, each 360° rotation of the lead screw corresponds to a 50 Å change in wavelength, hence the origin of the numerical factor in the denominator of the sine term. The α and β are amplitude and phase factors, respectively.

The standard deviations of the least-squares fits of the uranium calibration lines were typically $\leq$0.01 Å, implying a similar measurement accuracy for the resolved fluorescence spectra. Although this had been verified in earlier work[68], a test of our optical alignment was undertaken by using the automated spectrometer to obtain wavelength measurements of scattered laser light for which the frequency was known to a high degree of accuracy from the internal wavemeter of the 699-29 ring dye laser. The results of these determinations, shown in table 3.1, indicate that the automated scanning monochromator is capable of measuring, on average, to an accuracy of better than 0.030 cm^{-1}.

3.3 Doppler Limited Excitation

The technique of laser excitation, in contrast to resolved fluorescence, is used primarily to obtain information on an excited electronic state. The

$\tilde{A}^2\Pi$ - $\tilde{X}^2\Sigma^+$ and $\tilde{B}^2\Sigma^+$ - $\tilde{X}^2\Sigma^+$ systems of SrOH, which are studied in the present work using laser excitation, are ideally suited to such investigations. These electronic transitions fall in the red and orange regions of the spectrum, which is very convenient for cw dye laser excitation.

For all excitation energies used in this work, the dye laser was pumped by the 514 nm line of a Coherent Innova 100 Ar^+ plasma tube. The pump power was maintained at $\approx$ 6.0 W, requiring a current varying between 43 and 49 A depending on the condition of the plasma tube and cleanliness of the Brewster windows and intracavity mirrors. Laser excitation spectra were obtained using a Coherent model 699-29 ring dye laser operating in single mode. The DCM and R6G laser dyes (Lambda Physik) were used for the work on the $\tilde{A}^2\Pi$ - $\tilde{X}^2\Sigma^+$ and $\tilde{B}^2\Sigma^+$ - $\tilde{X}^2\Sigma^+$ systems, respectively. The single mode output power of the dye laser varied from 100 mW to 600 mW depending on the output frequency and the age of the dye.

The laser frequency was determined by the internal wavemeter of the 699-29 dye laser which, according to the manufacturer's specifications[71], provides frequency measurement to an accuracy of better than 200 MHz at 6000 Å. During all excitation scans the integrity of the wavemeter was verified by recording I_2 fluorescence simultaneously. Comparison of the I_2 measurements to those of the standard I_2 atlas[72,73] resulted in small corrections of 0.005 cm^{-1} or less where necessary. Based on the standard deviations from the least-squares fits of our experimental measurements, the accuracy of the corrected excitation measurements was estimated to be $\approx$ 0.0035 cm^{-1}.

During initial experiments, the laser excitation spectra were recorded by detecting the total undispersed LIF. This detection scheme employed a spatial filter and long pass cut-off filter in conjunction with a low grade photomultiplier tube. Background chemiluminescence was suppressed by using a

mechanical chopper (PAR model 125A) and lock-in amplifier (PAR model 186A) to modulate the LIF. Owing to the presence of numerous overlapping band systems, the spectra obtained using this method were extremely congested. As a result, this method of detecting total LIF was abandoned in favor of a more discriminating detection scheme.

A considerable simplification of the laser excitation spectra was realized through the use of a monochromator as a tunable bandpass filter. With this detection scheme, the image of the LIF was incident on the slit of the monochromator. A slit width of 0.8 mm corresponding to a spectral resolution of $\approx$ 8 Å was used for the majority of the excitation spectra. In situations where the LIF signal was weak, the slit width was increased up to 3 mm. Alternatively, where spectral congestion was especially problematic, the discriminating ability of our selective detection scheme was enhanced by reducing the slit width to as low as 200 μm. As with the total fluorescence detection method described above, phase sensitive detection was used to suppress the background chemiluminescence even though the majority was eliminated through the spatial filtering afforded by the monochromator.

The selective detection scheme used in this work was based on the ground state vibrational spacings. Initially, the previous determinations of Nakagawa *et al.*[22] provided the fundamental vibrational frequencies of the ν_1 and ν_2 modes of SrOH. The resolved fluorescence experiments, which were run concurrently, later provided improved vibrational spacings that were used in subsequent excitation scans. For excitation of bands with $\Delta v_2 = +1$, $\Delta v_2 = +2$, and $\Delta v_1 = +1$, the dominant emissions to the ground state were characterized by $\Delta v_n = 0$. Consequently, by maintaining the monochromator to the red of the laser frequency by an amount corresponding to the appropriate ground state vibrational spacing, the LIF is selectively detected. In addition to reducing

the spectral complexity and enhancing the signal strength, this method of selective detection proved to be a valuable diagnostic tool.

Implementation of the vibrational selective detection scheme was relatively straightforward. As the dye laser was scanned up in frequency the monochromator drum wavelength was decreased by the necessary amount. Using a slit wavelength of 0.8 mm, the spectral bandpass of the monochromator provided sufficient leeway such that adjustment of the drum wavelength was required only once for every 5 cm^{-1} change in laser frequency. The spectral enhancement achieved using this method enabled most of the bands observed to be followed from the lowest J up to very high J ($\geq$ 80½). The only limiting factor in this respect was caused by overlapping of hotbands belonging to the same progression. The vibrational selective detection scheme could not completely suppress such bands because of the small anharmonicity of the ground state vibrations.

It was found that the vibrational selective method described herein is far more sensitive to anomalous branch intensities than the more familiar *PR* separation method. This kind of anomaly in the rotational branch structure is an interference effect that arises by modification of the Hönl-London factors when one of the states is perturbed. In understanding the origin of this enhanced sensitivity of the vibrational selective method to anomalous branch intensities, it should be emphasized that there are two important differences in these detection schemes. Unlike the *PR* separation method where near resonant fluorescence (i.e. to the same vibrational level) is detected, the present experimental scheme detects fluorescence to an excited vibrational level of the ground state lying at anywhere from $\approx$ 350 to 750 cm^{-1} above the vibrational level from which excitation occurred. Furthermore, whereas with the *PR* method, *P* branch excitation, for instance, is monitored through *R*

branch fluorescence or vice versa, using the vibrational selective detection method, *P* branch excitation is monitored through *P* branch fluorescence. Consequently the intensity anomaly may be magnified by the vibrational selective detection method, while there is an implicit averaging of the Hönl-London factors by the *PR* method.

Because of perturbations in the $\tilde{A}^2\Pi$ state, strong intensity irregularities were observed in the rotational branch structure of $\tilde{A}(010) \leftarrow \tilde{X}(000)$ and $\tilde{A}(010) \leftarrow \tilde{X}(010)$ bands of SrOH. Several branches were either anomalously weak or were completely missing in the excitation scans obtained using the vibrational selective detection method. Since the observation of both *P* and *R* branches was necessary in terms of providing ground state combination differences that are crucial to the unambiguous assignment of rotational quantum number, a non-resonant *PR* separation method was used to observe the anomalously weak branches. In all cases, the missing or weak branches were detected with a high signal to noise (S/N) ratio.

3.4 Intermodulated Fluorescence

The dominant contribution to the spectral linewidths in the laser excitation experiments described above was from Doppler broadening which arises because of the thermal motion of the absorbing or emitting molecules. At the reduced pressures used in our Broida oven source, the observed FWHM of rotationally resolved excitation features of SrOH were typically 0.016 cm^{-1}. At this resolution, much of the rotational structure in the $A(010)$ - $X(000)$ sub-bands was concealed on account of the extensive blending of coincident rotational transitions. In the present work, the technique of intermodulated fluorescence (IMF) is employed to overcome the limitations imposed by Doppler broadening.

A block diagram of the IMF experiment, first described by Sorem and Schawlow[74], is shown in figure 3.3. The output of the ring dye laser was split into pump and probe beams of equal intensity using a 50/50 beam splitter. The two counterpropagating and collinear beams, modulated at different frequencies f_1 and f_2, intersected the chemiluminescent flame in the horizontal plane. A dove prism was used to rotate the horizontal image of the LIF into coincidence with the vertical slit of the monochromator. Dispersed LIF was then detected using the vibration selective detection method described earlier.

Based on the saturation effect, a narrow absorption is observed when the counterpropagating pump and probe beams are in resonance with the same group of molecules having a zero velocity component along the beam axis. To be exact, the pump and probe beams were not precisely collinear for the present work, but were crossed at a small angle ($\approx$ 0.3 mrad) such that the region of intersection was coincident with the chemiluminescent flame. Although it may have been preferable to employ an arrangement in which the pump and probe beams were exactly overlapped, the optical feedback introduced into the resonant cavity caused severe difficulties with the single mode dye laser operation. At the small crossing angle used in this work, the beam overlap was sufficient such that a reasonably strong IMF signal was readily observed.

Doppler profiles were eliminated by chopping frequencies in the ratio of 3:5 where a difference frequency of $\approx$ 135 Hz was used for demodulation. Linewidths were further reduced by decreasing the pressure inside the Broida oven to between 2 to 3 torr. Under these conditions the IMF profiles were characterized by a FWHM of less than 100 MHz. Attempts to operate at pressures below 2 torr resulted in a precipitous attenuation of the LIF signal.

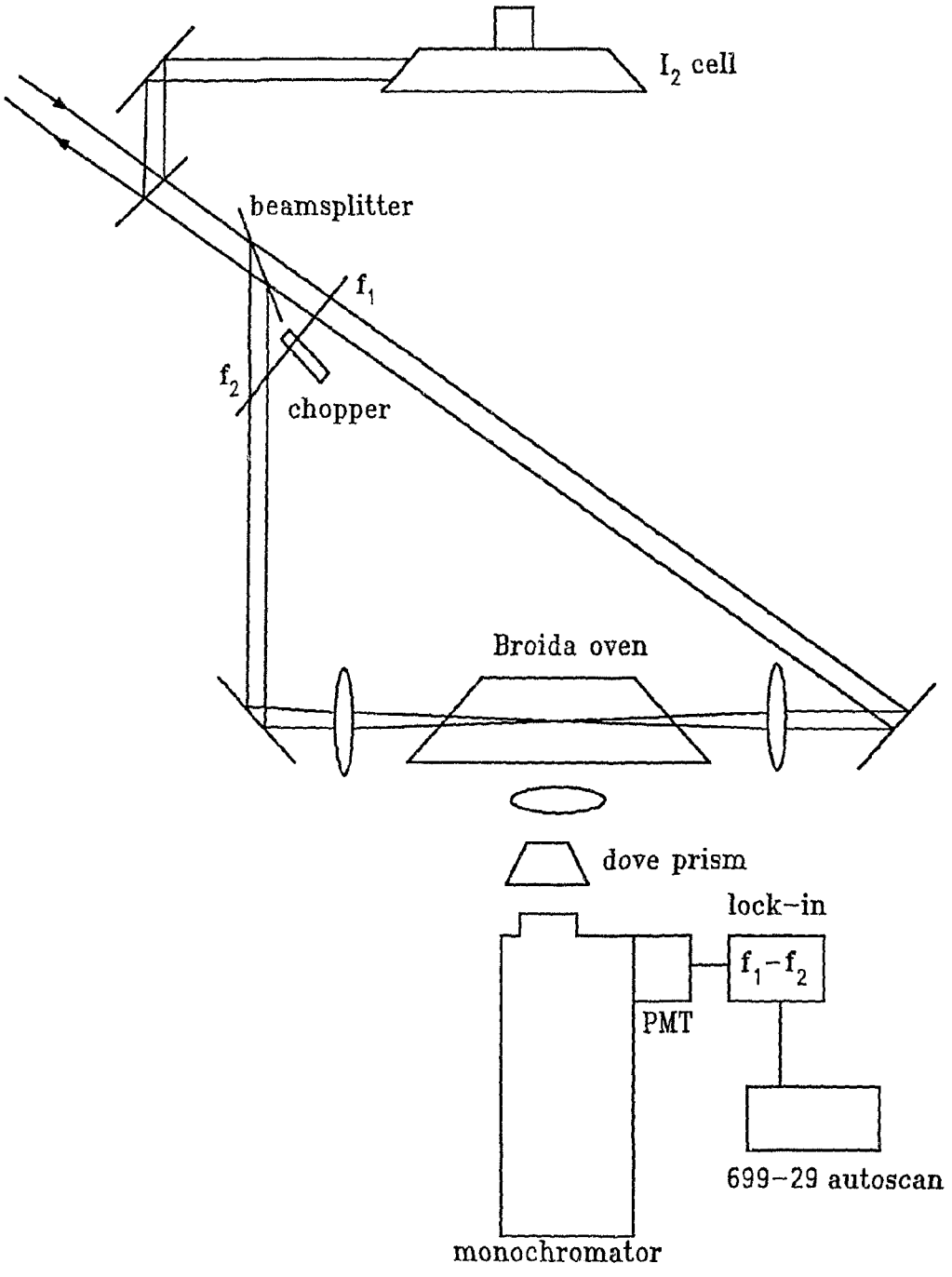

Figure 3.3: Schematic diagram for intermodulated fluorescence (IMF) experiment.

Chapter 4

A Review of Empirical Energy Level Formulae for Linear Triatomic Molecules

The total Hamiltonian for a linear triatomic molecule may be conveniently partitioned into vibronic and rotational components[75],

$$H = H_{EV} + H_{ROT}\,, \tag{4.1}$$

where the operator H_{EV} is a function of the electronic and vibrational coordinates and H_{ROT} may contain both rotational as well as vibrational and electronic coordinates. The following discussion concerning the representation of the observed molecular spectra by empirical formulae will follow the usual approach of considering the vibronic and rotational energies separately.

4.1 Vibronic Energy

As linear triatomic molecules, the alkaline earth monohydroxides have four vibrational degrees of freedom ($3N$ - 5) distributed over 3 normal modes of vibration, one of which is doubly degenerate. In non-degenerate electronic states (Σ states), the vibrational energy is represented by a simple power series expression[76]:

$$G(v_1,v_2,v_3) = \sum_i \omega_i(v_i + d_i/2) + \sum_i \sum_{k>i} x_{ik}(v_i + d_i/2)(v_k + d_k/2) + g_{22}\ell^2. \tag{4.2}$$

Here, each vibrational level is labelled by the vibrational quantum numbers v_1, v_2 and v_3, as discussed earlier. The parameters ω_i and x_{ik} are the harmonic vibrational frequencies and anharmonicity constants, respectively. The degeneracy, d_i, of the v_1 and v_3 stretching vibrations is unity whereas the bending vibration has a degeneracy of 2. The final term in eq. (4.2)

applies only to the degenerate bending vibration and is a consequence of the vibrational angular momentum, ℓ, associated with v_2. Although the concept of an angular momentum arising from a vibrational motion may at first seem anomalous, this can be considered to arise from excitation of one quantum in each of the two degenerate and orthogonal bending vibrations superimposed with a 90° phase difference. The resulting motion will involve a rotation of the nuclei about the z-axis, thereby giving rise to an angular momentum. The quantum number ℓ, which represents the magnitude of the projection of the vibrational angular momentum on the z-axis in units of $h/2\pi$, can take on only integer values given by

$$\ell = v_2, v_2 - 2, \ldots 1 \text{ or } 0 . \tag{4.3}$$

The symmetry species of the vibrational level is determined by ℓ, where values of $\ell = 0, 1, 2 \ldots$ corresponding to Σ, Π, $\Delta, \ldots$ vibrational levels, respectively. From eq. 4.3, it is apparent that vibrational levels with $v_2 \geq 2$ necessarily have more than one value of ℓ which, as a result of quartic anharmonicities in the bending potential, are not degenerate, but undergo a splitting of a magnitude that is determined by the parameter g_{22}. The different ℓ components of the vibrational levels with two or more quanta in the bending mode are distinguished by a superscript adjacent to v_2 as in (v_1, v_2^l, v_3).

While the Born-Oppenheimer approximation of separating electronic and nuclear motions may be applied to linear triatomic molecules in Σ electronic states, in orbitally degenerate electronic states ($\Lambda \geq 1$), the presence of complex vibrational-electronic interactions necessitates a more sophisticated approach. As first realized by Teller[77], the twofold degeneracy of a Π electronic state is removed when the linear configuration of the nuclei is disrupted by the bending vibration. The implications of this interaction have

a profound effect on the vibronic energy level structure of the $\tilde{A}^2\Pi(010)$ Renner-Teller components analyzed in this work. Accordingly, a brief summary of the results from several theoretical treatments of the vibronic energy levels of linear triatomic molecules in Π electronic states will be presented.

There are three angular momenta that are of importance in characterizing the vibronic wave functions of a linear triatomic molecule: (i) the total electron orbital angular momentum L, (ii) the electron spin angular momentum S, and (iii) the vibrational angular momentum G. The projections of these angular momenta on the internuclear axis are designated as Λ, Σ, and ℓ, respectively. In degenerate electronic states, the vibrational angular momentum ℓ is coupled with the orbital angular momentum Λ, such that

$$K = \Lambda + \ell \ , \tag{4.4}$$

where the resultant K is referred to as the vibronic angular momentum. Accordingly, states with $K = 0, 1, 2 \ldots$ are now designated as Σ, Π, $\Delta \ldots$ vibronic states. When electron spin is considered, it is necessary to define an additional quantum number P,

$$P = \Lambda + \Sigma + \ell \ . \tag{4.5}$$

Here, P is referred to as the resultant vibronic angular momentum including spin. Using the symbols defined above, the vibronic levels are labelled according to ${}^{2S+1}K_P$. Following spectroscopic convention, the vibronic state label is preceded by a designation of the electronic state and vibrational level as in $\tilde{A}^2\Pi(010)^2\Delta_{3/2}$, for example.

The quantum numbers Λ, Σ, ℓ, K and P are signed, where positive and negative values represent projections of the corresponding angular momenta on the linear axis in opposite directions. The relative signs of the projection quantum numbers are important in constructing wave functions with the

necessary transformation properties. However, in the following discussion of vibronic energy levels, only the unsigned (positive) values of these quantities will be considered.

Before presenting a more detailed description of the Renner-Teller effect, it is insightful to first consider the nature of the vibrational-electronic coupling on a purely *a priori* basis. The degeneracy of electronic states with $\Lambda \geq 1$ is a consequence of the cylindrical symmetry associated with a linear configuration. When the bending mode is excited and the nuclei move off axis, this element of symmetry is destroyed and the degeneracy is removed. The non-linear configuration of the nuclear charges creates a temporary electric dipole moment which perturbs the orbital motion of the electrons. As a result, the electronic motion is coupled to the instantaneous configuration of the nuclei and the Born-Oppenheimer approximation of separating electronic and nuclear motions breaks down. The bending potential for electronic states with $\Lambda > 0$ is then characterized by two curves that touch at the linear limit. This splitting of the potential energy curves for the bending vibration of a linear triatomic molecule is illustrated in figure 4.1. The diagram considers the case corresponding to small vibronic interaction, which is representative of the Renner-Teller effect in the alkaline earth monohydroxides.

The Renner-Teller effect may be considered equally well in the linear or bent molecule formalism. The choice is somewhat arbitrary since the two possibilities correspond to limiting cases, where, in practice, there is a smooth transition from the linear to bent limit. At one extreme is the linear molecule which is characterized by two rotational degrees of freedom and four vibrational degrees of freedom, two of which are distributed in the bending mode. The opposite extreme is the bent molecule with three degrees of freedom

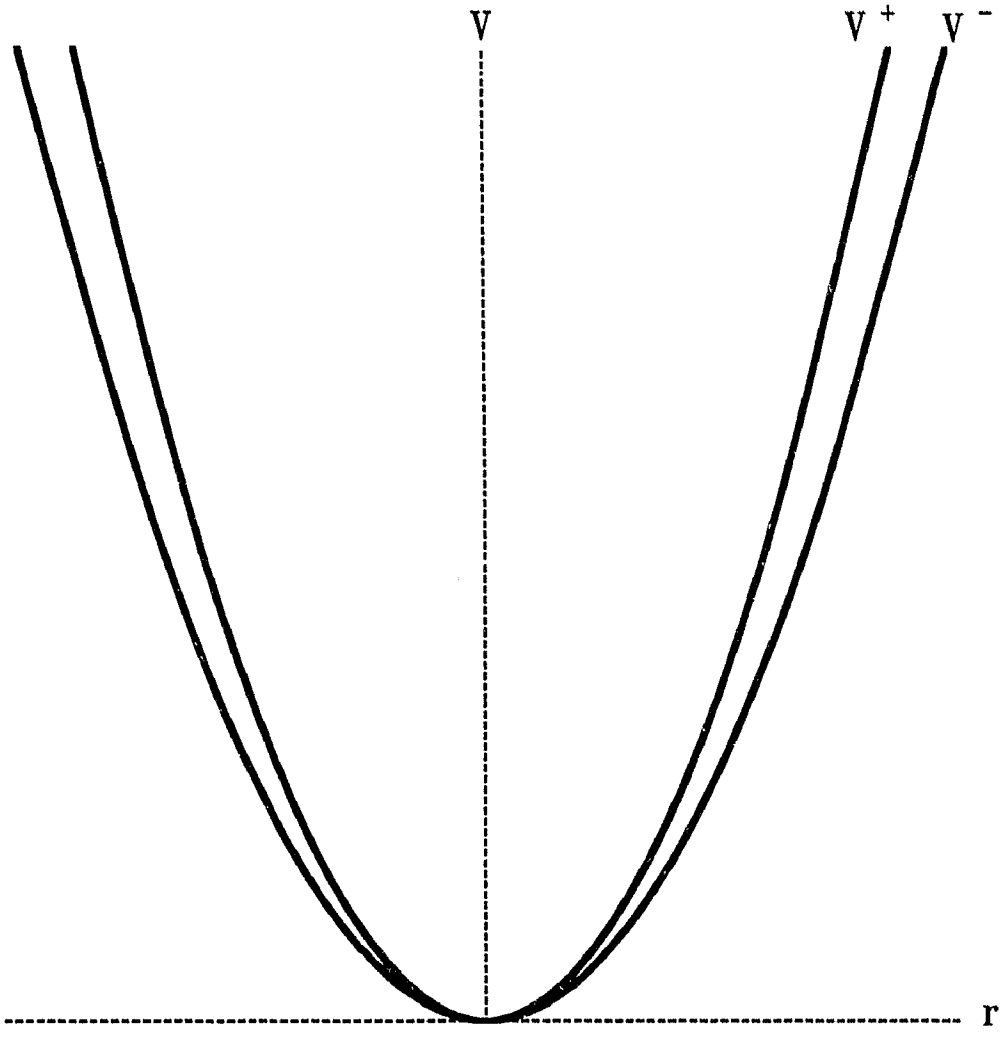

Figure 4.1: Potential functions for bending vibration in a Π electronic state.

for both the vibrational and rotational motions. The bending vibration is no longer degenerate in the bent molecule: evidently, one component of the bending vibration in the linear limit becomes a-axis rotation (z-axis in the linear case) in the bent molecule. Since both CaOH and SrOH are linear molecules, it is more natural to consider the Renner-Teller effect using the linear formalism. This choice of basis has the added advantage that the projection (ℓ) of the vibrational angular momentum on the linear axis remains well defined.

Rather than merely presenting the vibronic energy level expressions for a linear molecule in a Π electronic state that have been derived in the literature, this section will also consider the formulation of the problem and the general approach to its solution. Such an approach is essential to understanding many of the subtle effects that arise from the presence of a non-zero orbital angular momentum.

Neglecting x- and y-axis rotations, the Hamiltonian for the bending vibration of a linear triatomic molecule in a degenerate electronic state may be given as[79]

$$H = H_{EL}(\rho = 0) + H_B + H_{ROT}^{(z)} + H_{EL}^{'}. \tag{4.6}$$

Here, the bending coordinate ρ represents the amplitude of the displacement from the linear equilibrium and $H_{EL}(\rho = 0)$ is the zero order Hamiltonian for the linear configuration. H_B is the radial portion of H corresponding to the bending vibration kinetic energy and the operator $H_{ROT}^{(z)}$ represents the vibrational angular motion of the nuclei about the z-axis, which, in the absence of a non-zero electron spin, is defined according to[79]

$$H_{ROT}^{(z)} = \frac{h}{8\pi^2 c I^{(z)}} (J_z - L_z)^2 . \tag{4.7}$$

The $H_{EL}^{'}$ in eq. 4.6 is the perturbation operator that couples vibrational and

electronic angular momentum where[79,80],

$$H'_{EL} = V_0(\rho) + j_1 \rho\cos(\nu - \chi) + j_2 \rho^2\cos2(\nu - \chi) + \ldots \quad (4.8)$$

The vibrational and electronic angular coordinates χ and ν represent the orientation of the molecular plane and the azimuthal angle of the electrons with respect to an arbitrary reference plane, respectively. $V_0(\rho)$ is the potential of the bending vibration as a function of the bending coordinate ρ. The parameters j_1 and j_2 contain the effects of averaging each electron over the radial wave functions. The two cosine terms give rise to coupling between vibrational and electronic angular momenta. The first of these terms, $j_1 \rho\cos(\nu - \chi)$, is referred to as the dipolar operator and mixes electronic states with $\Delta\Lambda = \pm1$[80] (Herzberg-Teller coupling). The $j_2 \rho^2\cos2(\nu - \chi)$ term is of most interest, however, since it couples electronic states subject to $\Delta\Lambda = \pm2$,[79,80] and thus couples the $\Lambda = +1$ and $\Lambda = -1$ basis functions of a Π electronic state. Although this latter term has been called the Renner-Teller operator,[79-81] and indeed contributes to this effect in first order, the $j_1 \rho\cos(\nu - \chi)$ term may also make significant contributions in second order, as is the case in $\tilde{X}^2\Pi$ NCO[82] and NCS[83].

Using the Hamiltonian of eq. 4.6, the vibronic energies are obtained by the solution of the Schrödinger equation,

$$\left[H_B + H_{ROT}^{(z)} + V_0(\rho) + j_2 \rho^2\cos2(\nu - \chi) \right] \Psi(\nu, \chi, \rho) = E\, \Psi(\nu, \chi, \rho) \,. \quad (4.9)$$

The vibronic eigenfunctions $\Psi(\nu, \chi, \rho)$ are linear combinations of two separate eigenfunctions $\Psi^{\pm}$, reflecting the different eigenvalues ($\pm \Lambda$) of the L_z operator in eq. 4.7. The $\Psi^{\pm}$ wave functions may be resolved into electronic and vibrational parts according to[79]

$$\Psi^{\pm}(\nu, \chi, \rho) = \psi^{\pm}_{EL}(\nu - \chi) \cdot 2\pi^{-1/2} e^{iK\chi} \cdot \psi^{\pm}_{\nu,K}(\rho) \,, \quad (4.10)$$

where K is the eigenvalue of the J_z operator. Substituting these wave

functions in eq. 4.9, the solution to the Schrödinger equation can be represented by two coupled differential equations:[79]

$$\begin{bmatrix} H_B + U_K^-(\rho) - E & H_K(\rho) \\ H_K(\rho) & H_B + U_K^+(\rho) - E \end{bmatrix} \begin{bmatrix} \psi_{v,K}^- \\ \psi_{v,K}^+ \end{bmatrix} = 0 . \qquad (4.11)$$

The form of the potential $U_K^{\pm}(\rho)$ and the function $H_K(\rho)$ which couples the two vibrational potentials is determined by the choice of basis functions in eq. 4.10. Using a linear basis, these functions are[79]:

$$U_K^{\pm}(\rho) = V_0(\rho) + (h/8\pi^2 cI^{(z)})(K \pm \Lambda)^2 \qquad (4.12)$$

$$H_K(\rho) = \tfrac{1}{2} j_2 \rho^2 . \qquad (4.13)$$

Here $V_0(\rho)$ is the mean of the two Born-Oppenheimer potentials shown in figure 4.1 and the coupling function $H_K(\rho)$ represents half of the electrostatic splitting due to the Renner-Teller effect.

The solutions to eq. 4.11 can be considerably simplified by making several approximations. The approach taken originally by Renner[78] was to assume a harmonic potential for $V_0(\rho)$, in which case the $H_B + U_K^{\pm}$ in the coupled Shrödinger equations becomes the well known 2-*D* harmonic oscillator Hamiltonian. Using this approach, the perturbation of H_K couples the $\Lambda = +1$ and $\Lambda = -1$ eigenfunctions with the same $|K|$ subject to $\Delta v_2 = 0, \pm 2$. After taking sum and difference basis functions, the solutions to eq. 4.11 are conveniently grouped into three separate cases; (i) $K = 0$, (ii) $v_2 > K - 1$ ($K \neq 0$) and (iii) $v_2 = K - 1$. The energies of the Σ vibronic levels ($K = 0$) are given by[76,78,79,84]

$$G(v_2, K = 0) = \omega_2(v_2 + 1)(1 \pm \epsilon)^{1/2} , \qquad (4.14)$$

where ϵ is the Renner-Teller parameter and is defined according to

$$\epsilon = \frac{k^+ - k^-}{k^+ + k^-} . \qquad (4.15)$$

The $k^{\pm}$ are the force constants corresponding to the upper/lower potentials in figure 4.1. The $K = 0$ states occur in pairs having well defined symmetry species of Σ^+ and Σ^-. The + and - labels are used to describe wavefunctions that are either symmetric or antisymmetric with respect to reflection through a plane intersecting the z-axis. This transformation property of the vibronic eigenfunctions is unique to the Σ states and may be attributed to the fact that the coupling is made electronically diagonal only for $K = 0$ states by taking the sum and difference basis functions.

In states with $K \neq 0$, this coupling does not vanish. The vibronic energies for states with $K < v_2 + 1$ are[76,78,79,84]

$$G(v_2, K < v_2 + 1) = \omega_2(v_2 + 1)(1 - \epsilon^2/8) \pm \tfrac{1}{2}\, \epsilon\omega_2\left[(v_2 + 1)^2 - K^2\right]^{1/2} . \qquad (4.16)$$

The vibronic energy of the $K = v_2 + 1$ "unique" levels represent a special case and are affected by Renner-Teller interactions only in higher order. This is most easily seen by considering the first level of a $^1\Pi$ state which corresponds to the $v_2 = 0$, $\ell = 0$ basis level. This vibronic level is unpaired in the sense that there are no other states with the same $|K|$ value that lie, within the harmonic approximation, at the same energy. The Renner-Teller perturbation matrix element, which couples vibronic components diagonal in v_2 with $\Delta\ell = \pm 2$, cannot then couple the unique level to a degenerate level. Consequently, the Renner-Teller interaction mixes the unique levels only through the $\Delta v_2 = 2$ matrix elements which affects the energy levels in second order only. Fc the unique levels, the vibronic energies vary according to [76,78,79,84]

$$G(v_2, K = v_2 + 1) = \omega_2(v_2 + 1) - \epsilon^2\omega_2 K(K + 1)/8 . \qquad (4.17)$$

The effect of a non-zero electron spin angular momentum has a profound

effect on the Renner-Teller interaction in Π electronic states. The first theoretical treatment of the combined effects of Renner-Teller and spin-orbit coupling was carried out by Pople[81] who introduced the spin-orbit interaction,

$$H_{SO} = A L_z S_z, \tag{4.18}$$

as a perturbation to the Hamiltonian energy matrix used by Renner[78]. The expressions given in eqs. 4.14 and 4.16 for the $K = 0$ and $K < v_2 + 1$ vibronic levels are modified by the spin-orbit interaction according to[75,76,79,81]

$$G(v_2, K < v_2 + 1, \Sigma) = \omega_2(v_2 + 1) \pm r - (\epsilon^2/8)\omega_2(v_2 + 1)(1 \pm A K \Sigma/r) \tag{4.19}$$

where,

$$r = \tfrac{1}{2}\left\{ A^2 + \epsilon^2\omega_2^2\left[(v_2 + 1)^2 - K^2\right] \right\}^{1/2}. \tag{4.20}$$

For each K where $v_2 > 1$, and $0 < K < v_2 + 1$, four vibronic levels are obtained by taking $\Sigma = \pm \tfrac{1}{2}$.

As a consequence of the unpaired nature of the unique levels, the $|+\Lambda\rangle$ and $|-\Lambda\rangle$ factors are not appreciably mixed as they are for the non-unique levels. Thus, the expectation value of the orbital angular momentum $\langle L_z \rangle$ is not appreciably quenched and in multiplet states the spin-orbit interaction is only slightly modified by the Renner-Teller interaction. This weak second order dependence of the Renner-Teller interaction in the unique levels is manifest through an effective spin-orbit coupling constant A_{eff},

$$A_{eff} = A\left[1 - (\epsilon^2/8)K(K + 1)\right], \tag{4.21}$$

which is usually only slightly smaller than A since, in most cases, $\epsilon \ll 1$. Accordingly, in the presence of a spin-orbit interaction, the expression of eq. 4.17 is modified by the addition of $\pm \tfrac{1}{2}A_{eff}$. The pattern of vibronic energy levels associated with the bending mode in a $^1\Sigma$, $^1\Pi$ and $^2\Pi$ electronic

states is shown in figure 4.2 for the case where $A \gg \epsilon\omega_2$.

Investigations of the Renner-Teller effect in CCO[85,86], NCO[85,87] and NCN[85,86,88] have revealed the presence of small but persistent discrepancies between the vibronic energy level expressions given above and those observed experimentally. In particular, this was reflected in the energy separations between Renner-Teller components within the same vibrational level. An examination of this problem by Brown[85] revealed a term that arises due to vibronic mixing with other electronic states. This second order contribution to the vibronic energies is expressed in terms of an effective Hamiltonian for the $^2\Pi$ electronic state, where, within the harmonic approximation, the only non-zero matrix element is[85]

$$\langle \Lambda, v_2, \ell \,|\, g_K(G_z + L_z)L_z \,|\, \Lambda, v_2, \ell \rangle = g_K K\Lambda \,. \tag{4.22}$$

The g_K parameter is defined explicitly as[85]

$$g_K = \frac{\hbar}{8\pi c} \sum_{\eta'} \frac{(-1)^p \langle \eta \,|\, V_{11} \,|\, \eta' \rangle^2}{(\Delta E)^2} \,, \tag{4.23}$$

where the V_{11} operator is the dipolar term in the perturbation operator of eq. 4.8. The summation is carried out over electronic states η', where p is an even or odd integer for Σ or Δ states, respectively. Consequently, vibronic mixing with Σ states leads to positive contributions to g_K while mixing with Δ states gives rise to negative contributions. Typically the g_K term is small, usually being on the order of approximately 3 to 5 cm^{-1}.

A more rigorous derivation of the vibronic energy level expressions for a linear triatomic molecule in degenerate electronic states has been given by Brown and Jorgensen[84]. These authors have extended the perturbation calculation to fourth order, where both spin-orbit interactions and the effects of small anharmonicities are included. Since these modified

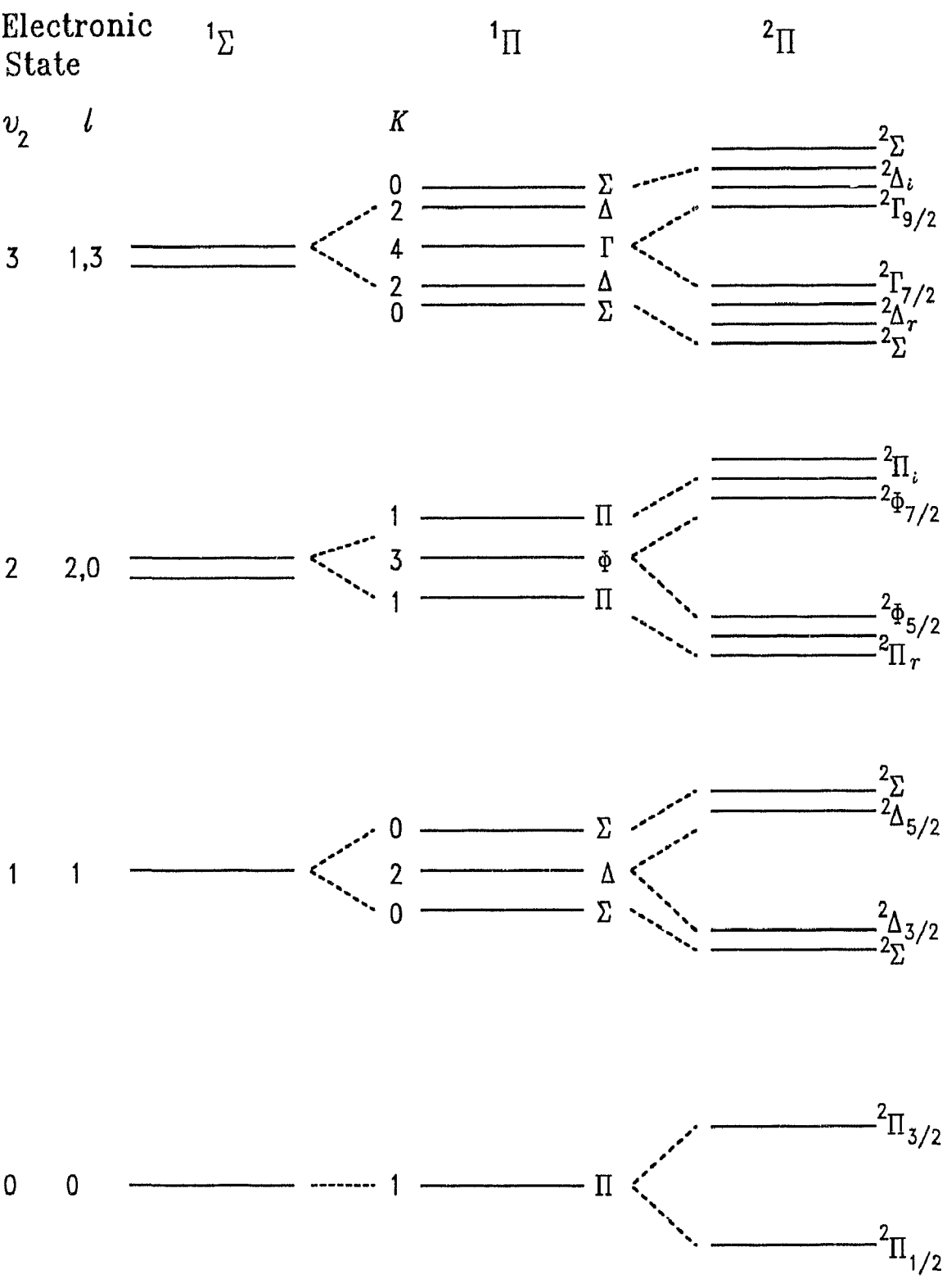

Figure 4.2: Vibronic energy levels for linear triatomic molecules in $^1\Sigma$, $^1\Pi$ and $^2\Pi$ electronic states.

expressions have a complex dependence on v_2 and K, general formulae are not given here; for the specific case of the $v_2 = 1$ components, however, the expressions simplify to:

$$G(\Delta) = 2\omega_2 - \tfrac{3}{4}\epsilon^2\omega_2 - \frac{21}{64}\epsilon^4\omega_2 - \frac{3}{16}\epsilon^2A^2/\omega_2 \pm \tfrac{1}{2}A(1 - \tfrac{3}{4}\epsilon^2) + 2g_K \quad (4.24)$$

$$G(\Sigma) = 2\omega_2 - \tfrac{1}{4}\epsilon^2\omega_2 - \frac{5}{64}\epsilon^4\omega_2 - \frac{1}{16}\epsilon^2A^2/\omega_2 \pm \sqrt{A^2(1 - \tfrac{3}{4}\epsilon^2) + 4\epsilon^2\omega^2(1 + \epsilon^2/32)^2} \quad (4.25)$$

The quartic anharmonicity constants have been omitted from the above expressions since they are expected to result in only relatively minor contributions to the vibronic energies and cannot be determined without data for several excited bending levels.

4.2 Rotational Energy Level Expressions

As shown in the previous section, the presence of a non-zero orbital angular momentum has a profound effect on the vibronic energies of a linear triatomic molecule. Certainly there is a correspondingly large effect on the rotational structure. In considering the modification of the rotational energy levels, it is necessary to take account of the orbital angular momentum in the selection of an appropriate basis function representation. Although the choice of basis has no influence on the eigenvalues, the selection is usually determined as a matter of computational convenience or through a consideration of the angular momenta coupling scheme that is most closely approximated in the molecule. The angular momenta L, S, and G couple with the rotation of the nuclear framework, R, to form a resultant J referred to as the total angular momentum exclusive of nuclear spin. The five limiting cases that describe various coupling schemes are designated as Hund's cases (a) through (e).

Because the spin angular momentum is uncoupled from the linear axis in Σ

electronic states, the $\tilde{B}^2\Sigma^+$ and $\tilde{X}^2\Sigma^+$ state rotational energies are discussed in a case (b) representation. On the other hand, in the $\tilde{A}^2\Pi$ state of SrOH, the situation is more complex and, depending on the vibronic level, the coupling is best approximated by either Hund's case (a), (b) or (c). The remainder of this chapter will be devoted to a consideration of the coupling schemes, basis functions and rotational energy level expressions appropriate to the low-lying electronic states of SrOH and CaOH.

For a $^2\Sigma$ electronic state, the internal magnetic field associated with the orbital angular motion of the electrons is insufficient to cause the total electron spin angular momentum $\boldsymbol{S}$ to undergo a precession about the internuclear axis. The spin uncoupling operator $B\bullet\boldsymbol{J}^{\pm}\boldsymbol{S}^{\pm}$ decouples $\boldsymbol{S}$ from the internuclear axis (z-axis) and, consequently, Σ, the projection of the spin angular momentum along the z-axis, is no longer defined and ceases to be a good quantum number. The coupling of angular momenta is then best approximated by Hund's case (b), which is illustrated in fig. 4.3, where $\boldsymbol{N}$, the total angular momentum exclusive of electron and nuclear spin, is formed according to

$$\boldsymbol{L} + \boldsymbol{G} + \boldsymbol{R} = \boldsymbol{N}, \tag{4.26}$$

where $\boldsymbol{R}$ is the rotational angular momentum of the nuclei and $\boldsymbol{L}$ and $\boldsymbol{G}$ are the orbital and vibrational angular momenta as indicated earlier. The total angular momentum from coupling of $\boldsymbol{N}$ with the spin angular momentum is then

$$\boldsymbol{N} + \boldsymbol{S} = \boldsymbol{J}. \tag{4.27}$$

Accordingly, the appropriate case (b) basis functions can be represented as $|\eta: K S N J\rangle$, where η is the electronic state.

A vector diagram for Hund's case (a) coupling is shown in figure 4.4. In this limiting case, the orbital, vibrational and spin angular momenta are all

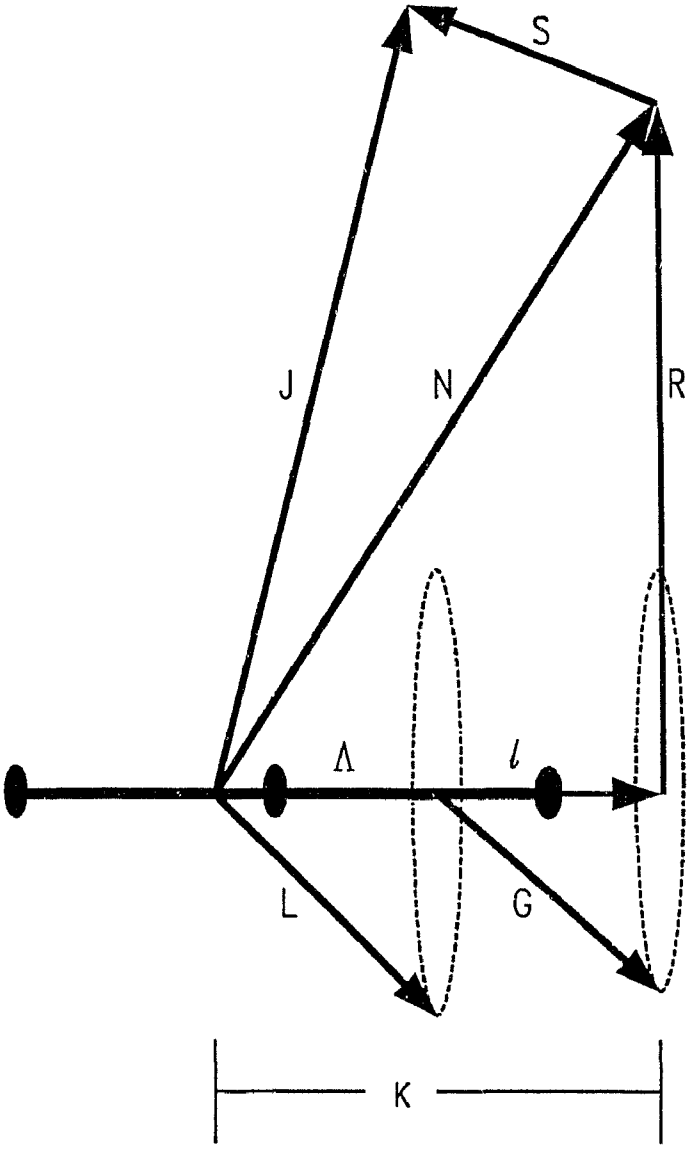

Figure 4.3: Vector diagram for Hund's case (b) coupling in a linear triatomic molecule.

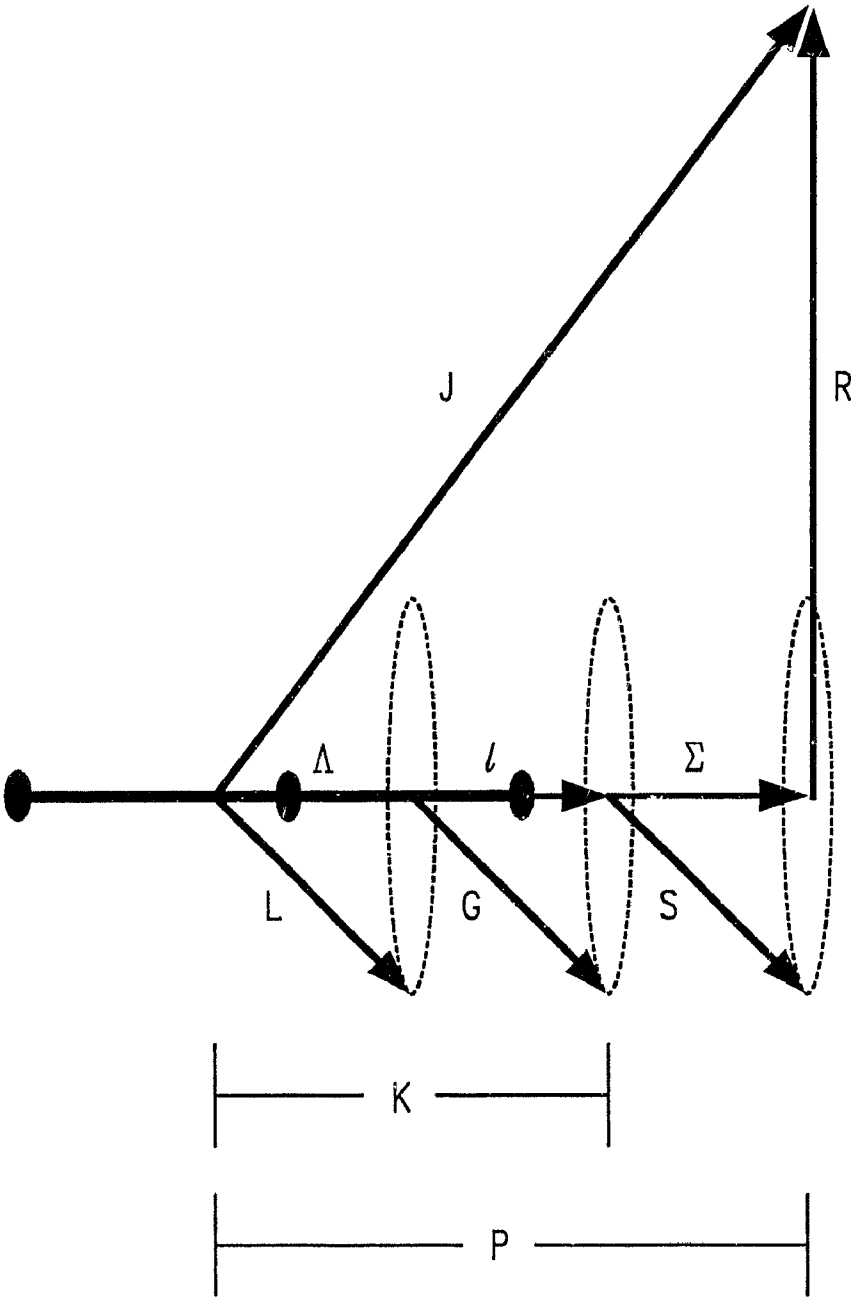

Figure 4.4: Vector diagram for Hund's case (a) coupling in a linear triatomic molecule.

strongly coupled to the internuclear axis. Considering rotation of the nuclei, the resultant $\boldsymbol{J}$ is formed according to

$$\boldsymbol{L} + \boldsymbol{G} + \boldsymbol{S} + \boldsymbol{R} = \boldsymbol{J}. \tag{4.28}$$

The case (a) basis has the maximum number of well defined components along the internuclear axis (Λ, ℓ, Σ, K, P). This enables the matrix elements of H_{SO} and H_{ROT} to be readily evaluated using simple raising and lowering operators[89] and consequently, the Hund's case (a) basis, denoted here as $|\eta: \Lambda, v_2, \ell, \Sigma; J, P\rangle$, is used most often.

Hund's case (c) coupling is more common in molecules containing heavy atoms where the spin-orbit interaction is very strong. In these situations, the orbital, vibrational and spin angular momenta form an intermediate resultant $\boldsymbol{J}_a$,

$$\boldsymbol{L} + \boldsymbol{G} + \boldsymbol{S} = \boldsymbol{J}_a \tag{4.29}$$

which then couples with $\boldsymbol{R}$ to form $\boldsymbol{J}$ (see figure 4.5). In contrast to the case (a) basis, the quantum numbers Λ, ℓ, and Σ are no longer strictly defined; only P, the projection of $\boldsymbol{J}_a$ on the internuclear axis, remains a good quantum number.

4.2.1 Rotational Energy Expressions for Non-degenerate Electronic States

With the exception of the degenerate bending vibrational levels, the rotational energy level expressions for linear triatomic molecules in $^2\Sigma$ electronic states are the same as those for diatomic molecules. Following Herzberg,[76] the usual case (b) expressions are,

$$F_1(N) = B_v N(N+1) - D_v[N(N+1)]^2 + \tfrac{1}{2}\gamma_v N \tag{4.30}$$

$$F_2(N) = B_v N(N+1) - D_v[N(N+1)]^2 - \tfrac{1}{2}\gamma_v(N+1). \tag{4.31}$$

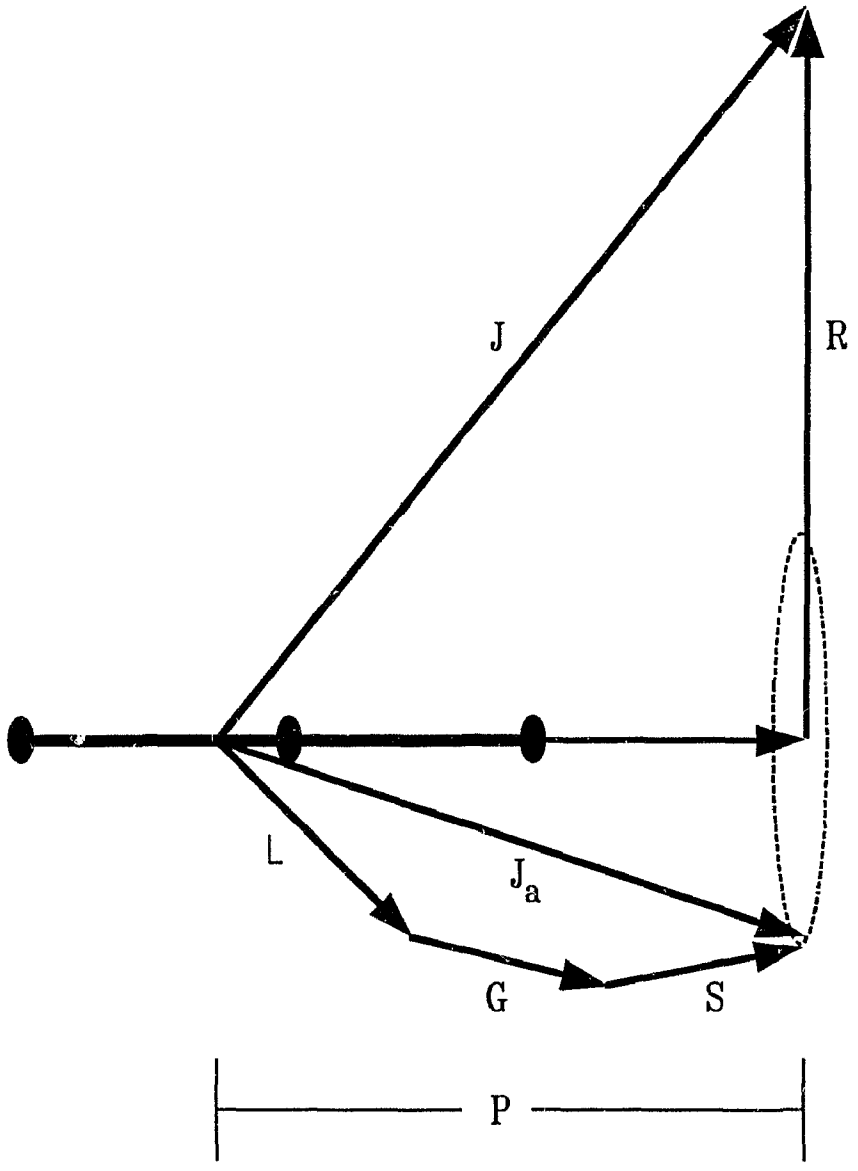

Figure 4.5: Vector diagram for Hund's case (c) coupling in a linear triatomic molecule.

Here the effective parameters B_v and γ_v are the familiar rotational and spin-rotation constants respectively. The constant D_v represents centrifugal distortion correction to the effective B_v rotational constant.

The fine structure associated with the degenerate bending levels is complicated by additional interactions for which there is no analogy in diatomic molecules. In particular, Corriolis interactions tend to couple the σ and π vibrational modes and lead to a splitting between the e and f parity levels in states with $\ell \geq 1$. This splitting, which may be viewed as arising from an uncoupling of the vibrational angular momentum from the linear axis, has been called ℓ-type doubling. To understand the origin of this effect, it is necessary to consider the effective Hamiltonian for a $^2\Sigma$ electronic state, which may be given as[90]

$$H = B\left[(J_x - S_x - G_x)^2 + (J_y - S_y - G_y)^2\right] + \gamma\,(S_z^2 - S^2 + J_xS_x + J_yS_y)\ , \quad (4.32)$$

where the effects of centrifugal distortion are neglected in this form of the Hamiltonian. The first term gives the energy of the rotating molecule and the second term is used to represent the spin rotation interaction where the operator used is of the form

$$H_{SR} = \gamma\,(J - S - G) \cdot S\ . \quad (4.33)$$

Terms arising from the spin-rotation interaction that are off-diagonal in v are omitted. The Hamiltonian of eq. 4.32 may be written using standard molecule fixed raising and lowering operators,

$$H = B(J^2 - J_z^2 + S^2 - S_z^2) + \gamma(S_z^2 - S^2) + (\tfrac{1}{2}\gamma - B)(J_+S_- + J_-S_+)$$

$$- B(J_+G_- + J_-G_+) + B(S_+G_- + S_-G_+) + B(G_x^2 + G_y^2)\ . \quad (4.34)$$

The terms containing the $G_\pm$ operator will have non-zero matrix elements off-diagonal in the vibrational quantum number v_2 and give rise to the

phenomenon of ℓ-type doubling. Using second order perturbation theory, interactions off-diagonal in v_2 may be treated using an effective Hamiltonian, where, in doublet electronic states, the ℓ-type doubling matrix elements arise from an effective operator of the form[90]

$$H_l = -\frac{B^2}{\Delta v}\left(J_+S_+G_-^2 + J_-S_-G_+^2 \right) + \frac{B^2}{\Delta v}\left(J_+^2G_-^2 + J_-^2G_+^2 \right) . \qquad (4.35)$$

where the energy denominator Δv represents the separation of the interacting vibrational levels. The evaluation of matrix elements involving the **G** operator involve consideration of the 2-D harmonic oscillator and a slightly more complicated form of the operator. This has been considered by Merer and Allegretti[90] and leads to $\Delta\ell = \pm 2$ matrix elements of the type

$$\langle \ell, \Sigma |\ H^{(2)} |\ \ell\pm2, \Sigma\rangle = \tfrac{1}{4}\, q_v^{\mathrm{v}}\left[(v_2\mp\ell)(v_2\pm\ell+2)\right]^{1/2}\left[J(J+1) - (\ell+\Sigma)(\ell+\Sigma\pm1)\right]^{1/2} \times\left[J(J+1) - (\ell+\Sigma\pm1)(\ell+\Sigma\pm2)\right]^{1/2} \qquad (4.36)$$

$$\langle \ell, \Sigma\pm1 |\ H^{(2)} |\ \ell\pm2, \Sigma\rangle = -\tfrac{1}{2}\, q_v^{\mathrm{v}}\left[(v_2\mp\ell)(v_2\pm\ell+2)\right]^{1/2}\left[J(J+1) - (\ell+\Sigma\pm1)(\ell+\Sigma\pm2)\right]^{1/2} \times\left[J(J+1) - (\ell+\Sigma\pm1)(\ell+\Sigma\pm2)\right]^{1/2}\left[S(S+1) - \Sigma(\Sigma\pm1)\right]^{1/2} . \qquad (4.37)$$

Here, q_v^{v} is referred to as the ℓ-type doubling parameter and according to Nielsen *et al.*[91,92], is given by

$$q^{\mathrm{v}} = -\frac{2B_e^2}{\omega_2}\left[1 + 4\sum_i \frac{\zeta_{2i}^2\omega_2^2}{\omega_i^2 - \omega_2^2} \right] \qquad (4.38)$$

For the $v_2 = 1$ (Π vibronic) level of a $^2\Sigma$ electronic state, the non-interacting 2 × 2 matrices corresponding to the *e* and *f* parity levels are readily diagonalized and yield the familiar energy level expressions[76,87,93]

$$F_1(N, {}^{e}_{f}) = B_v\left[N(N+1) - \ell^2\right] - D_v\left[N(N+1) - \ell^2\right]^2 + \tfrac{1}{2}\gamma_v N \pm \tfrac{1}{2} q_v^{\mathrm{v}} N(N+1) \qquad (4.39)$$

$$F_2(N, {}^{e}_{f}) = B_v\left[N(N+1) - \ell^2\right] - D_v\left[N(N+1) - \ell^2\right]^2$$

$$- \tfrac{1}{2}\gamma_v(N+1) \mp \tfrac{1}{2} q_v^{v} N(N+1) , \qquad (4.40)$$

where the usual case (b) notation for Σ electronic states is employed.

The $v_2 = 2$ level in a Σ electronic state is split into Σ ($\ell = 0$) and Δ ($\ell = 2$) vibronic components that are separated by $4g_{22}$. As with the $v_2 = 1$ vibrational level, terms in the Hamiltonian containing the $G_{\pm}$ operator mix vibrational levels off-diagonal in v_2. Using the effective operator of eq. 4.35, these interactions are transformed into the diagonal v_2 blocks and in the case of the $v_2 = 2$ level, lead to off-diagonal matrix elements between the Σ and Δ components. Typically, the effects of this ℓ-uncoupling phenomenon are relatively minor and are manifest primarily through a small splitting of the e and f parity components of the Δ levels. For the $\ell = 0$ component, the rotational energy level expressions of eqs. 4.30 and 4.31 may be used, whereas for the $\ell = 2$ levels, the rotational energy is given by[76,93]

$$F_1(N, {}^{e}_{f}) = B_v\left[N(N+1) - \ell^2\right] - D_v\left[N(N+1) - \ell^2\right]^2$$

$$+ \tfrac{1}{2}\gamma_v N + \Phi(N, {}^{e}_{f}) \qquad (4.41)$$

$$F_2(N, {}^{e}_{f}) = B_v\left[N(N+1) - \ell^2\right] - D_v\left[N(N+1) - \ell^2\right]^2$$

$$- \tfrac{1}{2}\gamma_v(N+1) + \Phi(N, {}^{e}_{f}) . \qquad (4.42)$$

The $\Phi(N, {}^{e}_{f})$ terms in eqs. 4.41 and 4.42 lead to ℓ-type splittings that vary approximately as $q_{\text{eff}}^{v} N(N+1)[N(N+1) - 2]$. It should be emphasized that the q_{eff}^{v} here is not the ℓ-type doubling parameter in eq. 4.38, rather is merely an effective parameter where in general $q_{\text{eff}}^{v} \ll q^{v}$.

4.2.2 Rotational Energy Expressions for $^2\Pi$ Electronic States

For vibrational levels of a $^2\Pi$ electronic state in which there is no

TABLE 4.1: Matrix representation of a Hund's case(a) $^2\Pi$ state.

$\mid {}^2\Pi_{3/2}; J \pm \rangle$	$\mid {}^2\Pi_{1/2}; J \pm \rangle$
$T_v + \frac{1}{2}[A_v + A_{D_v}(z - 2)] + B_v(z - 2) - D_v[(z - 2)^2 + z - 1]$	$-[B_v - 2D_v(z - 1) \mp \frac{1}{2} q_v(J + \frac{1}{2})] (z - 1)^{1/2}$
$-[B_v - 2D_v(z - 1) \mp \frac{1}{2} q_v(J + \frac{1}{2})] (z - 1)^{1/2}$	$T_v - \frac{1}{2}[A_v + A_{D_v} z] + B_v z - D_v(z^2 + z - 1) \mp \frac{1}{2} (p_v + 2q_v) (J + \frac{1}{2})$

$z = (J + \frac{1}{2})^2$; the upper/lower signs refer to e/f levels.

excitation of the degenerate bending mode, $K = 1$ and the rotational energies are well represented by the standard Hund's case (a) expressions for diatomic molecules in $^2\Pi$ electronic states. Using the matrix elements of Kotlar *et al.*[94], the 2 × 2 Hamiltonian is given explicitly in table 4.1. The p^e and q^e here are the Λ-type doubling parameters that arise when second order corrections to the Hamiltonian are included. The Λ-type doubling constants are obtained through a van Vleck transformation and "fold-in" the effects of distant perturbing Σ electronic states, where the parameters p^e and q^e are defined according to[94]

$$p_v^e = 2\sum_{v'} \frac{\langle v|\ AL_+\ |v'\rangle\langle v|\ BL_+\ |v'\rangle}{E_v - E_{v'}} \tag{4.43}$$

$$q_v^e = 2\sum_{v'} \frac{\langle v|\ BL_+\ |v'\rangle^2}{E_v - E_{v'}} \tag{4.44}$$

Here AL_+ and BL_+ represent off-diagonal contributions from the spin-orbit and rotational Hamiltonians, respectively. The term in the denominator, $E_v - E_{v'}$, is the energy separation of the interacting vibrational levels in the Π and Σ electronic states.

When the degenerate bending mode is excited, the rotational energy levels of a $^2\Pi$ state are modified by both spin-orbit and Renner-Teller interactions. The most comprehensive derivation of rotational energy level expressions has been carried out by Hougen[75]. In this treatment, the vibronic levels of the $^2\Pi$ electronic state are divided into three groups: the $K = 0$ (Σ vibronic) states, the $K = v_2 + 1$ "unique" levels, and pairs of states with $0 \neq K \neq v_2 + 1$. In the present work, the observation of the bending mode is limited to the $v_2 = 1$ level for which the vibronic structure is characterized by four Renner-Teller components, namely the $\kappa^2\Sigma$, $^2\Delta_{5/2}$, $^2\Delta_{3/2}$, and $\mu^2\Sigma$

sub-states. The ensuing discussion of rotational energies will only consider expressions for these levels.

$K = 0$ Levels

The $^2\Sigma$ vibronic states are obtained when the projection of the vibrational angular momentum ℓ is of equal and opposite magnitude to that of the electronic orbital angular momentum Λ and we have $K = \Lambda + \ell = 0$. In the $v_2 = 1$ manifold, the two Σ states correspond to the components of highest and lowest energy and are designated as κ and μ, respectively. The μ and κ labels do not describe any particular intrinsic quality of the Σ states, rather, are merely convenient labels introduced by Hougen[75]. In the absence of spin-orbit interaction, the vibronic eigenfunctions of the two Σ states will have the species of Σ^- and Σ^+. However, in a strict sense, the $\pm$ labels are no longer applicable for non-zero spin-orbit interaction.[75,81] Despite this, even for a strong spin-orbit coupling, the Σ states may be designated as $\Sigma^{(+)}$ and $\Sigma^{(-)}$ denoting the leading character of a Σ^+ or Σ^- state, respectively.

The $^2\Sigma$ sub-states in the $v_2 = 1$ moiety are obtained when the orbital angular momentum is cancelled by the vibrational angular momentum and, unlike $^2\Sigma$ states of diatomic molecules, may be characterized as Hund's case (a) or (c). In other situations, where the spin is uncoupled from the linear axis, the $^2\Sigma$ states may be most appropriately viewed in a case (b) representation. In the $\tilde{A}^2\Pi$ state of SrOH, where the spin-orbit splitting is large and $A \gg \epsilon\omega_2$, the $^2\Sigma$ and $^2\Delta$ components occur in pairs that lie very close to one another. The upper and lower pairs of vibronic components may then be considered as two separate electronic states corresponding to the $\Omega = ½$ and $\Omega = {}^3/_2$ components of a Hund's case (c) state.

The appropriate energy level expressions for the $K = 0$ states are [75]

$$F[\,\kappa^2\Sigma,\, J(-)^{J\pm\frac{1}{2}}\,] = T_{ev} + r + \tfrac{1}{4}B_{\rm eff}^{\kappa} + B_{\rm eff}^{\kappa}\,(J+1)$$

$$- [D_{\rm eff}^{\kappa}\, J^2(J+1)^2 \pm 2D\sin 2\beta (J+\tfrac{1}{2})^3\,] \pm \tfrac{1}{2}\,p(J+\tfrac{1}{2}) \qquad (4.45)$$

$$F[\,\mu^2\Sigma,\, J(-)^{J\mp\frac{1}{2}}\,] = T_{ev} - r + \tfrac{1}{4}B_{\rm eff}^{\mu} + B_{\rm eff}^{\mu}\,J(J+1)$$

$$- [D_{\rm eff}^{\mu}\, J^2(J+1)^2 \pm 2D\sin 2\beta (J+\tfrac{1}{2})^3\,] \pm \tfrac{1}{2}\,p(J+\tfrac{1}{2}) \qquad (4.46)$$

where the parameters in eqs. 4.45 and 4.46 are defined according to

$$B_{\rm eff}^{\kappa} = B[1 + (B/2r)\cos^2 2\beta\,] \qquad (4.47)$$

$$B_{\rm eff}^{\mu} = B[1 - (B/2r)\cos^2 2\beta\,] \qquad (4.48)$$

$$p = 2B\sin 2\beta \qquad -2B \le p \le 2B \qquad (4.49)$$

$$D_{\rm eff}^{\kappa} = D[1 + (2B/r)\cos^2 2\beta\,] \qquad (4.50)$$

$$D_{\rm eff}^{\mu} = D[1 - (2B/r)\cos^2 2\beta\,] \qquad (4.51)$$

$$r = \tfrac{1}{2}\left\{A^2 + [\,(v_2+1)^2 - K^2\,]\epsilon^2\omega_2{}^2\right\}^{\frac{1}{2}} \qquad (4.52)$$

$$r\sin 2\beta = \tfrac{1}{2}\,\epsilon\omega_2\left\{(v_2+1)^2 - K^2\right\}^{\frac{1}{2}} \qquad (4.53)$$

$$r\cos 2\beta = \tfrac{1}{2}\,A. \qquad (4.54)$$

Based on these expressions, the large apparent spin-rotation of the Σ states is a function of the electrostatic parameter $\epsilon\omega_2$.

$K = 2$ States

The $^2\Delta$ vibronic level forms the innermost pair of sub-states in the $v_2 = 1$ level. As a unique level, the spin-orbit splitting is only slightly modified by the Renner-Teller interaction. In a case (a) notation, the rotational energy levels are given by[75]

$$F(J > K - \tfrac{1}{2}) = C' + B[(J + \tfrac{1}{2})^2 - K^2] \pm \tfrac{1}{2}[4B^2(J + \tfrac{1}{2})^2 + A_{\text{eff}}(A_{\text{eff}} - 4BK)]^{\frac{1}{2}}$$

$$- D(J + \tfrac{1}{2})^4[1 \pm 4\{4(J + \tfrac{1}{2})^2 + Y(Y - 4K)\}^{-\frac{1}{2}}] \quad (4.55)$$

where

$$C' = -(v_2 + 1)(v_2 + 2)(\epsilon\omega_2/8) \quad (4.56)$$

Here $Y = A_{\text{eff}}/B$ and the effective spin-orbit coupling constant correct to third order is $A_{\text{eff}} = A(1 - \frac{3}{4}\epsilon^2)$. The effect of Λ-type doubling, which is expected to be very small, can be modeled by the inclusion of an additional term having a form approximated by J^{2P} [75].

Chapter V

Investigation of Excited Vibrational Levels in the $\tilde{X}^2\Sigma^+$ State of CaOH and CaOD by Resolved Fluorescence Spectroscopy

5.1 Introduction

As discussed earlier, dispersed fluorescence provides an extremely powerful means of accessing excited vibrational levels of an electronic ground state. While CaOH and CaOD have been the subject of numerous spectroscopic investigations[3,23-32,35,36,38] over the last decade, remarkably little is known of the ground $\tilde{X}^2\Sigma^+$ electronic state. Prior to our dispersed fluorescence work[29], the observation of rotational structure in both isotopomers had been confined to the $\tilde{X}^2\Sigma^+(000)$ level. For CaOH the most accurate rotational constants have been provided by the microwave work of Ziurys *et al.*[36] and the pump/probe MODR experiments of Scurlock and co-workers[3]. In the case of CaOD, the most precise rotational constants for the (000) level are those obtained from optical work[23,31]. Tentative assignments of the ground state vibrational structure of CaOH and CaOD have been obtained from low resolution dispersed fluorescence from the $\tilde{A}^2\Pi(000)$ level[23].

In an earlier investigation[28] of the rotational structure of the $\tilde{A}^2\Pi$ - $\tilde{X}^2\Sigma^+$ (100) - (000) bands of both CaOH and CaOD, evidence of a strong Fermi resonance interaction between the $\tilde{A}(100)$ and $\tilde{A}(020)$ levels was found. Although the $\tilde{A}(020)$ levels were not observed in this work, the Fermi resonance was manifest through severe perturbations in the $(100)^2\Pi_{3/2}$ and the $(100)^2\Pi_{1/2}$ sub-states of CaOH and CaOD, respectively. While these perturbations complicated the rotational analysis of the 1_0^1 band, it was realized that the $\tilde{A}(100) \sim \tilde{A}(020)$ Fermi resonance provided a convenient window to simultaneously access both the ν_1 stretching and ν_2 bending manifolds of the ground state via

$\tilde{A}^2\Pi \rightarrow \tilde{X}^2\Sigma^+$ fluorescence. In this experimental scheme, the $\tilde{A}(100) \rightarrow \tilde{X}(020)$ band gains transition strength through intensity borrowing on account of the significant $\tilde{A}(020)$ character present in the $\tilde{A}(100)$ levels. As a result, fluorescence to the $\tilde{X}(020)$ level in addition to the $\tilde{X}(v_n00)$, v_n = 1, 2, 3 . . . levels can be studied via resolved fluorescence following excitation of the $\tilde{A}(100) \leftarrow \tilde{X}(000)$ band.

Using a computer interfaced scanning monochromator, excited vibrational levels of the $\tilde{X}^2\Sigma^+$ state of CaOH and CaOD have been observed via dispersion of LIF from selectively populated rotational levels of the $\tilde{A}^2\Pi(100)$ state. The rotational structure of the (100), (200) and (300) stretching vibrational levels as well as the (020) bending level including both the $\ell = 0$ and $\ell = 2$ components are well established in the present work for both CaOH and CaOD. The $\tilde{A}(100) \rightarrow \tilde{X}(400)$ transition is extremely weak and was observed only for CaOH.

5.2 Experimental

The experimental details of the dispersed fluorescence experiments have been described in chapter 3. The results presented in this chapter are obtained from approximately 150 separate resolved fluorescence scans of rotationally resolved excitation features. The progression in the stretching vibration was observed following excitation of selected P and R lines of the least perturbed spin-orbit component of the $\tilde{A}(100)$ level of CaOH and CaOD based on the line measurements of ref. 28. Since the vibrational spacings of the ground state ν_1 mode are approximately 600 cm^{-1}, separate resolved fluorescence scans were recorded for fluorescence to the (100), (200), (300) and (400) levels. Typically, each scan varied in length from about 20 to 50 cm^{-1} and took and average of 20 minutes to record. Since our main interest was

in the term values and rotational constants, data for each vibrational level were limited to rotational transitions ranging in J from 3½ to 30½. The only exception was the $\tilde{A}(100) \rightarrow \tilde{X}(100)$ band of CaOD, for which a few high J lines ($J \leq 48½$) were obtained to allow for a determination of the centrifugal distortion constant.

Access to the (020) bending level of the ground state was achieved by populating selected rotational levels of the $\tilde{A}(100)$ level perturbed by Fermi resonance with the $\tilde{A}(020)$ level. This corresponded to excitation of $\tilde{A}(100)^2\Pi_{3/2} \leftarrow \tilde{X}(000)^2\Sigma^+$ sub-band of CaOH and the $\tilde{A}(100)^2\Pi_{1/2} \leftarrow \tilde{X}(000)^2\Sigma^+$ sub-band of CaOD. Both the $\ell = 0$ and $\ell = 2$ components of the (020) level were observed in the same resolved fluorescence scans and by extending the scan to shorter wavelengths, the $\tilde{A}(100) \rightarrow \tilde{X}(100)$ fluorescence could also be observed. Accordingly, the dispersed fluorescence scans involving the bending mode levels were somewhat longer, varying from $\approx$ 100 to 150 cm^{-1} in length and were calibrated by 15 uranium lines as opposed to the 8 to 10 calibration lines used in the stretching progression scans.

5.3 The (100) ~ (020) Fermi Resonance

In the $\tilde{A}^2\Pi$ states of CaOH and CaOD, there is a near degeneracy of vibronic components associated with the (100) and (020) vibrational level. In such cases where an accidental degeneracy or more correctly near degeneracy arises, the levels may interact via anharmonic terms in the vibrational potential energy expressions that are otherwise neglected. This phenomenon is referred to as a Fermi resonance in honor of E. Fermi who first observed this effect in the (100) and (020) vibrational levels of CO_2[95].

The $\tilde{A}(100) \sim \tilde{A}(020)$ Fermi resonance interaction in CaOH and CaOD is of concern in the present work only insofar as it provides a perturbation

facilitated mechanism to probe the $v_2 = 2$ levels of the $\tilde{X}^2\Sigma^+$ ground state which may otherwise be difficult to study owing to the Franck-Condon factors. Detailed theoretical treatments of Fermi resonance interactions which are of particular relevance to the case at hand have been given by Hougen[96] and Woodward, Fletcher and Brown[97] For the purposes of the present discussion, however, only a simple qualitative consideration will be presented. The $\tilde{A}(100) \sim \tilde{A}(020)$ Fermi resonance in CaOH has recently been the subject of a thorough deperturbation analysis by Li and Coxon[30].

As a result of Renner-Teller and spin-orbit interactions, the (020) level is split into upper and lower $^2\Pi$ states, designated as $\kappa^2\Pi$ and $\mu^2\Pi$ respectively, and a $^2\Phi$ vibronic level which is located midway between the $^2\Pi$ states (see fig. 4.2). The (100) ~ (020) Fermi diad involves interactions between the $(100)^2\Pi$ level and the $\mu^2\Pi$ and $\kappa^2\Pi$ sub-states of the (020) vibrational level. The interaction is diagonal in the quantum number P, thus the three states are grouped into two non-interacting blocks with $P = |½|$ and $P = |3/2|$. The off-diagonal matrix elements are independent of J and are expressed in terms of two parameters W_1 and W_2 defined by Hougen[96]. An energy level diagram of the $\tilde{A}(100)$ level and the $K = 1$ components of the (020) level of CaOH, based on the analysis of ref. 30, is shown in fig. 5.1. In the absence of the Fermi resonance interaction, the unperturbed energies of the $(100)^2\Pi_{3/2}$ and $(020)\mu^2\Pi_{3/2}$ sub-states are separated by only 1.5 cm^{-1}. The eigenfunctions of these vibronic sub-states are completely mixed by the strong Fermi resonance interactions and thus the vibronic labels become arbitrary, reflecting only the nominal character of the wavefunctions at the lowest J value[30]. Consequently, the nominal $\tilde{A}(100)^2\Pi_{3/2}$ levels have a significant $\tilde{A}(020)$ character, and the $\tilde{A}(100)^2\Pi_{3/2} \rightarrow \tilde{X}(020)^2\Sigma^+$ sub-bands can acquire significant transition strength by intensity borrowing. The $\tilde{A}(100)^2\Pi_{1/2}$ sub-

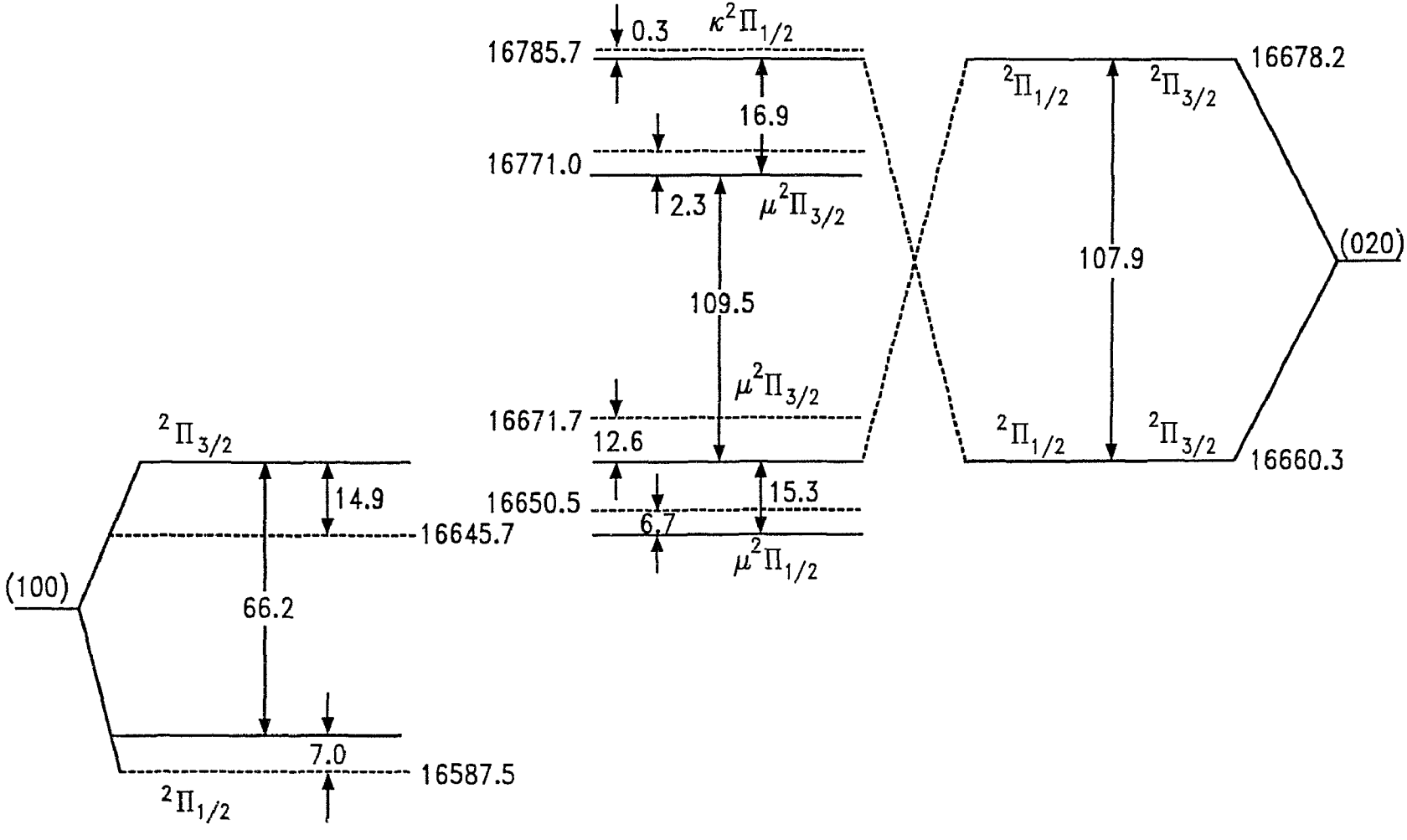

Figure 5.1: Energy level diagram of the $\tilde{A}^2\Pi$ (100) ~ (020) Fermi resonance based on ref. 30. The broken lines represent the observed levels at $J = 1/2$; the solid lines represent the levels when the Fermi resonance parameters are set to zero.

state of CaOH is only weakly perturbed by the Fermi resonance and thus retains a strong transition strength in the stretching progression. This was essential to the successful observation of the weak $\Delta v_1 = 3$ and $\Delta v_1 = 4$ bands. Although a similar analysis of the $\tilde{A}(100) \sim \tilde{A}(020)$ Fermi resonance in CaOD has not yet been undertaken, based on an earlier rotational analysis of the $\tilde{A}(100) \leftarrow \tilde{X}(000)$ band system and an approximate knowledge of the fundamental bending frequency, a $\tilde{A}(100)^2\Pi_{1/2} \sim \tilde{A}(020)\kappa^2\Pi_{1/2}$ Fermi resonance has been inferred[28]. Accordingly, the intensity of the $\tilde{A}(100)^2\Pi_{1/2} \rightarrow \tilde{X}(020)$ sub-bands in CaOD are considerably enhanced by a similar intensity borrowing mechanism.

5.4 Resolved LIF Spectra

The rotationally resolved dispersed fluorescence spectrum of the $\tilde{A}(100) \rightarrow \tilde{X}(v_1 00)$ bands exhibited a structure characteristic of a typical $^2\Pi$ case (a) - $^2\Sigma$ case (b) transition. Thus, for each sub-band, 6 branches are expected. However, owing to the small spin-rotation splitting in the ground state ($\gamma = 0.0011596(2)$ cm^{-1} for $\tilde{X}(000)$[36]), a maximum of only four branches can be resolved at the resolution afforded by our monochromator. A typical dispersed fluorescence spectrum of the $\tilde{A}(100) \rightarrow \tilde{X}(100)$ emissions of CaOD obtained by exciting the $\tilde{A}(100) \leftarrow \tilde{X}(000)$ $R_2(18½)$ line is shown in fig. 5.2. The transitions labelled as R_2 lines are actually $R_2(J) + Q_{21}(J+1)$ lines and in accord with the intensities expected for a typical $^2\Pi$ case (a) - $^2\Sigma$ case (b) transition, are approximately two to three times the intensity of the $P_2(J + 2)$ lines. In addition to the main lines, many extra features caused by collisional energy transfer also appear in the spectrum. In fig. 5.2, the collisional lines on each side of the main $R_2(18½)$ and $P_2(20½)$ lines have been assigned and were included in the least-squares fit. It was found that a

Figure 5.2: Dispersed LIF spectrum of the $\tilde{A}(100) \rightarrow \tilde{X}(100)$ fluorescence following excitation of the $\tilde{A}(100) \leftarrow \tilde{X}(000)$ $R_2(18½)$ rotational transition of CaOD.

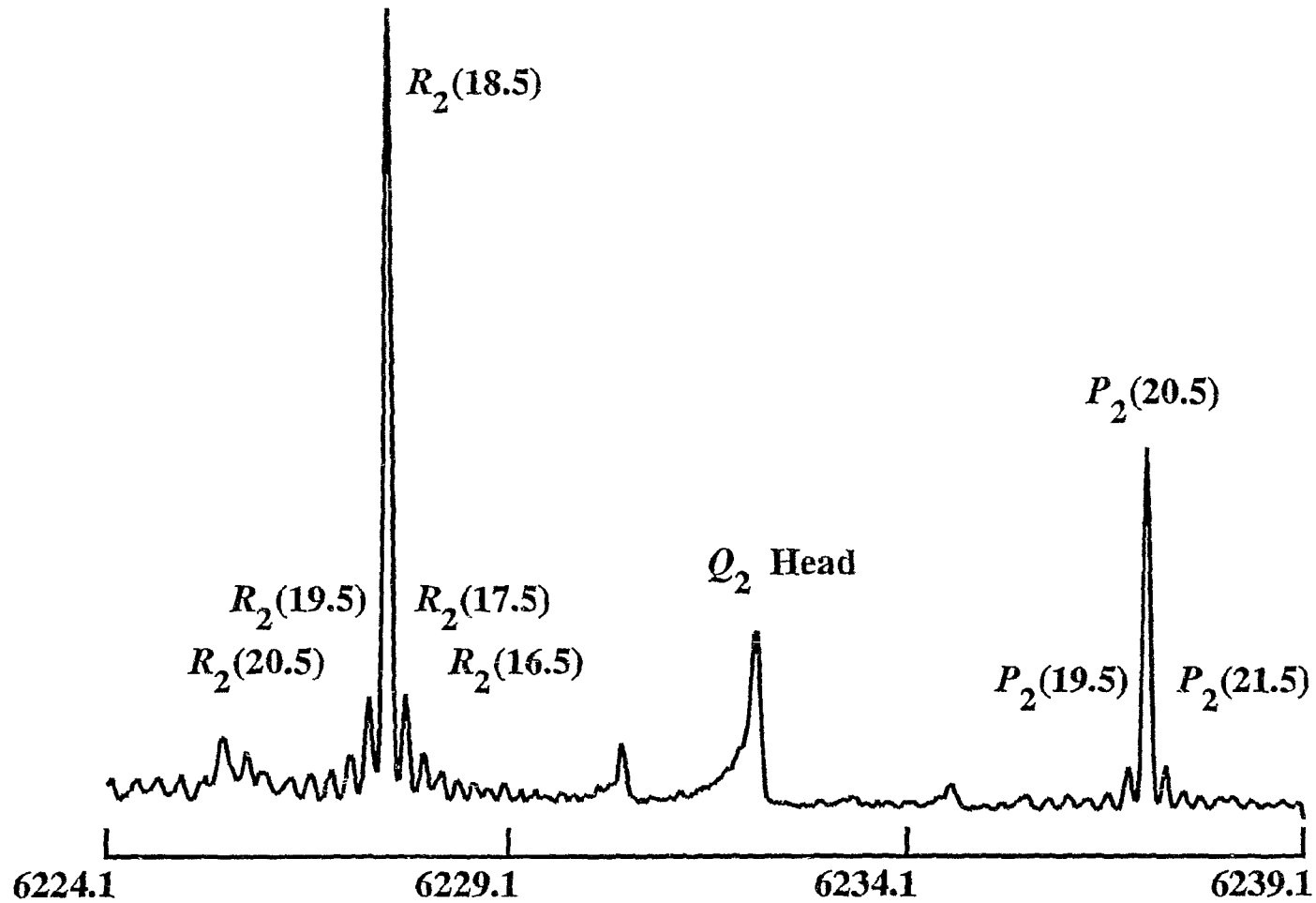
R_2(18.5)
P_2(20.5)
Q_2 Head
R_2(19.5)
R_2(17.5)
R_2(20.5)
R_2(16.5)
P_2(19.5)
P_2(21.5)
6224.1
6229.1
6234.1
6239.1
Wavelength/Å

Figure 5.2

maximum of up to three collisional lines on each side of the main line could be measured to the same accuracy as the main line. Other lines further away from the main line had poorer lineshapes and were considerably broadened; these lines were excluded from the fit unless an average line position could be obtained from several different spectra. The Q_2 head in fig. 5.2 is formed by parity changing collisions. For the weaker bands, most notably the 1_3^1 and 1_4^1 bands, the S/N was poorer and the collision induced lines were obscured by background chemiluminescence.

In accord with expected trends in the Franck-Condon factors based on the similarities of the $\tilde{A}^2\Pi$ and $\tilde{X}^2\Sigma^+$ state potential energy surfaces, the intensities of the bands in the stretching progression decreased rapidly with increasing $|\Delta v_1|$. For CaOH, the fluorescence intensities to the (100), (200), and (300) levels was approximately in the ratio of $1 : 0.1 : 0.008$. The $\tilde{A}(100) \rightarrow \tilde{X}(400)$ band was extremely weak and only the stronger of the two fluorescence lines was observed in each resolved fluorescence scan. A similar pattern of relative intensities was observed in CaOD, although the overall intensity of the $\tilde{A}^2\Pi$ - $\tilde{X}^2\Sigma^+$ system was considerably weaker than for CaOH. The (100) $\rightarrow$ (400) band of CaOD was too weak to permit observation.

The (020) level in the $\tilde{X}^2\Sigma^+$ state is split by anharmonicity into $\ell = 0$ (Σ) and $\ell = 2$ (Δ) components. The dispersed fluorescence spectra obtained by populating the $\tilde{A}(100)$ spin-orbit component of CaOH and CaOD most strongly perturbed by the Fermi resonance was characterized by emissions to both ℓ components of the (020) level. The rotational structure of the $(100)^2\Pi_{3/2} \rightarrow (020)^2\Sigma^+$ sub-band was similar to that associated with the ν_1 mode discussed previously. In the case of the $\ell = 2$ component, the inferred pattern of rotational energy levels is characteristic of a Hund's case (b) coupling where each J value of the F_1 and F_2 spin components is split by a

small amount on account of the ℓ-type doubling interaction. A rotational energy level diagram for a $^2\Pi$ case (a) - $^2\Delta$ case (b) transition is shown in fig. 5.3. As a result of the perturbation facilitated approach to accessing the $v_2 = 2$ levels, only those branches arising from the most perturbed spin-orbit member of the $\tilde{A}(100)$ level were observed. Owing to the small spin-rotation splitting in the ground state, the $R_2 + {}^RQ_{21}$ and $Q_2 + {}^QP_{21}$ branches of CaOD were blended for all J values observed. A typical dispersed fluorescence spectrum of the emission to the (020) and (100) ground state levels following excitation of the $\tilde{A}(100) \leftarrow \tilde{X}(000)$ $R_2(18½)$ rotational transition is shown in fig. 5.4. Although there are numerous overlapping features that can be attributed to coincident excitations, the comparatively high resolution afforded by our monochromator is sufficient to clearly resolve the features associated with the $(020)^2\Sigma^+$, $^2\Delta$ and $(100)^2\Sigma^+$ levels. The relative intensities of the fluorescence to the (100) and (020) levels are very nearly equal, and indicate that the $\tilde{A}(100)$ and $\tilde{A}(020)$ levels are completely mixed by the Fermi resonance interaction. For both CaOH and CaOD, the relative intensities of the fluorescence to the (020) level increased with increasing J; however, for CaOD, the intensity of the $\tilde{A}(100) \rightarrow \tilde{X}(020)$ emissions was much lower than the corresponding $\tilde{A}(100) \rightarrow \tilde{X}(100)$ fluorescence. This provides a clear indication that the (100) ~ (020) Fermi resonance interaction is somewhat weaker in CaOD.

An additional feature of the fluorescence to the (020) levels of CaOH, which is illustrated in fig. 5.4, was that the P_2 lines were much weaker than the R_2 lines. An opposite effect was observed in CaOD and in both cases the anomalous intensities are attributable to interference effects arising from the Fermi-resonance perturbation in the upper state levels. Although no detailed analysis of the relative intensities was attempted, this is believed

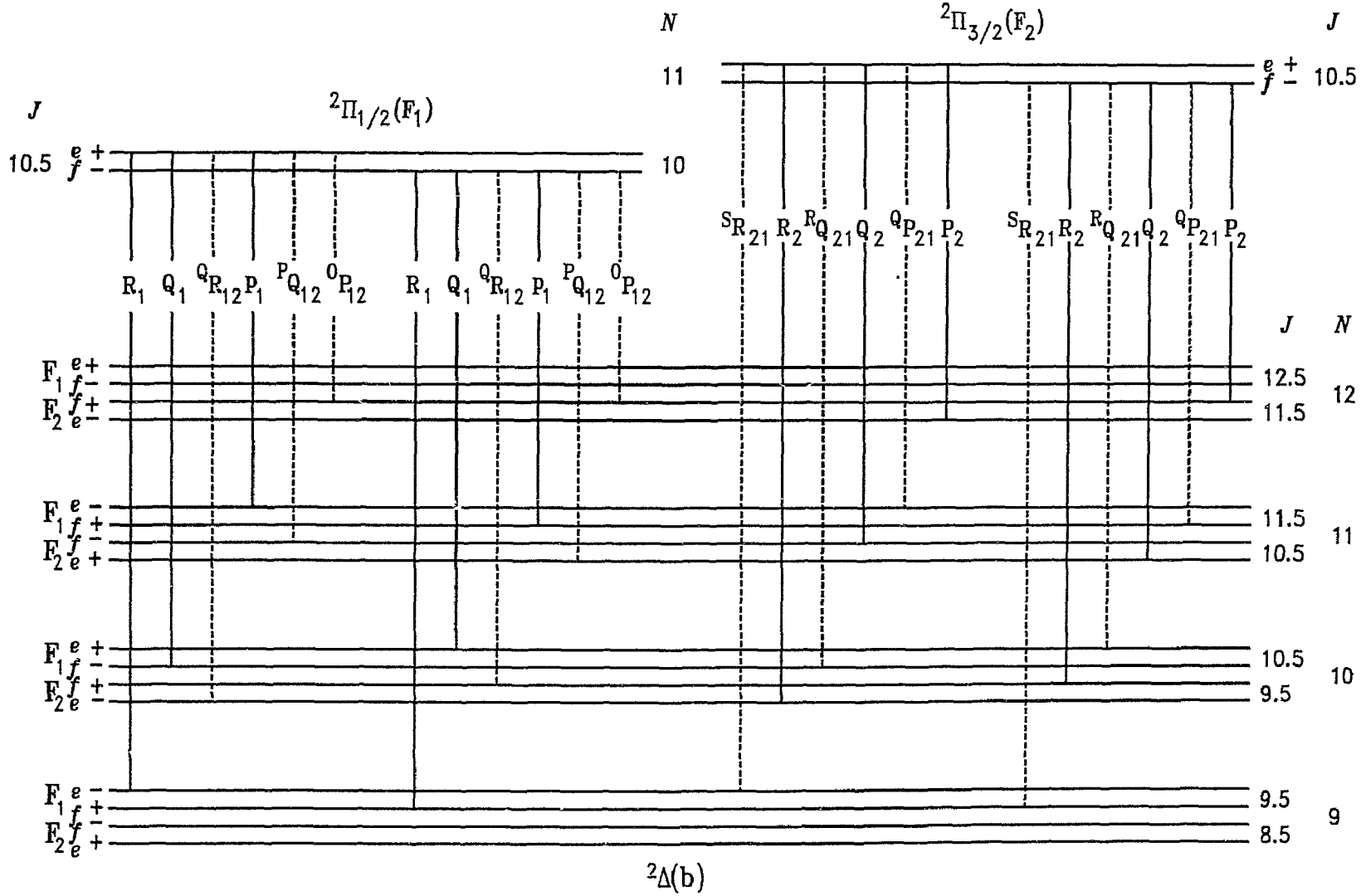

Figure 5.3: Rotational energy level diagram for a $^2\Pi$(a)–$^2\Delta$(b) vibronic transition. The main and satellite branches are represented by solid and broken lines, respectively

Figure 5.4: Dispersed LIF spectrum of the $\tilde{A}(100) \rightarrow \tilde{X}(100)$ and $\tilde{A}(100) \rightarrow \tilde{X}(020)$ fluorescence following excitation of the $\tilde{A}(100) \leftarrow \tilde{X}(000)$ $R_2(12½)$ rotational transition of CaOH.

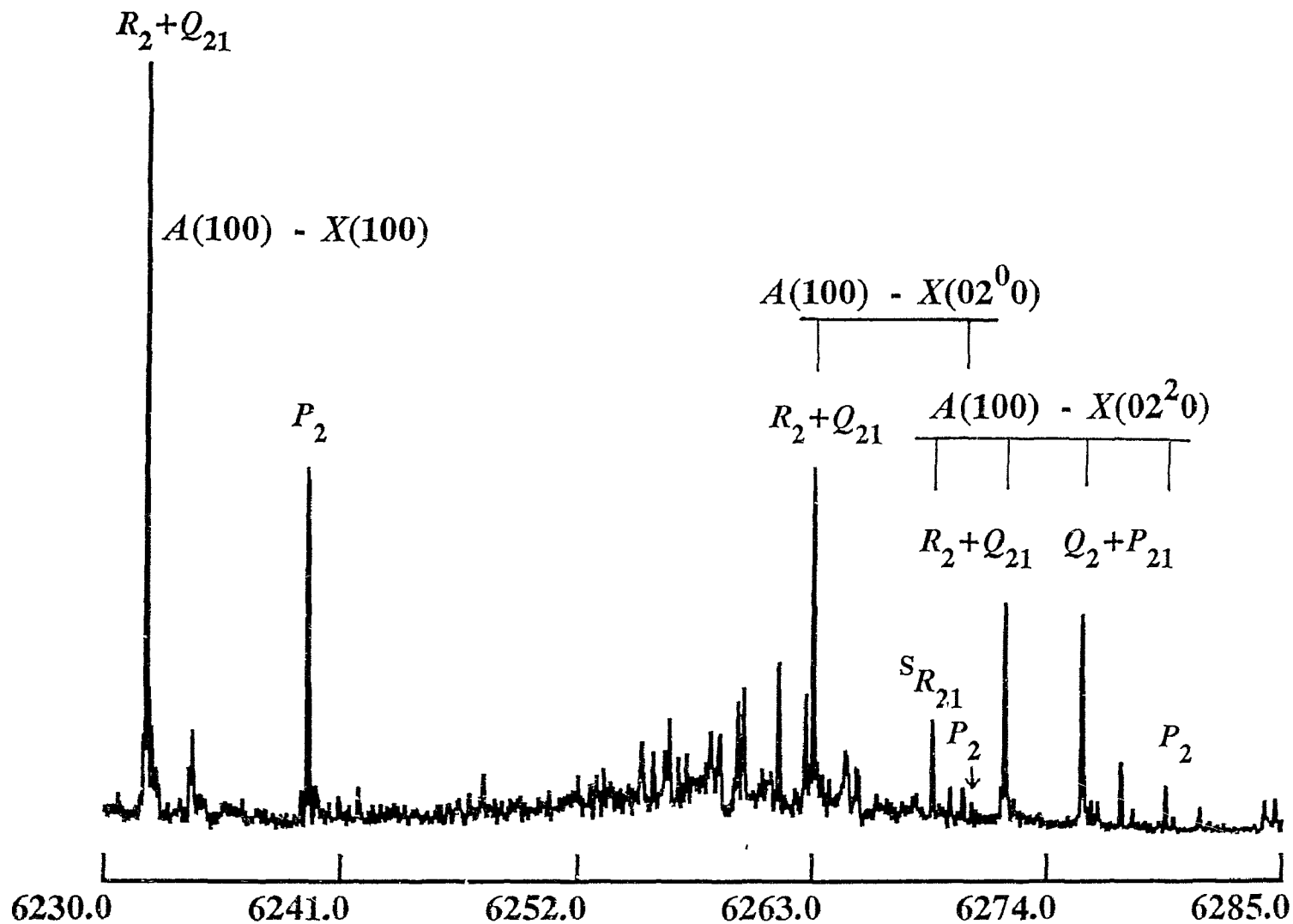
R_2+Q_{21}
$A(100)$ - $X(100)$
$A(100)$ - $X(02^00)$
P_2
R_2+Q_{21}
$A(100)$ - $X(02^20)$
R_2+Q_{21}
Q_2+P_{21}
$^SR_{21}$
P_2
P_2
6230.0
6241.0
6252.0
6263.0
6274.0
6285.0
Wavelength/Å

Figure 5.4

to reflect the difference between the (100) ~ (020) Fermi resonance interactions in CaOH and CaOD. A more comprehensive explanation is precluded owing to the lack of information concerning the $\tilde{A}(100) \sim \tilde{A}(020)$ Fermi-Resonance in CaOD.

5.5 Results and Discussion

The representation of the $\tilde{A}^2\Pi(100)$ rotational energy levels was based on the earlier laser excitation investigation of the $\tilde{A}^2\Pi(100) \leftarrow \tilde{X}^2\Sigma^+(000)$ band.[28] The Fermi resonance perturbation of the $\tilde{A}^2\Pi(100)$ levels prevented the data from the $^2\Pi_{1/2}$ and $^2\Pi_{3/2}$ spin-orbit components from being fit together using the matrix model of table 4.1. Instead, the F_1 and F_2 levels were fit separately to the following expressions,

$$F_{1v}(J, {}^{e}_{f}) = T_v^{(1)} + B_v^{(1)}J(J+1) - D_v^{(1)}J^2(J+1)^2 + H_v^{(1)}J^3(J+1)^3$$

$$\mp \tfrac{1}{2}P_v(J+\tfrac{1}{2}) \mp \tfrac{1}{2}P_{Dv}J(J+1)(J+\tfrac{1}{2}\mp 1) \qquad (5.1)$$

$$F_2(J, {}^{e}_{f}) = T_v^{(2)} + B_v^{(2)}J(J+1) - D_v^{(2)}J^2(J+1)^2 + H_v^{(2)}J^3(J+1)^3$$

$$\mp Q_v(J-\tfrac{1}{2})(J+\tfrac{1}{2})(J+3/2)\,, \qquad (5.2)$$

where the two sets of constants $T_v^{(1)}$, $T_v^{(2)}$, $B_v^{(1)}$, $B_v^{(2)}$, . . . are effective molecular parameters. In the absence of a perturbation, the P_v and Q_v are related to the lambda-doubling parameters p^e and q^e by[28]

$$P_v = p_v^e + 2q_v^e \qquad (5.3)$$

$$Q_v = \left(\frac{B_v}{A_v}\right)\left[q_v^e + \tfrac{1}{2}\,p_v^e\left(\frac{B_v}{A_v}\right)\right]. \qquad (5.4)$$

Since the uncertainty in the line positions measured in the resolved fluorescence experiments is an order of magnitude greater than that of the earlier laser excitation work, the effective constants for the $\tilde{A}^2\Pi$ state were

held fixed to the values established in ref. 28. The rotational energy of the $\tilde{X}^2\Sigma^+$ state levels were described by the expressions of eqs. 4.30 - 4.31 and 4.41 - 4.42 for the levels with $\ell = 0$ and $\ell = 2$, respectively.

The main interest in the present work has been to establish accurate term values and rotational constants B_v for a number of vibrational levels in the ground state for CaOH and CaOD. Accordingly, given the limited resolution (~ 0.3 cm^{-1}) and accuracy (0.05 cm^{-1}) of our monochromator combined with a paucity of high J data ($J \leq 30½$ in most cases), several of the molecular constants of the $\tilde{X}^2\Sigma^+$ state vibrational levels were either held fixed or set to zero in the least-squares fitting. In general, the spin-rotation constant γ_v experiences only a small variation with v, and was held fixed at the $\tilde{X}^2\Sigma^+(000)$ value of 0.00111 cm^{-1} determined in ref. 25. Similarly, the centrifugal distortion constants D_v'' were not determined and were also held fixed to the values found for the $\tilde{X}^2\Sigma^+(000)$ level of 3.869×10^{-7}[25] and 2.73×10^{-7}[28] cm^{-1} for CaOH and CaOD, respectively. In the only exception, the $\tilde{A}(100) - \tilde{X}(100)$ band of CaOD, the rotational levels were observed up to $J = 48½$: in this case, the fitted value of D_v'' for the (100) level was well determined as $2.83(10) \times 10^{-7}$ cm^{-1}, which is in excellent agreement with the value for the (000) level quoted above. The effective ℓ-type doubling constant for the $(020)^2\Delta$ level, which is expected to be very small, was set to zero.

The measured line positions for all the bands observed in this work along with the residuals (observed - calculated) are given in tables 5.1 and 5.2. The variances of the fits are close to unity, indicating that the estimated uncertainty in the measurements is reasonable. The vibrational and rotational constants derived from the least-squares fits are summarized in table 5.3. The vibrational term values may be compared to the ground state vibrational spacings given by Hilborn *et al.*[23] which are based on a low resolution

Table 5.1: Resolved LIF Line Positions[a] (cm^{-1}) in The $A^2\Pi$ - $X^2\Sigma$ System of CaOH

	$A(100)$ - $X(100)$							
J	Q_1		P_{12}		Q_2		R_{21}	
4½							16040.823	-0.007
5½	15979.099	-0.007			16033.472	-0.056	16041.872	-0.016
6½			15970.447	-0.030	16033.237	-0.022	16042.916	-0.040
7½	15979.939	0.072			16032.971	-0.029		
8½	15980.272	0.010	15968.639	0.055				
9½			15967.641	-0.011				
10½	15981.112	0.028					16047.344	0.022
11½	15981.517	0.007	15965.863	0.042	16032.039	-0.020		
12½			15964.910	-0.011				
13½	15982.425	0.031					16050.728	0.035
14½			15963.140	-0.012	16031.420	-0.032		
15½	15983.340	0.022					16053.074	0.088
16½	15983.829	0.033	15961.425	-0.001	16031.117	0.023	16054.240	0.093
17½			15960.601	0.022	16030.950	0.020		
18½							16056.575	0.081
19½	15985.273	-.020			16030.662	0.033	16057.623	-0.059
20½	15985.811	-.001	15958.067	-0.036	16030.439	-0.053		
21½			15957.299	-0.001			16060.129	0.046
22½					16030.267	0.019	16061.215	-0.082
23½					16030.111	-0.028	16062.421	-0.100
24½					16029.969	-0.072	16063.792	0.039
25½					16029.974	0.023		
26½								
27½							16067.423	-0.079
28½					16029.687	-0.053	16068.747	-0.023
29½					16029.628	-0.061		

Table 5.1 (Continued)

	$A(100)$ - $X(100)$				$A(100)$ - $X(200)$			
J	R_2		P_2		Q_1		P_{12}	
4½					15377.680	0.029		
5½							15370.391	-0.008
6½								
7½					15378.849	-0.008		
8½					15379.303	0.014	15367.643	-0.007
9½							15366.733	-0.031
10½					15380.210	0.015	15365.875	-0.017
11½	16040.452	-0.053			15380.696	0.025	15365.037	0.002
12½	16040.920	-0.052			15381.179	0.018	15364.217	0.024
13½			16022.564	-0.011	15381.701	0.035	15363.339	-0.027
14½			16021.687	-0.029	15382.198	0.012	15362.568	0.013
15½					15382.748	0.027	15361.703	-0.055
16½					15383.293	0.023	15360.999	0.023
17½					15383.802	-0.033	15360.236	0.026
18½					15384.346	-0.068	15359.437	-0.022
19½					15385.013	0.004	15358.662	-0.061
20½					15385.583	-0.035	15358.060	0.057
21½					15386.190	-0.052	15357.278	-0.020
22½					15386.872	-0.010		
23½					15387.562	0.026		
24½					15388.223	0.017	15355.291	0.016
25½					15388.929	0.039	15354.649	0.017
26½					15389.596	0.006		
27½					15390.316	0.011		
28½					15391.034	-0.001	15352.791	-0.007
29½					15391.820	0.039	15352.181	-0.037

Table 5.1 (Continued)

	$A(100) - X(300)$				$A(100) - X(400)$	
J	Q_1		P_{12}		Q_1	
4½	14784.804	0.013				
5½			14777.656	0.068		
6½	14785.693	0 063				
7½	14786.005	-0.073	14775.809	0.001		
8½	14786.510	-0.035	14774.857	-0.089		
9½			14774.110	0.006		
10½	14787.508	-0.028				
11½	14787.978	-0.083	14772.435	-0.043		
12½	14788.662	0.058	14771.664	-0.031		
13½	14789.080	-0.087	14770.990	0.060		
14½			14770.158	-0.027	14205.866	-0.073
15½	14790.252	-0.099			14206.603	0.005
16½			14768.704	-0.050	14207.327	0.046
17½	14791.585	-0.028			14207.996	0.009
18½	14792.312	0.040	14767.303	-0.099	14208.640	-0.077
19½	14792.850	-0.101	14766.735	-0.020	14209.470	0.001
20½	14793.596	-0.054	14766.032	-0.096	14210.402	0.157
21½			14765.499	-0.022	14211.034	-0.011
22½						
23½	14795.887	0.025				
24½			14763.847	0.027		
25½					14214.422	-0.054
26½	14798.286	0.036				
27½			14762.307	0.008		

Table 5.1 (Continued)

	$A(100) - X(02^00)\ ^2\Sigma^+$					
J	Q_2		R_{21}		R_2	
4½			15961.133	-0.024		
5½	15953.802	-0.034	15962.166	-0.041		
6½	15953.542	-0.014	15963.303	0.038		
7½	15953.271	-0.012				
8½						
9½						
10½			15967.570	-0.003		
11½	15952.224	-0.047			15960.714	-0.003
12½					15961.155	-0.008
13½			15970.864	-0.019		
14½	15951.522	-0.071				
15½			15973.232	0.104		
16½	15951.216	0.036	15974.342	0.081		
17½	15951.002	0.017				
18½			15976.645	0.095		
19½	15950.634	0.016				
20½						
21½			15980.120	0.083		
22½	15950.126	0.000				
23½						
24½						
25½	15949.702	-0.001				
26½						
27½			15987.158	-0.051		
28½	15949.261	-0.089	15988.374	-0.055		
29½	15949.170	-0.079				

Table 5.1 (Continued)

	$A(100)$ - $X(02^20)$ $^2\Delta$							
J	Q_2		R_{21}		R_2		P_2	
4½			15938.174	0.046	15934.762	-0.046		
5½	15930.809	-0.010	15939.219	0.036	15935.166	-0.034		
6½	15930.543	-0.003	15940.241	-0.006	15935.570	-0.030	15926.202	0.037
7½	15930.263	-0.018					15925.255	0.028
8½							15924.283	-0.015
9½								
10½			15944.594	0.004	15937.273	-0.016		
11½	15929.300	-0.012	15945.724	0.001	15937.833	0.074		
12½	15929.054	-0.063	15946.824	-0.021	15938.182	-0.036	15920.688	0.017
13½	15928.915	0.003	15947.910	-0.028	15938.610	-0.038	15919.832	0.021
14½	15928.649	-0.029					15918.949	0.007
15½			15950.247	0.034	15939.628	0.032	15918.076	0.032
16½	15928.339	0.040	15951.402	0.040	15940.112	0.029		
17½	15928.166	0.043					15916.272	-0.066
18½			15953.693	0.006	15941.087	0.003	15915.555	0.057
19½	15927.832	0.036						
20½							15913.768	-0.078
21½			15957.142	-0.095	15942.634	-0.014		
22½	15927.371	-0.001						
23½							15911.448	0.014
24½			15960.881	0.020	15944.265	-0.023		
25½	15927.028	0.002						
26½							15909.125	0.022

[a]For each transition, the table shows the measured line position and the residual, $\Delta\bar{\nu} = \bar{\nu}_{obs} - \bar{\nu}_{calc}$, where $\bar{\nu}_{calc}$ are calculated from the fitted parameters.

Table 5.2: Resolved LIF line positions[a] (cm^{-1}) in the $A^2\Pi$ -$X^2\Sigma^+$ system of CaOD

	$A(100)$ - $X(100)$			
J	R_2	P_2	Q_2	R_{21}
3½	16044.795 0.011			
4½	16045.165 -0.001			
5½	16045.527 -0.035	16038.145 -0.018		
6½	16045.971 -0.002	16037.340 -0.001		
7½	16046.382 -0.017			
8½	16046.823 -0.016	16035.754 0.013		
9½	16047.284 -0.009	16034.949 -0.014		16053.344 0.038
10½	16047.778 0.016	16034.168 -0.031	16040.629 -0.048	
11½	16048.226 -0.019			
12½	16048.680 -0.063	16032.722 0.005	16040.379 -0.050	
13½	16049.197 -0.059	16031.968 -0.029		
14½	16049.735 -0.047			
15½	16050.278 -0.045	16030.547 -0.055		
16½	16050.837 -0.042	16029.889 -0.037		
17½	16051.442 -0.006	16029.221 -0.044		
18½	16052.023 -0.009	16028.585 -0.034		
19½	16052.668 0.037	16027.960 -0.027		
20½	16053.269 0.026	16027.333 -0.037		
21½	16053.907 0.037	16026.740 -0.027		
22½	16054.550 0.039	16026.143 -0.036		
23½	16055.216 0.049	16025.589 -0.017		
24½	16055.890 0.054	16025.008 -0.039		
25½	16056.561 0.041	16024.476 -0.027		
26½	16057.238 0.020	16023.958 -0.015		
27½	16057.948 0.019	16023.422 -0.036		
28½	16058.689 0.034	16022.937 -0.021		
29½	16059.440 0.045			
30½	16060.185 0.036			
.				
.				
.				
40½				16093.235 -0.007
41½			16043.501 0.000	
42½				16096.282 -0.008
43½			16044.172 -0.001	
44½				
45½				
46½				
47½			16045.702 0.009	
48½			16046.097 -0.013	

Table 5.2 (continued)

	$A(100) - X(100)$				$A(100) - X(200)$			
J	P_1		R_1		R_2		P_2	
3½			15979.966	0.057	15445.617	0.050		
4½			15980.980	0.047	15445.949	-0.020		
5½	15974.541	0.051					15438.992	0.003
6½	15974.361	0.052			15446.812	-0.015	15438.189	-0.006
7½			15984.122	0.056	15447.286	0.002		
8½					15447.751	-0.009		
9½	15973.883	0.051			15448.252	-0.001	15435.961	0.038
10½					15448.764	-0.002		
11½					15449.320	0.024	15434.482	-0.019
12½	15973.477	0.030			15449.850	0.005		
13½			15990.648	0.041	15450.381	-0.031	15433.165	0.011
14½			15991.761	0.029				
15½	15973.188	0.034			15451.614	0.012		
16½	15973.096	0.020			15452.214	-0.010		
17½			15995.146	-0.016	15452.857	-0.007	15430.677	-0.004
18½			15996.332	0.008	15453.490	-0.033		
19½	15972.922	0.022			15454.161	-0.038		
20½	15972.890	0.029			15454.865	-0.029	15429.055	0.034
21½			15999.843	-0.020	15455.608	0.001		
22½			16001.058	-0.002	15456.330	-0.008		
23½	15972.830	0.033			15457.081	-0.007	15427.563	0.036
24½	15972.789	-0.005			15457.854	-0.001		
25½					15458.673	0.033		
26½					15459.436	-0.007		

Table 5.2 (continued)

	$A(100) - X(300)$				$A(100) - X(02^00)\ ^2\Sigma^+$			
J	R_2		P_2		R_1		P_1	
3½	14852.179	0.022			16065.653	0.030		
4½	14852.601	0.025			16066.645	0.016		
5½			14845.547	-0.071			16060.181	0.017
6½			14844.851	0.003			16059.974	0.017
7½	14853.993	0.028			16069.648	-0.034		
8½								
9½			14842.639	-0.033			16059.387	0.016
10½	14855.581	0.028			16072.782	-0.005		
11½	14856.118	-0.008						
12½			14840.648	-0.046			16058.858	0.019
13½			14840.082	0.003	16075.898	-0.042		
14½	14857.973	-0.003			16076.948	-0.054		
15½	14858.671	0.035					16058.383	0.026
16½			14838.415	0.049			16058.205	-0.002
17½			14837.692	-0.147	16080.176	-0.041		
18½	14860.733	-0.015			16081.270	-0.028		
19½							16057.806	0.018
20½			14836.399	0.008			16057.709	0.050
21½	14863.032	-0.024			16084.552	-0.015		
22½					16085.617	-0.048		
23½			14835.140	-0.001			16057.332	0.034
24½	14865.569	0.011					16057.214	0.027
25½								
26½	14867.310	-0.023	14834.104	0.015				

Table 5.2 (continued)

	$A(100) - X(02^20)\ ^2\Delta$							
J	R_1		Q_1		P_1		P_{12}	
5½					16044.180	-0.027	16040.544	-0.032
6½					16043.987	-0.014	16039.768	0.002
7½								
8½			16048.941	0.062				
9½					16043.440	0.017	16037.379	0.006
10½								
11½			16050.240	0.067				
12½					16042.923	0.023	16035.017	-0.018
13½								
14½			16051.502	-0.018				
15½			16051.982	0.002	16042.456	0.026	16032.689	-0.063
16½					16042.298	0.014	16031.972	-0.030
17½	16064.241	-0.058						
18½	16065.333	-0.052	16053.418	0.026				
19½			16053.889	0.015	16041.857	-0.024	16029.787	0.000
20½					16041.814	0.057	16029.068	0.008
21½	16068.633	-0.038						
22½	16069.728	-0.047	16055.388	0.043				
23½			16055.880	0.035	16041.452	0.037	16026.902	-0.006
24½					16041.311	0.000	16026.189	-0.011

[a]For each transition, the table shows the measured line position and the residual, $\Delta\bar{\nu} = \bar{\nu}_{obs} - \bar{\nu}_{calc}$, where $\bar{\nu}_{calc}$ are calculated from the fitted parameters.

Table 5.3: Molecular constants[a] for vibrational levels in the $X^2\Sigma^+$ state of CaOH and CaOD.

	CaOH		CaOD	
	$T_{[v]}$	$B_{[v]}$	$T_{[v]}$	$B_{[v]}$
(000)	[0.0]	0.334354(8)[b]	[0.0]	0.30286(4)[c]
(100)	609.015(10)	0.33219(3)	604.903(7)	0.30102(2)
(200)	1210.150(8)	0.32995(2)	1204.159(7)	0.29905(2)
(300)	1803.054(15)	0.32772(4)	1797.605(11)	0.29729(3)
(400)	2387.272(77)	0.32579(20)		
(020) $^2\Sigma^+$	688.671(15)	0.33303(4)	519.151(12)	0.30246(12)
(020) $^2\Delta$	713.040(9)	0.33252(3)	536.334(15)	0.30233(4)
ω_1^e	612.822(25)[d]		607.786(44)[d]	
X_{11}^o	-3.747(21)[d]		-2.859(18)[d]	
$\omega_2^o + 2X_{22}^o$	344.336[e]		259.576[e]	
g_{22}	6.092[f]		4.296[f]	
$B(000)$	0.334352(11)[g]		0.302861(27)[g]	
α_1	0.002200(10)[g]		0.001877(22)[g]	

[a]Values in parentheses are one standard error in units of the last digit of the corresponding constant.

[b]From Ref. [25].

[c]From Ref. [28].

[d]From least squares fits of the $T(v_1,0,0)$ values.

[e]Determined from $T_{[v]}$ for (020) $^2\Sigma^+$.

[f]Determined from the splitting of the (02^00) and (02^20) levels; the contribution from $-B\ell^2$ is not included.

[g]From least squares fits of the $B(v_1,0,0)$ values, see Fig. 5.5.

bandhead analysis of dispersed LIF. In contrast, the vibrational energies obtained from the present rotationally resolved dispersed fluorescence measurements are determined unambiguously, and are not subject to the uncertainty introduced by the approximation of equating the bandhead position with the band origin. In general, the vibrational spacings determined in ref. 23 are in reasonably good agreement (within 4 cm^{-1}) with the results obtained in this work. In the only exception, the (010) - (000) and (030) - (010) spacings for $\tilde{X}^2\Sigma^+$ CaOD are given as 240 cm^{-1} and 480 cm^{-1}, respectively. The vibrational term energies of the $(020)^2\Sigma$ and $(020)^2\Delta$ levels are determined in the present work as 519.151(12) cm^{-1} and 536.334(12) cm^{-1}, respectively, which would imply a fundamental bending frequency in the vicinity of 260 cm^{-1}, significantly different from the value of 240 cm^{-1} determined in the earlier work. This discrepancy is most probably due to an erroneous assignment in the low resolution dispersed fluorescence spectrum.

Owing to the paucity of vibrational data for the $\tilde{X}^2\Sigma^+$ states of CaOH and CaOD, it is convenient to refer the vibrational term energies to the lowest (000) level[76]

$$G_0(v_1,v_2,v_3) = \sum_i \omega_i^0 v_i + \sum_i \sum_{k\geq i} x_{ik}^0 v_i v_k + \sum_i \sum_{k\geq i} g_{ik} \ell_i \ell_k \,. \tag{5.5}$$

Using the term values obtained from this work, the constants ω_1^0, x_{11}^0, $\omega_2^0 + 2x_{22}^0$ and g_{22} have been determined and are given in table 5.3. The ω_i^0 used herein are not the pure harmonic frequencies, but rather they contain small anharmonic contributions according to[76]

$$\omega_i^0 = \omega_i + x_{ii}\, d_i + \tfrac{1}{2} \sum_k x_{ik} d_k + \ldots \tag{5.6}$$

The constant g_{22} is a consequence of anharmonicity in the bending potential and serves to remove the degeneracy between the purely planar ($\ell = 0$) and somewhat elliptical ($\ell = 2$) bending vibrations. Typically, g_{22} is of the same

order of magnitude as the anharmonicity constants x_{ik}[76] and, in the present work, is determined to be 6.092 cm^{-1} and 4.296 cm^{-1} for CaOH and CaOD, respectively. In some cases, anomalously large values of g_{22} can provide indications of non-linearity since the $\ell = 0$ and $\ell = 2$ components of the $v_2 = 2$ level in the linear limit correlate with different vibrational levels in the bent molecule limit. The values of g_{22} found in the present work, however, are not sufficiently large to suggest a non-linear or quasilinear structure; rather, their magnitudes are more probably a consequence of the large amplitude of the bending vibration.

From the rotational constants B_v in table 5.3, the vibration-rotation interaction constant α_1 can be determined for the $\tilde{X}^2\Sigma^+$ states of CaOH and CaOD using the expression[76]

$$B_v = B_e - \sum_i \alpha_i(v_i + d_i/2) , \qquad (5.7)$$

where the degeneracy, d_i, is unity for the v_1 mode. Plots of B_v versus v_1, which are shown in fig. 5.5, provide no evidence of a detectable deviation from non-linearity. A similar dependence in the bending mode, as implied by eq. 5.7, is not expected to provide a reliable estimate of α_2. For the structurally similar alkali metal monohydroxides CsOH/CsOD and RbOH/RbOD, the effective rotational constant B_v exhibits a complex and anomalous dependence on v_2[57,58]. As with CaOH and CaOD, the rotational constant of the alkali metal monohydroxides are characterized by an initial negative slope in a B_v versus v_2 plot. This behavior is in marked contrast to the majority of linear triatomic molecules in which B_v increases with increasing v_2. This complex dependence of B_v on v_2 is reliably modeled by[57,58,98]

$$B_v = \bar{B}_e - \alpha_2 (v_2 + 1) + \gamma_2(v_2 + 1)^2 + \gamma_{ll}\ell^2 . \qquad (5.8)$$

Since the terms in γ_2 and γ_{ll} can introduce significant contribution to B_v

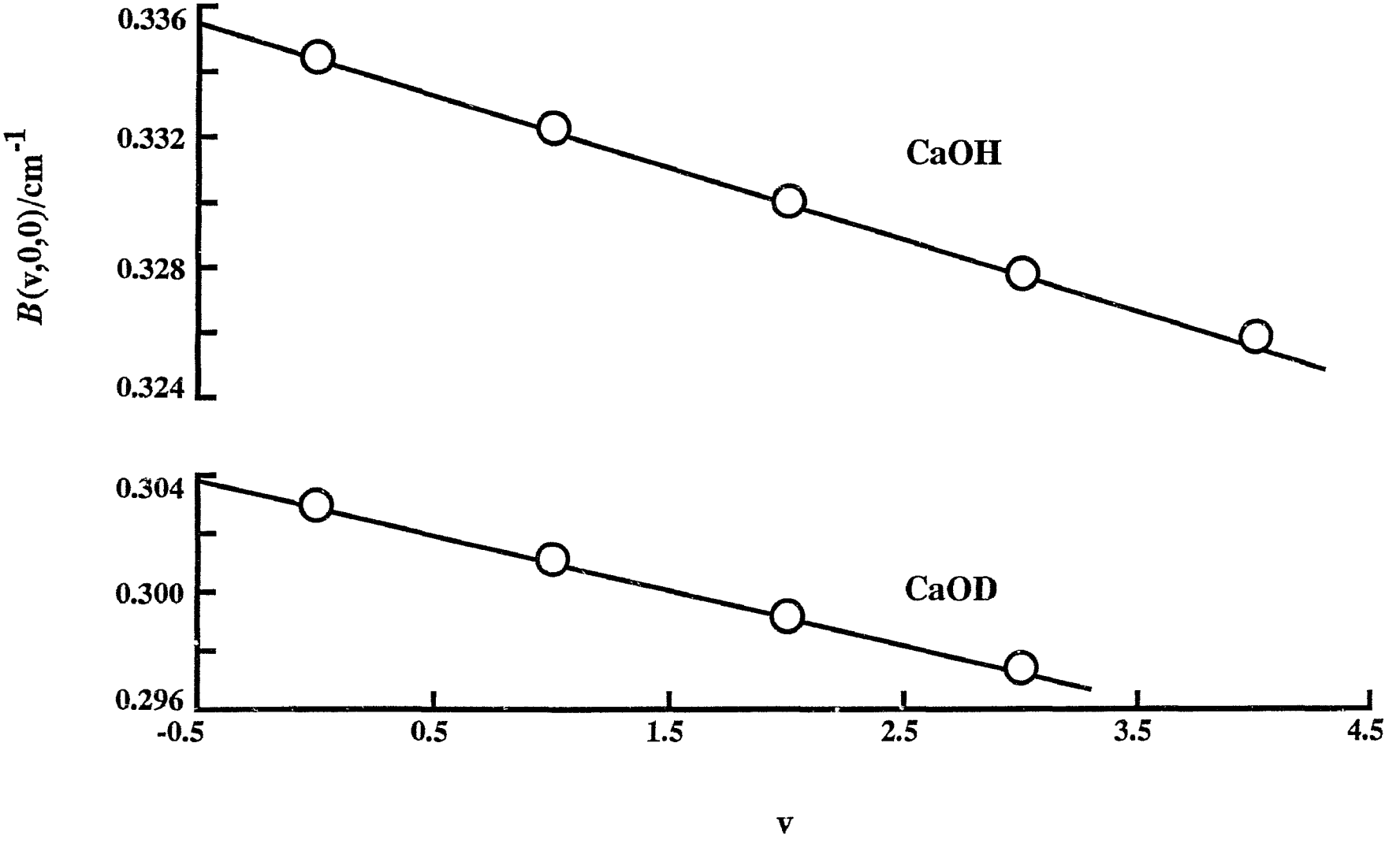

Fig. 5.5: Plots of B vs. v for the X state of CaOH and CaOD

even at low v_2, a reliable determination of α_2 is precluded in the present case.

In the time that has elapsed since the work presented in this chapter has been completed, additional data have been obtained for the ground state vibrational levels of CaOH and CaOD. As part of the ongoing and systematic investigations into the low-lying electronic states of the alkaline earth monohydroxides undertaken in this laboratory, resolved fluorescence spectra obtained from excitation of the $(010)^2\Sigma^{(+)}$, $^2\Sigma^{(-)} \leftarrow (000)^2\Sigma^+$ parallel bands in the $\tilde{A}^2\Pi$ - $\tilde{X}^2\Sigma^+$ system of CaOH have yielded vibration and rotation constants for the $\tilde{X}^2\Sigma^+(010)$ level[31]. In addition, laser excitation of numerous hotbands of the $\tilde{C}^2\Delta$ - $\tilde{X}^2\Sigma^+$ transition by Jarman and Bernath[35] has provided data fc. the $\tilde{X}(010)$ and $\tilde{X}(020)^2\Sigma^+$ levels of CaOD. Using the new data for the (010) levels, it is of interest to calculate the quasi-linearity parameter γ defined by Winnewisser[99], which in the linear limit becomes,

$$\gamma = \frac{G_v(010)}{G_v(02^00)} . \tag{5.9}$$

The value of γ reflects the tendency of the (010)Π vibronic level to draw very close to the lowest Σ level in bent or quasi-linear molecules ($\gamma \rightarrow 0$) rather than lying midway between the (000)Σ and (020)Σ levels as is the case for the linear configuration ($\gamma \rightarrow$ ½). As a matter of convenience, the transformed parameter γ_0 is used, where[99]

$$\gamma_0 = 1 - 4\gamma . \tag{5.10}$$

According to Winnewisser[99], for " well behaved linear molecules", γ_0 varies from -1.02 to -0.98, whereas, in the bent molecule limit, γ_0 typically lies between 0.96 and 1.00. The $\tilde{X}^2\Sigma^+$ states of CaOH and CaOD are certainly at the linear extreme with γ_0 values of -1.0497 and -1.0537, respectively. That the γ_0 are outside the typical linear limit is hardly surprising, since this range

is based on the assumption that anharmonic contributions are less than 1% of γ. Given the relatively low frequency and large amplitude of the bending vibration in CaOH and CaOD, it is reasonable to expect a correspondingly large anharmonicity, hence the extreme value of γ_0.

5.6 Conclusions

The vibrational structure associated with the $\tilde{A}^2\Pi$ - $\tilde{X}^2\Sigma^+$ electronic transition of CaOH and CaOD is complicated by extreme congestion and overlapping of adjacent band systems. The similarity of vibrational spacings in the ground and excited electronic states combined with the effective vibrational temperature in the Broida oven source ($\approx$ 700 K) leads to a near continuum of rovibronic transitions in the dense sequence structure of the $\tilde{A}^2\Pi$ - $\tilde{X}^2\Sigma^+$ system. This is further exacerbated by the inherent complexity created by the presence of Renner-Teller, Fermi resonance and spin-orbit interactions in the $\tilde{A}^2\Pi$ state. Through the use of dispersed LIF following excitation of rotationally resolved features in the $\tilde{A}^2\Pi(100) \leftarrow \tilde{X}^2\Sigma^+(000)$ bands of CaOH and CaOD, considerable progress has been made in elucidating the vibrational and rotational structure associated with the $\tilde{X}^2\Sigma^+$ state. In addition, the perturbation facilitated approach to obtaining access to the $\tilde{X}(020)$ levels has proven highly effective in overcoming the limitations imposed by the restrictive Franck-Condon factors.

The data obtained in the present work provides the first detailed spectroscopic data for excited vibrational levels in the $\tilde{X}^2\Sigma^+$ state of CaOH and CaOD. The data obtained for the bending vibration is of particular interest in that it underscores the manifestation of large amplitude bending motions.

Chapter VI

High Resolution Laser Spectroscopy of Excited Bending Vibrations ($v_2 \leq 2$) of the $\tilde{B}^2\Sigma^+$ and $\tilde{X}^2\Sigma^+$ Electronic States of SrOH: Analysis of ℓ-type Doubling and ℓ-type Resonance

6.1 Introduction

In the present work, the use of a vibrational selective detection scheme leads to a substantial enhancement of the LIF signal and has been utilized as a means of probing excited bending vibrational levels in the $\tilde{B}^2\Sigma^+$ - $\tilde{X}^2\Sigma^+$ system of SrOH at Doppler-limited resolution. Since overlapping band systems are essentially completely suppressed, the complexity of the resulting spectra is greatly reduced, rendering assignment and analysis fairly straightforward.

Several of the transitions observed in this work, specifically the $(02^20)^2\Delta \leftarrow (010)^2\Pi$, $(010)^2\Pi \leftarrow (000)^2\Sigma^+$, and $(02^00)^2\Sigma^+ \leftarrow (010)^2\Pi$ bands, are vibrationally forbidden ($\Delta v_2 = \pm 1$) components of an allowed electronic transition. However, since the $\tilde{B}^2\Sigma^+$ and $\tilde{A}^2\Pi$ electronic states of SrOH are separated by only $\approx$ 1700 cm^{-1}[22,33], the $\tilde{B}^2\Sigma^+$ state can acquire $^2\Pi$ character through vibronic mixing. While the exact mechanism of this mixing is uncertain, Jungen and Merer[79] have suggested that the Herzberg-Teller interaction is expected to induce forbidden bands for most unsymmetrical linear triatomics. Some other notable examples where nominally forbidden $\Delta v_2 = \pm 1$ bands in the bending mode of linear triatomics have been observed include NCS[100], HCN^+[101], NCO[93,87] and CaOH[31,35].

In this chapter, the results of a high resolution laser excitation and dispersed fluorescence investigation of excited bending vibrations in the $\tilde{B}^2\Sigma^+$ - $\tilde{X}^2\Sigma^+$ system of SrOH are reported. A complete rotational analysis of

vibrational levels with $v_2 \leq 2$ for SrOH in both the $\tilde{B}^2\Sigma^+$ and $\tilde{X}^2\Sigma^+$ states is presented. Although the $\ell = 0$ (Σ) and $\ell = 2$ (Δ) components of the (020) vibrational level are well separated, by 32.703 and 30.259 cm^{-1} for the $\tilde{B}^2\Sigma^+$and $\tilde{X}^2\Sigma^+$ electronic states, respectively, the effects of an ℓ-type resonance have been observed and the off-diagonal matrix element connecting these states has been evaluated in a case (b) basis. An earlier investigation[22] of the $\tilde{B}^2\Sigma^+(010)\Pi \leftarrow \tilde{X}^2\Sigma^+(010)\Pi$ transition determined the relative magnitude of the ℓ-type doublings; however, absolute *e/f* parity assignments were not possible. In the present work, the (010)Π levels of both states are observed in perpendicular-type transitions, thereby enabling unambiguous parity assignment and accurately establishing the vibrational term values.

6.2 Experimental

Two distinct experimental schemes were used for this work: vibrational selective laser excitation and resolved fluorescence. In both cases, a detailed description has been presented earlier in chapter 3. The ground state vibrational spacings used in the selective detection scheme were initially based on the work of Nakagawa, Hilborn and Harris[22]. For both the $\Delta v_2 = +1$ and $\Delta v_2 = +2$ transitions observed in this work, the dominant $\Delta v_2 = 0$ emissions were detected. The background suppression and preferential enhancement achieved in the selective detection scheme enabled the observation of numerous band systems in virtual isolation from coincident excitation features. The only notable exception was the $(02^20)^2\Delta \leftarrow (010)^2\Pi$ band, for which the *P*-branch was fortuitously coincident with the *R*- branch of the $(02^00)^2\Sigma^+ \leftarrow (010)^2\Pi$ band. The transitions studied and frequency differences used for the work presented in this chapter are summarized in figure 6.1.

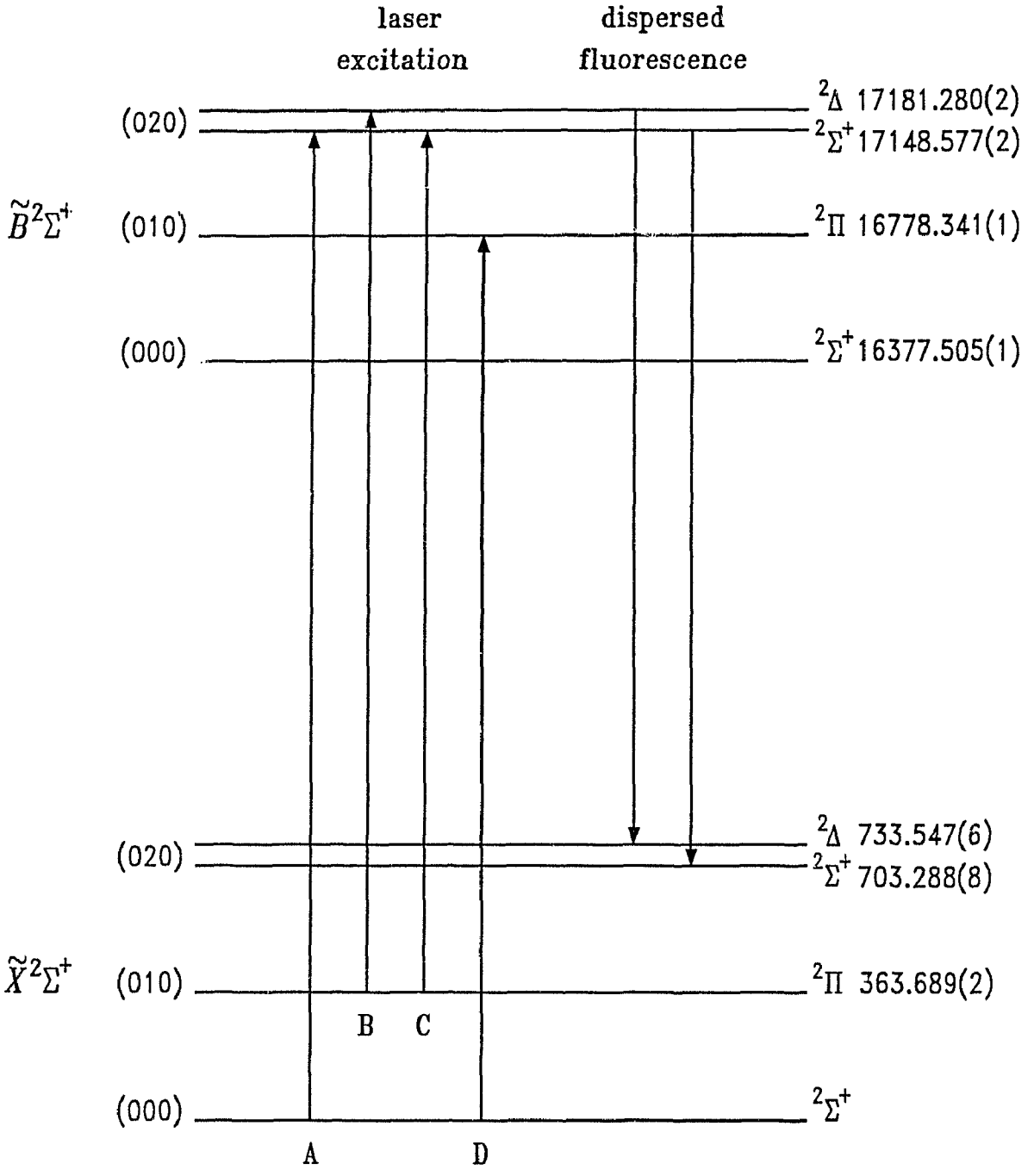

Figure 6.1: Energy level diagram summarizing the six transitions analyzed in the present work. Frequency differences used in selective detection were 703, 368, 339 and 363 cm^{-1} for the A, B, C and D transitions, repectively. The term value for $\tilde{B}^2\Sigma^+(000)^2\Sigma^+$ is taken from ref. 22.

Fluorescence from optically pumped individual rovibronic transitions to the $(010)^2\Pi$, $(02^00)^2\Sigma$ and $(02^20)^2\Delta$ levels of the $\tilde{B}^2\Sigma^+$ state was dispersed, providing access to excited bending levels in the ground state. In contrast to the laser excitation, only the more intense parallel $\Delta v_2 = 0$ bands were investigated in the dispersed fluorescence experiments (see figure 6.1).

6.3 Rotational Analysis and Discussion

The efficacy and diagnostic utility of the vibrational selective detection method was clearly evident in the relative ease with which the rotational assignments of the laser excitation spectra were made. An illustration of the spectral simplicity characteristic of the excitation spectrum is shown in figure 6.2. Since excitation was from either the $(000)\Sigma^+$ or $(010)\Pi$ level of the ground state, for which molecular constants have been previously determined[22,33,37], the rotational quantum number of the *P*- and *R*- branches could be readily assigned by the use of combination differences. Owing to a small effective spin-rotation splitting of the ground state, however, the rotational numbering could be changed by one unit depending on whether the line belonged to the F_1 or F_2 spin manifold. This ambiguity was resolved in the least-squares fits since only one of the two possibilities yielded effective spin-rotation constants of the same sign as those established in earlier work. This method was not reliable for the intense *Q* branches, which are associated with the perpendicular transitions observed in excitation. The presence of a combination defect on account of the ℓ-type doubling, as well as the compact rotational structure of the *Q*- branches, made such assignments questionable. Rotational assignments for the *Q*- branches were therefore made on the basis of the spacings between the *P* and *R* lines in the dispersed fluorescence scans. In the end, this approach was also used to

Figure 6.2: A portion of the Doppler-limited laser excitation spectrum of the $(02^{0}0)^{2}\Sigma^{+}$ - $(000)^{2}\Sigma^{+}$ band of the $\tilde{B}^{2}\Sigma^{+}$ - $\tilde{X}^{2}\Sigma^{+}$ system of SrOH.

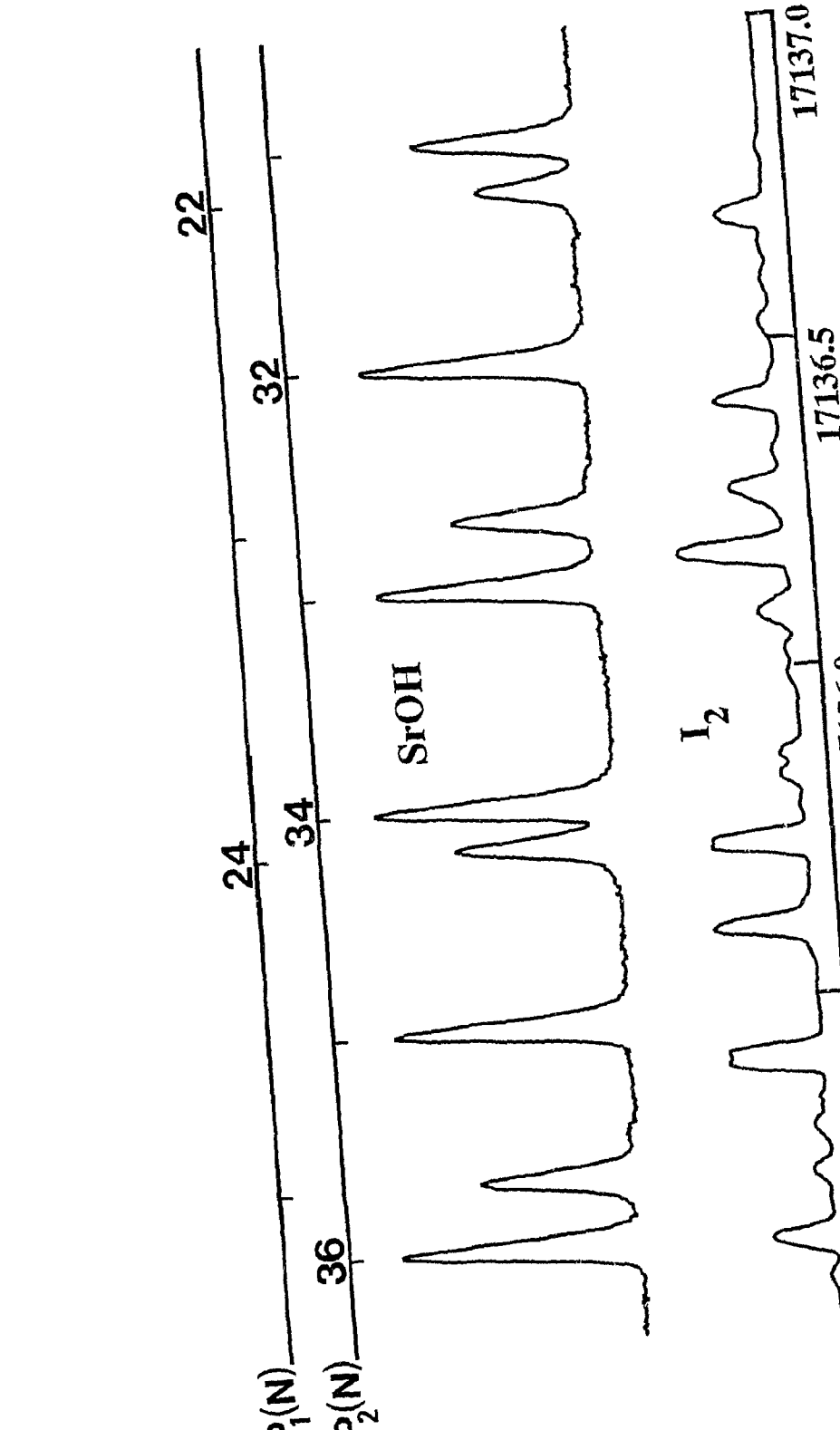
22
24
32
34
36
$P_1(N)$
$P_2(N)$
SrOH
I_2
17135.0
17135.5
17136.0
17136.5
17137.0
Wavenumber (cm^{-1})

Figure 6.2

independently verify the rotational assignments of the *P*- and *R*- branches, where resolved fluorescence spectra were recorded for a minimum of two adjacent lines in each branch.

The rotational assignments of the resolved fluorescence scans followed directly from the excitation spectra. For these transitions $\Delta K = 0$: consequently, only two single (*P* and *R*) lines were observed in fluorescence provided only one rotational level of the upper state was populated.

Although expressions for the rotational term values for linear triatomic molecules in $^2\Sigma^+$ electronic states have been given earlier (chapter 4), in view of the precision of the data and the highly excited rotational energy levels observed in this work ($N \leq 90$), it was necessary to include additional terms to account for the effects of centrifugal distortion. The rotational energy level expressions are given explicitly as,

(a) $v_2 = 0$ *or* 2, $\ell = 0$; $^2\Sigma^+$ *vibronic state*

$$F_1(N, e) = B_v\, N(N+1) - D_v\, N^2(N+1)^2 + H_v\, N^3(N+1)^3 + \tfrac{1}{2}\,\gamma_v\, N + \tfrac{1}{2}\,\gamma_v^D\, N^2(N+1) \qquad (6.1)$$

$$F_2(N, f) = B_v\, N(N+1) - D_v\, N^2(N+1)^2 + H_v\, N^3(N+1)^3 - \tfrac{1}{2}\,\gamma_v\,(N+1) - \tfrac{1}{2}\,\gamma_v^D\, N(N+1)^2 \qquad (6.2)$$

(b) $v_2 = 1$, $\ell = 1$; $^2\Pi$ *vibronic state*

$$F_1(N, {}^{e}_{f}) = B_v\,[N(N+1) - 1] - D_v\,[N(N+1) - 1]^2 + H_v\,[N(N+1) - 1]^3 + \tfrac{1}{2}\,\gamma_v\, N + \tfrac{1}{2}\,\gamma_v^D\, N^2(N+1) \pm \tfrac{1}{2}\, q_v^{v}\, N(N+1) \pm \tfrac{1}{2}\, q_v^D [N(N+1)]^2 \qquad (6.3)$$

$$F_2(N,{}^{e}_{f}) = B_v[N(N+1) - 1] - D_v[N(N+1) - 1]^2 + H_v[N(N+1) - 1]^3$$

$$- \tfrac{1}{2}\gamma_v(N+1) - \tfrac{1}{2}\gamma_v^D N(N+1)^2 \mp \tfrac{1}{2}q_v^v N(N+1) \mp \tfrac{1}{2}q_v^D[N(N+1)]^2 \qquad (6.4)$$

(c) $v_2 = 2$, $\ell = 2$; $^2\Delta$ *vibronic state*

$$F_1(N,{}^{e}_{f}) = B_v[N(N+1) - 4] - D_v[N(N+1) - 4]^2 + H_v[N(N+1) - 4]^3$$

$$+ \tfrac{1}{2}\gamma_v N + \tfrac{1}{2}\gamma_v^D N^2(N+1) + \Phi(N,{}^{e}_{f}) \qquad (6.5)$$

$$F_2(N,{}^{e}_{f}) = B_v[N(N+1) - 4] - D_v[N(N+1) - 4]^2 + H_v[N(N+1) - 4]^3$$

$$- \tfrac{1}{2}\gamma_v(N+1) - \tfrac{1}{2}\gamma_v^D N(N+1)^2 + \Phi(N,{}^{e}_{f}) \qquad (6.6)$$

The higher order centrifugal distortion constant H_v and the ℓ-type doubling centrifugal distortion parameter q_v^D were found to result in modest improvements in the quality of the least-squares fit. In contrast, the parameter γ_v^D, representing the centrifugal distortion correction to the effective spin-rotation, had a much larger impact and was included for the $\tilde{B}^2\Sigma^+$ state vibrational levels, which exhibit an anomalously large γ_v due to the effects of second order $H_{SO} \times H_{ROT}$ interactions with the nearby $\tilde{A}^2\Pi$ state. As discussed earlier, the $\Phi(N,{}^{e}_{f})$ terms in eqs. 6.5 and 6.6 lead to ℓ-type splittings between the e and f parity levels of the $^2\Delta$ vibronic levels, given approximately as $q_{eff}^v N(N+1)[N(N+1) - 2]$. Recent microwave measurements on the $\tilde{X}^2\Sigma^+$ ground state of SrOH and SrOD by Anderson *et al.*[37] have provided very accurate determinations of the molecular constants for the (000) level. Accordingly, the parameters B_v'', D_v'', and γ_v'' were held fixed to the microwave values.

Initially, data from each of the bands observed in this work were treated separately by least-squares fitting. However, as pointed out by Albritton *et al.*[102], molecular constants determined in this way are highly correlated and

may differ significantly from their true values. In the present study, several of the observed vibrational levels are common to more than one transition. Consequently, the final least-squares fit of the entire data simultaneously served to lessen the correlation of errors for the $\tilde{B}^2\Sigma^+$ and $\tilde{X}^2\Sigma^+$ state molecular constants. Resolved fluorescence data were given a lower weight than the more accurate excitation measurements in accord with their respective uncertainties. The energy level expressions of eqs. 6.5 and 6.6 were not employed directly in this fit, rather, the ℓ-type doubling in SrOH was modeled by inclusion of the off-diagonal $(02^00)^2\Sigma^+ \sim (02^20)^2\Delta$ matrix elements presented in the latter part of this chapter. The combined data set contained approximately 1700 individual lines, however, owing to local perturbations in the $\tilde{B}^2\Sigma^+$ state vibrational levels, only some 1200 lines were included in the final fit. These perturbations are clearly evident in figs. 6.3, 6.4 and 6.5, where reduced rotational term values for the $(010)^2\Pi$, $(02^00)^2\Sigma$ and $(02^20)^2\Delta$ vibronic levels of the $\tilde{B}^2\Sigma^+$ state are plotted as a function of the rotational quantum number N. The measured line positions and residuals are given in tables 6.1 - 6.6: the molecular parameters determined from the fit are listed in table 6.7. Each of the bands is now considered separately.

$(02^00)^2\Sigma^+ \leftarrow (000)^2\Sigma^+$

Similar to $^2\Sigma^+ - {}^2\Sigma^+$ transitions of diatomic molecules, strong P_1, P_2, R_1, and R_2 branches are observed for this band. A perturbation is observed in the F_2 spin component where there is clear evidence of a level crossing between the $N = 9$ and 10 rotational levels (see fig. 6.4). In the region of the crossing, energy levels are shifted up to 1 cm^{-1} and the effects of the perturbation, in terms of high residuals, are observed over a long range in N ($N \leq 49$). Low N values of the F_1 spin component ($N \leq 22$) are also perturbed,

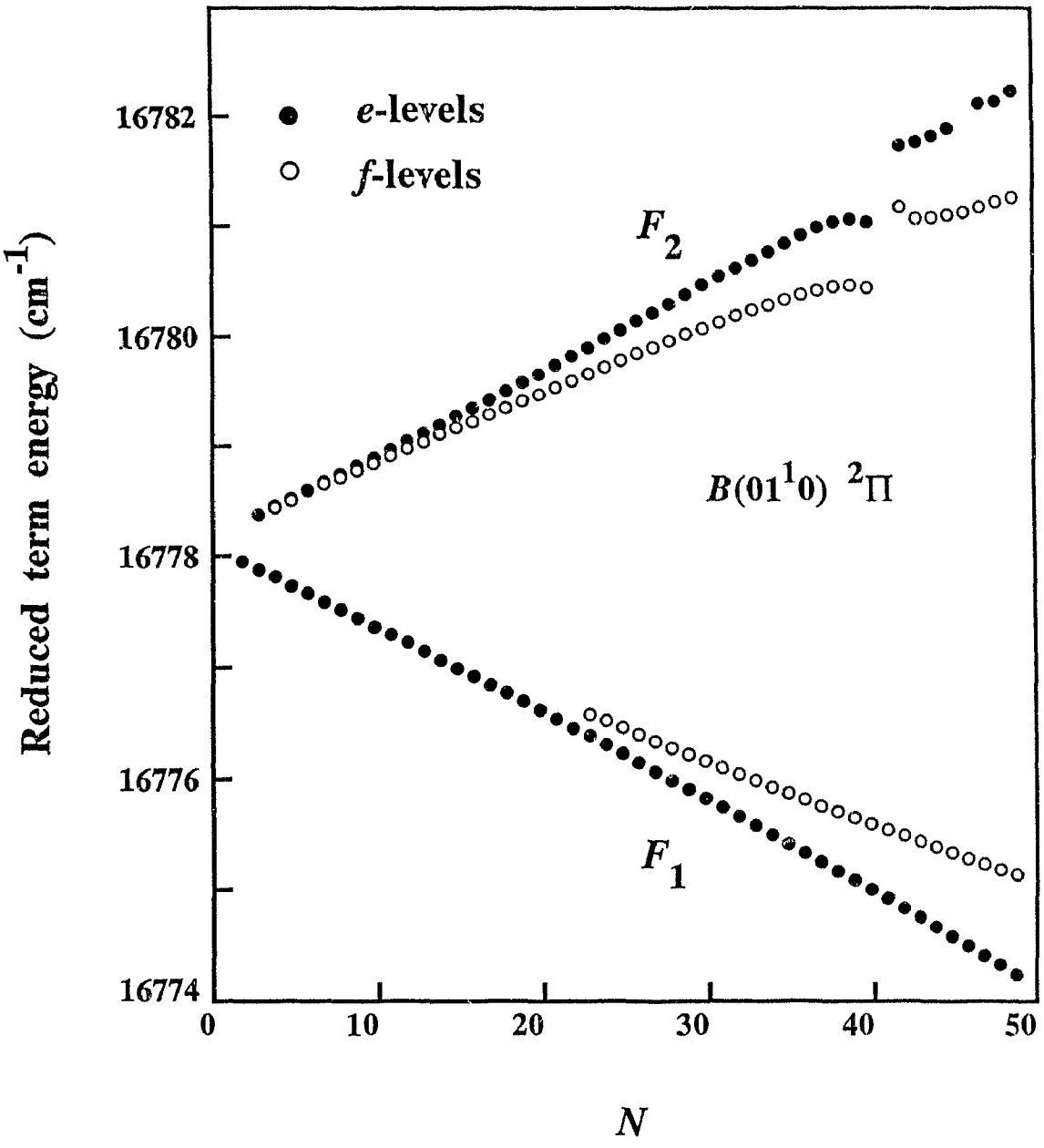

Figure 6.3: Reduced term energy plot for the $\tilde{B}(010)^2\Pi$ state of SrOH. The F_1 levels show no detectable perturbation, whereas the F_2 component shows evidence of a level crossing at $N \approx 41$. The vertical scale is expanded by subtraction of $B_v N(N+1) - D_v N^2(N+1)^2$ from the energies.

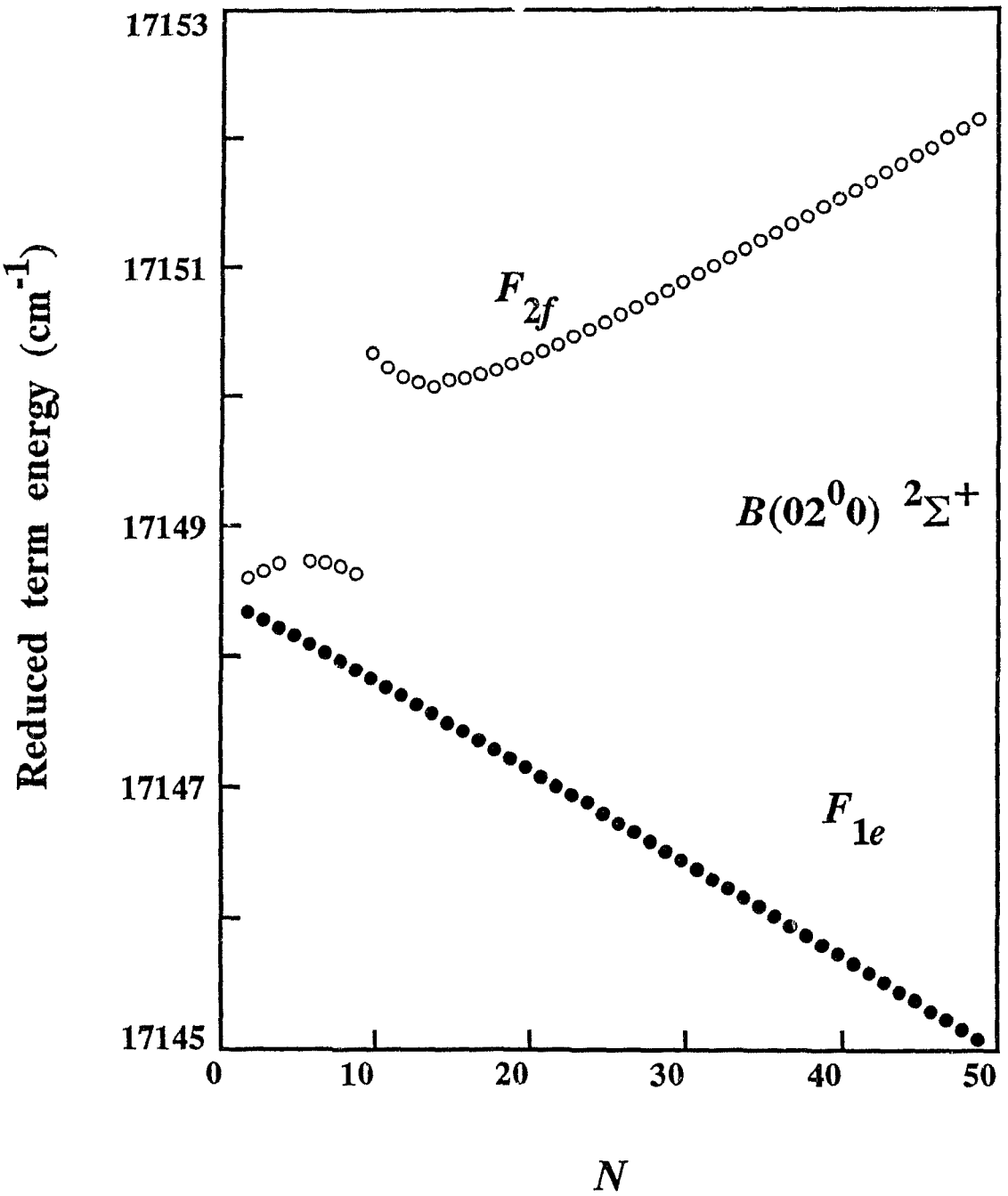

Figure 6.4: Reduced term energy plot for the $\tilde{B}(02^0 0)^2\Sigma^+$ state of SrOH showing a level crossing at $N \approx 10$ in the F_2 component. The vertical scale is expanded by subtraction of $B_v N(N+1) - D_v N^2(N+1)^2$ from the energies.

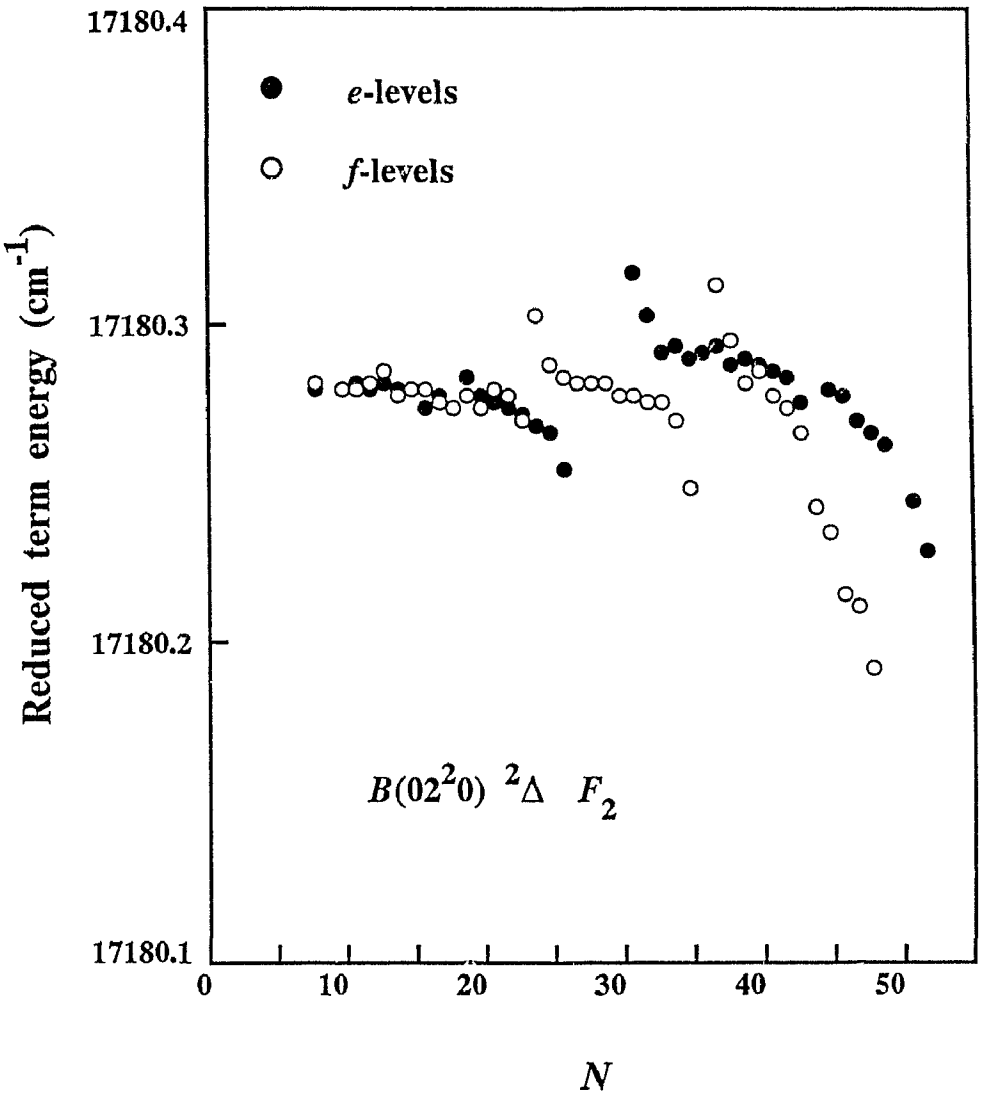

Figure 6.5: Reduced term energy plot for the F_2 levels of SrOH $\tilde{B}(02^20)^2\Delta$. The F_{2f} levels show clear indications of two level crossings at $N \approx 24$ and $N = 36$. In the F_{2e} levels, only one crossing at $N \approx 28$ is obvious. The negative deviation for $N > 40$ may be caused by extrapolation of the spin-rotation splitting rather than the effects of a perturbation. The vertical scale is expanded by subtraction of $B_v N(N + 1) - D_v N^2(N + 1)^2$ from the energies.

TABLE 6.1: Line Positions[a] (cm^{-1}) for the $B^2\Sigma^+ - X^2\Sigma^+$ (010)Π - (000)Σ^+ Band of SrOH.
The table shows $\bar{\nu}_{obs}$, the measured wavenumbers (cm^{-1}), and the residuals, $\bar{\nu}_{obs} - \bar{\nu}_{calc}$.

N	P_1		Q_1		R_1		P_2		Q_2		R_2	
2	16777.025	0.001										
3	16776.460	-0.002			16779.832	-0.005			16778.403	0.000	16780.475	-0.002
4	16775.900	-0.003			16780.285	0.002			16778.501	0.009	16781.067	0.000
5	16775.354	0.005			16780.729	-0.004	16775.996	0.002	16778.588	0.001	16781.645	-0.015
6	16774.793	-0.006			16781.185	-0.002	16775.585	-0.002	16778.689	0.003	16782.249	-0.007
7	16774.251	-0.001			16781.645	0.000			16778.794	0.005	16782.855	-0.002
8	16773.706	-0.003			16782.107	0.001	16774.794	0.011[b]	16778.902	0.005	16783.456	-0.005
9	16773.170	-0.001			16782.569	-0.003	16774.385	-0.003	16779.018	0.008	16784.061	-0.008
10	16772.632	-0.004			16783.036	-0.005	16773.992	-0.004	16779.133	0.006	16784.677	-0.004
11	16772.095	-0.010[b]			16783.514	0.000	16773.602	-0.005	16779.256	0.007		
12	16771.577	-0.001			16783.988	-0.003	16773.221	-0.002	16779.387	0.012	16785.938	0.022
13	16771.056	0.001			16784.470	-0.001	16772.841	-0.002	16779.515	0.009	16786.524	-0.016
14	16770.533	-0.003			16784.966	0.010	16772.461	-0.005	16779.651	0.009	16787.158	-0.009
15	16770.017	-0.004			16785.442	-0.002	16772.095	0.001[b]	16779.799	0.017	16787.790	-0.007
16	16769.504	-0.005			16785.938	0.002[b]	16771.721	-0.004	16779.942	0.016	16788.456	0.024[c]
17	16769.003	0.001			16786.428	-0.003	16771.351	-0.010	16780.092	0.016	16789.072	0.002
18	16768.497	-0.001			16786.931	0.001	16770.992	-0.008[c]	16780.248	0.019[c]	16789.712	0.000[c]
19	16768.004	0.005			16787.431	-0.003	16770.632	-0.011[c]	16780.407	0.020[c]	16790.338	-0.020[c]
20	16767.508	0.005			16787.938	-0.002	16770.278	-0.012[c]	16780.569	0.019[c]	16791.003	-0.004[c]
21	16767.015	0.003			16788.456	0.005[b]	16769.928	-0.013[c]	16780.744	0.027[c]	16791.655	-0.005[c]
22	16766.525	0.001			16788.970	0.005	16769.581	-0.014[c]	16780.917	0.028[c]	16792.313	-0.003[c]
23	16766.035	-0.005[b]	16777.710	-0.001	16789.487	0.004	16769.241	-0.013[c]	16781.090	0.025[c]	16792.983	0.007[c]
24	16765.564	0.004	16777.749	-0.001	16790.004	-0.001	16768.906	-0.010[c]	16781.276	0.030[c]	16793.632	-0.008[c]
25	16765.090	0.005	16777.791	-0.002	16790.533	0.003	16768.569	-0.014[c]	16781.460	0.029[c]	16794.308	0.000[c]
26	16764.614	0.001	16777.838	-0.002	16791.062	0.003	16768.241	-0.012[c]	16781.655	0.034[c]	16794.968	-0.011[c]
27	16764.148	0.003	16777.891	-0.001	16791.596	0.005	16767.919	-0.008[c]	16781.842	0.027[c]	16795.644	-0.010[c]
28	16763.682	0.001	16777.946	-0.003	16792.132	0.004	16767.591	-0.015[c]	16782.040	0.027[c]	16796.321	-0.011[c]
29	16763.225	0.005	16778.008	-0.002	16792.672	0.005	16767.273	-0.014[c]	16782.251	0.035[c]	16796.997	-0.017[c]
30	16762.765	0.001	16778.074	-0.001	16793.218	0.007	16766.960	-0.013[c]	16782.466	0.042[c]	16797.686	-0.013[c]
31	16762.316	0.004	16778.145	0.000	16793.763	0.005	16766.642	-0.021[c]	16782.670	0.034[c]	16798.374	-0.014[c]
32	16761.864	0.000	16778.217	-0.003	16794.308	-0.001[b]	16766.332	-0.025[c]	16782.878	0.026[c]	16799.047	-0.033[c]
33	16761.420	0.001	16778.296	-0.003	16794.866	0.003	16766.035	-0.019[c]	16783.090	0.017[c]	16799.740	-0.036[c]
34	16760.979	0.000	16778.381	-0.001	16795.422	0.001	16765.726	-0.029[c]	16783.312	0.014[c]	16800.433	-0.043[c]
35	16760.541	-0.001	16778.470	0.000	16795.988	0.006	16765.424	-0.037[c]	16783.534	0.006[c]	16801.127	-0.052[c]
36	16760.106	-0.004	16778.560	-0.003	16796.549	0.002	16765.125	-0.045[c]	16783.760	-0.002[c]	16801.804	-0.081[c]

TABLE 6.1 (continued)

N	P_1		Q_1		R_1		P_2		Q_2		R_2	
37	16759.678	-0.003	16778.657	-0.003	16797.115	-0.001	16764.826	-0.057[c]	16783.987	-0.013[c]	16802.499	-0.096[c]
38	16759.258	0.002	16778.761	0.000	16797.686	-0.002[b]	16764.526	-0.073[c]	16784.193	-0.050[c]	16803.171	-0.138[c]
39	16758.836	0.000	16778.866	-0.001	16798.265	0.002	16764.224	-0.096[c]	16784.381	-0.110[c]	16803.819	-0.207[c]
40	16758.419	0.000	16778.976	-0.002	16798.838	-0.004	16763.905	-0.140[c]	16784.522	-0.220[c]		
41	16758.004	-0.002	16779.092	-0.001	16799.426	0.001	16763.559	-0.214[c]			16805.823	0.353[c]
42	16757.599	0.002	16779.210	-0.002	16800.010	-0.001			16785.565	0.306	16806.443	0.246
43	16757.189	-0.003	16779.333	-0.003	16800.602	0.001	16763.647	0.406[c]	16785.776	0.252[c]	16807.119	0.192[c]
44	16756.791	0.000	16779.464	0.000	16801.190	-0.004	16763.226	0.245[c]	16786.010	0.217[c]	16807.823	0.162[c]
45	16756.393	-0.001	16779.596	-0.001	16801.803	0.013[b]	16762.922	0.197[c]	16786.268	0.202[c]	16808.542	0.144[c]
46	16756.001	0.000	16779.733	-0.001	16802.389	-0.001	16762.642	0.169[c]			16809.271	0.132[c]
47	16755.609	-0.002	16779.874	-0.001	16802.991	-0.003	16762.368	0.144[c]	16786.884	0.258[c]	16810.004	0.121[c]
48	16755.224	-0.002	16780.020	-0.001	16803.604	0.003	16762.111	0.132[c]	16787.097	0.184[c]	16810.742	0.112[c]
49	16754.843	-0.002	16780.173	0.001	16804.205	-0.006	16761.864	0.126[c]	16787.393	0.189[c]	16811.495	0.114[c]
50	16754.464	-0.003	16780.328	0.002	16804.824	-0.001	16761.615	0.114[c]			16812.247	0.112[c]
51	16754.092	-0.002	16780.487	0.001	16805.439	-0.003	16761.380	0.112[c]			16813.006	0.114[c]
52	16753.723	-0.001	16780.652	0.003	16806.058	-0.004	16761.148	0.109[c]			16813.767	0.114[c]
53	16753.357	-0.001	16780.818	0.001	16806.684	-0.002	16760.919	0.106[c]			16814.529	0.113[c]
54	16753.000	0.003	16780.990	0.000	16807.312	-0.001	16760.700	0.108[c]			16815.299	0.116[c]
55	16752.643	0.004	16781.169	0.002	16807.943	-0.001	16760.490	0.116[c]				
56	16752.287	0.002	16781.347	-0.001	16808.575	-0.003	16760.276	0.116[c]			16816.846	0.118[c]
57	16751.937	0.002	16781.536	0.002	16809.217	0.001	16760.061	0.111[c]			16817.622	0.117[c]
58	16751.590	0.000	16781.725	0.001	16809.850	-0.007	16759.851	0.107[c]			16818.403	0.118[c]
59	16751.248	0.000	16781.919	0.000	16810.499	-0.002						
60	16750.911	0.001	16782.121	0.003	16811.150	0.001	16759.465	0.122[c]				
61	16750.580	0.004	16782.324	0.002	16811.797	-0.003						
62	16750.250	0.004	16782.530	0.000	16812.451	-0.003	16759.080	0.123[c]				
63	16749.922	0.002	16782.742	0.000	16813.112	0.000	16758.902	0.132[c]				
64	16749.602	0.004	16782.960	0.001	16813.767	-0.006[b]	16758.718	0.131[c]				
65	16749.285	0.005	16783.180	0.000	16814.435	-0.002						
66	16748.972	0.005	16783.406	0.000								
67	16748.658	0.001	16783.636	0.000								
68	16748.348	-0.003	16783.866	-0.005								
69	16748.048	-0.001										

[a]Unless indicated otherwise, line positions have an assigned uncertainty of 0.004 cm^{-1}.

[b]Blended line with assigned uncertainty of 0.02 cm^{-1}.

[c]Perturbed line, excluded from the fit.

TABLE 6.2: Line Positions[a] (cm^{-1}) for the $B^2\Sigma^+$-$X^2\Sigma^+$ $(02^00)\Sigma^+$-$(000)\Sigma^+$ band of SrOH. The table shows $\bar{\nu}_{obs}$, the measured wavenumbers (cm^{-1}), and the residuals, $\bar{\nu}_{obs} - \bar{\nu}_{calc}$.

N	P_1		R_1		P_2		R_2	
1			17149.338	-0.100[c]			17149.608	-0.192[c]
2	17147.391	-0.118[c]	17149.782	-0.091[c]	17147.562	-0.168[c]	17150.160	-0.220[c]
3	17146.839	-0.105[c]	17150.227	-0.083[c]	17147.123	-0.187[c]		
4	17146.292	-0.090[c]	17150.684	-0.066[c]	17146.669	-0.224[c]	17151.244	-0.304[c]
5	17145.751	-0.071[c]	17151.131	-0.062[c]	17146.219	-0.260[c]	17151.778	-0.358[c]
6	17145.195	-0.070[c]	17151.584	-0.055[c]	17145.751	-0.317[c]	17152.289	-0.439[c]
7	17144.651	-0.061[c]	17152.040	-0.047[c]	17145.298	-0.362[c]	17152.784	-0.538[c]
8	17144.107	-0.054[c]	17152.496	-0.043[c]	17144.813	-0.442[c]	17153.258	-0.661[c]
9	17143.563	-0.050[c]	17152.954	-0.039[c]	17144.312	-0.540[c]	17155.487	0.969[c]
10	17143.026	-0.042[c]	17153.418	-0.032[c]	17143.782	-0.671[c]	17155.904	0.783[c]
11	17142.508	-0.018[c]	17153.884	-0.026[c]	17145.022	0.966[c]	17156.363	0.637[c]
12	17141.956	-0.031[c]	17154.351	-0.022[c]	17144.441	0.778[c]	17156.859	0.525[c]
13	17141.424	-0.027[c]	17154.819	-0.020[c]	17143.908	0.636[c]	17157.365	0.420[c]
14	17140.892	-0.026[c]	17155.288	-0.019[c]	17143.409	0.525[c]	17157.960	0.401[c]
15	17140.367	-0.021[c]	17155.764	-0.014[c]	17142.918	0.418[c]	17158.517	0.342[c]
16	17139.841	-0.020[c]	17156.238	-0.014[c]	17142.507	0.389[c]	17159.097	0.302[c]
17	17139.327	-0.010[c]	17156.719	-0.010[c]	17142.083	0.344[c]	17159.679	0.263[c]
18	17138.801	-0.014[c]	17157.199	-0.009[c]	17141.663	0.301[c]	17160.278	0.237[c]
19	17138.281	-0.016[c]	17157.685	-0.005[c]	17141.256	0.267[c]	17160.883	0.215[c]
20	17137.770	-0.011[c]	17158.169	-0.006[c]	17140.858	0.239[c]	17161.495	0.197[c]
21	17137.257	-0.012[c]	17158.659	-0.004[c]	17140.467	0.216[c]	17162.110	0.179[c]
22	17136.751	-0.008[c]	17159.152	-0.001	17140.084	0.197[c]	17162.733	0.167[c]
23	17136.247	-0.005[c]	17159.662	0.016[b]	17139.705	0.180[c]	17163.357	0.153[c]
24	17135.742	-0.006	17160.141	0.000	17139.327	0.161[c]	17163.983	0.139[c]
25	17135.238	-0.009	17160.640	0.001	17138.961	0.151[c]	17164.618	0.131[c]
26	17134.743	-0.006	17161.142	0.002	17138.595	0.138[c]	17165.245	0.113[c]
27	17134.250	-0.004	17161.646	0.003[b]	17138.233	0.127[c]	17165.888	0.108[c]
28	17133.763	0.001	17162.151	0.002	17137.876	0.117[c]	17166.531	0.100[c]
29	17133.268	-0.005	17162.661	0.003	17137.525	0.111[c]	17167.176	0.092[c]
30	17132.789	0.003	17163.172	0.003	17137.172	0.100[c]	17167.824	0.085[c]
31	17132.297	-0.005	17163.685	0.003	17136.825	0.092[c]	17168.475	0.078[c]
32	17131.823	0.001	17164.202	0.004	17136.483	0.086[c]	17169.129	0.071[c]
33	17131.345	0.001	17164.722	0.005	17136.143	0.079[c]	17169.787	0.066[c]
34	17130.870	0.002	17165.247	0.009	17135.803	0.070[c]	17170.447	0.061[c]
35	17130.398	0.002	17165.766	0.005	17135.468	0.063[c]	17171.107	0.054[c]
36	17129.948	0.021[b]	17166.290	0.003	17135.135	0.055[c]	17171.773	0.050[c]
37	17129.462	0.002	17166.818	0.003	17134.808	0.051[c]	17172.430	0.034[c]
38	17128.997	0.001	17167.346	0.000	17134.486	0.049[c]	17173.112	0.042[c]
39	17128.534	-0.001	17167.880	0.001	17134.164	0.044[c]	17173.783	0.036[c]
40	17128.069	-0.008	17168.417	0.003	17133.846	0.040[c]	17174.452	0.026[c]
41	17127.620	-0.001	17168.953	0.002	17133.530	0.036[c]	17175.134	0.027[c]
42	17127.168	0.000	17169.493	0.002	17133.215	0.030[c]	17175.817	0.026[c]
43	17126.723	0.005	17170.032	-0.001	17132.908	0.029[c]	17176.496	0.020[c]
44	17126.271	0.000	17170.582	0.004	17132.599	0.024[c]	17177.182	0.018[c]
45	17125.822	-0.004	17171.116	-0.008	17132.297	0.023[c]	17177.859	0.005[c]

TABLE 6.2. (continued)

N	P_1		R_1		P_2		R_2	
46	17125.385	0.001	17171.676	0.003	17131.993	0.017[c]	17178.559	0.013[c]
47	17124.946	0.001	17172.224	0.000	17131.697	0.017[c]	17179.248	0.008[c]
48	17124.509	0.000	17172.772	-0.005	17131.399	0.012[c]	17179.950	0.014[c]
49	17124.076	0.001	17173.332	0.000	17131.103	0.007[c]	17180.641	0.006[b]
50	17123.641	-0.003	17173.890	0.000[b]	17130.821	0.013[c]	17181.333	-0.002[b]
51	17123.214	-0.001	17174.452	0.003[b]	17130.527	0.005	17182.042	0.005
52	17122.788	-0.001	17175.006	-0.005[b]	17130.243	0.004[b]	17182.740	-0.001
53	17122.361	-0.005	17175.572	-0.002	17129.948	-0.010[b]	17183.451	0,004
54	17121.943	-0.002	17176.138	-0.001	17129.681	0.001	17184.156	0.001[b]
55	17121.523	-0.004	17176.700	-0.007	17129.407	0.002	17184.858	-0.007[b]
56	17121.108	-0.003	17177.274	-0.002[b]	17129.129	-0.002	17185.578	0.002
57	17120.696	-0.002	17177.859	0.011[b]	17128.859	-0.002	17186.292	0.002
58	17120.287	-0.001	17178.416	-0.005	17128.588	-0.004	17187.003	-0.002
59	17119.878	-0.002	17178.994	-0.002	17128.323	-0.003[b]	17187.721	-0.001[b]
60	17119.470	-0.004	17179.574	0.001	17128.069	0.006[b]	17188.450	0.010[b]
61	17119.068	-0.003	17180.148	-0.004	17127.798	-0.003	17189.157	-0.004
62	17118.667	-0.004	17180.734	0.001[b]	17127.539	-0.004	17189.881	-0.002
63	17118.273	0.000	17181.333	0.018[b]	17127.279	-0.007	17190.609	0.002
64	17117.874	-0.003	17181.903	0.004	17127.028	-0.004	17191.330	-0.002
65	17117.486	0.002	17182.479	-0.006	17126.780	0.000	17192.064	0.005
66	17117.094	0.001	17183.078	0.005	17126.527	-0.004[b]	17192.795	0.008
67	17116.704	-0.001	17183.674	0.012	17126.271	-0.012[b]	17193.519	0.002
68	17116.319	0.000	17184.252	-0.001	17126.035	-0.003	17194.250	0.001
69	17115.934	-0.001	17184.858	0.012	17125.796	0.001	17194.983	0.001
70	17115.553	-0.001	17185.440	0.000	17125.548	-0.007	17195.715	-0.001
71	17115.173	-0.002	17186.033	-0.003	17125.324	0.008	17196.454	0.002
72	17114.796	-0.003	17186.634	0.001	17125.083	0.003		
73	17114.426	0.001	17187.232	0.000	17124.852	0.006		
74	17114.055	0.002	17187.834	0.001	17124.615	0.001		
75	17113.684	0.001			17124.382	-0.003		
76	17113.321	0.005			17124.148	-0.009		
77	17112.955	0.004						
78	17112.592	0.004						
79	17112.229	0.001						
80	17111.871	0.002						
81	17111.515	0.002						
82	17111.160	0.001						
83	17110.810	0.002						
84	17110.461	0.003						
85	17110.110	-0.001						
86	17109.767	0.001						
87	17109.422	-0.001						
88	17109.081	-0.001						
89	17108.744	0.001						
90	17108.403	-0.004						
91	17108.067	-0.006						

[a]Unless indicated otherwise, line positions have an assigned uncertainty of 0.004 cm^{-1}.

[b]Blended line with assigned uncertainty of 0.02 cm^{-1}.

[c]Perturbed line, excluded from the fit.

TABLE 6.3: Line Positions[a] (cm^{-1}) for the $B^2\Sigma^+ - X^2\Sigma^+$ $(02^00)\Sigma^+ - (010)\Pi$ Band of SrOH.
The table shows $\bar{\nu}_{obs}$, the measured wavenumbers (cm^{-1}), and the residuals, $\bar{\nu}_{obs} - \bar{\nu}_{calc}$.

N	P_1		Q_1		R_1		P_2		Q_2		R_2	
2	16783.974	-0.100[c]			16786.348	-0.089[c]						
3	16783.411	-0.106[c]			16786.811	-0.072[c]						
4	16782.868	-0.092[c]			16787.262	-0.067[c]						
5	16782.327	-0.080[c]			16787.713	-0.065[c]						
6	16781.787	-0.072[c]			16788.173	-0.059[c]						
7	16781.255	-0.062[c]										
8	16780.721	-0.058[c]			16789.111	-0.046[c]						
9	16780.181	-0.065[c]			16789.583	-0.043[c]						
10	16779.672	-0.046[c]			16790.063	-0.037[c]						
11	16779.153	-0.041[c]			16790.547	-0.031[c]						
12	16778.651	-0.023[c]			16791.037	-0.023[c]						
13	16778.132	-0.027[c]			16791.522	-0.025[c]					16794.069	0.416[c]
14	16777.609	-0.040[c]			16792.012	-0.026[c]					16794.681	0.391[c]
15	16777.119	-0.024[c]			16792.516	-0.018[c]			16787.090	0.343[c]	16795.271	0.340[c]
16	16776.620	-0.022[c]			16793.017	-0.017[c]					16795.878	0.302[c]
17	16776.129	-0.017[c]			16793.529	-0.009[c]			16787.283	0.268[c]	16796.492	0.267[c]
18	16775.641	-0.013[c]			16794.036	-0.011[c]	16778.480	0.279[c]			16797.120	0.241[c]
19	16775.150	-0.017[c]			16794.552	-0.008[c]	16778.132	0.273[c]	16787.535	0.237[c]	16797.738	0.200[c]
20	16774.670	-0.014[c]			16795.069	-0.009[c]	16777.756	0.235[c]	16787.660	0.215[c]	16798.397	0.197[c]
21	16774.191	-0.015[c]			16795.592	-0.008[c]	16777.401	0.213[c]	16787.795	0.200[c]	16799.043	0.176[c]
22	16773.722	-0.010[c]			16796.124	-0.002	16777.056	0.197[c]	16787.938	0.189[c]	16799.704	0.166[c]
23	16773.254	-0.009[c]			16796.657	0.001	16776.711	0.176[c]	16788.065	0.158[c]	16800.368	0.154[c]
24	16772.790	-0.008			16797.187	-0.004	16776.377	0.161[c]	16788.216	0.148[c]	16801.044	0.151[c]
25	16772.331	-0.007			16797.738	0.008[b]	16776.057	0.157[c]	16788.369	0.136[c]	16801.707	0.130[c]
26	16771.875	-0.008			16798.273	-0.001	16775.728	0.138[c]	16788.527	0.126[c]	16802.383	0.118[c]
27	16771.426	-0.006			16798.824	0.003	16775.411	0.127[c]	16788.685	0.112[c]	16803.068	0.110[c]
28	16770.997	0.011[b]	16784.604	-0.006	16799.375	0.002	16775.100	0.118[c]	16788.856	0.108[c]	16803.759	0.105[c]
29	16770.545	0.001[b]	16784.643	-0.001	16799.930	0.001	16774.795	0.110[c]	16789.025	0.098[c]	16804.451	0.096[c]
30	16770.107	0.000[b]	16784.681	-0.001[b]	16800.492	0.003	16774.491	0.098[c]	16789.204	0.094[c]	16805.132	0.072[c]
31	16769.676	0.002[b]	16784.721	-0.002	16801.044	-0.010[b]	16774.191	0.087[c]	16789.378	0.082[c]	16805.847	0.078[c]
32	16769.255	0.009[b]	16784.769	0.000	16801.626	0.003[b]	16773.903	0.082[c]	16789.562	0.076[c]	16806.556	0.074[c]
33	16768.824	0.002	16784.817	0.000	16802.200	0.005	16773.620	0.078[c]	16789.749	0.070[c]	16807.263	0.064[c]
34	16768.404	0.001	16784.870	0.001	16802.776	0.004	16773.337	0.070[c]	16789.943	0.068[c]	16807.981	0.061[c]
35	16767.991	0.003[b]	16784.928	0.003	16803.359	0.006	16773.254	0.258[c]	16790.132	0.057[c]	16808.703	0.058[c]
36	16767.577	-0.001	16784.975	-0.009[b]	16803.939	0.001	16772.790	0.060[c]	16790.345	0.067[c]	16809.425	0.051[c]
37	16767.174	0.002	16785.048	0.001	16804.531	0.003	16772.519	0.050[c]	16790.534	0.049[c]	16810.151	0.044[c]
38	16766.770	-0.001	16785.114	0.001	16805.132	0.011	16772.260	0.048[c]	16790.737	0.041[c]	16810.887	0.042[c]
39	16766.375	0.000	16785.186	0.003	16805.727	0.009	16772.001	0.042[c]	16790.951	0.042[c]	16811.622	0.036[c]

TABLE 6.3 (continued)

N	P_1		Q_1		R_1		P_2		Q_2		R_2	
40	16765.984	0.002	16785.260	0.004	16806.320	0.001	16771.750	0.039[c]	16791.160	0.034[c]	16812.360	0.029[c]
41	16765.585	-0.009[b]	16785.332	-0.001	16806.924	-0.001	16771.499	0.032[c]	16791.379	0.032[c]	16813.110	0.030[c]
42	16765.215	0.004	16785.414	0.001	16807.531	-0.003	16771.257	0.030[c]	16791.601	0.031[c]	16813.853	0.020[c]
43	16764.833	0.001	16785.497	0.000	16808.147	0.000	16770.997	0.005[c]	16791.822	0.024[c]	16814.613	0.024[c]
44	16764.457	-0.001	16785.585	0.002	16808.766	0.001	16770.786	0.025[c]	16792.046	0.018[c]	16815.371	0.021[c]
45	16764.087	-0.001	16785.676	0.002	16809.385	-0.001	16770.545	0.010[c]	16792.288	0.026[c]	16816.130	0.015[c]
46	16763.704	-0.018[b]	16785.770	0.002	16810.012	0.001	16770.330	0.017[c]	16792.516	0.017[c]	16816.897	0.014[c]
47	16763.358	-0.003	16785.869	0.004	16810.639	-0.001	16770.107	0.012[c]	16792.751	0.012[c]	16817.665	0.010[c]
48	16763.001	-0.003			16811.273	0.001	16769.895	0.014[c]	16792.983	0.000[c]	16818.445	0.014[c]
49	16762.653	0.001	16786.069	0.000	16811.908	-0.001	16769.676	0.004[c]	16793.224	-0.006[c]		
50	16762.309	0.005[b]	16786.180	0.004	16812.548	-0.002	16769.482	0.015[c]	16793.487	0.007	16819.997	0.003
51	16761.959	-0.001	16786.287	0.000	16813.189	-0.005	16769.255	-0.011[b]			16820.780	-0.001
52	16761.621	0.001	16786.400	0.000	16813.853	0.011[b]	16769.078	0.009	16793.994	0.005	16821.570	-0.001
53	16761.285	0.000	16786.518	0.001[b]	16814.496	0.002	16768.882	0.005[b]	16794.254	0.005	16822.366	0.000
54	16760.954	-0.001	16786.637	-0.001	16815.147	-0.002	16768.692	0.003	16794.520	0.008	16823.160	-0.004
55	16760.628	0.000	16786.761	0.000	16815.809	0.000	16768.507	0.002[b]	16794.777	-0.001	16823.967	0.002
56	16760.305	-0.001	16786.885	-0.003	16816.470	-0.002	16768.327	0.001	16795.030	-0.017	16824.765	-0.005
57	16759.995	0.006[b]	16787.018	0.000	16817.138	0.000	16768.151	0.001	16795.322	0.003	16825.578	-0.001
58	16759.677	0.002	16787.169	0.018[b]	16817.814	0.005[b]			16795.593	-0.002	16826.389	-0.002
59	16759.364	-0.002	16787.290	0.002	16818.484	0.001	16767.812	0.000	16795.873	0.000	16827.205	-0.002
60	16759.062	0.001	16787.438	0.010[b]	16819.151	-0.009	16767.646	-0.003	16796.144	-0.010	16828.023	-0.003
61	16758.759	-0.002	16787.572	0.002	16819.842	0.000			16796.436	-0.003	16828.845	-0.004
62	16758.463	-0.001	16787.720	0.004	16820.521	-0.005	16767.335	0.000	16796.723	-0.003	16829.671	-0.004
63	16758.173	0.001	16787.868	0.002	16821.215	0.000			16797.004	-0.013		
64	16757.886	0.001	16788.020	0.002	16821.904	-0.003			16797.312	0.001		
65	16757.604	0.003	16788.177	0.004	16822.598	-0.004	16766.893	-0.003	16797.605	-0.002		
66	16757.323	0.001	16788.335	0.003	16823.295	-0.006			16797.908	0.001		
67	16757.046	0.000			16823.995	-0.009	16766.628	0.004	16798.212	0.003		
68	16756.774	-0.001			16824.705	-0.005	16766.501	0.008	16798.521	0.007		
69	16756.507	-0.002			16825.420	0.001						
70	16756.247	0.001			16826.124	-0.008	16766.247	0.002				
71	16755.991	0.003			16826.848	0.000	16766.135	0.008				
72	16755.737	0.004			16827.567	-0.001						
73	16755.487	0.004			16828.289	-0.002						
74	16755.238	0.001			16829.015	-0.002						
75	16754.999	0.004			16829.748	0.001						

[a]Unless indicated otherwise, line positions have an assigned uncertainty of 0.004 cm^{-1}.

[b]Blended line with assigned uncertainty of 0.02 cm^{-1}.

[c]Perturbed line, excluded from the fit.

TABLE 6.4: Line Positions[a] (cm^{-1}) for the $B^2\Sigma^+ - X^2\Sigma^+$ $(02^20)\Delta$ - (010)Π Band of SrOH. The table shows $\bar{\nu}_{obs}$, the measured wavenumbers (cm^{-1}), and the residuals, $\bar{\nu}_{obs} - \bar{\nu}_{calc}$.

N	P_{1f}		P_{1e}		R_{1f}		R_{1e}	
3	16815.220	0.009[b]	16815.220	0.001[b]	16818.592	0.016[b]	16818.592	0.008[b]
4	16814.655	0.003[b]	16814.655	-0.008[b]	16819.023	0.005[b]	16819.023	-0.006[b]
5	16814.101	0.005[b]	16814.101	-0.008[b]	16819.477	0.013[b]	16819.477	0.000[b]
6	16813.550	0.007[b]	16813.550	-0.010[b]	16819.937	0.025[b]	16819.937	0.008[b]
7	16813.007	0.014[b]	16813.007	-0.009[b]	16820.389	0.025[b]	16820.389	0.003[b]
8	16812.455	0.008	16812.474	-0.002	16820.823	0.004	16820.849	0.002
9	16811.905	0.001	16811.936	-0.004	16821.289	0.012	16821.305	-0.007
10	16811.364	0.000	16811.407	-0.001	16821.743	0.005	16821.784	0.003
11	16810.832	0.004	16810.880	0.000	16822.201	-0.001	16822.257	0.002
12	16810.300	0.006	16810.360	0.004	16822.673	0.003	16822.733	0.002
13	16809.782	0.018[b]	16809.845	0.009	16823.142	0.002	16823.218	0.006
14	16809.240	0.002	16809.323	0.002	16823.612	-0.002	16823.697	0.000
15	16808.706	-0.008	16808.811	0.002	16824.091	0.000	16824.181	-0.005
16	16808.199	0.005	16808.306	0.005	16824.577	0.006[b]	16824.671	-0.007
17	16807.679	0.002	16807.800	0.002	16825.055	0.001	16825.175	0.000
18	16807.168	0.005	16807.310	0.011	16825.539	-0.001	16825.673	-0.002
19	16806.659	0.006	16806.797	-0.006[b]	16826.024	-0.005	16826.179	0.000
20	16806.142	-0.004[b]	16806.315	0.003	16826.532	0.011[b]	16826.689	0.002
21	16805.643	0.001	16805.835	0.010[b]	16827.018	0.002	16827.202	0.003
22	16805.142	0.001	16805.337	-0.005	16827.516	0.002	16827.715	0.000
23	16804.646	0.002	16804.864	0.001	16828.017	0.001	16828.235	0.000
24	16804.159	0.009	16804.392	0.004	16828.518	-0.002	16828.758	0.000
25	16803.663	0.004	16803.928	0.011[b]	16829.023	-0.004	16829.285	-0.001
26	16803.176	0.005	16803.453	0.003	16829.537	-0.001	16829.814	-0.003
27	16802.686	-0.001	16802.998	0.011	16830.052	0.001	16830.351	0.000
28	16802.203	-0.003	16802.524	-0.005	16830.565	-0.002	16830.889	-0.001
29	16801.708	-0.021[b]	16802.073	-0.001	16831.081	-0.005	16831.429	-0.004
30	16801.256	0.002	16801.623	-0.001	16831.604	-0.005	16831.977	-0.002
31	16800.786	0.003	16801.188	0.011[b]	16832.131	-0.003	16832.528	-0.001
32	16800.304	-0.011[b]	16800.735	0.000	16832.660	-0.002	16833.078	-0.005
33	16799.856	0.005	16800.304	0.007[b]	16833.192	-0.001	16833.638	-0.002
34	16799.376	-0.013[b]	16799.856	-0.007	16833.726	-0.001	16834.200	-0.002
35	16798.931	0.000	16799.435	0.002	16834.265	0.002	16834.761	-0.006
36	16798.473	-0.004	16799.007	-0.001	16834.802	-0.001	16835.337	0.002
37	16798.021	-0.004	16798.585	-0.001	16835.337	-0.009	16835.899	-0.009[b]
38	16797.578	0.001	16798.169	0.001	16835.899	0.008[b]	16836.480	-0.004
39	16797.123	-0.009[b]	16797.736	-0.019[b]	16836.442	0.003[b]	16837.063	-0.001
40	16796.686	-0.005	16797.343	-0.003	16836.988	-0.003	16837.646	-0.002
41	16796.252	0.000	16796.939	-0.002	16837.544	-0.001	16838.236	0.001
42	16795.812	-0.005	16796.549	0.009[b]	16838.103	0.002[b]	16838.826	0.000
43	16795.376	-0.009[b]	16796.144	0.001	16838.660	-0.001	16839.422	0.001
44	16794.967	0.010[b]	16795.746	-0.004	16839.217	-0.006	16840.023	0.003
45	16794.518	-0.014[b]	16795.376	0.014[b]	16839.790	0 001	16840.624	0.002
46	16794.107	-0.003	16794.967	-0.010[b]	16840.357	0.000	16841.228	0.000
47	16793.692	0.001	16794.595	-0.002	16840.926	-0.002	16841.837	0.000
48	16793.277	0.001	16794.225	0.004	16841.501	0.000	16842.452	0.001
49	16792.859	-0.004	16793.847	-0.002	16842.082	0.005	16843.068	0.001

TABLE 6.4 (continued)

N	P_{1f}		P_{1e}		R_{1f}		R_{1e}	
50	16792.453	-0.002	16793.484	0.002	16842.658	0.001	16843.689	0.001
51	16792.030	-0.019[b]	16793.118	0.000	16843.240	0.002	16844.313	0.001
52	16791.656	0.009[b]	16792.756	-0.003	16843.815	-0.008[b]	16844.958	0.018[b]
53	16791.246	-0.002	16792.401	-0.003	16844.412	0.002	16845.587	0.015[b]
54	16790.850	-0.002	16792.030	-0.023[b]	16844.999	-0.001	16846.200	-0.007[b]
55	16790.459	-0.001	16791.711	0.004	16845.587	-0.006[b]	16846.844	-0.002
56	16790.066	-0.005[b]	16791.370	0.006	16846.200	0.011[b]	16847.490	0.001
57	16789.672	-0.013[b]	16791.012	-0.015[b]	16846.784	-0.003	16848.135	-0.001
58	16789.299	-0.003	16790.691	-0.002	16847.389	0.001	16848.781	-0.005[b]
59	16788.919	-0.004	16790.356	-0.008[b]	16847.992	0.001	16849.443	0.003
60	16788.538	-0.009	16790.066	0.027[b]	16848.586	-0.012[b]	16850.100	0.003
61								
62					16849.816	-0.002	16851.419	-0.005
63					16850.431	-0.002		

N	Q_{1ef}		Q_{1fe}		Q_{2ef}		Q_{2fe}	
9					16817.732	0.002		
10					16817.842	0.001		
11					16817.959	0.003	16817.909	0.005
12					16818.075	0.000	16818.017	0.003
13					16818.201	0.003	16818.136	0.009[b]
14					16818.330	0.005	16818.242	-0.001
15					16818.459	0.003	16818.364	0.002
16					16818.592	0.001[b]	16818.482	-0.002
17					16818.732	0.002	16818.592	-0.017[b]
18					16818.868	-0.005	16818.732	-0.006
19					16819.017	-0.002[b]	16818.868	-0.002
20					16819.168	-0.002	16819.017	0.013[b]
21					16819.318	-0.006	16819.141	-0.001
22					16819.475	-0.007	16819.279	-0.005
23					16819.639	-0.006	16819.417	-0.011[c]
24					16819.802	-0.009	16819.595	0.020[c]
25					16819.966	-0.015[c]	16819.734	0.008[c]
26					16820.129	-0.026[c]	16819.881	0.002
27							16820.035	-0.001
28			16816.456	-0.002			16820.195	-0.001
29			16816.498	-0.004			16820.358	-0.001
30			16816.549	0.000			16820.520	-0.005[c]
31			16816.603	0.002			16820.685	-0.009[c]
32			16816.659	0.003			16820.854	-0.012[c]
33			16816.721	0.006	16821.492	0.012[c]	16821.022	-0.020[c]
34	16816.311	-0.003	16816.786	0.007	16821.695	0.011[c]	16821.200	-0.020[c]
35	16816.354	-0.001	16816.853	0.007	16821.901	0.008	16821.362	-0.040[c]
36	16816.397	-0.001	16816.910	-0.007	16822.111	0.006	16821.583	-0.003[c]
37	16816.456	0.012	16816.996	0.005	16822.338	0.017[b]	16821.790	0.016[c]

TABLE 6.4 (continued)

N	Q_{1ef}		Q_{1fe}		Q_{2ef}		Q_{2fe}	
38	16816.498	0.004	16817.076	0.006	16822.540	-0.001	16821.967	0.002[c]
39	16816.549	0.002	16817.154	0.002	16822.766	0.002		
40	16816.603	0.001	16817.242	0.003	16822.992	0.000[b]		
41	16816.659	-0.002	16817.330	0.001	16823.219	-0.004[b]		
42	16816.721	-0.003	16817.425	0.002				
43	16816.786	-0.003	16817.521	0.000				
44	16816.854	-0.003[b]	16817.621	-0.001				
45	16816.910	-0.019[b]	16817.725	-0.003				
46	16816.996	-0.008	16817.827	-0.010[b]				
47	16817.076	-0.006	16817.947	-0.003[b]				
48	16817.154	-0.009	16818.065	-0.002				
49	16817.242	-0.005	16818.186	-0.002				
50	16817.330	-0.004	16818.313	0.001				
51	16817.425	0.000	16818.443	0.003[b]				
52	16817.521	0.002	16818.572	0.000[b]				
53	16817.621	0.005	16818.711	0.003				
54	16817.725	0.009[b]	16818.853	0.005				
55	16817.827	0.008[b]	16818.994	0.003[b]				
56	16817.947	0.021[b]	16819.158	0.020[b]				
57	16818.030	-0.006	16819.291	0.002				
58	16818.158	0.009	16819.454	0.010				
59	16818.272	0.007	16819.604	0.002				
60	16818.394	0.009	16819.762	-0.003				
61	16818.509	0.001	16819.925	-0.006				
62	16818.639	0.005	16820.100	-0.001				
63	16818.765	0.002	16820.269	-0.005				
64	16818.897	0.001	16820.455	0.003				
65	16819.032	0.000[b]	16820.631	-0.002				
66	16819.158	-0.014[b]	16820.821	0.003				
67	16819.311	-0.004[b]	16821.012	0.005				
68	16819.455	-0.006[b]						
69	16819.605	-0.006						
70	16819.762	-0.002[b]						
71	16819.926	0.005[b]						
72	16820.084	0.002						
73	16820.242	-0.004						

TABLE 6.4 (continued)

N	P_{2f}		P_{2e}		R_{2f}		R_{2e}	
4	16815.175	0.014[b]	16815.175	0.025[b]	16819.809	0.001[b]	16819.809	0.012[b]
5	16814.753	0.001[b]	16814.753	0.015[b]	16820.389	-0.011[b]	16820.389	0.002[b]
6	16814.345	-0.001[b]	16814.345	0.015[b]	16821.000	0.004[b]	16821.000	0.021[b]
7	16813.940	-0.005[b]	16813.940	0.017[b]	16821.587	-0.009[b]	16821.587	0.014[b]
8	16813.550	0.003[b]	16813.550	0.031[b]	16822.178	-0.021[b]	16822.178	0.007[b]
9	16813.156	0.002	16813.119	0.001	16822.805	-0.002	16822.769	-0.002
10					16823.415	-0.003	16823.379	0.004
11	16812.382	0.003	16812.329	0.002	16824.034	0.000	16823.980	-0.002
12	16811.997	-0.001	16811.936	0.000	16824.656	0.003	16824.577	-0.015[b]
13	16811.621	0.000	16811.548	-0.001	16825.269	-0.008	16825.202	-0.003
14	16811.251	0.004	16811.163	-0.001	16825.902	-0.002	16825.818	-0.003
15	16810.880	0.002	16810.782	-0.001	16826.532	-0.003	16826.440	0.000
16	16810.513	0.000	16810.404	-0.001	16827.166	-0.004	16827.059	-0.003
17	16810.153	0.001	16810.016	-0.015[b]	16827.804	-0.004	16827.680	-0.007
18	16809.782	-0.013[b]	16809.658	-0.001	16828.448	-0.003	16828.314	-0.001[b]
19	16809.432	-0.010	16809.281	-0.010	16829.090	-0.007	16828.943	-0.004
20	16809.089	-0.004	16808.929	0.003	16829.747	-0.001	16829.577	-0.004
21	16808.741	-0.007	16808.559	-0.006	16830.397	-0.005	16830.219	0.001[c]
22	16808.402	-0.005	16808.199	-0.007	16831.049	-0.011[c]	16830.843	-0.016[c]
23	16808.063	-0.007	16807.834	-0.017[c]			16831.486	-0.016[c]
24	16807.721	-0.016[c]	16807.488	-0.011[c]	16832.389	0.002[c]	16832.131	-0.017[c]
25			16807.132	-0.018[c]	16833.056	0.000	16832.767	-0.031[c]
26	16807.086	0.003[c]	16806.797	-0.008[c]	16833.726	-0.003		
27	16806.762	0.000	16806.447	-0.015[c]	16834.401	-0.004		
28	16806.447	0.001			16835.078	-0.008		
29	16806.142	0.009			16835.758	-0.012[c]		
30	16805.835	0.011			16836.442	-0.016[c]	16836.121	0.033[c]
31	16805.509	-0.011[c]			16837.136	-0.013[c]	16836.772	0.018[c]
32	16805.210	-0.009[c]	16804.834	0.035[c]	16837.829	-0.016[c]	16837.434	0.010[c]
33	16804.910	-0.012[c]	16804.497	0.021[c]	16838.521	-0.023[c]	16838.103	0.007[b]
34	16804.618	-0.012[c]	16804.157	0.001[c]	16839.217	-0.029[c]	16838.778	0.007
35	16804.326	-0.016[c]	16803.850	0.010[b]			16839.451	0.001
36	16804.014	-0.043[c]	16803.527	0.001	16840.681	0.018[c]	16840.131	0.001
37			16803.226	0.010	16841.377	0.001[c]	16840.815	0.001
38	16803.527	0.026[c]	16802.925	0.016	16842.082	-0.012[c]	16841.501	0.000[b]
39	16803.226	-0.002[c]	16802.612	0.007	16842.802	-0.013[c]	16842.188	-0.002
40			16802.307	0.002	16843.520	-0.019[c]	16842.880	-0.002
41	16802.686	-0.010[c]	16802.012	0.005	16844.239	-0.028[c]	16843.573	-0.004[c]
42					16844.958	-0.041[c]	16844.262	-0.012[c]
43	16802.154	-0.026[c]	16801.416	-0.006[c]	16845.674	-0.061[c]	16844.958	-0.017[c]
44	16801.891	-0.037[c]			16846.402	-0.072[c]	16845.674	-0.003[c]
45			16800.843	-0.007[c]	16847.122	-0.094[c]	16846.370	-0.013[c]
46			16800.557	-0.011[c]	16847.863	-0.100[c]	16847.070	-0.022[c]
47					16848.586	-0.126[c]	16847.777	-0.026[c]
48	16800.856	-0.105[c]					16848.484	-0.032[c]
49	16800.605	-0.124[c]						
50							16849.899	-0.053[c]
51							16850.604	-0.069[c]

[a]Unless indicated otherwise, line positions have an assigned uncertainty of 0.004 cm^{-1}.

[b]Blended line with assigned uncertainty of 0.02 cm^{-1}.

[c]Perturbed line, excluded from the fit.

TABLE 6.5: Line Positions[a] (cm^{-1}) for the $B^2\Sigma^+ - X^2\Sigma^+$ $(02^00)\Sigma^+$-$(02^00)\Sigma^+$ Band of SrOH. The table shows $\bar{\nu}_{obs}$, the measured wavenumbers (cm^{-1}), and the residuals, $\bar{\nu}_{obs} - \bar{\nu}_{calc}$.

N	P_1		R_1		P_2		R_2	
1			16446.105	-0.047[b]			16446.350	-0.163[b]
2	16444.135	-0.092[b]	16446.516	-0.075[b]			16446.907	-0.190[b]
3	16443.616	-0.052[b]	16446.994	-0.040[b]	16443.883	-0.151[b]	16447.454	-0.232[b]
4	16443.085	-0.029[b]	16447.459	-0.024[b]	16443.431	-0.194[b]		
5	16442.538	-0.027[b]	16447.916	-0.020[b]	16442.978	-0.244[b]		
6	16441.992	-0.029[b]					16449.059	-0.423[b]
7	16441.453	-0.029[b]	16448.866	0.009[b]			16449.583	-0.508[b]
8			16449.353	0.028[b]	16441.809	-0.232[b]	16450.057	-0.647[b]
9	16440.401	-0.017[b]	16449.796	-0.003[b]	16441.144	-0.513[b]	16452.328	1.005[b]
10	16439.905	0.011[b]			16440.614	-0.664[b]	16452.738	0.792[b]
11	16439.365	-0.010[b]	16450.767	0.008[b]	16441.862	0.958[b]	16453.208	0.634[b]
12					16441.328	0.793[b]		
13	16438.355	0.003[b]	16451.745	0.005[b]	16440.809	0.637[b]		
14			16452.224	-0.013[b]				
15	16437.340	-0.009[b]	16452.748	0.009				
16	16436.833	-0.022[b]						
17	16436.360	-0.006	16453.769	0.011				
18			16454.266	-0.009			16457.306	0.200[b]
19	16435.406	0.003	16454.823	0.027			16457.932	0.159[b]
20	16434.887	-0.042	16455.337	0.014	16437.959	0.195[b]	16458.622	0.178[b]
21	16434.469	0.009	16455.878	0.024	16437.612	0.172[b]	16459.348	0.228[b]
22	16434.000	0.004	16456.400	0.010	16437.299	0.178[b]		
23	16433.538	0.002			16437.030	0.223[b]	16460.605	0.119[b]
24	16433.068	-0.014	16457.461	-0.014			16461.310	0.134[b]
25					16436.339	0.145[b]		
26	16432.175	-0.014	16458.547	-0.033	16435.980	0.086[b]	16462.712	0.142[b]
27							16463.385	0.111[b]
28	16431.290	-0.026	16459.708	0.005	16435.441	0.131[b]	16464.108	0.126[b]
29					16435.115	0.089[b]		
30	16430.470	0.008	16460.846	0.001	16434.898	0.152[b]	16465.504	0.091[b]
31								
32	16429.637	0.009	16462.008	0.003	16434.306	0.105[b]	16466.903	0.041[b]
33								
34	16428.816	0.002	16463.205	0.022	16433.756	0.080[b]	16468.398	0.069[b]
35							16469.139	0.070[b]
36	16428.104	0.084	16464.395	0.015	16433.243	0.073[b]	16469.875	0.062[b]
37			16464.995	0.010	16433.031	0.107[b]		
38	16427.256	0.011	16465.630	0.036	16432.737	0.054[b]	16471.341	0.025[b]
39	16426.830	-0.035	16466.256	0.048				
40	16426.498	0.008	16466.775	-0.052	16432.233	0.017[b]	16472.840	0.004[b]
41	16426.157	0.038						
42	16425.716	-0.038	16468.001	-0.076	16431.736	-0.031[b]	16474.357	-0.016
43								
44	16424.979	-0.059	16469.355	0.011	16431.323	-0.015	16475.886	-0.041
45			16469.995	0.010				
46	16424.319	-0.022	16470.552	-0.077	16430.875	-0.053	16477.422	-0.076

TABLE 6.5 (Continued)

N	P_1		R_1		P_2		R_2	
47	16424.032	0.033					16478.366	0.076
48	16423.594	-0.069			16430.483	-0.054		
49			16472.605	0.016	16430.387	0.039		
50								
51	16422.714	0.032					16481.530	0.030
52			16474.629	0.042				
53					16429.701	0.060		
54	16421.794	0.049	16475.954	0.014			16483.994	0.043
55								
56	16421.177	0.033			16429.204	0.044	16485.643	0.038
57								
58					16428.912	0.050		
59			16479.379	-0.016				
60							16488.922	-0.039
61	16419.688	-0.038						
62					16428.266	-0.058	16490.614	-0.050
63							16491.490	-0.031
64					16428.083	0.001	16492.377	-0.005
65					16427.957	-0.011		
66					16427.882	0.023	16494.121	0.005
67								
68					16427.678	0.023		

[a]Unless indicated otherwise, line positions have an assigned uncertainty of 0.03 cm^{-1}.

[b]Perturbed line, excluded from the fit.

TABLE 6.6: Line Positions[a] (cm^{-1}) for the $B^2\Sigma^+ - X^2\Sigma^+$ $(02^20)\Delta$-$(02^20)\Delta$ Band of SrOH. The table shows $\bar{\nu}_{obs}$, the measured wavenumbers (cm^{-1}), and the residuals, $\bar{\nu}_{obs} - \bar{\nu}_{calc}$.

N	P_{1f}		P_{1e}		R_{1f}		R_{1e}	
3					16449.424	-0.046	16449.424	-0.046
4								
5	16445.014	0.010	16445.014	0.010	16450.355	-0.017	16450.355	-0.017
6								
7	16443.909	-0.013	16443.909	-0.013				
.								
.								
.								
18					16456.715	0.019	16456.775	0.079
19					16457.243	0.027	16457.282	0.067
20	16437.350	-0.015	16437.370	0.006			16457.816	0.077
21	16436.902	0.007	16436.938	0.044			16458.292	0.024
22			16436.434	0.005				
23			16435.999	0.031			16459.341	0.000
24							16459.871	-0.013
25			16435.028	-0.034			16460.429	-0.002
26			16434.594	-0.023				
27			16434.143	-0.033	16461.534	-0.009	16461.517	-0.024
28					16462.101	-0.004		
29	16433.316	0.002	16433.301	-0.009	16462.665	-0.007		
30	16432.860	-0.029			16463.274	0.030	16463.234	-0.006
31	16432.467	-0.002						
32	16432.049	-0.005	16432.056	0.008				
33								
34					16465.552	-0.024		
35								
36	16430.441	-0.004						
37							16467.377	0.011
38					16467.983	-0.001	16467.971	-0.003
39			16429.288	0.010				
40	16428.923	0.007	16428.892	-0.010				
41								
42					16470.479	0.012		
43								
44	16427.468	-0.002						
45								
46					16473.008	-0.017		
47								
48	16426.110	0.003					16474.294	-0.011
49								
50			16425.436	0.016	16475.631	-0.028		
51								
52	16424.817	-0.010						

TABLE 6.6 (Continued)

N	P_{2f}		P_{2e}		R_{2f}		R_{2e}	
4					16450.726	0.022	16450.726	0.022
5					16451.305	0.005	16451.305	0.005
6	16445.240	-0.012	16445.240	-0.012				
7	16444.867	0.011	16444.867	0.011				
.								
.								
.								
19					16460.147	0.000	16460.142	-0.005
20					16460.802	-0.012	16460.800	-0.015
21	16439.820	-0.012	16439.847	0.014			16461.465	-0.022
22	16439.507	-0.002	16439.484	-0.027			16462.148	-0.015
23			16439.186	-0.007				
24			16438.874	-0.007				
.								
.								
.								
31							16468.460	-0.002
32					16469.151	-0.029	16469.151	-0.034
33			16436.303	0.010	16469.846	-0.061	16469.889	-0.024
34	16436.034	0.011	16436.040	0.010				
35	16435.746	-0.018	16435.777	0.005				
36								
37					16472.859	-0.002		
38								
39	16434.797	0.019			16474.389	0.024	16474.381	0.005
40							16475.154	0.018
41	16434.303	-0.012	16434.396	0.065				
42			16434.156	0.047				

[a]Line positions have an assigned uncertainty of 0.03 cm^{-1}.

TABLE 6.7: Least-squares parameters[a] for the $B^2\Sigma^+$ and $X^2\Sigma^+$ states of SrOH

		$(01^10)^b$	$(01^10)^c$	$(02^00)^c$		$(02^20)^c$
$B^2\Sigma^+$	T_v		16778.341(1)	17148.577(2)		17181.280(2)
	B_v	0.25134(4)	0.2513132(12)	0.2506490(15)		0.2503788(14)
	$10^7 D_v$	2.22(8)	2.2962(26)	2.3647(52)		2.3377(34)
	$10^{13} H_v$		[9.2]	9.2(10)		[9.2]
	γ_v	-0.1439(6)	-0.14047(6)	-0.143090(35)		-0.140194(23)
	$10^7 \gamma_v^D$		[3.4]	3.41(8)		[3.4]
	$10^4 q_v$	3.87(14)	-3.622(8)		-3.22(9)	
	$10^{10} q_v^D$		-7.1(22)		-118(22)	
$X^2\Sigma^+$	T_v	360 ± 3	363.689(2)	703.288(8)		733.547(6)
	B_v	0.24859(4)	0.2485815(13)	0.248164(9)		0.247972(11)
	$10^7 D_v$	2.19(8)	2.2097(32)	2.094(36)		2.335(48)
	$10^{13} H_v$		[1.6]	[1.6]		[1.6]
	$10^3 \gamma_v$	0.2(6)	2.409(15)	2.34(16)		3.11(18)
	$10^4 q_v$	4.05(13)	-3.9503(46)		-4.9(7)	
	$10^{10} q_v^D$		6.0(13)		[-116]	

[a]All parameters are in cm^{-1} units; values in parentheses are one standard error, in units of the least significant digit of the corresponding parameter; values in square brackets indicate parameters constrained at fixed values in the least-squares fit; with the exception of H_v which was determined as $1.58(27) \times 10^{-13}$ cm^{-1}, the constants for $X(000)$ were fixed to the values of ref. (37), $B_0 = 0.24919981(2)$, $D_0 = 2.1744(2) \times 10^{-7}$, and $\gamma_0 = 2.4275(4) \times 10^{-3}$ cm^{-1}.

[b]From Nakagawa *et al.* (22).

[c]This work.

albeit to a much lesser extent.

$(02^20)^2\Delta \leftarrow (010)^2\Pi$

In this band, strong Q_1 and Q_2 branches appear in addition to the P_1, P_2, R_1, and R_2 branches. The satellite branches, for which $\Delta N \neq \Delta J$, are not observed with any appreciable intensity. Each of the six main branches are doubled owing to ℓ-type doubling in both states. Since this splitting of the *e/f* parity levels is much larger in the ground state $(010)^2\Pi$ level, doubled branches are observed even for low N values ($N \geq 9$). The F_1 levels are well behaved, but the *e* and *f* parity components of the $\tilde{B}(02^20)^2\Delta$ F_2 spin manifold both show indications of multiple level crossings (see fig. 6.5). As a consequence, many line positions associated with the F_2 levels are omitted from the fit. The magnitude of the ℓ-type doubling constant q_v^v was well determined for both states, but the absolute sign and hence the actual parity assignments could not be established unequivocally from this transition alone: two equally satisfactory fits could be achieved by switching the parity assignments and adjusting the rotational quantum number accordingly. The effective ℓ-type doubling constant for the $^2\Delta$ state was determined to be $|q_{\text{eff}}^v| = 4.37(7) \times 10^{-9}$ cm^{-1} and is of opposite sign to that of the $^2\Pi$ state, where $|q^v| = 3.9503(46) \times 10^{-4}$ cm^{-1}.

$(02^00)^2\Sigma^+ \leftarrow (010)^2\Pi$

Although data for both levels of this band were available from other transitions observed in this work, an analysis of the $\tilde{B}(02^00)^2\Sigma^+ \leftarrow \tilde{X}(010)^2\Pi$ band was undertaken to confirm, on a purely experimental basis, the *e/f* parity assignments of the $\tilde{X}(010)^2\Pi$ level, thereby eliminating any ambiguity in the assignments of the $\tilde{B}(02^20)^2\Delta \leftarrow \tilde{X}(010)^2\Pi$ band. This was essential in the present work on account of the numerous perturbations in the upper state

levels. The parity assignments followed immediately upon linking the $\tilde{X}(010)^2\Pi$ state to the upper $(02^00)^2\Sigma^+$ level. The ℓ-type doubling constant is unequivocally determined as q_v^v = -3.9503(46) × 10^{-4} cm^{-1}, which agrees remarkably well with the estimate by Nakagawa *et al.*[22] of the magnitude of q_v^v, 4.05(13) × 10^{-4} cm^{-1}. The negative sign of q_v^v is consistent with the expression of Nielsen *et al.*[91,92], and moreover, a negative value for q_v^v of similar magnitude has also been observed for the $\tilde{X}(010)^2\Pi$ vibrational level of CaOH[31]. The $\tilde{X}(010)^2\Pi$ vibrational level of SrOH is accurately located at 363.689(2) cm^{-1}, as compared with the previous estimate of 360 ± 3 cm^{-1}[22]. This establishes the splitting in the $\tilde{B}^2\Sigma^+$ state between the $v_2 = 2$, $\ell = 0$ and $\ell = 2$ components as 32.703 cm^{-1}, yielding g_{22}= 8.1758(7) cm^{-1}.

(010)$^2\Pi \leftarrow$ *(000)*$^2\Sigma^+$

In their analysis of the $\tilde{B}(010)^2\Pi \leftarrow \tilde{X}(010)^2\Pi$ transition, Nakagawa *et al.*[22] reported an anomalous ℓ-type doubling in the $\tilde{B}^2\Sigma^+$ state whereby the F_1 spin manifold exhibited a much larger splitting than the corresponding F_2 levels. This effect was attributed to an electronic perturbation caused by the $\tilde{A}^2\Pi(010)$ $\mu^2\Sigma$ and $\kappa^2\Sigma$ vibronic states. Subsequently, Brazier and Bernath[33] located the $\tilde{A}^2\Pi(000)$ level at 14674.332(2) cm^{-1} which, neglecting the spin-orbit and Renner-Teller effects, places the $\tilde{A}^2\Pi(010)$ manifold approximately 1700 cm^{-1} below the $\tilde{B}^2\Sigma^+(010)^2\Pi$ level, suggesting this perturbation to be a relatively long range interaction. The plot in fig. 6.3 of reduced rotational term energies for $\tilde{B}^2\Sigma^+(010)^2\Pi$ as a function of N indicates a level crossing in the F_2 manifold between N = 40 and N = 41. Using the standard expressions for a $^2\Pi$ vibronic state, all F_1 and F_2 levels up to N = 16 are reasonably well represented, giving q_v^v = -3.622(8) × 10^{-4} cm^{-1}, which is consistent with the ground state value. In the previous analysis[22],

the effects of the level crossing were considered to be less extensive; only F_2 levels for $32 \leq N \leq 52$ were omitted from the fit. Based on the present study, it is more reasonable to attribute any anomalous ℓ-type doubling phenomenon in the $\tilde{B}^2\Sigma^+(010)^2\Pi$ state to the effects of the local perturbation rather than to a long range electronic perturbation caused by interactions with the $\mu^2\Sigma$ and $\kappa^2\Sigma$ vibronic components of the $\tilde{A}^2\Pi(010)$ manifold. This contention is supported for two reasons: first, ℓ-type doubling in the F_2 spin manifold of the $\tilde{B}^2\Sigma^+(01^10)^2\Pi$ state was observed by Nakagawa *et al.*[22] only as a splitting of the P_2 and R_2 branches at high N. Consequently, the ℓ-type splittings observed for the F_2 manifold, which are extremely sensitive to the presence of perturbations, are strongly influenced by the level crossing. Second, a perturbation caused by interaction with the $\tilde{A}^2\Pi(010)^2\Sigma$ states would also have a significant effect on the F_1 levels. The ℓ-type splittings observed in the F_1 spin manifold of the $\tilde{B}(010)^2\Pi$ level are entirely consistent with those of the $\tilde{X}(010)^2\Pi$ level with the fitted values of q_v^v being of the same sign and having a similar magnitude.

$(02^00)^2\Sigma^+ \rightarrow (02^00)^2\Sigma^+$ and $(02^20)^2\Delta \rightarrow (02^20)^2\Delta$

Despite the lower accuracy of the resolved fluorescence measurements, a complete set of rotational constants was determined for the $\tilde{X}(02^00)^2\Sigma^+$ and $\tilde{X}(02^20)^2\Delta$ levels. Although poorly determined, the effective ℓ-type doubling constant for the $^2\Delta$ component, $q_{eff}^v = 9.7(31) \times 10^{-9}$ cm^{-1}, was found to be similar to that for the $\tilde{B}^2\Sigma^+(02^20)$ level. Having established the vibrational term energies of the upper vibrational levels, the origins of the resolved fluorescence transitions fix the position of the ground state $(02^20)^2\Delta$ and $(02^00)^2\Sigma^+$ levels. These levels are separated by 30.259 cm^{-1} yielding a determination of the anharmonicity constant $g_{22} = 7.5646(25)$ cm^{-1}.

6.4 Molecular Constants

In the $\tilde{B}^2\Sigma^+$ and $\tilde{X}^2\Sigma^+$ states of SrOH, the variation of the rotational constant B_v with increasing excitation of the degenerate bending mode exhibits peculiarities, which in general, are uncharacteristic for linear triatomic molecules. Specifically, a plot of B_v versus v_2 is not linear as expected for most triatomic molecules and moreover exhibits a negative slope. Although such effects may be associated with a quasi-linear structure[99], a similar dependence has also been observed in a structurally analogous class of molecules, namely the alkali metal monohydroxides[57,58,98]. Accordingly, the variation of B_v with v_2 is instead reliably modeled by the expression given in eq. 5.8. Using the values of Nakagawa *et al.*[22] and Anderson *et al.*[37] for B_v of the (000) levels of the $\tilde{B}^2\Sigma^+$ and $\tilde{X}^2\Sigma^+$ states, respectively, α_2, γ_{22}, and γ_{ll} have been determined for both states, and are given in table 6.8. The constant α_2, which represents the main influence of vibration on B_v for low v_2, is positive for both the $\tilde{B}^2\Sigma^+$ and $\tilde{X}^2\Sigma^+$ states. The ground state value, α_2 = 7.3(4) × 10^{-4} cm^{-1}, is very similar to that for CaOH[31] (6.52(7) × 10^{-4} cm^{-1}), CsOH[58] (6.34 × 10^{-4} cm^{-1}) and ^{85}RbOH[57] (1.11 × 10^{-3} cm^{-1}).

In a detailed account of vibration-rotation interactions in CsOH and RbOH, Lide and Matsumura[98] have shown that α_2 may be partitioned according to

$$\alpha_2 = (\alpha_2)_{h1} + (\alpha_2)_{h2} + (\alpha_2)_{anh} \qquad (6.7)$$

Here, the first term arises from Coriolis contributions, where $(\alpha_2)_{h1}$ = ½ q_v^v, with q_v^v being the ℓ-type doubling constant for the v_2 = 1 level. The second and third terms are referred to as the pseudoanharmonic and true anharmonic terms respectively. The pseudoanharmonic term $(\alpha_2)_{h2}$ arises because the rectilinear coordinates used to represent the bending vibrations

TABLE 6.8: Molecular Constants (cm^{-1}) for the $B^2\Sigma^+$ and $X^2\Sigma^+$ states of SrOH

	$B^2\Sigma^+$	$X^2\Sigma^+$
α_2	1.05(7) × 10^{-3} [a]	7.3(4) × 10^{-4} [b]
γ_2	6.4(22) × 10^{-5} [a]	5.3(15) × 10^{-5} [b]
$\gamma_{\ell\ell}$	-6.76(5) × 10^{-5} [a]	-4.8(14) × 10^{-5} [b]
ω_2^o	399.785(2) [c]	360.605(6)
x_{22}^o	-7.124(2) [c]	-4.480(5)
g_{22}	8.1758(7) [c]	7.5646(25)

[a]Calculated using B_{000} = 0.25224(2) cm^{-1} from Nakagawa *et al.* (22).

[b]Calculated using B_{000} from Anderson *et al.* (37).

[c]Calculated using T_e for $B^2\Sigma^+$ from Nakagawa *et al.* (22).

are poor approximations of the true motion of the respective nuclei. According to Pliva,[103] the $(\alpha_2)_{h2}$ term is attributable to the non-linear nature of the transformation of the instantaneous molecular coordinates to normal coordinates. The usual negative sign of α_2 in most linear triatomics is a result of the dominance of $(\alpha_2)_{h2}$ which is always negative. In CsOH and RbOH, however, the combination of a large bending amplitude and relatively small M-O force constant leads to a dominant contribution from $(\alpha_2)_{anh}$ which is positive, hence the positive value of α_2. Based on the structural similarity of SrOH to the alkali metal monohydroxides and on similarities in the fundamental vibrational frequencies, which reflect the nature of the harmonic force field, we expect a similar explanation is equally valid in the present case.

The vibrational term values for the bending mode, referred to the (000) level are given by[104],

$$G_0(0, v_2, 0) = \omega_i^0 v_2 + x_{22}^0 v_2^2 + g_{22}\ell^2 \qquad (6.8)$$

where ω_2^0 and x_{22}^0 have their usual meanings. Estimates of these parameters for both electronic states are given in table 6.8. In the approximation that neglects third and higher order anharmonic constants, x_{22}^0 can be taken as equal to x_{22}. A comparison of the values of x_{22} for the two states would suggest that the bending potential is considerably more anharmonic for the $\tilde{B}^2\Sigma^+$ state. The value of g_{22} has been accurately determined in this work as 7.5646(25) and 8.1758(7) cm^{-1} for the $\tilde{B}^2\Sigma^+$ and $\tilde{X}^2\Sigma^+$ states, respectively. The ground state value of g_{22} in SrOH, which is a consequence of the quartic anharmonicity in the bending potential, is significantly larger than the corresponding value in CaOH (g_{22} = 6.092 cm^{-1}).

The experimental determinations of the vibrational energies for the two lowest excited bending vibrational levels of SrOH allows the quasi-linearity

parameter, discussed in the previous chapter, to be evaluated. Using the values given in table 6.7 and the $T_{ev}(000)$ for the $\tilde{B}^2\Sigma^+ \leftarrow \tilde{X}^2\Sigma^+$ system from ref. 22, the quasi-linearity parameter γ_o is determined as 1.0685 and 1.0793 for the $\tilde{B}^2\Sigma^+$ and $\tilde{X}^2\Sigma^+$ states, respectively. As with CaOH, we find the quasi-linearity parameter is at the extreme linear limiting case where, in fact, the anharmonic contribution to γ is greater than the upper limit of 1% as suggested by Winnewisser[99].

6.5 Rotational ℓ-type Doubling and ℓ-type Resonance

As discussed in chapter 4, the phenomena of ℓ-type doubling and ℓ-type resonance arise through Coriolis interactions between the stretching (σ) and degenerate bending (π) modes via terms containing the $G_{\pm}$ operator. The principal matrix element responsible for ℓ-type doubling and ℓ-type resonance in a signed case (b) basis is[34,103,105],

$$\langle v_1,v_2^l,v_3;\ N,\ell |\ \boldsymbol{H}\ |\ v_1,v_2^{l\pm2},v_3;\ N,\ell\pm2\rangle$$

$$= \tfrac{1}{4}\, q_v^v\Big[(v_2\mp\ell)(v_2\pm\ell+2)[N(N+1)-\ell(\ell\pm1)][N(N+1)-(\ell\pm1)(\ell\pm2)]\Big]^{1/2}. \qquad (6.9)$$

The ℓ-type doubling parameter q_v^v experiences a small variation with rotational and vibrational quantum number and accordingly the following substitution is required[106],

$$q_{vJ}^v = q_e^v + \sum q_{vi}^v(v_i + d_i/2) + q_v^D N(N+1)\ . \qquad (6.10)$$

Direct microwave observations of ℓ-type splittings in the $v_2 = 2$ vibrational level of HCN and DCN[107] have shown this treatment to be inadequate for highly precise measurements for vibrational levels with $v_2 \geq 2$. It then becomes necessary to consider matrix elements of the type[107,34]

$$\langle v_1,v_2^l,v_3;\ N,\ell|\ \boldsymbol{H}\ |\ v_1,v_2^{l\pm4},v_3;\ N,\ell\pm4\rangle = \rho_v^{\mathrm{v}}\Big\{\ \big[N(N+1)-\ell(\ell\pm1)\big]$$

$$\times\big[N(N+1)-(\ell\pm1)(\ell\pm2)\big]\big[N(N+1)-(\ell\pm2)(\ell\pm3)\big]\big[N(N+1)-(\ell\pm3)(\ell\pm4)\big]\ \Big\}^{1/2} \quad (6.11)$$

However, since the contributions from q_v^D and ρ_v^{v} to the ℓ-type doubling in (020) are highly correlated[107], the present fits were performed with ρ_v^{v} fixed at zero, as in the similar treatment for OCS[108].

The off-diagonal matrix element in the $v_2 = 1$ level of Σ electronic states connects states with $\ell = 1$ and $\ell = -1$ in the signed basis. Taking Wang combinations of the appropriate case (b) functions[109],

$$|\eta;|K|SNJ\pm\rangle = 2^{-1/2}\ \big[\ |\eta;KSNJ\rangle \pm (-1)^{J+S-1}|\eta;-KSNJ\rangle\ \big], \quad (6.12)$$

where η represents the vibrational quantum number, the interaction is diagonalized and is represented by q_v^{v} in eqs. 6.3 and 6.4. The net effect is a removal of the *e/f* degeneracy associated with the Π vibrational level and is referred to as ℓ-type doubling[110]. Using the expressions for q_v^{v} given by Nielsen *et al.*[91,92] (eq. 4.38), it is possible to obtain estimates of the Coriolis term $4\sum_i \dfrac{\zeta_{2i}^2\omega_2^2}{\omega_i^2 - \omega_2^2}$ using the experimentally determined values of q_v^{v}. Given the determination of α_1 and B_{000} of ref. 22, setting $\omega_2 = \omega_2^{\mathrm{o}}$, and taking $\alpha_3(\mathrm{SrOH}) = \alpha_3(\mathrm{RbOH})$[57], we obtain estimates of 0.12 and 0.14 for the $\tilde{B}^2\Sigma^+$ and $\tilde{X}^2\Sigma^+$ states, respectively. These results can be compared with the "typical" value of 0.3 for this Coriolis term suggested by Townes and Schawlow[111].

As indicated earlier, the $\ell = 0$ and $\ell = \pm 2$ components of the $v_2 = 2$ vibrational level also interact via the matrix element of eq. 6.9. By convention, such an interaction is referred to as an ℓ-type resonance to indicate the approximate degeneracy of the interacting levels. In some cases, such as in the $\tilde{A}^2\Sigma^+(020)$ vibrational level of N_2O^+[112], where the ℓ-type

resonance is particularly strong, ℓ is uncoupled from the linear axis. For weaker interactions the net effect is primarily a splitting of the e and f parity levels in the Δ state (see fig. 6.6). In SrOH, the $^2\Sigma^+$ and $^2\Delta$ components of the $v_2 = 2$ vibrational level were observed for the $\tilde{B}^2\Sigma^+$ and $\tilde{X}^2\Sigma^+$ electronic states enabling the off-diagonal matrix element to be evaluated directly. This involved removing the diagonal term $q_{\rm eff}^{\rm v}$ of eqs. 6.5 and 6.6 and constructing the appropriate interaction matrix. In the parity basis of eq. 6.12, the interaction matrix takes the form

$$e\text{-levels} \qquad \begin{vmatrix} E_{F2}(^2\Delta) & 0 & 0 \\ 0 & E_{F1}(^2\Delta) & W_{20} \\ 0 & W_{20} & E(^2\Sigma^+) \end{vmatrix} \qquad (6.13)$$

$$f\text{-levels} \qquad \begin{vmatrix} E_{F2}(^2\Delta) & 0 & -W_{20} \\ 0 & E_{F1}(^2\Delta) & 0 \\ -W_{20} & 0 & E(^2\Sigma^+) \end{vmatrix} \qquad (6.14)$$

where $W_{20} = [q_v^{\rm v} + q_v^D N(N+1)]\{[N(N+1)][N(N+1)-2]\}^{1/2}$. For the $\tilde{B}^2\Sigma^+$ state, $q_v^{\rm v}$ and q_v^D are found to be -3.22(9) × 10^{-4} and -1.18(22) × 10^{-8} cm^{-1}, respectively. The small difference of $q_v^{\rm v}$ from that for (010) yields an estimate for q_{22} in eq. 6.10 of 4.0(9) × 10^{-5} cm^{-1}. The q_v^D parameter, however, is significantly larger in magnitude than that of the (010) level. As discussed earlier, however, q_v^D for (020) is an effective parameter that absorbs the effect of the matrix elements connecting states with $\Delta\ell = \pm 4$. For the $\tilde{X}^2\Sigma^+$ state, the ℓ-type doubling constant was found to be -4.9(7) × 10^{-4} cm^{-1}, with the constant q_v^D fixed to the $\tilde{B}(020)$ value.

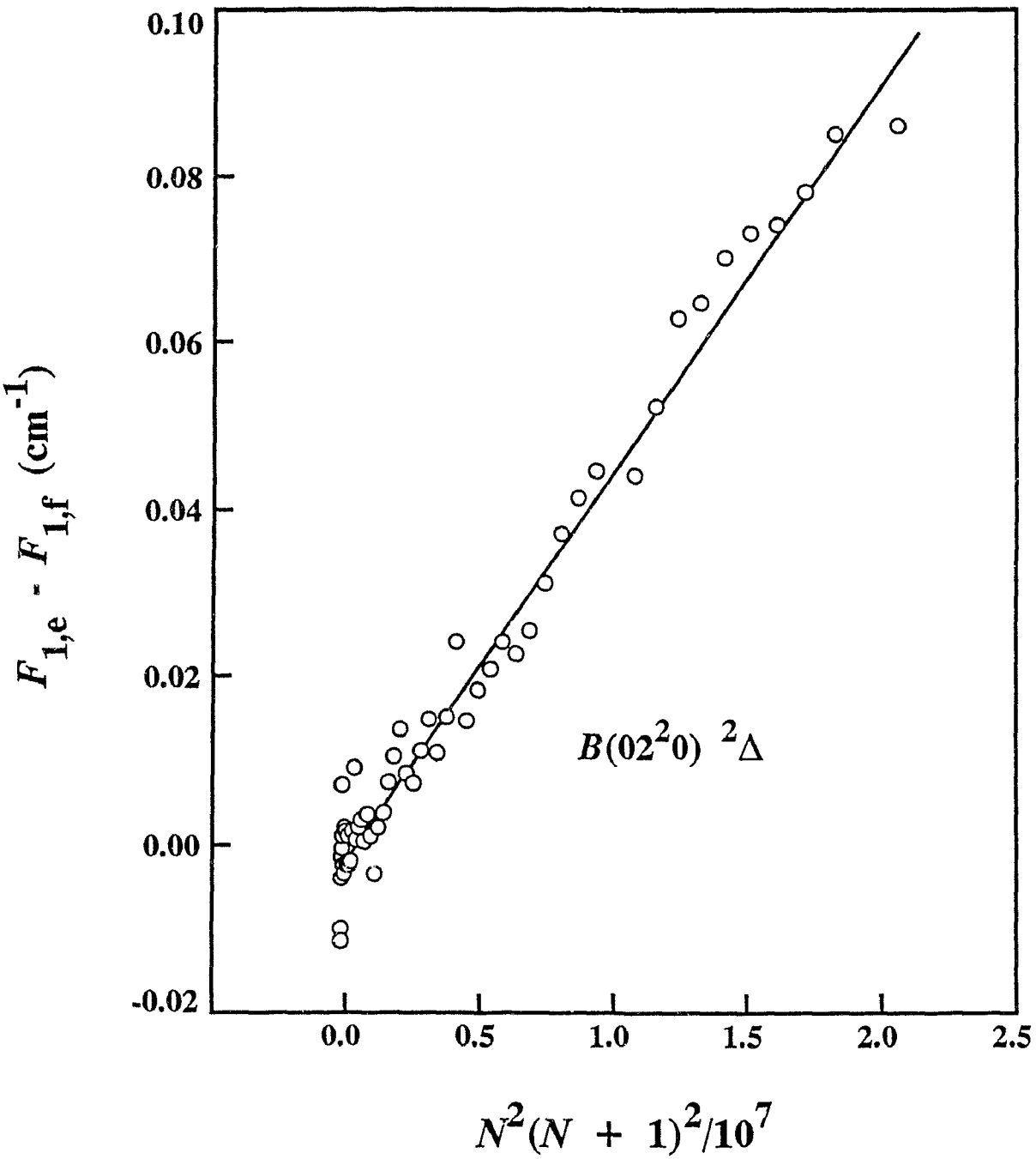

Figure 6.6: Plot of *e/f* splitting in the F_1 levels of SrOH $\tilde{B}^2\Sigma^+$ $(02^20)^2\Delta$.

6.6 Perturbations

The effects of rotational perturbations in the $\tilde{B}^2\Sigma^+$ vibrational levels lead to a contamination of the purely physical meaning of the molecular constants. Although this is mitigated to some extent in the least-squares fits by the exclusion of lines in the crossing regions, only a full deperturbation analysis can remove the insidious effects of the perturbations. Consequently, the statistical uncertainties of the molecular constants listed in tables 6.7 and 6.8 are not reliable estimates of their deviations from the true values. Rather, the quoted standard deviations are more a measure of the statistical uncertainty with which the respective parameters can be determined assuming the model to be ideal and the data free of any systematic perturbation or error. Since observations of the perturbing states are limited to a few weak additional rotational lines in the crossing regions of the $(010)^2\Pi$ and $(02^00)^2\Sigma$ states, a deperturbation analysis is not feasible. Nevertheless, based on these additional lines, the vibronic energy of the perturbing states of the $\tilde{B}(010)^2\Pi$ and $\tilde{B}(02^00)^2\Sigma^+$ vibrational levels is estimated as 16800 ± 15 and 17152 ± 1 cm^{-1}, respectively. The most recent theoretical calculations place the $\tilde{C}^2\Delta$ electronic state at 20175 cm^{-1}[43], suggesting the perturbing states must be excited vibrational levels of the $\tilde{A}^2\Pi$ electronic state. Based on the analysis of the $\tilde{A}^2\Pi$ - $\tilde{X}^2\Sigma^+$ system presented in chapter 7, the fundamental vibrational frequencies ν_1 and ν_2 are determined as 542.595 and 381.362 cm^{-1}, respectively. The $\tilde{B}^2\Sigma^+$ state lies at an energy of approximately 1700 cm^{-1} above the $\tilde{A}^2\Pi$ state, implying that the unidentified perturbers of the $\tilde{B}^2\Sigma^+$ state have the equivalent of ≈ 4 quanta in the ν_1 mode or ≈ 5-7 quanta in the bending vibration. Given the uncertainty imposed by the unknown anharmonic constants and the high density of vibronic states arising

from the combined presence of Renner-Teller and spin-orbit interactions in the $\tilde{A}^2\Pi$ state, it is not possible, as yet, to unambiguously identify the perturbing states. Nevertheless, it would appear that vibronic components of the $\tilde{A}(310)$ and $\tilde{A}(320)$ manifolds are ideal candidates as perturbers of the $\tilde{B}(010)$ and $\tilde{B}(020)$ levels, respectively, since they involve a change of vibrational quanta in only one of the normal modes.

6.7 Conclusions

The work presented in this chapter has provided detailed spectroscopic information on excited bending vibrational levels with $v_2 \leq 2$ for the $\tilde{B}^2\Sigma^+$ and $\tilde{X}^2\Sigma^+$ states of SrOH. Although an anomalous behavior was observed with respect to the dependence of the rotational constant with v_2, there appears to be little difficulty in accommodating this observation within the framework of a linear model.

Chapter VII

Intermodulated Fluorescence, Laser Excitation and Dispersed Fluorescence Investigations of the $\tilde{A}^2\Pi$ - $\tilde{X}^2\Sigma^+$ System of SrOH.

7.1 Introduction

The effects of electronic orbital angular momentum in linear triatomic molecules have been the subject of numerous theoretical investigations[75,77-82,84,85,113-125]. Beginning with Renner's seminal paper on the interaction of electronic and nuclear angular momenta in 1934[78], a considerable amount of attention has been devoted to various aspects of the Renner-Teller effect. Despite this rather intense theoretical scrutiny, there exists a paucity of experimentally studied examples of the Renner-Teller effect. Indeed, nowhere is this more evident than in the fact that the first experimental observation of the Renner-Teller effect in NH_2 by Dressler and Ramsay[126] was not until some 25 years after Renner's first work on this subject. Certainly this underscores the view that orbital angular momentum effects in linear triatomic molecules remained little more than a spectroscopic curiosity for many years. More recently, sophisticated and increasingly higher order theoretical treatments of the Renner-Teller effect have provided complex vibronic energy level expressions which have been adequately tested for only a few molecules. To date, most experimental investigations of the Renner-Teller effect have involved only lighter atoms such as those found in the class of 15-electron molecules (NCO, BO_2, NCS, CO_2^+, N_3, and N_2O^+) or, to a lesser extent, the 12 to 14-electron species such as C_3, CCN, CNC, and NCN, for example. It is of considerable interest, therefore, to obtain high resolution experimental data for excited bending vibrations in degenerate electronic states of heavier molecules. In this

respect, the SrOH radical represents an ideal candidate for study and at present appears to be the only molecule containing a 5^{th} row atom for which the Renner-Teller effect has been analyzed.

Vibronic levels of the orbitally degenerate $\tilde{A}^2\Pi$ electronic states of the group IIA monohydroxides possessing a non-zero vibrational angular momentum are subject to a Born-Oppenheimer breakdown through the Renner-Teller (RT) effect. High resolution investigations of the $\tilde{A}^2\Pi$ state are by no means trivial undertakings: the spectroscopy is complex owing to the combination of RT and spin-orbit interactions in addition to the presence of low frequency stretching and degenerate bending vibrations. This is further exacerbated by vibronic mixing with other low-lying electronic states which can be manifest in a variety of ways, including rotational perturbations, off-diagonal spin-orbit interactions and through the Herzberg-Teller (HT) effect. Although previous investigations of the RT effect in alkaline earth monohydroxides have been carried out, they have been limited to CaOH[30,31,35]. Vibronic mixing is expected to be more severe in the heavier members of this class of molecules SrOH and BaOH, where the spin-orbit interaction is large and the low-lying excited electronic states are closer in energy. Most certainly this is in part responsible for the lack of detailed information concerning the bending vibration in the $\tilde{A}^2\Pi$ states of SrOH and BaOH.

The aim of the present work is a high resolution investigation of the rotational structure associated with several bands in the $\tilde{A}^2\Pi$ - $\tilde{X}^2\Sigma^+$ system of SrOH involving the ν_1 stretching and ν_2 bending mode. In contrast to the $\tilde{B}^2\Sigma^+$ and $\tilde{X}^2\Sigma^+$ electronic states, comparatively little is known of the $\tilde{A}^2\Pi$ state, for which only the (000) vibrational level has been observed[33]. The rotational analysis of excited bending vibrations ($\upsilon_2 \leq 2$) of the $\tilde{B}^2\Sigma^+$ and $\tilde{X}^2\Sigma^+$ states of SrOH presented in chapter 6 underscored the need for more

detailed information on excited vibrational levels of the $\tilde{A}^2\Pi$ state. It was found that local perturbations arising from level crossings of the $\tilde{B}^2\Sigma^+(010)\Pi$ and $\tilde{B}^2\Sigma^+(02^00)\Sigma^+$ vibrational levels with higher vibrational levels of the $\tilde{A}^2\Pi$ state resulted in considerable (up to 1 cm^{-1}) energy level shifts. The lack of vibrational data on the $\tilde{A}^2\Pi$ state and the high density of vibronic states precluded an unambiguous identification of the perturbing states. As a result, a rotational analysis of numerous bands in the $\tilde{A}^2\Pi$ - $\tilde{X}^2\Sigma^+$ system of SrOH has been undertaken. The frequencies and assignments obtained from the excitation work have also been utilized to probe excited vibrational levels of the ground state via dispersed LIF. In particular, vibrational levels of the $\tilde{X}^2\Sigma^+$ state with $v_1 \leq 2$ and $v_2 \leq 3$ have been studied by this means.

The present high resolution investigation of the $\tilde{A}^2\Pi$ - $\tilde{X}^2\Sigma^+$ system of SrOH has revealed strong local perturbations caused by a level crossing of the $\tilde{A}^2\Pi(010)$ Renner-Teller components. These rotational perturbations, which are attributable to a *K*-resonance interaction between the Σ and Δ vibronic components, are a rather unusual manifestation of orbital angular momentum effects that, for lack of suitable data, has been observed previously only for BO_2[127]. The vibronic structure of the $v_2 = 1$ level of SrOH is determined by the quantity $A/\epsilon\omega_2$, where, as in the present case, the large magnitude of the spin-orbit coupling constant A relative to the electrostatic parameter $\epsilon\omega_2$ causes the $^2\Sigma$ and $^2\Delta$ components to lie very close to one another. Combined with the large apparent spin-rotation splitting of the $^2\Sigma$ components, this leads to a level crossing of the $\mu^2\Sigma^{(+)}$ and $^2\Delta_{3/2}$ sub-states. Perturbations of this kind have been referred to as *K*-resonance crossings[127] and are predicted for molecules in which $A \gg \epsilon\omega_2$. For SrOH, the *K*-resonance crossing in the $\tilde{A}^2\Pi(010)$ components and the concomitant anomalous intensities in the branch structure confers a high degree of complexity to the rotational

structure. Using Doppler-limited laser excitation and sub-Doppler IMF, the rotational structure of the $\tilde{A}(010)$ level is clearly resolved in this work and the local perturbations are accounted for in a deperturbation analysis that takes account explicitly of Renner-Teller, spin-orbit, Λ-type doubling and ℓ-type doubling interactions. The extensive and highly accurate data provide for the determination of a rather complete set of deperturbed molecular parameters. Analysis of the mixing percentages of the wavefunctions indicates that the normal basis state labels are inappropriate. The results include the first reliable estimate of the Renner-Teller parameter for SrOH (ϵ = -0.0791).

As with the investigation of the $\tilde{B}^2\Sigma^+$ - $\tilde{X}^2\Sigma^+$ system, vibrationally forbidden ($\Delta v_2 = \pm 1$) bands associated with the $\tilde{A}^2\Pi$ - $\tilde{X}^2\Sigma^+$ electronic transition of SrOH were observed. Similarly forbidden transitions have previously been observed to occur with appreciable intensity in several of the alkaline earth monohydroxides, notably CaOH[31,35], SrOH[33,34] and BaOH.[128,129] In the $\tilde{A}^2\Pi$ - $\tilde{X}^2\Sigma^+$ systems of these heavier alkaline earth monohydroxides, vibronic mixing of the $\tilde{A}^2\Pi$ state with other electronic states can result in the occurrence of parallel ($\Delta K = 0$) bands in a transition which is otherwise characterized by perpendicular ($\Delta K = \pm 1$) bands[130].

7.2 Experimental

The experiments in which the laser excitation spectrum of the $\tilde{A}(100)$ - $\tilde{X}(000)$ band system was recorded proved to be relatively straightforward. Using the selective detection scheme described earlier, the monochromator was maintained at a frequency of approximately 527 cm^{-1} to the red of the laser, such that LIF to the $\tilde{X}(100)$ level was selectively detected. Using this technique, coincident excitations were effectively suppressed and the $\tilde{A}(100)$ - $\tilde{X}(000)$ band was characterized by an exceptionally strong S/N. In

the case of the bands associated with the $\tilde{A}(010)$ vibronic components, it was assumed (correctly) that, based on previous work on the $\tilde{B}^2\Sigma^+$ - $\tilde{X}^2\Sigma^+$ system of SrOH,[34] as well as the ongoing parallel investigations of the $\tilde{A}^2\Pi$ - $\tilde{X}^2\Sigma^+$ system in CaOH[31,131] and CaOD[131], the $\tilde{A}(010)^2\Sigma^{(+)}$, $^2\Sigma^{(-)}$ vibronic levels could be reached directly in excitation from the $\tilde{X}(000)$ level. In these excitation experiments, both the $\tilde{A}(010)\kappa^2\Sigma$, $\mu^2\Sigma$ - $\tilde{X}(000)^2\Sigma^+$ sub-bands were readily observed using a selective detection scheme similar to that used for the ν_1 mode. However, the appearance of the lower $\mu^2\Sigma$ - $^2\Sigma^+$ sub-band was extremely complex and congested. It was subsequently realized that this complexity was due to the fact that the $(010)^2\Delta_{3/2}$ - $(000)^2\Sigma^+$ sub-band was being excited simultaneously. Owing to the small separation of the vibronic origins of the $\mu^2\Sigma$ and $^2\Delta_{3/2}$ components ($\approx$ 2.6 cm^{-1}) and the resultant severe blending, rotational assignments were extremely difficult. Accordingly, the sub-Doppler technique of IMF was employed to resolve the blended features of the lower spin-orbit components. The S/N and dynamic range of the IMF spectra were in general not as good as for the Doppler-limited excitation spectra, and many of the weaker transitions were either not saturated or were too weak relative to adjacent features to permit detection. Consequently, much of the Doppler limited excitation spectra of the $\mu^2\Sigma^{(+)} \leftarrow {}^2\Sigma^+$ and $^2\Delta_{3/2} \leftarrow {}^2\Sigma^+$ bands was complementary to the IMF data. The measurement accuracy of the Doppler-limited and IMF spectra was the same; in both cases it was imposed by limitations of the internal wavemeter of the 699-29 ring dye laser.

The upper $^2\Delta_{5/2}$ vibronic component was observed in the $\tilde{A}(010)^2\Delta_{5/2} \leftarrow \tilde{X}(010)^2\Pi$ hotband excitation. Although the dominant emissions from the excited $^2\Delta_{5/2}$ sub-state were to the $\tilde{X}(010)^2\Pi$ level, the $(010)^2\Delta_{5/2} \rightarrow (020)^2\Delta$ fluorescence was detected using a vibrational selective detection scheme. This method was advantageous in that all branches associated

with the $^2\Delta_{5/2} \leftarrow {}^2\Pi$ transition could, in principle, be observed in a single scan. The $\tilde{A}(000)^2\Pi_{3/2} \leftarrow \tilde{X}(000)^2\Sigma^+$ sub-band could not be completely suppressed, however, and several overlapping transitions from this band were also observed in the excitation spectrum.

For several of the sub-bands associated with the $\tilde{A}(010)$ moiety, there were strong intensity anomalies in the branch structure. These interference effects were especially problematic with respect to the P_2 branches of the $^2\Delta_{5/2} \leftarrow {}^2\Pi$ sub-band, which were not observed in the initial excitation scans. This difficulty could not be addressed simply by increasing the sensitivity of the detection system since excitation features of the $\tilde{A}(000) \leftarrow \tilde{X}(000)$ band were observed in the same region. Using a non-resonant *P-R* separation selective detection scheme, the P_2 branch region was ıned. A comparison of the excitation scans obtained using these two selective detection methods is shown in figure 7.1. In the non-resonant *P-R* detection scheme, the $\tilde{A}(000) \leftarrow \tilde{X}(000)$ transition is completely suppressed and the P_{2ee} and P_{2ff} branches of the $\tilde{A}(010)^2\Delta_{5/2} \leftarrow \tilde{X}(000)^2\Sigma^+$ sub-band are observed with a good S/N. This method of selective detection benefits ıom a considerable enhancement of the signal through the detection of the anomalously strong R_2 branch of the $\tilde{A}(010)^2\Delta_{5/2} \rightarrow \tilde{X}(020)^2\Delta$ transition in fluorescence. The strong irregularities in the branch structure of the bands observed in excitation are more apparent in the dispersed fluorescence spectra which are also presented in this chapter.

LIF from vibronic components of the $\tilde{A}(100)$ and $\tilde{A}(010)$ levels was dispersed and rotationally analyzed. Initially, the resolved fluorescence spectra were used to establish the vibronic identity of the bands observed in excitation. This was necessary since the vibrational temperature of the Broida oven source ($T_{VIB} \approx 700$ K) was sufficient for significant hot band excitation

Figure 7.1: Comparison of Doppler-limited laser excitation spectra obtained using different selective detection methods. The upper spectrum, which was recorded using a constant frequency difference of $\Delta\bar{\nu} = 370$ cm^{-1}, selectively detects excitation features of the $\tilde{A}(000)^2\Pi_{3/2}$ - $\tilde{X}(000)^2\Sigma^+$ sub-band. Using a non-resonant *P-R* selective detection scheme, this band system is nearly completely suppressed, revealing the P_2 branch of the $\tilde{A}(010)$ - $\tilde{X}(010)^2\Pi$ sub-band (lower spectrum).

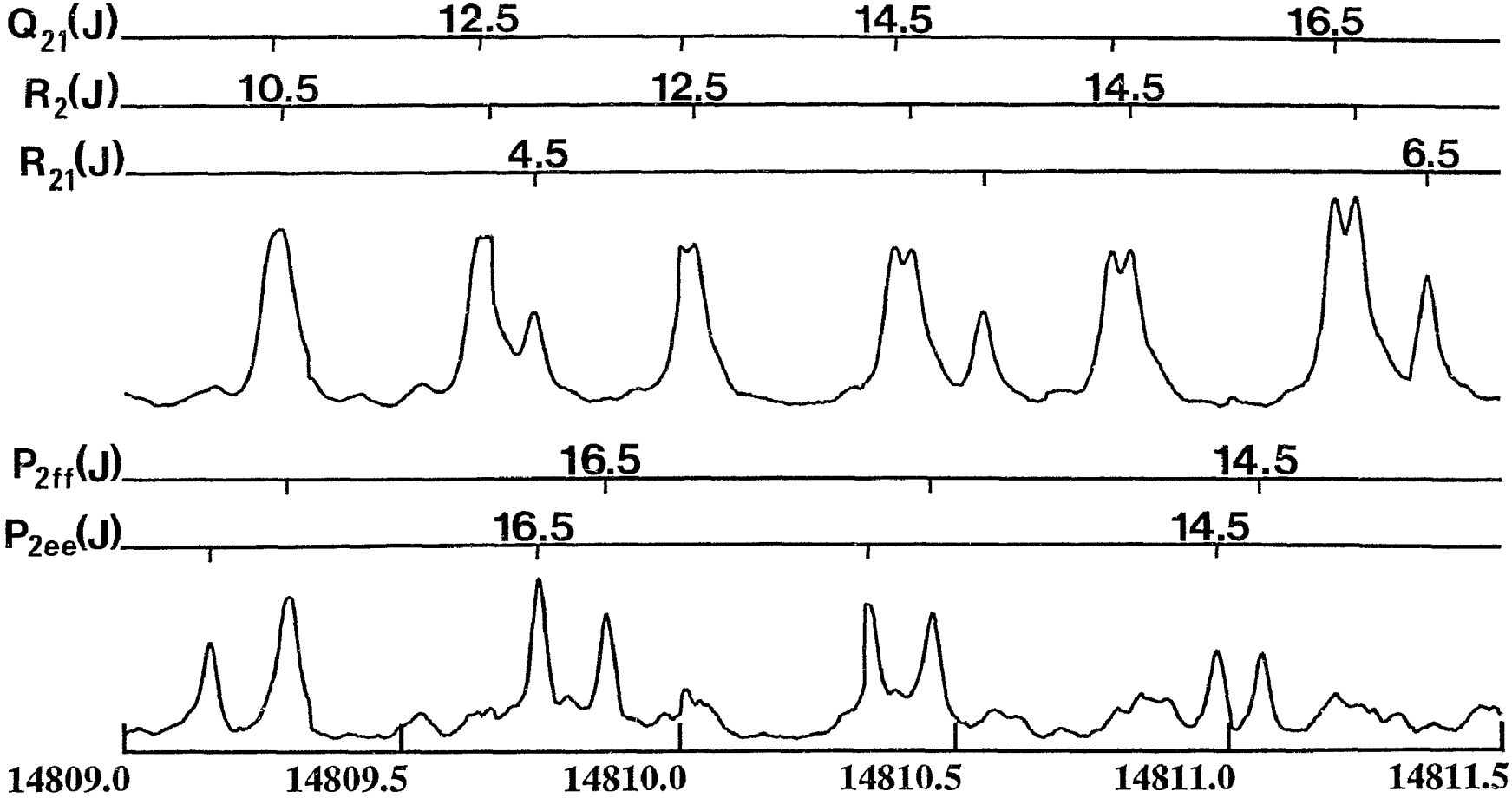
$Q_{21}(J)$
12.5
14.5
16.5
$R_2(J)$
10.5
12.5
14.5
$R_{21}(J)$
4.5
6.5
$P_{2ff}(J)$
16.5
14.5
$P_{2ee}(J)$
16.5
14.5
14809.0
14809.5
14810.0
14810.5
14811.0
14811.5
Wavenumber (cm^{-1})

Figure 7.1

from the (010), (020) and (100) levels. More importantly, the resolved fluorescence data provided decisive confirmation of the rotational quantum number assignments and the $\Sigma^{(+)}/\Sigma^{(-)}$ symmetry.

As illustrated in the previous chapters, dispersed LIF provides a valuable means by which excited vibrational levels in the ground $\tilde{X}^2\Sigma^+$ state may be probed. In the present work, fluorescence from $\tilde{A}(100)$ was used to access the $\tilde{X}(100)$ and $\tilde{X}(200)$ vibrational levels, while LIF from the $\tilde{A}(010)$ levels enabled the observation of the ground state vibrational levels with $v_2 \leq 3$. The $\tilde{A}(010) \rightarrow \tilde{X}(030)$ LIF was extremely weak and, although transitions associated with the $\tilde{X}(03^10)^2\Pi$ component were observed, unambiguous rotational assignments were precluded owing to the presence of numerous coincident transitions that had a comparable intensity.

In order to ascertain a more quantitative measure of the relative transition strength of the forbidden $\Delta v_2 = 1$ bands in the $\tilde{A}^2\Pi$ - $\tilde{X}^2\Sigma^+$ system of SrOH, relative intensity measurements of rotationally resolved features in absorption from $\tilde{X}(000)^2\Sigma^+$ to the $\tilde{A}(000)^2\Pi_{3/2}$ sub-state and to the $\kappa^2\Sigma^{(-)}$ and $\mu^2\Sigma^{(+)}$ RT components of the $\tilde{A}(010)$ level were undertaken. In some cases, unexpectedly large differences between the rotational line strength factors of the *P* and *Q* branches were observed and had to be considered explicitly in comparisons of relative intensities of different sub-bands. These effects were averaged by exciting a *P*-branch and detecting the corresponding *R*-branch fluorescence, or vice versa. Intensity comparisons between different sub-bands were based on an average of measurements for two different *J* values.

7.3 Excitation Spectra

For all Doppler-limited excitation spectra, each single line or blended line profile was reduced to a line measurement(s) by a least-squares fit to a

Gaussian function. This enabled virtually all lines, including blended features, to be fitted to within the estimated measurement accuracy of 0.0035 cm^{-1}. However, when systematic blending of lines at low J was a problem, as well as for a few isolated cases where weaker lines were completely overlapped by much stronger transitions, the experimental line positions could be in error by as much as 0.015 cm^{-1} and were assigned a correspondingly lower weight in the fit.

The bands of the $\tilde{A}^2\Pi$ - $\tilde{X}^2\Sigma^+$ system of SrOH observed in this work are summarized in figure 7.2. The combined data set containing all the laser excitation and dispersed LIF included more than 1500 individual rovibronic transitions. For several of the bands, excitation was from the $\tilde{X}(000)^2\Sigma^+$ level for which a precise millimeter wave study has been carried out by Anderson *et al.*[37] Accordingly, the molecular constants were constrained to the more precise microwave values. While our previous work[34] had determined molecular constants for the $\tilde{X}(010)^2\Pi$ level, the presence of numerous perturbations in the $\tilde{B}^2\Sigma^+$state were found to have contaminated the lower state rotational constants. As a result, the $X(010)^2\Pi$ constants fitted in this work provide improved estimates of their true values.

The (000)-(000) Band

Although the (000)-(000) band of the $\tilde{A}^2\Pi$ - $\tilde{X}^2\Sigma^+$ system has been studied previously at high resolution by Brazier and Bernath,[33] features attributable to this band overlapped the region in which the P_2 branch lines of the $(010)^2\Lambda_{5/2}$ - $(010)^2\Pi$ sub-band were expected (see fig. 7.1). On comparing the measurements to the line positions of ref. 33, it was apparent that numerous lines that had not been assigned previously were observed. In particular, a number of lines belonging to the R_2 branch were observed; this

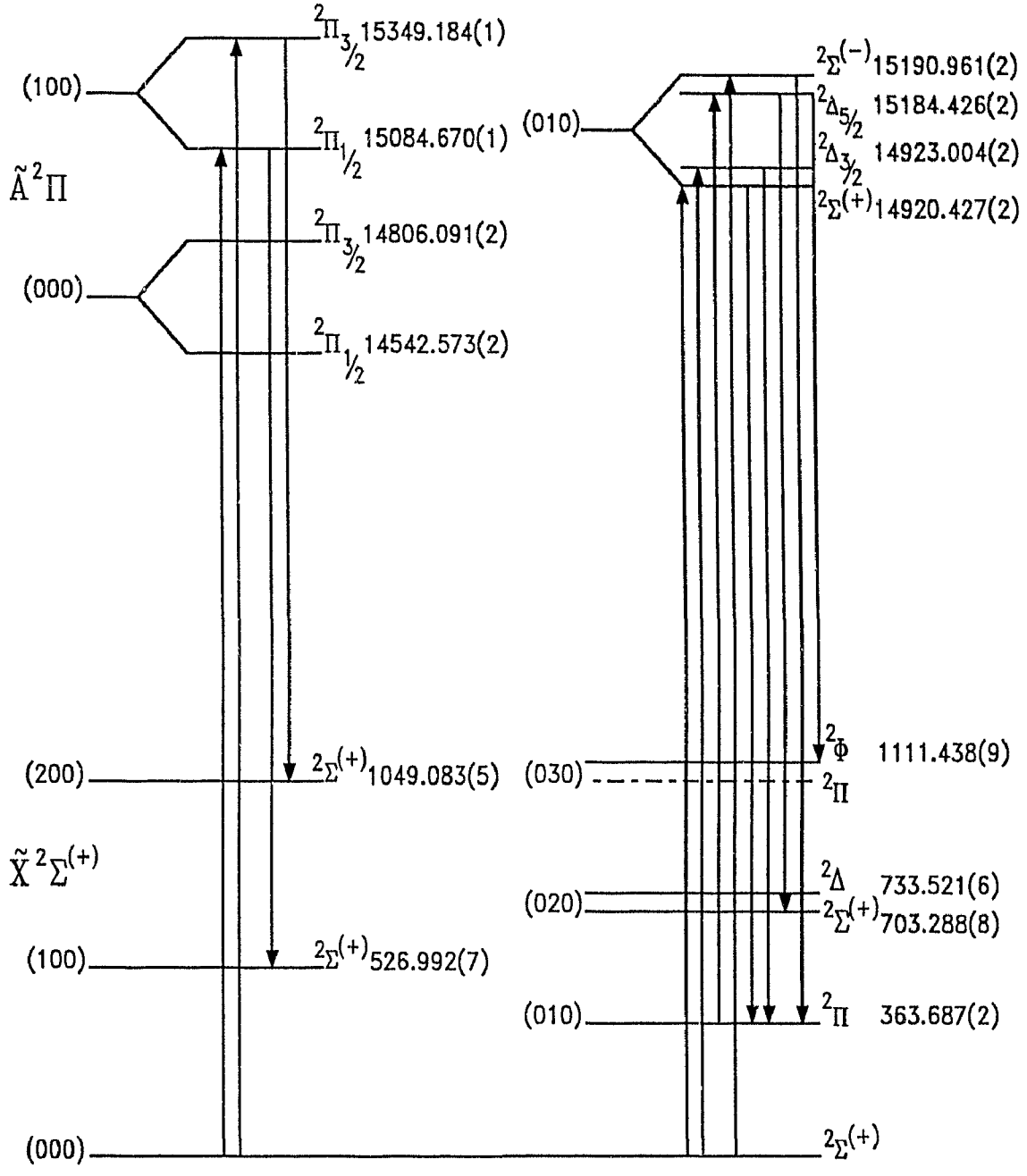

Figure 7.2: Energy level diagram for the low-lying vibronic levels of the $\tilde{A}^2\Pi$ and $\tilde{X}^2\Sigma^{(+)}$ states of SrOH showing transitions observed in the present work. The vibronic energies of the $\tilde{A}(010)$ components are for the "rotationless" ($J = -1/2$) levels; those for $\tilde{A}(000)$ and $\tilde{X}(020)$ are from refs. 33 and 34, respectively.

branch was completely missing in the earlier work. It was found that the present measurements were reproduced to within the experimental uncertainty using the model given in table 4.1 and the constants of ref. 33. The measurements and residuals are given in table 7.1.

The (100)-(000) Band

The rotational structure of the 1_0^1 band, which is very similar to that of the $\tilde{A}(000)$ - $\tilde{X}(000)$ band, is characteristic of a $^2\Pi$ case (a) - $^2\Sigma^+$ transition. All six branches for both sub-bands are observed; however, owing to the relatively small spin-rotation splitting in the ground state (γ_v = 0.0024275 cm^{-1} for $\tilde{X}^2\Sigma^+(000)^{(31)}$), the Q branches are coincident with P and R branches at low J. The blended doublets are resolved with increasing J where, for $J \geq 12½$, both branches are clearly visible. Based on the asymmetries in the peak profiles of the low J blended lines, line measurements which have the same experimental uncertainty as for the isolated lines can be extracted using the least-squares line profile fitting procedure described to earlier.

The rotational energy levels of the $\tilde{A}(100)^2\Pi$ level were modeled by the standard case (a) expressions of table 4.1. The line positions together with the residuals of the least-squares fit are given in table 7.2; the molecular constants obtained from this fit are given in table 7.3. With the ground state constants constrained, all the line positions (over 500) were reproduced to within experimental precision by only seven adjustable parameters.

The (010) $\mu^2\Sigma^{(+)}$, $\kappa^2\Sigma^{(-)}$ - (000) $^2\Sigma^+$ sub-bands

Assignment of the rotational quantum number and parity of the $(010)\kappa^2\Sigma \leftarrow (000)^2\Sigma^+$ band were made using the ground state combination differences of ref. 37. The assignments, however, were initially ambiguous in

TABLE 7.1. Line Positions[a] (cm^{-1}) for the $\tilde{A}^2\Pi$ - $\tilde{X}^2\Sigma^+$ $(000)^2\Pi_{3/2}$ - $(000)^2\Sigma^+$ sub-band of SrOH. The table shows $\bar{\nu}_{obs}$, the measured wavenumbers (cm^{-1}), and the residuals, $\bar{\nu}_{obs} - \bar{\nu}_{calc}$.

J	R_2		Q_{21}		R_{21}	
4½					14809.740	0.001
5½					14810.553	0.005
6½					14811.366	-0.001
7½					14812.197	0.002
8½					14813.033	0.000
9½					14813.886	0.005
10½	14809.288	0.005			14814.733	-0.005
11½	14809.645	-0.009	14809.257	0.002	14815.607	0.002
12½	14810.034	-0.001	14809.645	0.021[b]	14816.485	0.003
13½	14810.425	0.000	14810.006	0.005	14817.364	-0.003
14½	14810.824	-0.001	14810.389	0.000		
15½	14811.236	0.001	14810.786	-0.001		
16½	14811.654	0.001	14811.196	0.002		
17½	14812.080	-0.002	14811.615	0.004		
18½	14812.524	0.004	14812.036	-0.001		
19½	14812.975	0.007	14812.477	0.004		
20½	14813.426	0.001	14812.924	0.006		
21½	14813.886	-0.006	14813.376	0.002		
22½	14814.365	-0.004	14813.839	0.001		
23½	14814.849	-0.006	14814.316	0.004		
24½	14815.347	-0.004	14814.792	-0.003		
25½	14815.857	0.001	14815.294	0.005		
26½	14816.369	-0.002	14815.791	-0.001		
27½	14816.895	0.000	14816.311	0.007		
28½	14817.425	-0.005	14816.832	0.006		

[a]Unless indicated otherwise, line positions have an assigned uncertainty of 0.0035 cm^{-1}.
[b]Blended line with assigned uncertainty of 0.015 cm^{-1}.

TABLE 7.2: Line Positions[a] (cm^{-1}) for the $A^2\Pi \leftarrow X^2\Sigma^+$ $(100)^2\Pi$-$(000)^2\Sigma^+$ Band of SrOH. The table shows $\bar{\nu}_{obs}$, the measured wavenumbers (cm^{-1}), and the residuals, $\bar{\nu}_{obs} - \bar{\nu}_{calc}$.

J	P_1		Q_{12}		P_{12}	
½						
1½			15084.256	-0.003		
2½	15084.256	0.003	15084.098	0.000		
3½	15084.098	0.009	15083.939	-0.002	15081.673	-0.002
4½	15083.930	0.000	15083.791	0.001	15080.873	-0.003
5½	15083.777	0.000	15083.649	0.003	15080.080	-0.004
6½	15083.633	0.004	15083.508	0.002	15079.293	-0.004
7½	15083.490	0.002	15083.375	0.003	15078.518	0.002
8½	15083.356	0.004	15083.239	-0.006	15077.739	-0.003
9½	15083.228	0.006	15083.120	-0.003	15076.968	-0.004
10½	15083.106	0.009	15083.007	0.000	15076.203	-0.005
11½	15082.981	0.002	15082.897	0.001	15075.447	-0.004
12½	15082.872	0.006	15082.794	0.003	15074.694	-0.004
13½	15082.759	0.001	15082.691	-0.001	15073.951	-0.002
14½	15082.658	0.002	15082.599	0.000	15073.207	-0.005
15½	15082.562	0.001	15082.512	0.001	15072.472	-0.006
16½	15082.472	0.002	15082.430	0.001	15071.744	-0.005
17½	15082.390	0.003	15082.357	0.005	15071.023	-0.003
18½	15082.311	0.003	15082.286	0.004	15070.307	-0.003
19½	15082.238	0.003	15082.220	0.003	15069.599	0.000
20½	15082.163	-0.004	15082.163	0.006	15068.892	-0.001
21½	15082.106	0.001	15082.106	0.002	15068.190	-0.004
22½	15082.054	0.004	15082.054	-0.003	15067.497	-0.004
23½					15066.811	-0.002
24½					15066.130	-0.002
25½					15065.454	-0.001
26½					15064.783	-0.003
27½					15064.120	-0.003
28½					15063.461	-0.004
29½					15062.814	0.001
30½					15062.164	-0.003
31½					15061.527	0.000
32½					15060.895	0.001
33½					15060.266	0.000
34½					15059.645	0.001
35½					15059.030	0.002
36½					15058.417	-0.001
37½					15057.816	0.001
38½					15057.220	0.003
39½					15056.625	0.000
40½					15056.040	-0.001
41½					15055.459	-0.002
42½					15054.884	-0.003
43½					15054.321	0.000
44½					15053.758	-0.002
45½					15053.204	0.000
46½					15052.654	-0.001

TABLE 7.2 (Continued)

J	P_1		Q_{12}		P_{12}	
47½					15052.115	0.002
48½					15051.579	0.003
49½					15051.046	0.001
50½			15083.063	0.002	15050.522	0.000
51½			15083.181	0.000	15050.003	-0.001
52½			15083.310	0.003	15049.492	0.000
53½	15083.181	0.004	15083.438	0.000	15048.979	-0.007
54½	15083.310	0.004	15083.567	-0.008	15048.487	0.000
55½	15083.437	-0.003			15047.993	-0.001
56½					15047.505	-0.002
57½					15047.027	0.001
58½					15046.554	0.003
59½					15046.084	0.001
60½					15045.623	0.002
61½					15045.166	0.001
62½					15044.719	0.003
63½					15044.270	-0.002

J	Q_1		R_{12}		R_1	
½			15084.966	-0.002		
1½	15084.966	0.002	15085.162	0.001	15086.579	-0.004
2½	15085.162	0.007	15085.354	-0.005	15087.430	0.009
3½	15085.354	0.007	15085.559	-0.005	15088.266	0.002
4½	15085.559	0.006	15085.768	-0.006	15089.116	0.002
5½	15085.768	0.008	15085.985	-0.004	15089.975	0.006
6½	15085.984	0.010*	15086.205	-0.005		
7½	15086.193	0.001	15086.424	-0.013*	15091.696	0.000
8½	15086.420	0.003	15086.672	0.001	15092.571	0.003
9½	15086.642	-0.005	15086.908	-0.001	15093.446	0.000
10½	15086.882	-0.001	15087.150	-0.002	15094.332	0.004
11½	15087.122	-0.003	15087.402	-0.001	15095.220	0.002
12½	15087.369	-0.003	15087.661	0.003	15096.116	0.005
13½	15087.626	0.001	15087.920	0.001	15097.016	0.005
14½	15087.885	0.001	15088.185	-0.001	15097.922	0.005
15½	15088.148	0.000	15088.455	-0.003	15098.832	0.004
16½	15088.417	-0.002	15088.736	-0.001	15099.745	0.000
17½	15088.691	-0.003	15089.017	-0.004	15100.666	0.000
18½	15088.978	0.003	15089.312	0.002	15101.597	0.002
19½	15089.265	0.002	15089.605	-0.001	15102.520	-0.008
20½	15089.556	0.000	15089.907	0.001	15103.461	-0.005
21½	15089.855	0.001	15090.211	-0.002	15104.403	-0.007
22½	15090.163	0.005	15090.524	-0.001	15105.352	-0.009
23½	15090.468	0.000	15090.838	-0.005	15106.317	0.002
24½	15090.783	-0.001	15091.168	0.001	15107.276	0.000
25½	15091.106	0.001	15091.495	-0.001	15108.238	-0.005
26½	15091.431	-0.001	15091.829	-0.002	15109.208	-0.006
27½	15091.765	0.000	15092.171	0.000	15110.189	-0.002
28½	15092.104	0.002	15092.519	0.001	15111.169	-0.005

TABLE 7.2 (Continued)

J	Q_1		R_{12}		R_1	
29½	15092.450	0.004	15092.872	0.002	15112.159	-0.002
30½	15092.798	0.002	15093.228	0.001		
31½	15093.151	0.000	15093.593	0.002	15114.148	-0.006
32½	15093.512	0.001	15093.965	0.005	15115.151	-0.007
33½	15093.882	0.003	15094.332	-0.002	15116.165	-0.003
34½	15094.256	0.005	15094.713	-0.002	15117.181	-0.002
35½	15094.634	0.006	15095.098	-0.003	15118.197	-0.007
36½	15095.015	0.003	15095.495	0.002	15119.227	-0.003
37½	15095.399	-0.002	15095.889	-0.001	15120.262	0.001
38½	15095.796	0.000	15096.295	0.003	15121.303	0.005
39½	15096.198	0.001	15096.695	-0.006	15122.339	-0.001
40½	15096.605	0.002	15097.116	0.000	15123.387	0.000
41½	15097.016	0.001	15097.540	0.005	15124.439	-0.001
42½	15097.432	-0.001	15097.963	0.001	15125.498	0.000
43½	15097.856	0.000	15098.392	0.000	15126.562	0.000
44½	15098.283	-0.002	15098.832	0.003	15127.632	0.001
45½	15098.715	-0.004	15099.273	0.000	15128.705	0.000
46½	15099.165	0.005	15099.716	-0.005	15129.784	0.000
47½	15099.600	-0.005	15100.178	0.004	15130.869	0.001
48½	15100.054	-0.003	15100.628	-0.006	15131.959	0.000
49½	15100.521	0.007	15101.101	0.001	15133.056	0.002
50½	15100.982	0.005	15101.571	0.001		
51½	15101.443	-0.003	15102.051	0.004		
52½	15101.925	0.006	15102.528	-0.001		
53½	15102.404	0.004	15103.016	-0.001		
54½	15102.883	-0.002	15103.516	0.005		
55½	15103.371	-0.005				
56½	15103.866	-0.006				

J	P_2		Q_2		P_{21}	
1½			15348.195	-0.003		
2½			15347.965	-0.002	15348.195	0.003
3½			15347.744	0.002	15347.965	0.007
4½			15347.529	0.005	15347.735	0.003
5½			15347.318	0.004	15347.516	0.005
6½	15343.826	0.000	15347.109	0.000	15347.299	0.001
7½	15343.123	-0.001	15346.908	-0.004	15347.090	-0.001
8½	15342.426	-0.001	15346.716	-0.005	15346.884	-0.006
9½	15341.737	-0.001	15346.535	-0.001	15346.683	-0.014*
10½	15341.054	-0.002	15346.357	-0.002	15346.509	-0.001
11½	15340.377	-0.003	15346.187	-0.001	15346.333	0.002
12½	15339.709	-0.002	15346.023	-0.001	15346.156	-0.002
13½	15339.046	-0.003	15345.865	-0.002	15345.991	0.000
14½	15338.395	0.001	15345.716	0.000	15345.831	0.000
15½	15337.745	0.000	15345.574	0.002	15345.681	0.002
16½	15337.101	-0.002	15345.435	0.000	15345.534	0.001
17½	15336.469	0.001	15345.307	0.002	15345.393	0.001
18½	15335.841	0.001	15345.182	0.001	15345.261	0.001

TABLE 7.2 (Continued)

J	P_2		Q_2		P_{21}	
19½	15335.219	0.000	15345.069	0.004	15345.136	0.002
20½	15334.607	0.003	15344.957	0.002	15345.017	0.002
21½	15333.999	0.002	15344.851	-0.001	15344.906	0.003
22½	15333.395	-0.001	15344.755	0.000	15344.799	0.002
23½	15332.801	0.000	15344.662	-0.003	15344.697	-0.001
24½	15332.216	0.002	15344.577	-0.006	15344.604	-0.002
25½	15331.637	0.003	15344.510	0.004	15344.520	-0.001
26½	15331.062	0.001	15344.437	-0.001	15344.437	-0.006
27½	15330.495	0.001				
28½	15329.937	0.002				
29½	15329.382	0.000				
30½	15328.837	0.001				
31½	15328.302	0.005				
32½	15327.766	0.001				
33½	15327.241	0.001				
34½	15326.720	-0.002				
35½	15326.214	0.003				
36½	15325.705	-0.001				
37½	15325.213	0.004				
38½	15324.720	0.002				
39½	15324.237	0.003				
40½	15323.760	0.002				
41½	15323.289	0.001				
42½	15322.830	0.005				
43½	15322.373	0.003				
44½	15321.915	-0.005				
45½	15321.482	0.003				
46½	15321.042	-0.002				
47½	15320.617	0.001				
48½	15320.197	0.002				
49½	15319.781	-0.001			15344.520	0.000
50½	15319.372	-0.002			15344.604	-0.002
51½	15318.977	0.002			15344.697	0.000
52½	15318.583	0.001			15344.799	0.002
53½	15318.197	0.001			15344.906	0.003
54½	15317.817	0.000			15345.017	0.001
55½	15317.445	0.000			15345.136	0.000
56½	15317.085	0.004				
57½	15316.725	0.002				
58½	15316.373	0.001				
59½	15316.030	0.002				
60½	15315.697	0.005				
61½	15315.365	0.003				
62½	15315.045	0.006				
63½	15314.729	0.005				
64½	15314.415	-0.001				
65½	15314.116	0.002				
66½	15313.818	-0.002				
67½	15313.530	-0.002				
68½	15313.248	-0.004				
69½	15312.972	-0.007				
70½	15312.719	0.006				

TABLE 7.2 (Continued)

J	R_2		Q_{21}		R_{21}	
½	15349.192	-0.002				
1½	15349.458	-0.003	15349.192	0.002		
2½	15349.728	-0.006	15349.458	0.003		
3½	15350.006	-0.009	15349.728	0.002		
4½	15350.301	-0.001	15350.005	0.001		
5½	15350.601	0.005	15350.290	0.001	15353.570	-0.002
6½	15350.902	0.005	15350.584	0.004	15354.368	-0.001
7½	15351.215	0.011*	15350.884	0.006	15355.170	-0.001
8½	15351.516	-0.001	15351.186	0.003	15355.985	0.004
9½			15351.493	-0.002	15356.792	-0.005
10½			15351.811	-0.001	15357.622	0.002
11½					15358.449	-0.001
12½					15359.282	-0.004
13½	15353.183	-0.003			15360.127	-0.002
14½	15353.537	-0.003	15353.148	-0.003	15360.981	0.002
15½	15353.897	-0.003	15353.500	-0.002	15361.836	0.002
16½	15354.267	-0.001	15353.860	-0.001	15362.697	0.000
17½	15354.643	0.002	15354.223	-0.002	15363.562	-0.005
18½	15355.021	0.000	15354.597	0.001	15364.433	-0.009
19½	15355.408	0.000	15354.975	0.001	15365.324	0.000
20½	15355.800	-0.001	15355.358	0.000	15366.221	0.008
21½	15356.201	-0.001	15355.749	-0.001	15367.108	-0.001
22½	15356.609	0.001	15356.146	-0.001	15368.014	0.003
23½	15357.020	-0.002	15356.551	0.000	15368.914	-0.005
24½	15357.441	-0.001	15356.962	0.000	15369.835	0.001
25½	15357.865	-0.003	15357.379	-0.001	15370.757	0.001
26½	15358.303	0.002	15357.803	-0.001	15371.681	-0.003
27½	15358.740	-0.001	15358.234	-0.001	15372.622	0.003
28½	15359.187	0.000	15358.672	0.000	15373.562	0.002
29½	15359.640	0.000	15359.116	0.001	15374.506	-0.002
30½	15360.097	-0.002	15359.564	-0.001	15375.459	-0.002
31½	15360.565	0.000	15360.022	-0.001	15376.422	0.000
32½	15361.039	0.001	15360.485	-0.001	15377.387	-0.003
33½	15361.521	0.004	15360.957	0.001	15378.365	0.002
34½	15362.005	0.003	15361.433	0.000	15379.336	-0.007
35½	15362.491	-0.003	15361.920	0.004	15380.335	0.005
36½	15362.997	0.004	15362.406	0.001	15381.324	0.001
37½	15363.501	0.002	15362.905	0.003	15382.325	0.002
38½	15364.010	0.000	15363.404	-0.001	15383.328	0.000
39½	15364.526	-0.002	15363.917	0.003	15384.345	0.005
40½	15365.054	0.000	15364.433	0.003	15385.362	0.003
41½	15365.586	0.001	15364.956	0.003	15386.379	-0.005
42½	15366.117	-0.006	15365.482	0.000	15387.415	-0.001
43½	15366.666	-0.001	15366.013	-0.004	15388.456	0.002
44½	15367.218	0.000	15366.560	0.000	15389.500	0.002
45½	15367.776	0.001	15367.108	0.000	15390.544	-0.005
46½	15368.339	0.000	15367.660	-0.003	15391.604	-0.002
47½	15368.914	0.004	15368.226	0.002	15392.668	-0.001
48½	15369.487	0.000	15368.787	-0.005	15393.736	-0.002
49½	15370.070	0.000	15369.364	-0.003	15394.815	-0.001
50½	15370.654	-0.006	15369.950	0.002	15395.895	-0.002

TABLE 7.2 (Continued)

J	R_2		Q_{21}		R_{21}	
51½			15370.536	0.001	15396.980	-0.006
52½	15371.858	-0.001	15371.133	0.004		
53½	15372.466	-0.003	15371.725	-0.005		
54½	15373.091	0.007	15372.336	-0.001		
55½	15373.704	-0.003	15372.958	0.008		
56½	15374.331	-0.005	15373.562	-0.008		
57½	15374.967	-0.004	15374.189	-0.007		
58½			15374.824	-0.005		

[a]The accuracy of the measured line positions is 0.0035 cm^{-1}.

Lines excluded from the fit are flagged with an asterisk.

Table 7.3: Molecular constants for the SrOH molecule. All values are in cm^{-1}; values in parentheses correspond to 1σ in units of the last significant figure; square brackets are used to indicate constants fixed in the least-squares fit; the constants for $\tilde{X}(000)$ were fixed to the values of ref.37.

$\tilde{A}(100)^2\Pi^a$		$\tilde{X}(100)^2\Sigma^{+a}$		$\tilde{X}(200)\Sigma^{+a}$	
ν_1 [b]	542.595(1)	ν_1	526.992(7)	$2\nu_1$	1049.082(5)
A	264.5139(4)	B	[0.24772]	B	0.246318
B	0.2523946(17)	D	[2.15×10^{-7}]	D	[2.1744×10^{-7}]
D	$2.1636(11) \times 10^{-7}$	γ	[0.0024275]	γ	[0.0024275]
p^e	-0.0143111(14)				
q^e	$-1.950(33) \times 10^{-4}$				

[a]Determined in this work.

[b]Determined using $T_{ev}(000)$ from Ref. 33.

that depending on whether the symmetry of the $\kappa^2\Sigma$ state was assigned as $\Sigma^{(+)}$ or $\Sigma^{(-)}$, more than one possibility was viable. If the symmetry of the $\kappa^2\Sigma$ state is $^2\Sigma^{(-)}$, the assignment of rotational quantum number and parity of the four branches observed in the $\kappa^2\Sigma$ - $^2\Sigma^+$ band follows immediately from the rotational energy level diagram given by Herzberg[76] and the branches are labelled as $^SR_{21}$, $^QR_{12}$, $^QP_{21}$, $^OP_{12}$. Conversely, if the $\kappa^2\Sigma$ state is assigned as $^2\Sigma^{(+)}$, four main branches (P_1, P_2, R_1 and R_2) and possibly two satellite branches ($^RQ_{21}$ and $^PQ_{12}$) are expected. Least-squares fits to the expressions given by Hougen,[75] and listed explicitly in eqs. 4.45-4.54, were performed for both sets of assignments corresponding to the labelling of the $\kappa^2\Sigma$ state as $^2\Sigma^{(+)}/^2\Sigma^{(-)}$. It was found that for only one of the two possible sets of assignments did Hougen's effective spin-rotation parameter p fall within the $-2B \leq p \leq 2B$ range. The magnitude of the splitting parameter p arises from a consideration of second order corrections to the rotational energies of the Σ states. Accordingly, the symmetry is established as $\kappa^2\Sigma^{(-)}$ and the four branches are labelled as $^SR_{21}$, $^QR_{12}$, $^QP_{21}$ and $^OP_{12}$. The least squares fit of the $(010)\kappa^2\Sigma^{(-)} \leftarrow (000)^2\Sigma^+$ band using the Hougen expressions yielded $\hat{\sigma}^2 \approx 1$, indicating that the upper state energy levels were described adequately.

Excitation of the $\mu^2\Sigma^{(+)}$ level resulted in extremely complex and congested spectra which was puzzling until it was realized that the $^2\Delta_{3/2}$ sub-state was also being excited. A complete understanding of the rotational structure was achieved only after the Doppler-limited excitation spectra were combined with the IMF spectra and the results of repeated resolved fluorescence scans. In addition to the four main branches of the $\mu^2\Sigma^{(+)} \leftarrow ^2\Sigma^+$ band, an equally intense $^RQ_{12}$ satellite branch was observed. Not only did this confirm the symmetry identification of the $\kappa^2\Sigma^{(-)}$ state established earlier, it indicated that, although the orbital angular momentum of the $\mu^2\Sigma^{(+)}$ state is cancelled

by the vibrational angular momentum, the coupling is more representative of Hund's cases (a) or (c), rather than case (b). Clearly this is expected in SrOH given the large spin-orbit splitting in the $\tilde{A}^2\Pi$ state of 263 cm^{-1}. Moreover, the intensity measurements indicated that the $\mu^2\Sigma^{(+)} \leftarrow {}^2\Sigma^+$ band was 3 to 4 times stronger than the $\kappa^2\Sigma^{(-)} \leftarrow {}^2\Sigma^+$ band, which further buttresses the symmetry labelling of the Σ states. That the $\kappa^2\Sigma^{(-)} \leftarrow {}^2\Sigma^+$ transition is even observed is a consequence of the spin-orbit interaction which mixes the $\kappa^2\Sigma$ and $\mu^2\Sigma$ states. Through this mechanism, the $\kappa^2\Sigma^{(-)} \leftarrow {}^2\Sigma^+$ sub-band gains transition strength by intensity borrowing. In order to achieve an acceptable standard deviation with the Hougen expressions, it was necessary to perform separate fits for the *e* and *f* levels associated with the $\mu^2\Sigma^{(+)}$ state; a fit of the *e* and *f* levels simultaneously gave a completely unsatisfactory estimate of $\hat{\sigma}^2 > 1000$. The results of these fits yielded separate estimates of the rotational constant *B* and anomalous values of the centrifugal distortion constant. These effects were attributed to a *K*-type resonance with the nearly degenerate $^2\Delta_{3/2}$ state.

The $(010)^2\Delta_{3/2}$ - $(000)^2\Sigma^+$ sub-band

The $(010)^2\Delta_{3/2} \leftarrow (000)^2\Sigma^+$ sub-band was characterized by six branches; P_{21}, P_1, Q_{21}, P_{12}, Q_1 and R_1. A portion of the IMF spectrum near the P_1 and Q_{12} bandheads is shown in figure 7.3. Not unexpectedly, the $^2\Delta_{3/2}$ levels exhibited signs of a strong *K*-type resonance in the preliminary least-squares fits and consequently the *e* and *f* levels were fit separately. It seemed rather surprising that the $(010)^2\Delta_{3/2} \leftarrow (000)^2\Sigma^+$ sub-band, with $\Delta K = 2$, was observed and could be followed from $J = 1\frac{1}{2}$ through to $J = 70\frac{1}{2}$. The analogous transition to the $^2\Delta_{5/2}$ spin-orbit component was not observed at all, at least with the sensitivity obtained in this work.

Figure 7.3: A portion of the IMF spectrum of the $\tilde{A}(010)^2\Delta_{3/2}$ - $\tilde{X}(000)^2\Sigma^+$ sub-band of SrOH near the P_1 and Q_{12} heads.

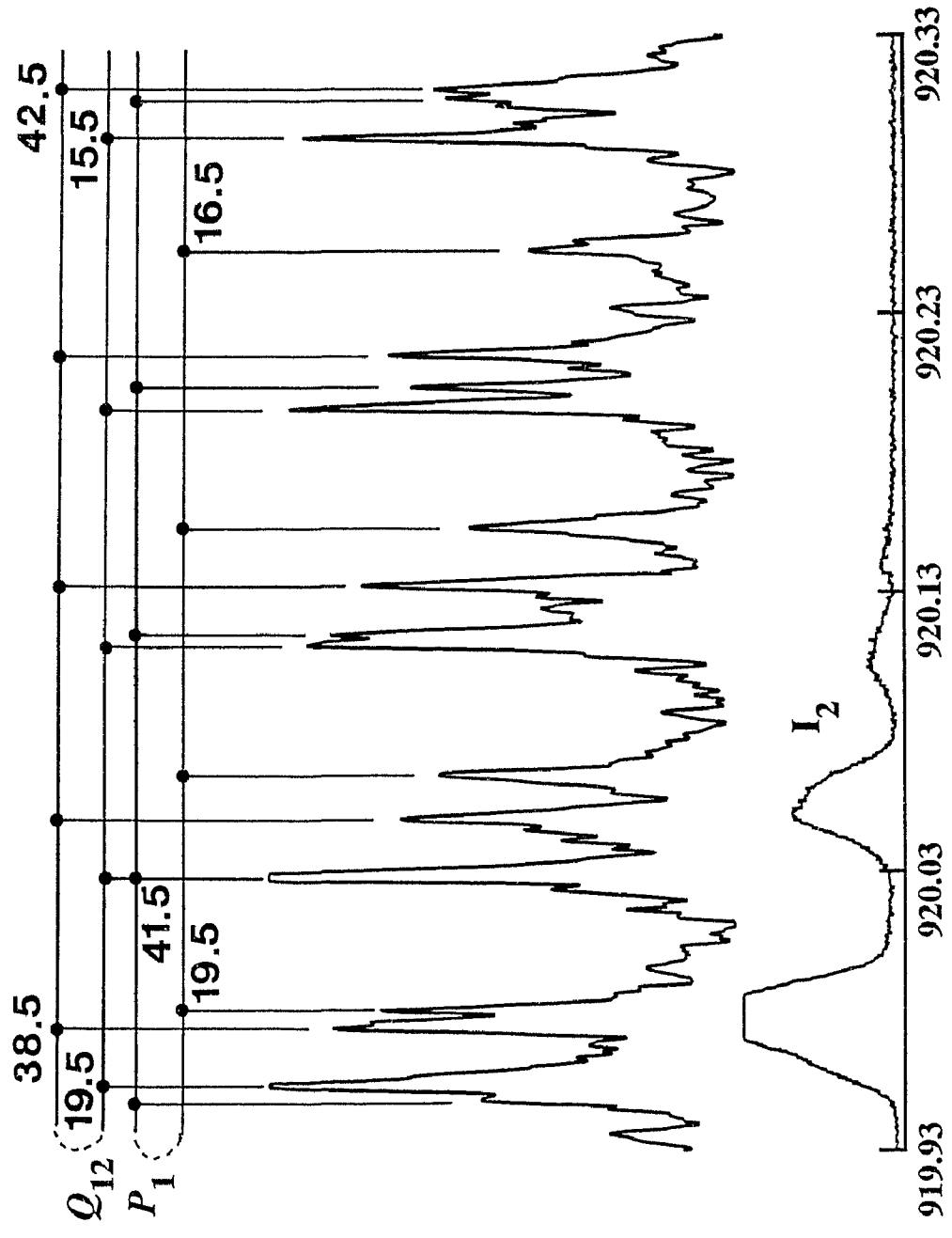
42.5
15.5
16.5
38.5
19.5
41.5
19.5
Q_{12}
P_1
I_2
919.93
920.03
920.13
920.23
920.33
Wavenumber/cm^{-1} - 14000

Figure 7.3

The $(010)^2\Delta_{5/2}$ - $(010)^2\Pi$ *sub-band*

The appearance of the $(010)^2\Delta_{5/2} \leftarrow (010)^2\Pi$ sub-band was analogous to that of a case (a) $^2\Pi_{3/2}$ - case (b) $^2\Pi$ transition of a diatomic molecule. Owing to the much larger ℓ-type splittings in the lower state, a doubling was observed in each of the six branches even at relatively low J (see figure 7.4). The R_{21} and P_2 branches were anomalously weak. Initially, the energy level expressions of Hougen[75] (eqs. 4.55-4.56) were used for the $^2\Delta$ state and, despite the apparent irregularities of the branch intensities in the $^2\Delta_{5/2} \leftarrow {}^2\Pi$ sub-band, the $^2\Delta_{5/2}$ sub-state levels were well represented.

7.4 Dispersed Fluorescence

A particularly interesting feature of the rotationally resolved dispersed fluorescence spectra was the ability to make direct comparisons of the relative intensities of the different rotational branches. Such comparisons were generally not possible in the excitation spectra since the detector response was obviously highly sensitive to the accuracy of the frequency difference used in the selective detection scheme. Since small deviations in the tracking frequency of the monochromator are unavoidable, comparisons of the relative intensities are unreliable. Moreover, the dynamic range of the 699-29 data channels was limited and frequently the LIF signal exceeded the maximum input range of 10 V dc.

The relative intensities of the rotational branches associated with the bands observed in the resolved fluorescence experiments provides a sensitive probe for the presence of perturbations in the $\tilde{A}^2\Pi$ state levels of SrOH. These effects are observed through a modification of the rotational line strengths or Hönl-London factors which can be altered differentially by perturbing

Figure 7.4: A portion of the Doppler-limited laser excitation spectrum of the $\tilde{A}(02^{0}0)^{2}\Delta_{5/2}$ - $\tilde{X}(010)^{2}\Pi$ sub-band of SrOH showing a doubling of the R_2 and Q_{21} branches.

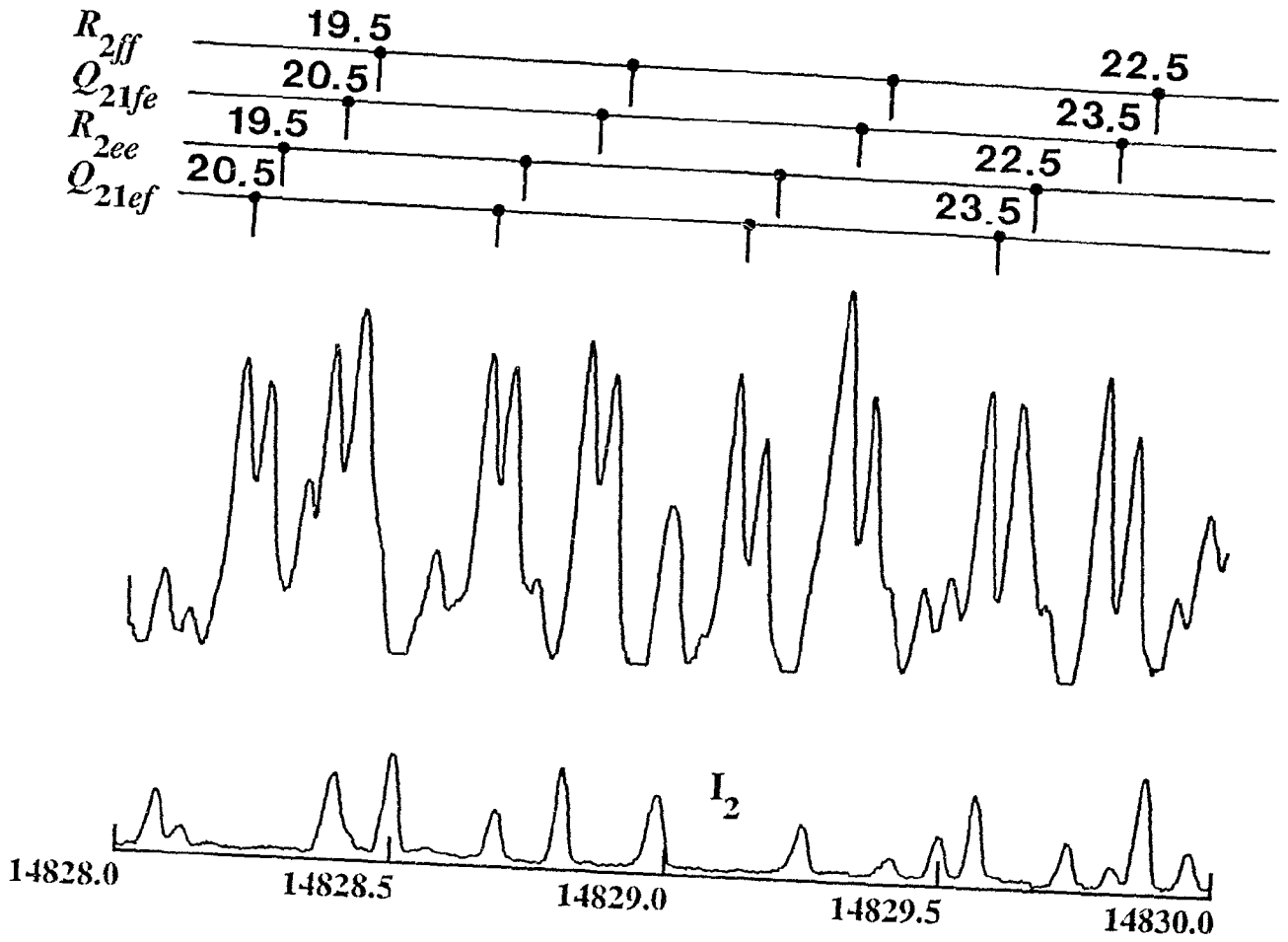
R_{2ff}
Q_{21fe}
R_{2ee}
Q_{21ef}
19.5
20.5
19.5
20.5
22.5
23.5
22.5
23.5
I_2
14828.0
14828.5
14829.0
14829.5
14830.0
Excitation Frequency (cm^{-1})

Figure 7.4

states belonging to a different symmetry species[89]. A quantitative model to explain the relative intensities observed in this work was not attempted, rather, the observation of interference effects is used to provide evidence of perturbations in the $\tilde{A}^2\Pi$ state levels that otherwise may not be evident from the excitation spectrum. For example, although the $\tilde{A}(000)^2\Pi$ rotational levels, which were studied in a previous high resolution investigation[33], were well represented by the standard model in table 4.1, the presence of strong interference effects in the dispersed fluorescence spectra indicated these upper state levels were perturbed. Such a conclusion would seem to contradict the apparent simplicity suggested by the earlier work, however, repeated dispersed fluorescence scans of the $\tilde{A}(000)^2\Pi_{3/2} \rightarrow \tilde{X}(010)$ sub-band consistently revealed an anomalously weak P branch (see figure 7.5). Such information also proved to be particularly useful in optimizing the selective detection scheme used in the excitation experiments.

The dispersed fluorescence experiments of the $\tilde{A}^2\Pi$ - $\tilde{X}^2\Sigma^+$system of SrOH involved the study of both the ν_1 stretching and ν_2 bending modes in the $\tilde{X}^2\Sigma^+$ state. The stretching progression was observed following excitation of the $\tilde{A}(100)^2\Pi$ vibrational level, while the bending levels were observed in fluorescence from the vibronic components of the $\tilde{A}(010)$ level.

Fluorescence from $\tilde{A}(100)$

Dispersed fluorescence from selected rotational transitions of the 1_0^1 band was used to access the $\tilde{X}(100)^2\Sigma^+$ and $\tilde{X}(200)^2\Sigma^+$ vibrational levels. The rotational structure was similar to that observed in the stretching progression of the $\tilde{A}^2\Pi$ - $\tilde{X}^2\Sigma^+$ system of CaOH and CaOD. As in this earlier work, the $\tilde{A}^2\Pi$ state constants were constrained to the values determined from the excitation data.

Figure 7.5: $\tilde{A}(000)^2\Pi_{3/2} \rightarrow \tilde{X}(010)^2\Pi$ dispersed fluorescence spectrum following excitation of the $R_2(12½)$ line of the $\tilde{A}(000)^2\Pi_{3/2} \leftarrow \tilde{X}(000)^2\Sigma^+$ sub-band of SrOH.

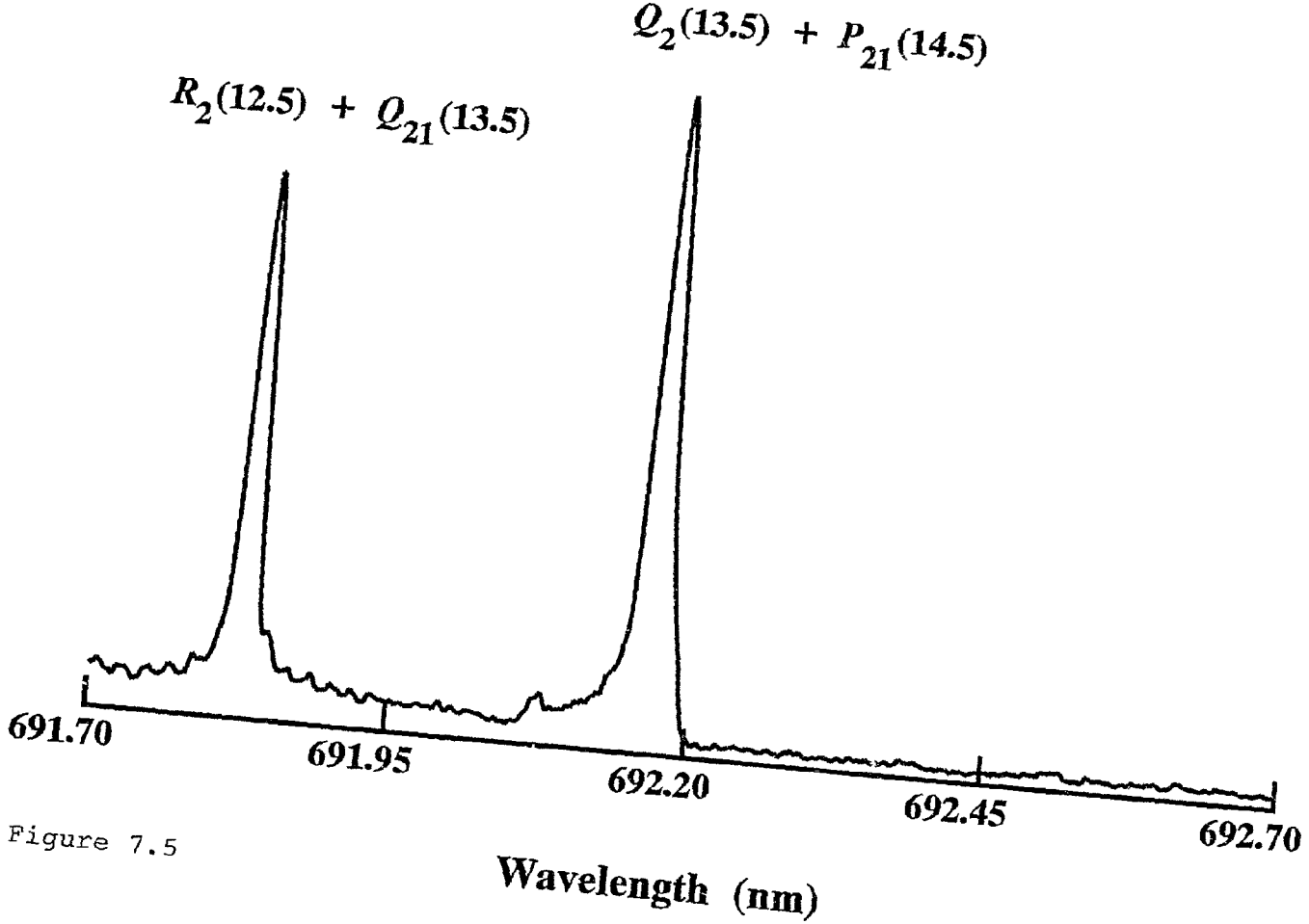
$Q_2(13.5) + P_{21}(14.5)$
$R_2(12.5) + Q_{21}(13.5)$
691.70
691.95
692.20
692.45
692.70
Wavelength (nm)

Figure 7.5

Although rotational constants for the $\tilde{X}(100)$ level had been obtained previously from an analysis of the $\tilde{B}(100) \leftarrow \tilde{X}(100)$ band by Nakagawa *et al.*[22], the fundamental vibrational frequency was not accurately known. Since the data were more comprehensive in this earlier work, the $\tilde{X}(100)$ rotational constants were fixed to the values determined in ref. 22 and only the vibrational term energy was fitted from the $\tilde{A}(100) \rightarrow \tilde{X}(100)$ data.

In contrast, considerably more data was obtained for the $\tilde{A}(100) \rightarrow \tilde{X}(200)$ band. In the least-squares fitting of this band, the parameters D_v'' and γ_v'' were fixed to the $\tilde{X}(010)$ values determined in this work. Based on our earlier analysis of the $\tilde{B}^2\Sigma^+$ - $\tilde{X}^2\Sigma^+$ system[34], a near degeneracy of the $\tilde{X}(200)^2\Sigma^+$ and $\tilde{X}(03^10)^2\Pi$ levels was predicted, and consequently it was expected that some indications of a perturbation would be evident. No such effects were apparent in the present work and the lower state rotational levels were well described by the standard $^2\Sigma^+$ model of eqs. 4.30-4.31, suggesting that any Coriolis interactions caused by the accidental degeneracy of the $(200)^2\Sigma^+$ and $(03^10)^2\Pi$ levels is weak. The line positions and residuals of the 1_1^1 and 1_2^1 bands are given in tables 7.4 and 7.5; the molecular constants obtained from the least-squares fit are listed in table 7.3.

Fluorescence from A(010)

Resolved fluorescence spectra arising from excitation of a single rotational level of the $\kappa^2\Sigma^{(-)}$ or $\mu^2\Sigma^{(+)}$ states and terminating on the $\tilde{X}(010)^2\Pi$ level consisted of three main lines and one satellite line. A typical pattern corresponding to the $(010)\kappa^2\Sigma^{(-)} \rightarrow (010)^2\Pi$ transition obtained by populating the J = 18½ level of the $\kappa^2\Sigma^{(-)}$ state is shown in figure 7.6. A resolved fluorescence scan corresponding to the $(010)\mu^2\Sigma^{(+)} \rightarrow (010)^2\Pi$ sub-band is illustrated in figure 7.7, where anomalous P/R intensity effects

TABLE 7.4: Line Positions[a] (cm^{-1}) for the $A^2\Pi$ - $X^2\Sigma^+$ $(100)\Pi_{1/2} \rightarrow (100)\Sigma^+$ Band of SrOH. The table shows $\bar{\nu}_{obs}$, the measured wavenumbers (cm^{-1}), and the residuals, $\bar{\nu}_{obs} - \bar{\nu}_{calc}$.

J	P_1		R_1	
5½			14560.059	0.039
6½			14563.950	0.052
7½	14556.576	-0.001		
8½	14556.477	0.012		

J	Q_1		R_{12}		P_{12}	
13½			14561.223	-0.018		
14½			14561.539	-0.014	14546.545	-0.034
15½					14545.873	-0.019
16½					14545.206	-0.008
17½					14544.536	-0.008
18½						
19½						
20½			14563.603	0.001	14542.571	-0.018
21½	14563.583	0.043	14563.968	-0.006	14541.930	-0.025
22½	14563.964	0.055			14541.325	-0.005
23½					14540.703	-0.011
24½					14540.078	-0.028
25½					14539.502	-0.006

[a]The accuracy of the measured line positions is 0.03 cm^{-1}.

TABLE 7.5: Line Positions[a] (cm^{-1}) for the $\tilde{A}^2\Pi$ - $\tilde{X}^2\Sigma^+$ $(100)^2\Pi$ - $(200)^2\Sigma^+$ band of SrOH. The table shows $\bar{\nu}_{obs}$ (measured wavenumbers in cm^{-1}) and the residuals ($\bar{\nu}_{obs}$ - $\bar{\nu}_{calc}$).

J	P_2		R_2		P_{21}		R_{21}	
1½			14300.414	0.019			14301.395	0.020
2½	14297.598	-0.057	14300.693	0.007	14299.123	-0.003	14302.215	0.059
3½			14301.015	0.026	14298.908	-0.002	14303.002	0.052
4½	14296.244	-0.011	14301.297	-0.008	14298.748	0.042	14303.817	0.061
5½	14295.571	-0.002	14301.650	0.016	14298.592	0.078		
6½	14294.878	-0.026	14302.003	0.028	14298.415	0.080		
7½	14294.247	0.000	14302.308	-0.020				
8½	14293.630	0.027	14302.732	0.038			14307.049	-0.056
9½	14292.961	-0.011						
10½	14292.392	0.039	14303.437	-0.025	14297.698	-0.046		
11½	14291.750	0.004						
12½	14291.150	-0.002	14304.266	-0.015				
13½			14304.699	-0.009			14311.502	-0.068
14½	14289.991	-0.011	14305.135	-0.014			14312.472	-0.028
15½			14305.571	-0.030			14313.370	-0.073
16½	14288.882	-0.020	14306.074	0.008	14297.240	0.007	14314.349	-0.049
17½			14306.500	-0.043			14315.333	-0.032
18½			14307.048	0.015			14316.400	0.056
19½			14307.521	-0.014	14297.166	0.020	14317.296	-0.040
20½			14308.029	-0.021			14318.327	-0.013
21½			14308.547	-0.030				
22½			14309.087	-0.029	14297.180	0.008		
23½			14309.673	0.006				
24½			14310.212	-0.019				
25½			14310.786	-0.022				
26½			14311.419	0.023			14324.611	-0.013
27½			14311.994	-0.003				
28½			14312.600	-0.011	14297.608	0.045		
29½			14313.237	0.001				
30½			14313.860	-0.015			14329.095	0.036
31½			14314.500	-0.025			14330.153	-0.045
32½			14315.181	-0.007			14331.289	-0.061
33½			14315.852	-0.011			14332.493	-0.020
34½			14316.546	-0.004			14333.688	-0.001
35½	14281.000	0.034	14317.279	0.029	14298.699[b]	0.108	14334.878	-0.001
36½			14317.982	0.020				
37½			14318.692	0.006				
38½			14319.420	-0.003				
39½			14320.187	0.015				
40½			14320.902	-0.031				
41½	14279.459	0.049	14321.694	-0.013				
42½			14322.490	-0.003				
43½			14323.289	-0.002				
44½			14324.119	0.018				
45½			14324.960	0.036				

[a]Unless indicated otherwise, line positions have an assigned uncertainty of 0.0035 cm^{-1}.
[b]Blended line with assigned uncertainty of 0.015 cm^{-1}.

Figure 7.6: $\tilde{A}(010)\kappa^2\Sigma^{(-)} \rightarrow \tilde{X}(010)^2\Pi$ dispersed fluorescence spectrum following excitation of the ${}^{O}P_{12}(19½)$ line of the $\tilde{A}(010)\kappa^2\Sigma^{(-)} \leftarrow \tilde{X}(000)^2\Sigma^{+}$ sub-band of SrOH.

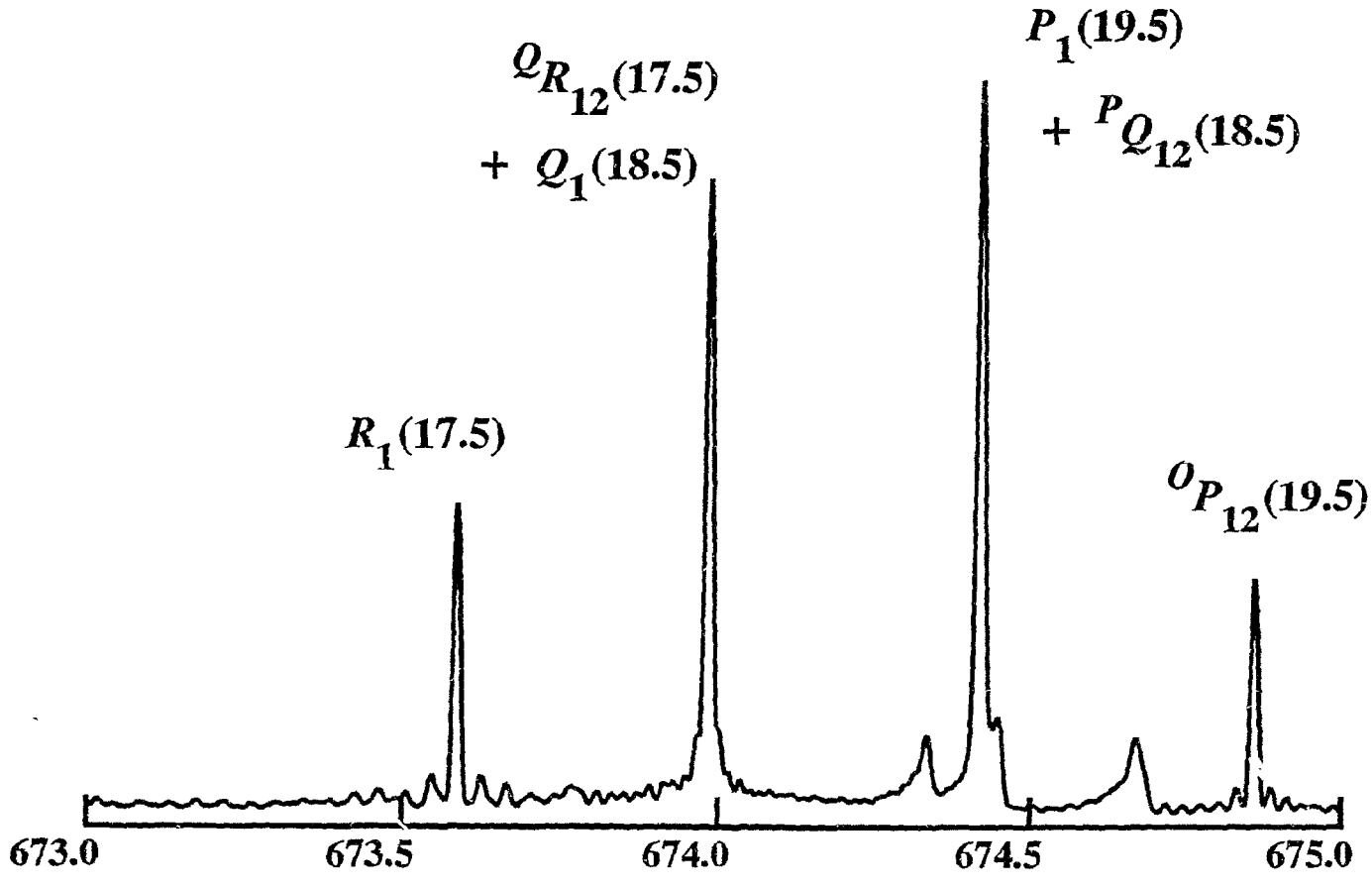
$^{Q}R_{12}(17.5)$
+ $Q_1(18.5)$
$P_1(19.5)$
+ $^{P}Q_{12}(18.5)$
$R_1(17.5)$
$^{O}P_{12}(19.5)$
673.0
673.5
674.0
674.5
675.0
Wavelength (nm)

Figure 7.6

Figure 7.7: $\tilde{A}(010)\mu^2\Sigma^{(+)} \rightarrow \tilde{X}(010)^2\Pi$ dispersed fluorescence spectrum following excitation of the ${}^{R}Q_{21}(23\frac{1}{2})$ line of the $\tilde{A}(010)\mu^2\Sigma^{(+)} \leftarrow \tilde{X}(000)^2\Sigma^{+}$ sub-band of SrOH.

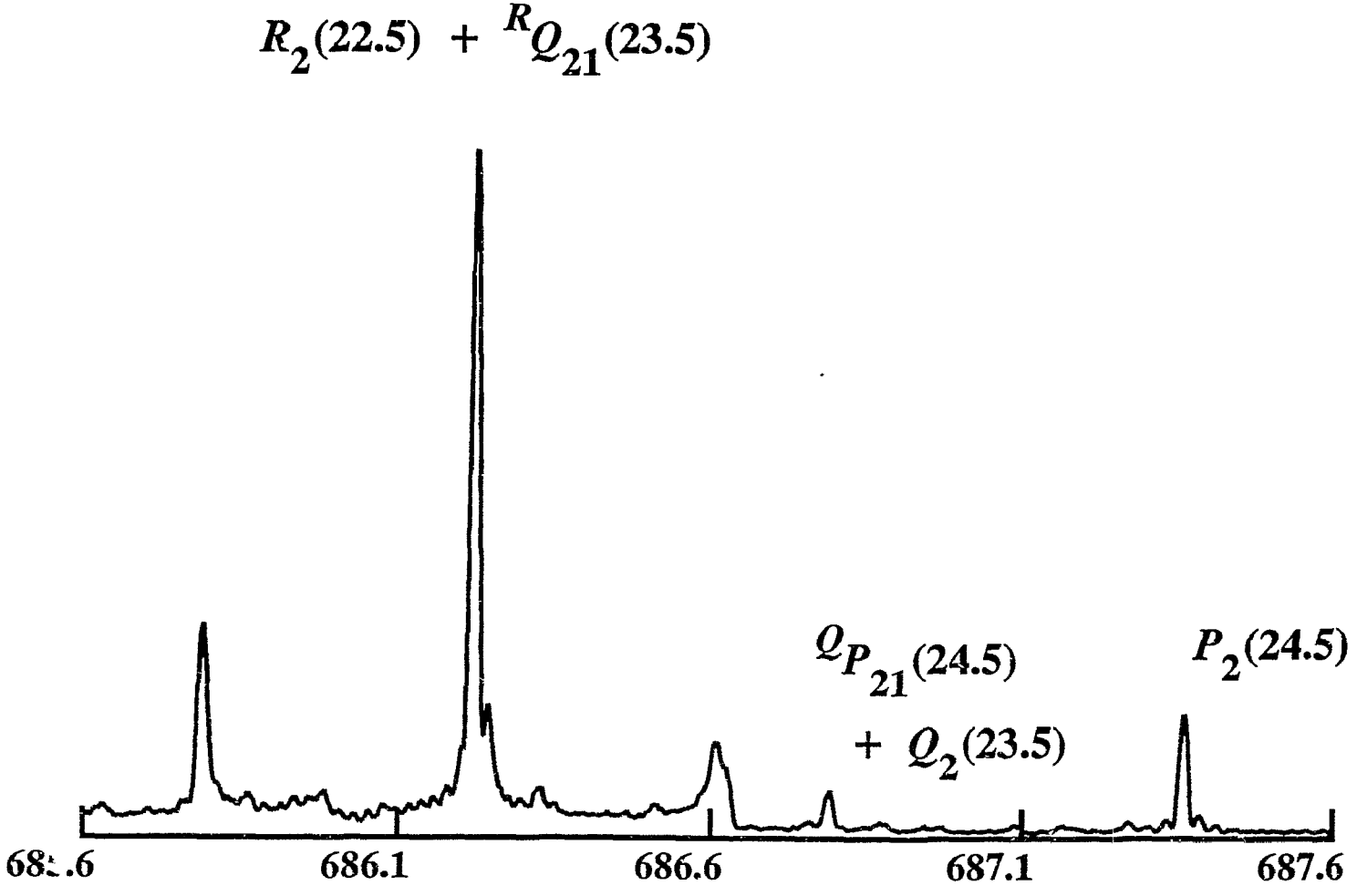
$R_2(22.5)$ + $^{R}Q_{21}(23.5)$
$Q_{P_{21}}(24.5)$
+ $Q_2(23.5)$
$P_2(24.5)$
686.1
686.6
687.1
687.6
Wavelength (nm)

Figure 7.7

are clearly evident.

Because the resolution afforded by the monochromator was insufficient to resolve the ground state spin-rotation splittings, it was expected that four well resolved lines would be observed for both the $(010)^2\Delta_{3/2} \rightarrow (010)^2\Pi$ and $(010)^2\Delta_{5/2} \rightarrow (02^20)^2\Delta$ sub-bands. Although all four lines were observed for the $^2\Delta_{3/2} \rightarrow {}^2\Pi$ sub-band, albeit with anomalous intensities (see figure 7.8), surprisingly, it was found that the R_{21} and P_2 lines of the $^2\Delta_{5/2} \rightarrow {}^2\Delta$ fluorescence were generally too weak to detect (see fig. 7.9). A conservative estimate would suggest that the P_2 branch is more than an order of magnitude weaker than the R_2 branch. Numerous resolved fluorescence scans revealed no apparent J-dependence to this effect. Furthermore, the excitation data provided no indication of J- or parity-dependent interactions of the $^2\Delta_{5/2}$ state other than a weak K-type resonance with the $\kappa^2\Sigma^{(-)}$ state. The occurrence of these intensity anomalies bears a striking similarity to those observed in the $(000)^2\Pi_{3/2} \rightarrow (010)^2\Pi$ sub-band for which the the P_2 branch was also completely missing (fig. 7.5). In both cases, the anomalous intensity patterns are attributed to interference effects arising from perturbations of the $\tilde{A}^2\Pi$ electronic state levels.

Initial attempts to observe $\tilde{A}(010) \rightarrow \tilde{X}(030)$ emissions following excitation of the $\tilde{A}(010)^2\Delta_{3/2}$ Renner-Teller component were unsuccessful owing to the low intensity of the resulting dispersed LIF signal. The $\tilde{A}(010)^2\Delta_{5/2} \rightarrow \tilde{X}(030)$ fluorescence was considerably more intense and both the $\ell = 1$ ($^2\Pi$) and $\ell = 3$ ($^2\Phi$) components of the lower vibrational level were observed. The $^2\Delta_{5/2} \rightarrow {}^2\Pi$ transition was approximately an order of magnitude weaker than the corresponding $^2\Delta_{5/2} \rightarrow {}^2\Phi$ emissions and consequently unambiguous rotational assignments were not possible in the former case. A typical dispersed LIF spectrum of the $^2\Delta_{5/2} \rightarrow {}^2\Phi$ band is shown in figure 7.10. As with the

Figure 7.8: $\tilde{A}(010)^2\Delta_{3/2} \rightarrow \tilde{X}(010)^2\Pi$ dispersed fluorescence spectrum following excitation of the $Q_{12}(14½) + Q_{12}(43½)$ lines of the $\tilde{A}(010)^2\Delta_{3/2} \leftarrow \tilde{X}(000)^2\Sigma^+$ sub-band of SrOH.

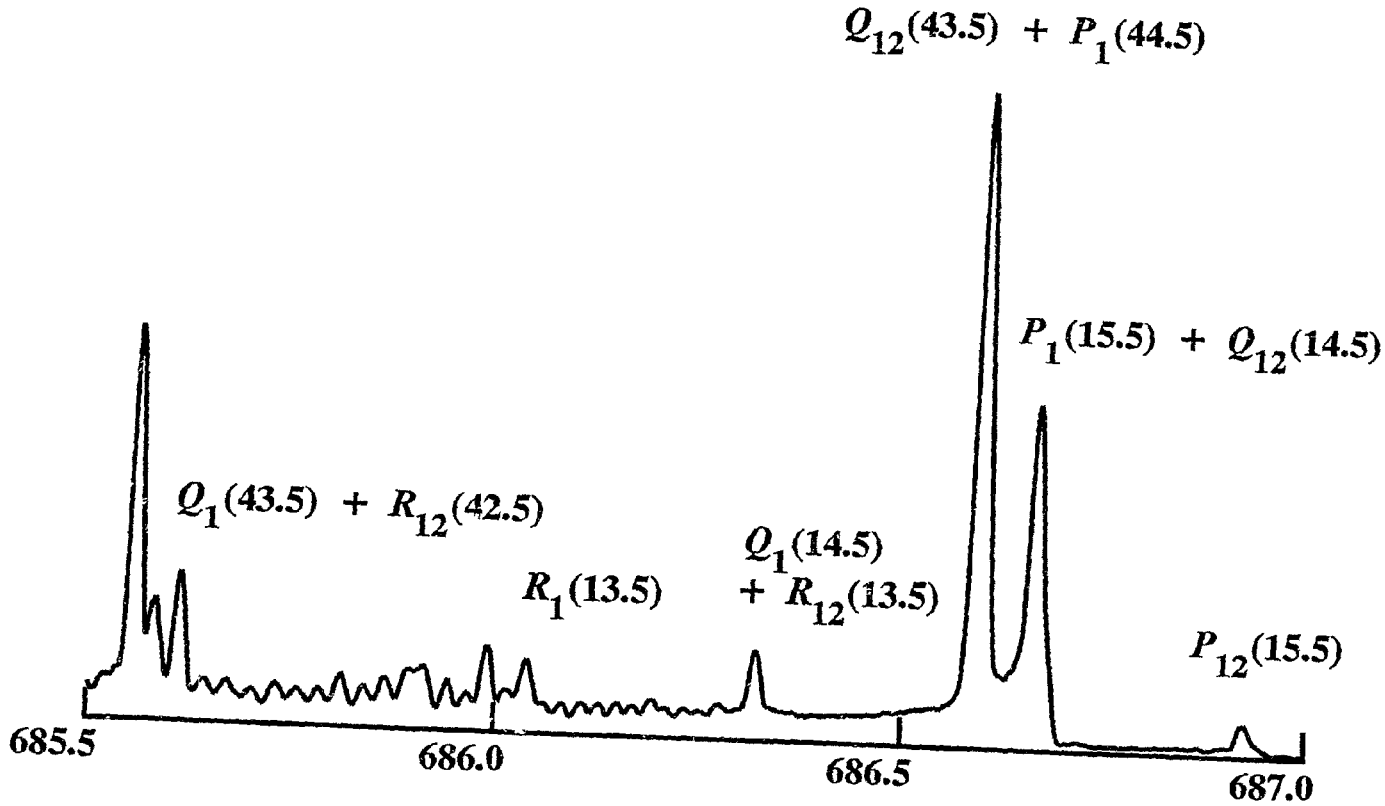
$Q_{12}(43.5) + P_1(44.5)$
$P_1(15.5) + Q_{12}(14.5)$
$Q_1(43.5) + R_{12}(42.5)$
$Q_1(14.5)$
$+ R_{12}(13.5)$
$R_1(13.5)$
$P_{12}(15.5)$
685.5
686.0
686.5
687.0
Wavelength (nm)

Figure 7.8

Figure 7.9: $\tilde{A}(010)^2\Delta_{5/2} \rightarrow \tilde{X}(02^20)^2\Delta$ dispersed fluorescence spectrum following excitation of the $Q_{21}(18½)$ line of the $\tilde{A}(010)^2\Delta_{5/2} \leftarrow \tilde{X}(000)^2\Sigma^+$ sub-band of SrOH.

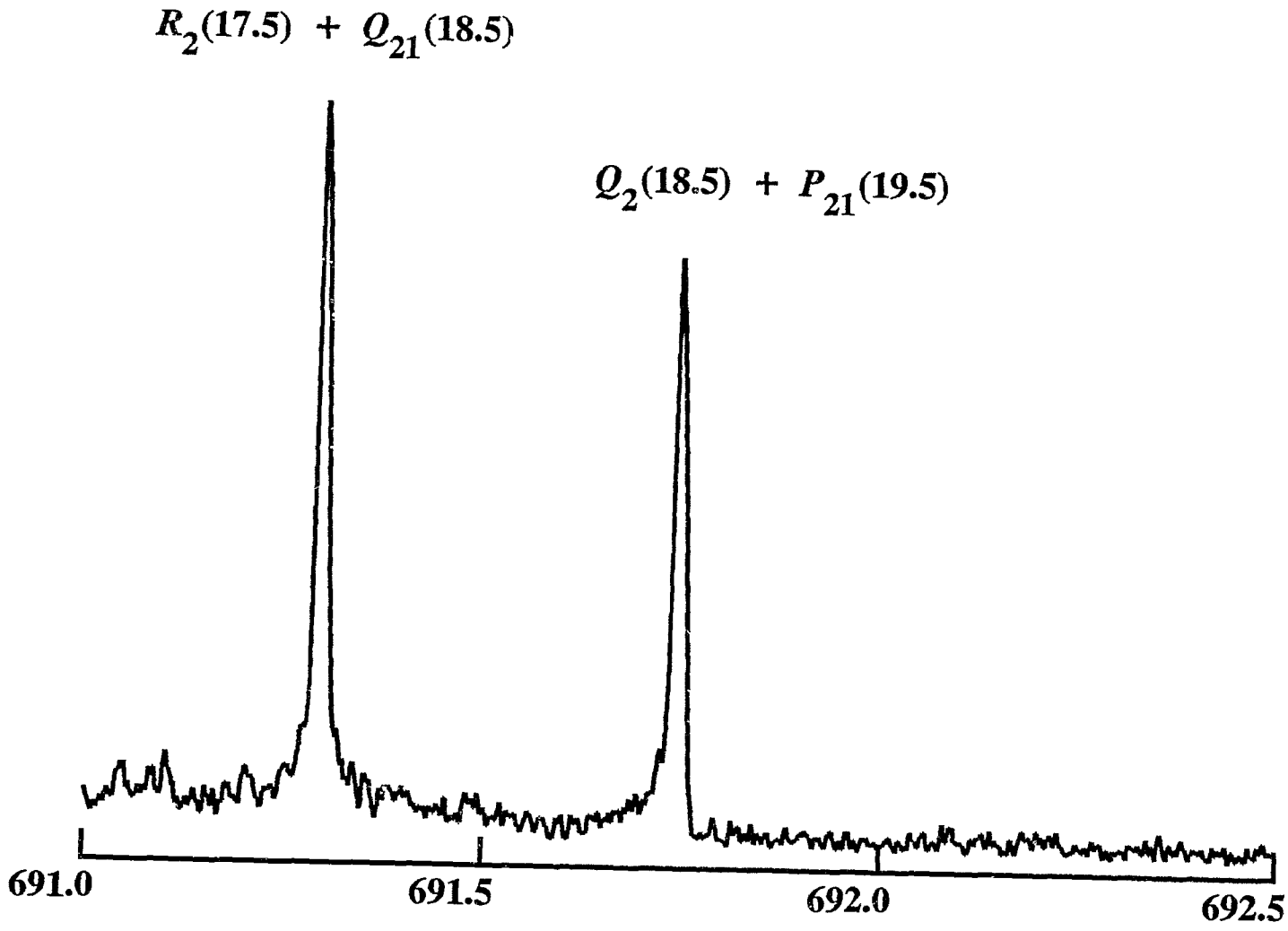
$R_2(17.5) + Q_{21}(18.5)$
$Q_2(18.5) + P_{21}(19.5)$
691.0
691.5
692.0
692.5
Wavelength (nm)

Figure 7.9

Figure 7.10: $\tilde{A}(010)^2\Delta_{5/2} \rightarrow \tilde{X}(03^30)^2\Phi$ dispersed fluorescence spectrum following excitation of the $Q_{21}(18½)$ line of the $\tilde{A}(010)^2\Delta_{5/2} \leftarrow \tilde{X}(000)^2\Sigma^+$ sub-band of SrOH.

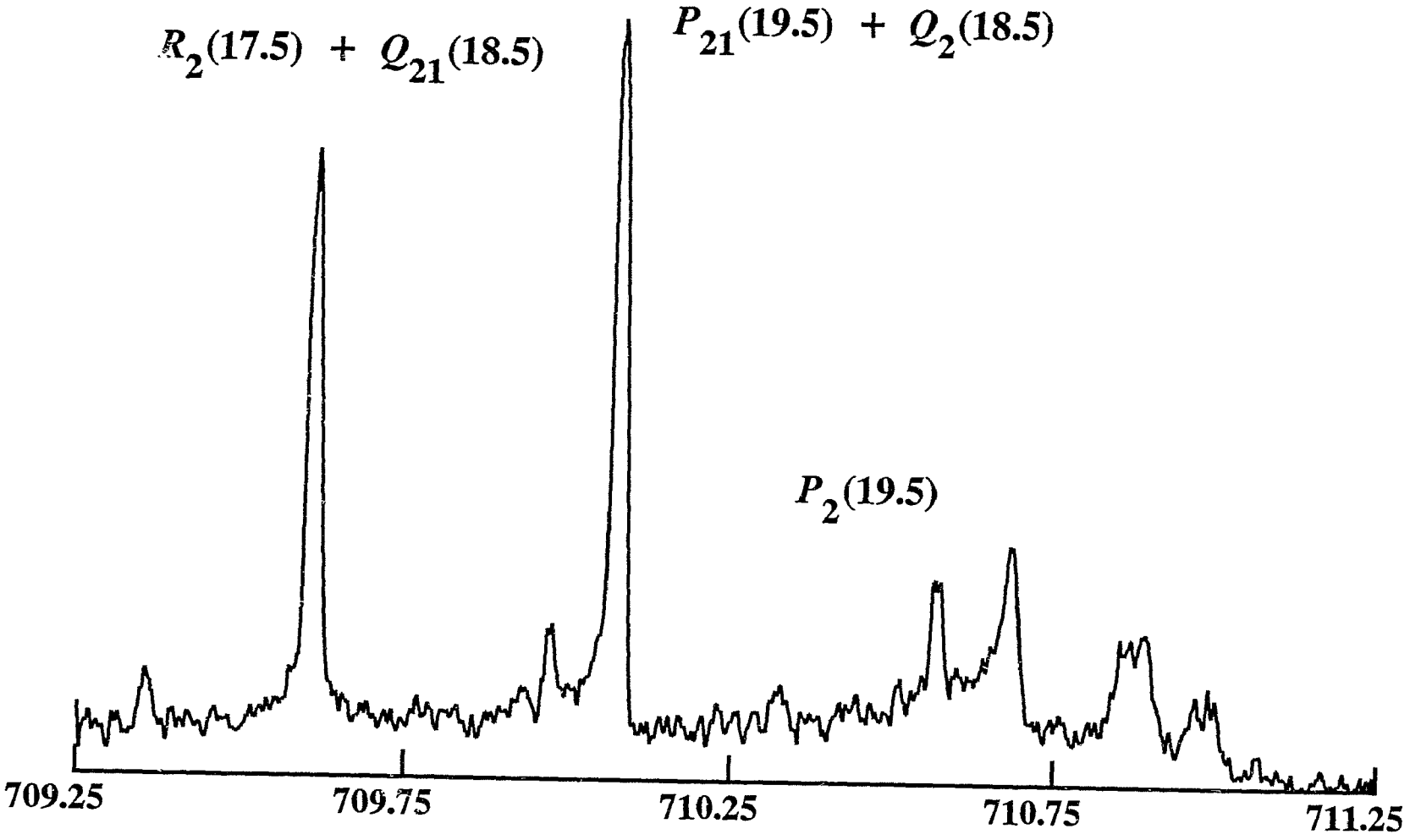
$R_2(17.5) + Q_{21}(18.5)$
$P_{21}(19.5) + Q_2(18.5)$
$P_2(19.5)$
709.25
709.75
710.25
710.75
711.25
Wavelength (nm)

Figure 7.10

$\tilde{A}(010)^2\Delta_{5/2} \rightarrow \tilde{X}(020)^2\Delta$ band, the P_2 branch is anomalously weak, but in most cases was observed.

As indicated previously, the dispersed fluorescence data involving the $\tilde{A}(010)$ RT components was eventually combined with the excitation data in a single least-squares fit. In accord with their estimated uncertainties, 0.0035 and 0.030 cm^{-1} for the excitation and dispersed fluorescence measurements, respectively, the two types of data were given relative weights by an amount equal to the inverse square of the estimated uncertainty. Since the excitation data were obviously given a much greater weight in the fitting, the $\tilde{X}(010)^2\Pi$ constants, with the exception of the vibrational term energy, were determined primarily from the hotband excitation data. In the case of the $\tilde{X}(020)^2\Delta$ and $\tilde{X}(030)^2\Phi$ components, the constants D_v and γ_v were fixed to the values obtained for the $\tilde{X}(010)^2\Pi$ level and only the vibrational term energy and rotational constants B_v were included as adjustable parameters: the effective ℓ-type doubling constants were fixed to zero in these fits.

7.5 Deperturbation Model and Results

The phenomenon of K-type resonance results from an interplay of Λ-type and ℓ-type doubling matrix elements. The Λ-doubling contributions are caused by interactions of the $\tilde{A}^2\Pi$ state with other Σ electronic states through the rotational and spin-orbit operators and can be expressed in terms of an effective operator that acts within the $v_2 = 1$ manifold[132];

$$H_\Lambda = \tfrac{1}{2}(p_v^e + 2q_v^e)(\Lambda_+^2 J_+ S_- + \Lambda_-^2 J_- S_+) + \tfrac{1}{2} q^e(\Lambda_+^2 J_+^2 + \Lambda_-^2 J_-^2) , \qquad (7.1)$$

where, using the phase choice of Brown *et al.*[132], the ladder operator $\Lambda_\pm^2$ has non-zero matrix elements according to;

$$\Lambda_\pm^2 |n\Lambda = \mp 1\rangle = -|n\Lambda = \pm 1\rangle . \qquad (7.2)$$

The electronic perturbation parameters p_v^e and q_v^e have their usual meanings as discussed in chapter 4. In the $v_2 = 1$ level of the $\tilde{A}^2\Pi$ state, this gives rise to off-diagonal terms between the Σ and Δ vibronic components. As with Σ electronic states, interactions of the $v_2 = 1$ level with other vibrational levels within the $^2\Pi$ electronic state can also occur via H_{ROT}, resulting in ℓ-type doubling. This can be treated in an analogous manner, where the effective operator H_l, given in eq. 4.35, results in matrix elements with $\Delta\ell = 2$ within the $v_2 = 1$ manifold according to eqs. 4.36 and 4.37.

A detailed matrix model describing *K*-type resonance and capable of simultaneously fitting all four RT components of the $v_2 = 1$ level of linear triatomic molecules in $^2\Pi$ electronic states was first developed by Bolman *et al.*[87] This treatment was later modified by Adam, Merer and Stuenenberg[127] in view of the higher precision of their data. More recently, the BO_2 model has been adapted to CaOH[31] in which a *K*-type resonance between the $\mu^2\Sigma$ and $^2\Delta_{3/2}$ components leads to difficulties in fitting the $^2\Sigma$ states to the energy level expressions given by Hougen[75].

A particularly interesting aspect of the matrix model developed by the Merer group was the inclusion of a spin-rotation interaction term on the diagonal elements of the Σ states. These authors suggested that the spin-rotation interaction may arise from a consideration of the effective form of the spin-rotation Hamiltonian where,[133]

$$H_{SR} = \gamma(\, N \cdot S) \,. \tag{7.3}$$

The γ used here is not to be confused with the effective spin-rotation constant p used by Hougen[75], rather, Adam *et al.*[127] have argued that this term represents the true spin-rotation interaction. The determination of the spin-rotation interaction in a $^2\Pi$ state is of considerable interest since it is almost always completely correlated with the centrifugal distortion

correction to the spin-orbit splitting A_D and is thus rarely evaluated.

The four symmetrized basis functions corresponding to the vibronic components of the $v_2 = 1$ vibrational level of the $\tilde{A}^2\Pi$ electronic state are obtained by taking the Wang sum and difference combinations of the appropriate case (a) basis functions[127];

$$|J, P,\pm\rangle = 2^{-1/2} \{|\Lambda,v_2,\ell, \Sigma; J, P\rangle \pm |-\Lambda,v_2,-\ell,-\Sigma; J,-P\rangle\}. \qquad (7.4)$$

As with CaOH, the spin-orbit coupling constant in SrOH is of opposite sign to that of BO_2; this has the effect of interchanging the $\mu^2\Sigma^{(+)}$ and $\kappa^2\Sigma^{(-)}$ basis functions of SrOH and CaOH relative to BO_2. The matrix model used in the current deperturbation analysis is given explicitly in table 7.6. The model allows for different values of B and D for the $\mu^2\Sigma^{(+)}$, $\kappa^2\Sigma^{(-)}$ and $^2\Delta$ vibronic components, as well as separate values of γ and γ_D for the two $^2\Sigma$ sub-states. The centrifugal distortion correction to the RT parameter used in ref. 31 was not included in the least-squares fits since it was found to be highly correlated to the spin-rotation terms. Centrifugal distortion corrections to the spin-orbit coupling constants of both the Σ and Δ states, denoted as A_D^Σ and A_D^Δ, are included and differ by factors of $(1 - \frac{3}{4}\epsilon^2)$ and $(1 - \frac{1}{4}\epsilon^2)$ respectively. The difference of the mean of the Σ states relative to that of the Δ state is defined in terms of the ΔT^Δ parameter of ref. 127.

All line positions and residuals from the IMF, Doppler-limited laser excitation and dispersed fluorescence data involving the $\tilde{A}(010)$ RT components are given in tables 7.7 to 7.15. No evidence of systematic residuals was indicated, and, in all, over 1200 line positions were included in this fit. As is usually the case, the parameters ϵ and $\epsilon\omega_2$ could not both be fitted simultaneously; accordingly, ϵ was held fixed since the values of the molecular parameters and quality of the fit were relatively insensitive to small changes in ϵ. The estimated value of ϵ used in the final fit was

Table 7.6: Matrix Elements for a $^2\Pi(010)$ State

$\|^2\Delta_{5/2},\pm\rangle$	$\|^2\Delta_{3/2},\pm\rangle$	$\|\kappa^2\Sigma,\pm\rangle$	$\|\mu^2\Sigma,\pm\rangle$
$T^\Sigma - \Delta T^\Delta + B^\Delta(z-6)$ $-D^\Delta(z^2-11z+32)$ $+ \frac{1}{2}[A^\Delta + A_D^\Delta(z-6)]$	$-B^\Delta(z-4)^{1/2}$ $+2D^\Delta(z-4)^{3/2}$	$\frac{1}{2}q^v(z^2-5z+4)^{1/2}$	$\pm\frac{1}{2}q^e(z^2-5z+4)^{1/2}$
	$T^\Sigma - \Delta T^\Delta + B^\Delta(z-2)$ $- D^\Delta z(z-3)$ $- \frac{1}{2}[A^\Delta + A_D^\Delta(z-2)]$	$(z-1)^{1/2}[\pm\frac{1}{2}(q^e z^{1/2} - q^v)]$	$(z-1)^{1/2} \times$ $[\mp\frac{1}{2}(p^e+2q^e) + \frac{1}{2}q^v z^{1/2}]$
		$T^\Sigma + \frac{1}{2}[A^\Sigma + A_D^\Sigma z] \mp \frac{1}{2}\gamma^{\Sigma(-)}z^{1/2}$ $+ B^{\Sigma(-)}z - D^{\Sigma(-)}z(z+1)$ $\mp \frac{1}{2}\gamma_D^{\Sigma(-)}z^{1/2}(z+1\pm 2z^{1/2})$	$-\frac{1}{2}(B^{\Sigma(-)} + B^{\Sigma(+)})z^{1/2}$ $+ (D^{\Sigma(-)} + D^{\Sigma(+)})z^{3/2}$ $\pm\epsilon\omega_2$
			$T^\Sigma - \frac{1}{2}[A^\Sigma + A_D^\Sigma z] \pm \frac{1}{2}\gamma^{\Sigma(+)}z^{1/2}$ $+B^{\Sigma(+)}z - D^{\Sigma(+)}z(z+1)$ $\pm \frac{1}{2}\gamma_D^{\Sigma(+)}z^{1/2}(z+1\mp 2z^{1/2})$

The basis functions $|K,P,\pm\rangle$ are defined by the combinations of case (a) functions, $|K,P,\pm\rangle = 2^{-1/2}\{|\Lambda,v_2,\ell,\Sigma;J,P\rangle \pm |-\Lambda,v_2,-\ell,-\Sigma;J,-P\rangle\}$ with $K = |\Lambda + \ell|$ and $P = |\Lambda + \ell + \Sigma|$. The upper and lower signs refer to the e and f levels, respectively, and $z = (J + \frac{1}{2})^2$. The spin-orbit parameters are defined by $A^\Delta = A(1 - \frac{3}{4}\epsilon^2)$, $A^\Sigma = A(1 - \frac{1}{4}\epsilon^2)$, $A_D^\Delta = A_D(1 - \frac{3}{4}\epsilon^2)$, and $A_D^\Sigma = A_D(1 - \frac{1}{4}\epsilon^2)$.

TABLE 7.7: Line positions[a] (cm^{-1}) for the $\tilde{A}^2\Pi$-$\tilde{X}^2\Sigma^+$ $(010)\kappa^2\Sigma^{(-)}$-$(000)^2\Sigma^+$ sub-band of SrOH. The table shows $\bar{\nu}_{obs}$, the measured wavenumbers (cm^{-1}), and the residuals, $\bar{\nu}_{obs} - \bar{\nu}_{calc}$.

J	$^{o}P_{12}$		$^{Q}R_{12}$		$^{Q}P_{21}$		$^{S}R_{21}$	
2½	15188.805	0.004	15191.754	-0.001				
3½	15188.034	0.002	15192.005	0.006			15194.411	-0.003
4½	15187.275	0.003	15192.253	0.002			15195.238	-0.011[b]
5½	15186.526	0.007	15192.505	-0.006			15196.090	-0.001
6½	15185.779	0.004	15192.774	-0.007	15189.766	0.002	15196.939	-0.003
7½	15185.040	0.001	15193.062	0.005	15189.618	0.008	15197.795	-0.005
8½	15184.314	0.003	15193.337	-0.006	15189.469	0.005	15198.664	-0.003
9½	15183.598	0.007	15193.634	-0.002	15189.331	0.004	15199.542	-0.001
10½	15182.885	0.005	15193.937	-0.001	15189.201	0.004	15200.423	-0.003
11½	15182.182	0.004	15194.246	-0.001	15189.077	0.002	15201.309	-0.008
12½	15181.486	0.002	15194.562	-0.003	15188.965	0.002	15202.211	-0.005
13½	15180.799	0.002	15194.888	-0.002	15188.858	-0.001	15203.127	0.003
14½	15180.120	0.001	15195.238	0.012[b]	15188.761	-0.001	15204.041	0.002
15½	15179.449	-0.001	15195.565	-0.003	15188.672	-0.001	15204.955	-0.007
16½	15178.792	0.004	15195.921	0.003	15188.589	-0.004	15205.892	-0.002
17½	15178.134	-0.001	15196.277	0.000	15188.513	-0.008	15206.833	-0.001
18½	15177.490	-0.001	15196.645	0.001	15188.450	-0.008	15207.781	-0.001
19½	15176.857	0.002	15197.016	-0.003			15208.735	-0.002
20½	15176.230	0.003	15197.404	0.001			15209.702	0.001
21½	15175.609	0.001	15197.795	0.001			15210.674	0.001
22½	15174.999	0.002	15198.190	-0.004			15211.651	-0.001
23½	15174.396	0.002	15198.600	-0.002			15212.640	0.000
24½	15173.799	-0.002	15199.019	0.000				
25½	15173.213	-0.002	15199.445	0.002			15214.619	-0.020[b]
26½	15172.638	0.000	15199.874	-0.002			15215.652	0.001
27½	15172.067	-0.002	15200.314	-0.002			15216.673	0.003
28½	15171.509	-0.001	15200.763	-0.002			15217.698	0.001
29½	15170.956	-0.002	15201.222	-0.001			15218.733	0.000
30½	15170.416	0.001	15201.684	-0.005			15219.781	0.005
31½	15169.884	0.004	15202.160	-0.002			15220.822	-0.005
32½	15169.354	-0.001	15202.644	0.000			15221.879	-0.007
33½	15168.840	0.003	15203.127	-0.007	15188.486	-0.002	15222.958	0.004
34½	15168.327	-0.001	15203.634	0.001	15188.559	0.002	15224.032	0.004
35½	15167.828	0.000	15204.138	-0.001	15188.635	0.002	15225.114	0.003
36½	15167.337	0.000	15204.654	0.000	15188.714	-0.003	15226.206	0.005
37½	15166.855	0.001	15205.176	-0.001	15188.804	-0.006	15227.306	0.006
38½	15166.377	-0.002	15205.716	0.008	15188.904	-0.007	15228.408	0.002
39½	15165.912	-0.002	15206.252	0.003	15189.030	0.010[b]	15229.526	0.006
40½	15165.457	0.001	15206.793	-0.003	15189.140	0.003	15230.645	0.003
41½	15165.010	0.001			15189.266	0.003	15231.773	0.002
42½	15164.570	0.001			15189.397	0.001	15232.912	0.003
43½	15164.139	0.001					15234.057	0.003
44½	15163.714	-0.002			15189.684	-0.005	15235.207	0.000
45½	15163.307	0.005					15236.368	0.000
46½	15162.898	0.000			15190.013	-0.001	15237.539	0.003
47½	15162.501	-0.002					15238.711	-0.002
48½	15162.118	0.002					15239.898	0.001

TABLE 7.7 (continued)

J	${}^{o}P_{12}$		${}^{Q}R_{12}$	${}^{Q}P_{21}$	${}^{s}R_{21}$	
49½	15161.735	-0.003			15241.090	0.001
50½	15161.367	-0.002			15242.284	-0.004
51½	15161.010	0.001			15243.496	0.000
52½	15160.657	-0.001			15244.710	0.000
53½	15160.317	0.001			15245.931	-0.002
54½	15159.983	0.000			15247.161	-0.002
55½	15159.658	0.000			15248.398	-0.003
56½	15159.343	0.000				
57½	15159.039	0.002				

[a]Unless indicated otherwise, line positions have an assigned uncertainty of 0.0035 cm^{-1}.
[b]Blended line with assigned uncertainty of 0.015 cm^{-1}.

TABLE 7.8: Line Positions[a] (cm^{-1}) for the $\tilde{A}^2\Pi$ - $\tilde{X}^2\Sigma^+$ $(010)\mu^2\Sigma^{(+)}$-$(000)^2\Sigma^+$ sub-band of SrOH. The table shows $\bar{\nu}_{obs}$, the measured wavenumbers (cm^{-1}), and the residuals, $\bar{\nu}_{obs}$ - $\bar{\nu}_{calc}$.

J	P_1		R_1		P_2		R_2		$^RQ_{21}$	
1							14921.434	-0.003		
2½			14922.858	0.000			14921.741	-0.003		
3½			14923.577	0.002	14917.951	0.000	14922.047	-0.007		
4½	14919.369	0.003	14924.296	0.000	14917.264	0.003	14922.364	-0.002		
5½	14919.080	-0.007	14925.032	0.010[b]	14916.582	0.008	14922.680	0.000		
6½	14918.811	-0.001	14925.751	-0.004	14915.893	0.003	14922.993	-0.003		
7½	14918.544	0.003	14926.491	0.000	14915.218	0.011[b]	14923.311	-0.003		
8½	14918.279	0.002	14927.234	-0.001	14914.523	-0.004	14923.635	0.000		
9½	14918.018	0.001	14927.982	-0.002	14913.846	-0.003	14923.962	0.004		
10½	14917.765	0.002	14928.733	-0.005	14913.168	-0.005	14924.286	0.001	14923.921	-0.012
11½	14917.513	-0.004	14929.504	0.005	14912.496	-0.005	14924.616	0.002	14924.258	0.002
12½	14917.273	-0.002	14930.267	0.000	14911.830	-0.001	14924.951	0.006	14924.588	0.004
13½	14917.039	-0.001	14931.045	0.004	14911.164	0.001	14925.283	0.002	14924.914	0.001
14½	14916.812	0.000	14931.823	0.002	14910.487	-0.013[b]	14925.624	0.003	14925.246	0.000
15½	14916.582	-0.007	14932.604	-0.004	14909.839	-0.001	14925.970	0.006	14925.585	0.002
16½	14916.375	0.000	14933.408	0.006	14909.182	-0.002	14926.316	0.004	14925.926	0.002
17½	14916.170	0.004	14934.201	-0.001	14908.529	-0.003	14926.663	-0.001	14926.271	0.001
18½	14915.963	-0.001	14935.009	0.000	14907.883	-0.001	14927.021	-0.001	14926.619	-0.001
19½	14915.771	0.001	14935.820	-0.003	14907.242	0.000	14927.385	0.001	14926.977	0.003
20½	14915.584	0.002	14936.640	-0.005	14906.606	0.002	14927.748	-0.002	14927.335	0.002
21½	14915.401	0.000	14937.471	-0.002	14905.968	-0.004	14928.120	-0.002	14927.696	-0.002
22½	14915.218	-0.010[b]	14938.302	-0.006	14905.345	0.001	14928.505	0.005	14928.069	0.001
23½	14915.063	0.002	14939.153	0.003	14904.726	0.003	14928.877	-0.006	14928.442	-0.001
24½	14914.905	0.002	14940.005	0.005	14904.110	0.004	14929.273	0.001	14928.822	-0.001
25½	14914.754	0.002	14940.863	0.007	14903.489	-0.007	14929.666	0.000	14929.210	0.000
26½	14914.603	-0.005	14941.718	-0.002			14930.064	-0.002	14929.601	-0.001
27½	14914.471	0.000					14930.474	0.001	14930.001	0.001
28½	14914.343	0.001	14943.475	0.006			14930.884	-0.001	14930.401	-0.003
29½	14914.212	-0.008	14944.354	0.000			14931.305	0.002	14930.817	0.004
30½	14914.105	0.000	14945.247	0.001			14931.724	-0.004	14931.226	-0.004
31½			14946.138	-0.007			14932.161	0.003	14931.652	0.000
32½	14913.897	-0.002	14947.047	-0.006			14932.593	-0.002	14932.076	-0.004
33½	14913.815	0.007	14947.971	0.004					14932.514	0.000
34½	14913.729	0.006	14948.893	0.005			14933.489	0.002	14932.952	-0.002
35½	14913.649	0.002	14949.818	0.001			14933.939	-0.004	14933.403	0.002
36½	14913.568	-0.009	14950.750	-0.003			14934.405	0.000	14933.854	-0.001
37½			14951.697	0.001			14934.879	0.006	14934.310	-0.004
38½			14952.647	0.001			14935.349	0.000	14934.783	0.003
39½			14953.602	-0.002			14935.828	-0.002	14935.258	0.005
40½			14954.570	0.001			14936.318	0.000	14935.731	0.000
41½			14955.541	0.000			14936.812	0.000	14936.214	-0.002
42½			14956.521	0.001			14937.315	0.003	14936.704	-0.004
43½			14957.506	-0.001			14937.819	0.000	14937.209	0.002
44½			14958.503	0.002			14938.335	0.002	14937.711	0.000
45½			14959.506	0.004			14938.854	0.001	14938.227	0.004
46½			14960.511	0.000			14939.386	0.006		
47½			14961.528	0.001			14939.912	-0.001	14939.261	-0.003
48½			14962.551	0.002			14940.453	0.000		

TABLE 7.8 (continued)

J	P_1	R_1	P_2	R_2	$^RQ_{21}$
49½		14963.578 -0.002		14940.998 -0.001	
50½		14964.612 -0.005		14941.553 0.001	
51½				14942.109 -0.002	
52½				14942.681 0.004	
53½				14943.251 0.001	
54½				14943.832 0.002	
55½				14944.416 0.000	
56½				14945.011 0.004	
57½				14945.606 -0.001	
58½				14946.209 -0.003	
59½				14946.823 -0.00₄	
60½				14947.442 -0.001	
61½				14948.090 0.022[b]	
62½				14948.698 -0.002	
63½				14949.334 -0.004	
64½				14949.984 0.001	
65½				14950.635 0.001	
66½				14951.294 0.002	
67½				14951.960 0.003	
68½				14952.631 0.003	
69½				14953.302 -0.004	

[a]Unless indicated otherwise, line positions have an assigned uncertainty of 0.0035 cm^{-1}.

[b]Blended line with assigned uncertainty of 0.015 cm^{-1}.

TABLE 7.9: Line Positions[a] (cm^{-1}) for the $\tilde{A}^2\Pi$ - $\tilde{X}^2\Sigma^+$ $(010)^2\Delta_{3/2}$ - $(000)^2\Sigma^+$ sub-band of SrOH. The table shows $\bar{\nu}_{obs}$, the measured wavenumbers (cm^{-1}), and the residuals, $\bar{\nu}_{obs} - \bar{\nu}_{calc}$.

J	P_1		R_1		Q_1	
1½					14923.522	0.001
2½	14922.531	0.008			14923.801	0.002
3½	14922.314	0.014[b]	14926.372	0.000	14924.094	0.006
4½	14922.096	0.009[b]	14927.181	0.004	14924.393	0.004
5½	14921.888	0.003	14927.989	-0.001	14924.694	-0.009[b]
6½	14921.690	-0.002	14928.813	0.001	14925.029	-0.001[b]
7½	14921.509	0.001	14929.658	0.014[b]	14925.374	0.005[b]
8½	14921.331	-0.004	14930.477	-0.007	14925.723	0.003
9½	14921.168	-0.002	14931.352	0.019[b]	14926.087	0.003
10½	14921.010	-0.004	14932.190	0.000	14926.464	0.005
11½	14920.866	0.000	14933.048	-0.008	14926.850	0.004
12½	14920.730	0.003	14933.939	0.009	14927.242	-0.002
13½	14920.597	0.000	14934.816	0.005	14927.655	0.000
14½	14920.472	-0.003	14935.699	-0.001		
15½	14920.361	0.000	14936.601	0.003		
16½	14920.253	-0.002	14937.504	0.001	14928.943	-0.006
17½	14920.153	-0.003	14938.416	0.001	14929.400	-0.002
18½	14920.065	-0.001	14939.336	0.001	14929.862	-0.001
19½	14919.980	-0.002	14940.264	0.002	14930.336	0.000
20½	14919.904	-0.003	14941.198	0.001		
21½	14919.836	-0.004	14942.139	0.001		
22½	14919.778	-0.002	14943.090	0.003	14931.823	0.015[b]
23½	14919.725	-0.003	14944.047	0.003	14932.316	0.000
24½	14919.678	-0.004	14945.010	0.004	14932.839	0.005
25½			14945.978	0.001	14933.359	-0.001
26½	14919.610	-0.004	14946.957	0.003	14933.894	-0.001
27½	14919.587	-0.005	14947.942	0.004		
28½	14919.570	-0.006	14948.933	0.003	14934.997	0.005
29½	14919.563	-0.005	14949.931	0.003	14935.555	0.003
30½			14950.939	0.006	14936.119	-0.001
31½	14919.570	-0.003	14951.953	0.008	14936.704	0.006
32½	14919.582	-0.005	14952.967	0.003	14937.287	0.004
33½	14919.603	-0.004	14953.995	0.005	14937.870	-0.006
34½			14955.024	0.001	14938.482	0.005
35½	14919.665	-0.004	14956.066	0.005		
36½	14919.709	-0.002	14957.111	0.003		
37½	14919.759	-0.002	14958.164	0.003		
38½	14919.816	-0.001	14959.223	0.003		
39½	14919.883	0.002				
40½	14919.949	-0.002				
41½	14920.029	0.000				
42½	14920.115	0.001				
43½	14920.203	-0.002				
44½	14920.307	0.003				

TABLE 7.9 (continued)

J	Q_{12}		P_{12}		R_{12}	
½					14923.522	-0 003
1½	14922.531	0.002			14923.801	-0.004
2½	14922.314	0.005[b]			14924.094	-0.003
3½	14922.096	-0.002[b]			14924.393	-0.007
4½	14921.902	0.003			14924.694	-0.023[b]
5½	14921.706	-0.001			14925.029	-0.017[b]
6½	14921.527	0.000	14918.241	0.001	14925.374	-0.013[b]
7½	14921.352	-0.003	14917.571	-0.002	14925.755	0.014[b]
8½	14921.192	-0.001	14916.915	-0.003	14926.124	0.017[b]
9½	14921.035	-0.004	14916.274	-0.001	14926.494	0.009
10½	14920.894	-0.001	14915.637	-0.008	14926.880	0.006
11½	14920.763	0.005	14915.027	0.000	14927.278	0.003
12½	14920.630	0.000	14914.420	0.000		
13½	14920.509	-0.001	14913.846	0.021[b]		
14½	14920.400	0.002	14913.238	-0.003	14928.548	0.003
15½	14920.293	-0.001	14912.672	0.002	14928.985	-0.004
16½	14920.196	-0.002	14912.112	0.004	14929.447	0.003
17½	14920.111	0.001	14911.554	-0.003	14929.905	-0.004
18½	14920.029	-0.002	14911.018	0.002		
19½	14919.954	-0.004	14910.487	0.000		
20½	14919.889	-0.003	14909.965	-0.001		
21½	14919.834	-0.001	14909.456	0.000		
22½	14919.782	-0.002	14908.957	0.003		
23½	14919.739	-0.003	14908.463	0.000		
24½	14919.704	-0.003	14907.981	0.001		
25½	14919.675	-0.004	14907.495	-0.012[b]		
26½			14907.041	-0.001		
27½			14906.589	0.002		
28½			14906.138	-0.002		
29½						
30½			14905.278	0.005		
31½	14919.665	0.000	14904.854	0.001		
32½	14919.685	-0.003	14904.440	-0.001		
33½	14919.715	-0.003	14904.035	-0.001		
34½	14919.753	-0.002	14903.640	-0.001		
35½	14919.799	-0.001	14903.252	-0.003		
36½	14919.848	-0.004	14902.873	-0.003		
37½	14919.907	-0.003	14902.504	-0.002		
38½	14919.975	-0.002	14902.147	0.003		
39½	14920.049	-0.001	14901.789	-0.001		
40½	14920.132	0.003	14901.445	0.000		
41½	14920.215	-0.002	14901.112	0.004		
42½	14920.311	-0.001	14900.778	-0.001		
43½	14920.416	0.003	14900.461	0.003		
44½	14920.522	0.001	14900.148	0.003		
45½	14920.637	0.001	14899.839	-0.001		
46½	14920.768	0.009	14899.540	-0.004		
47½	14920.891	0.002	14899.257	0.001		

TABLE 7.9 (continued)

J	Q_{12}		P_{12}		R_{12}
48½	14921.022	-0.004	14898.978	0.002	
49½	14921.175	0.006	14898.702	-0.002	
50½	14921.317	-0.003	14898.440	0.000	
51½	14921.476	-0.001	14898.182	-0.002	
52½	14921.640	-0.002	14897.934	-0.002	
53½	14921.815	0.000	14897.695	-0.001	
54½	14921.993	-0.001	14897.461	-0.003	
55½	14922.182	0.003	14897.237	-0.004	
56½	14922.368	-0.004	14897.027	0.003	
57½	14922.574	0.002	14896.813	-0.004	
58½	14922.776	-0.003	14896.614	-0.003	
59½	14922.993	0.000	14896.426	0.000	
60½			14896.248	0.006	
61½			14896.065	-0.001	
62½			14895.896	-0.003	
63½			14895.735	-0.005	
64½			14895.588	0.000	
65½			14895.444	-0.001	
66½			14895.308	-0.001	
67½			14895.180	-0.001	
68½			14895.060	-0.002	
69½			14894.958	0.007	
70½			14894.847	0.001	
71½			14894.754	0.002	

[a]Unless indicated otherwise, line positions have an assigned uncertainty of 0.0035 cm^{-1}.

[b]Blended line with assigned uncertainty of 0.015 cm^{-1}.

TABLE 7.10: Line Positions[a] (cm^{-1}) for the $\tilde{A}^2\Pi$ - $\tilde{X}^2\Sigma^+$ $(010)^2\Delta_{5/2}$ - $(010)^2\Pi$ sub-band of SrOH. The table shows $\bar{\nu}_{obs}$, the measured wavenumbers, and residuals, $\bar{\nu}_{obs} - \bar{\nu}_{calc}$.

J	Q_{21ef}		Q_{21fe}		P_{21ee}		P_{21f}	
2½	14821.773	0.002	14821.773	0.000				
3½	14822.051	0.000	14822.051	-0.005	14820.284	0.002	14820.284	0.007
4½	14822.348	0.009[b]	14822.348	0.001[b]	14820.079	0.011[b]	14820.079	0.019[b]
5½	14822.649	0.012[b]	14822.649	0.000[b]	14819.852	-0.010[b]	14819.852	0.002[b]
6½	14822.957	0.013[b]	14822.957	-0.004[b]	14819.657	-0.011[b]	14819.657	0.006[b]
7½	14823.264	0.004[b]	14823.263	-0.019[b]	14819.484	0.001	14819.456	-0.005
8½	14823.586	0.001[b]	14823.602	-0.011[b]	14819.298	-0.009	14819.274	-0.005
9½	14823.923	0.004[b]	14823.946	-0.009[b]			14819.114	0.007
10½	14824.260	-0.002[b]	14824.294	-0.012[b]	14819.008	0.020[b]	14818.962	0.018[b]
11½	14824.599	-0.016[b]	14824.658	-0.009[b]	14818.822	-0.020[b]	14818.788	-0.003
12½	14824.979	0.002	14825.038	-0.001	14818.691	-0.016[b]	14818.653	0.007[b]
13½	14825.344	-0.004	14825.417	-0.002	14818.566	-0.016[b]	14818.513	0.003
14½	14825.729	0.002	14825.805	-0.005	14818.455	-0.012[b]	14818.395	0.011[b]
15½	14826.117	0.001	14826.213	0.002			14818.262	-0.005
16½	14826.520	0.006	14826.623	0.002	14818.262	-0.004	14818.167	0.009[b]
17½	14826.928	0.007	14827.039	-0.002	14818.167	-0.013[b]		
18½	14827.338	0.001	14827.472	0.000	14818.095	-0.010[b]		
19½	14827.756	-0.006	14827.911	-0.001				
20½	14828.199	0.002	14828.362	0.000			14817.808	-0.011[b]
21½	14828.645	0.005	14828.823	0.002			14817.756	0.000
22½	14829.096	0.003	14829.293	0.002			14817.707	0.004
23½	14829.555	0.001	14829.771	0.000			14817.660	0.001
24½	14830.025	0.001	14830.266	0.006			14817.630	0.006
25½	14830.506	0.002	14830.764	0.005				
26½	14830.994	0.002	14831.272	0.004			14817.585	0.003
27½	14831.487	-0.003	14831.792	0.005				
28½	14831.993	-0.003	14832.318	0.003				
29½			14832.867	0.013[b]			14817.585	-0.002
30½	14833.032	-0.005	14833.408	0.006				
31½	14833.571	0.000	14833.962	0.003			14817.630	-0.007
32½	14834.110	-0.003	14834.524	-0.002	14818.095	0.000	14817.660	-0.015[b]
33½	14834.662	-0.003	14835.100	-0.003	14818.167	-0.001	14817.707	-0.016[b]
34½	14835.220	-0.005	14835.696	0.006				
35½	14835.798	0.003	14836.289	0.002	14818.338	-0.008		
36½	14836.376	0.003	14836.894	0.001	14818.455	0.005		
37½	14836.961	-0.001	14837.505	-0.004	14818.566	0.002		
38½	14837.556	-0.002	14838.135	0.000	14818.691	0.004	14818.095	-0.002
39½	14838.165	0.001	14838.771	0.001	14818.822	0.001	14818.191	-0.008
40½	14838.771	-0.006	14839.413	-0.002	14818.962	-0.003		
41½	14839.413	0.012[b]	14840.072	0.002				
42½	14840.038	0.004	14840.733	0.000				
43½	14840.677	0.002	14841.401	-0.006				
44½	14841.319	-0.006	14842.090	0.000				
45½	14841.990	0.005	14842.771	-0.012[b]				
46½	14842.653	0.001	14843.493	0.008				
47½	14843.326	-0.003	14844.188	-0.009[b]				
48½			14844.914	-0.004				
49½			14845.650	0.001				
50½			14846.384	-0.005				
51½								
52½			14847.898	0.000				

TABLE 7.10 (continued)

J	R_{2ee}		R_{2ff}		P_{2ee}		P_{2ff}	
1½	14821.773	-0.003	14821.773	-0.006				
2½	14822.050	-0.009[b]	14822.050	-0.013[b]				
3½	14822.348	-0.002[b]	14822.348	-0.010[b]				
4½	14822.649	-0.001[b]	14822.649	-0.013[b]				
5½	14822.957	-0.003[b]	14822.957	-0.019[b]				
6½	14823.264	-0.014[b]	14823.297	-0.003	14816.203	0.017[b]	14816.203	-0.005[b]
7½	14823.610	0.005	14823.639	0.005	14815.502	0.001	14815.530	0.001
8½	14823.946	0.004	14823.976	-0.002				
9½	14824.294	0.006	14824.329	-0.002	14814.160	0.003	14814.202	0.001
10½	14824.644	0.001	14824.691	-0.004	14813.507	0.007	14813.550	-0.002
11½	14825.011	0.004	14825.067	-0.002	14812.854	0.003	14812.917	0.004
12½	14825.378	-0.002	14825.450	-0.002	14812.210	-0.002	14812.282	-0.002
13½	14825.766	0.004	14825.846	0.001	14811.588	0.006	14811.663	-0.001
14½	14826.156	0.003	14826.249	0.000	14810.970	0.010	14811.061	0.006
15½	14826.558	0.004	14826.665	0.004	14810.349	0.000	14810.458	0.002
16½	14826.967	0.003	14827.083	-0.001	14809.748	0.001	14809.868	0.001
17½	14827.380	-0.002	14827.518	0.001	14809.155	0.001	14809.296	0.007
18½	14827.806	-0.004	14827.962	0.002	14808.571	0.001	14808.718	-0.001
19½	14828.244	-0.002	14828.411	-0.001	14807.998	0.002	14808.163	0.003
20½	14828.688	-0.005	14828.871	-0.003	14807.428	-0.002	14807.609	-0.003
21½	14829.147	0.000	14829.346	0.000	14806.871	-0.003	14807.074	0.000
22½	14829.612	0.001	14829.828	0.001	14806.326	-0.002	14806.542	-0.002
23½	14830.089	0.005	14830.321	0.001	14805.785	-0.005	14806.021	-0.005
24½	14830.565	-0.001	14830.818	-0.003	14805.263	0.001	14805.516	-0.002
25½	14831.052	-0.004	14831.337	0.005	14804.743	0.000	14805.019	0.000
26½	14831.554	-0.003	14831.853	-0.001	14804.232	-0.001	14804.533	0.002
27½	14832.062	-0.004	14832.378	-0.007	14803.750	0.017[b]	14804.054	0.002
28½			14832.929	0.005	14803.241	-0.002	14803.595	0.011[b]
29½	14833.119	0.008	14833.475	-0.001	14802.765	0.004	14803.127	0.001
30½	14833.649	0.002	14834.030	-0.005	14802.291	0.002	14802.682	0.004
31½	14834.190	-0.002	14834.603	-0.002	14801.822	-0.004	14802.242	0.002
32½	14834.745	-0.001	14835.183	-0.002	14801.380	0.008	14801.815	0.003
33½	14835.305	-0.004	14835.775	0.001	14800.927	-0.001	14801.380	-0.014[b]
34½	14835.882	0.001	14836.376	0.003	14800.496	0.003	14800.984	-0.002
35½	14836.465	0.003	14836.980	-0.002	14800.068	0.001	14800.590	0.002
36½	14837.047	-0.005	14837.596	-0.004	14799.653	0.001	14800.201	0.001
37½	14837.653	0.001	14838.228	0.000	14799.241	-0.001	14799.827	0.004
38½	14838.254	-0.005	14838.866	0.000	14798.846	-0.001	14799.455	-0.001
39½	14838.866	-0.010[b]	14839.506	-0.007	14798.459	0.000	14799.095	-0.004
40½	14839.506	0.004	14840.170	-0.000	14798.088	0.008	14798.750	-0.001
41½	14840.139	0.002	14840.840	0.003	14797.714	0.003	14798.415	0.002
42½	14840.788	0.007	14841.516	0.004			14798.088	0.002
43½	14841.429	-0.004	14842.195	-0.003	14797.000	-0.001	14797.773	0.004
44½	14842.090	-0.005	14842.896	0.003			14797.462	0.001
45½	14842.771	0.006	14843.597	-0.001			14797.163	-0.001
46½	14843.447	0.003	14844.315	0.003			14796.874	-0.003
47½	14844.124	-0.009	14845.044	0.008			14796.597	-0.003
48½	14844.830	0.000						
49½	14845.536	0.000						
50½	14846.256	0.005						
51½								
52½	14847.705	-0.003						

TABLE 7.10 (continued)

J	Q_{2ef}		$^{2}_{2fe}$		R_{21ee}		R_{21ff}	
1½					14822.767	-0.001	14822.767	0.000
2½					14823.546	-0.001	14823.546	0.002
3½	14820.079	0.000[b]	14820.079	0.008[b]				
4½	14819.852	-0.023[b]	14819.852	-0.012[b]	14825.128	-0.006	14825.128	0.002
5½	14819.657	-0.026[b]	14819.657	-0.010[b]	14825.936	-0.006	14825.936	0.006
6½	14819.484	-0.017[b]	14819.484	0.005[b]	14826.769	0.009	14826.750	0.007
7½	14819.328	-0.001	14819.298	-0.002				
8½	14819.167	0.002	14819.114	-0.017[b]	14828.446	0.020[b]		
9½	14819.008	-0.005	14818.962	-0.008				
10½	14818.856	-0.014[b]	14818.822	0.004	14830.125	-0.006		
11½			14818.668	-0.008				
12½			14818.540	-0.003				
13½	14818.513	0.011	14818.425	0.006				
14½	14818.395	-0.004	14818.302	-0.002				
15½	14818.302	-0.004	14818.191	-0.008				
16½			14818.095	-0.008				
17½								
18½								
19½								
20½			14817.808	-0.001				
21½			14817.756	-0.002				
22½			14817.707	-0.009				
23½								
24½			14817.660	-0.001				
25½								
26½								
27½								
28½								
29½								
30½	14818.095	-0.012[b]	14817.707	-0.006				
31½	14818.167	-0.006	14817.756	0.001				
32½			14817.808	0.003				
33½	14818.338	0.002						
34½	14818.425	-0.007						
35½	14818.540	0.002						
36½	14818.653	-0.002	14818.095	0.000[b]				
37½	14818.788	0.007	14818.191	0.001				
38½	14818.920	0.003	14818.302	0.007				
39½	14819.062	-0.001						
40½	14819.215	-0.004						
41½	14819.380	-0.005						
42½	14819.558	-0.003						
43½	14819.744	-0.002						

[a]Unless indicated otherwise, line positions have an assigned uncertainty of 0.0035 cm^{-1}.
[b]Blended line with assigned uncertainty of 0.01[illegible] cm^{-1}.

TABLE 7.11: Line Positions[a] (cm^{-1}) for the $\tilde{A}^2\Pi$ - $\tilde{X}^2\Sigma^+$ $(010)\kappa^2\Sigma^{(-)}$ - $(010)^2\Pi$ sub-band of SrOH. The table shows $\bar{\nu}_{obs}$, the measured wavenumbers, and the residuals, $\bar{\nu}_{obs}$ - $\bar{\nu}_{calc}$.

J	${}^{o}P_{12}$		P_1		${}^{P}Q_{12}$		Q_1	
6½					14825.583	-0.028	14829.062	-0.031
7½	14821.708	0.047	14825.583	-0.010				
8½					14825.152	-0.024	14829.667	0.008
9½	14820.221	-0.025	14825.152	-0.001				
.								
.								
15½	14816.277	0.036						
16½	14815.635	0.026						
17½	14814.974	-0.013			14823.653	-0.017	14832.716	0.020
18½	14814.370	-0.004	14823.653	0.028	14823.526	-0.022	14833.111	0.028
19½	14813.780	0.008	14823.526	0.025				
20½	14813.165	-0.015						
21½	14812.600	0.002						

J	${}^{Q}R_{12}$		R_1		P_2		Q_2	
5½	14829.062	-0.047						
6½							14826.244	0.007
7½	14829.667	-0.013	14833.612	0.001	14822.249	0.013	14826.096	-0.011
8½					14821.606	0.003		
.								
.								
13½			14838.527	0.051			14825.456	-0.080
14½			14839.343	0.025	14817.956	-0.039	14825.408	-0.067
15½			14840.164	-0.006			14825.371	-0.054
16½	14832.716	-0.023	14841.036	0.006	14816.862	-0.004		
17½	14833.111	-0.017	14841.935	0.036				
18½			14842.801	0.023				
19½			14843.706	0.041				

J	${}^{Q}P_{21}$		R_2		${}^{R}Q_{21}$		${}^{S}R_{21}$	
5½			14829.700	0.004			14832.690	0.012
6½			14830.045	-0.012	14829.700	0.020	14833.565	0.026
7½	14826.244	0.025			14830.045	0.006		
8½	14826.096	0.010						
.								
.								
13½			14832.824	-0.015				
14½	14825.456	-0.045	14833.277	0.004	14832.824	0.020	14840.777	-0.002
15½	14825.408	-0.030			14833.277	0.042		
16½	14825.371	-0.014						

[a]Line positions have an assigned uncertainty of 0.03 cm^{-1}; blending of the P_1 + ${}^{P}Q_{12}$, Q_1 + ${}^{Q}R_{12}$, Q_2 + ${}^{Q}P_{21}$ and R_2 + ${}^{R}Q_{21}$ branches was not resolved. Since the satellite and main lines were of similar intensity and the splittings of the blended lines were within experimental uncertainty, each blended line measurement was assigned to both transitions.

TABLE 7.12: Line Positions[a] (cm^{-1}) for the $\tilde{A}^2\Pi$ - $\tilde{X}^2\Sigma^+$ $(010)\mu^2\Sigma^{(+)}$ - $(010)^2\Pi$ sub-band of SrOH. The table shows $\bar{\nu}_{obs}$, the measured wavenumbers, and the residuals, $\bar{\nu}_{obs} - \bar{\nu}_{calc}$.

J	R_2		$^RQ_{21}$		Q_2		P_2		$^QP_{21}$	
13½	14561.979	-0.042								
14½	14562.350	-0.036	14561.979	-0.006	14554.454	-0.021				
15½			14562.350	0.002	14554.310	-0.026	14546.599	-0.033	14554.454	0.012
16½							14545.974	-0.031	14554.310	0.014
17½										
18½										
19½										
20½										
21½										
22½	14565.468	-0.061								
23½	14565.890	-0.063	14565.468	-0.004						
24½	14566.349	-0.035	14565.890	-0.003			14541.175	-0.043		
25½			14566.349	0.027			14540.602	-0.050		
26½							14540.055	-0.038		

[a]Line positions have an assigned uncertainty of 0.03 cm^{-1}; the $^SR_{21}$ branch was too weak to be observed; data for the rotational levels associated with the F_1 spin component of the $\mu^2\Sigma^{(+)}$ state were not obtained for this sub-band; blending of the R_2 + $^RQ_{21}$ and Q_2 + $^QP_{21}$ branches was not resolved; since the splittings were within experimental uncertainty, blended measurements were assigned to both transitions.

TABLE 7.13: Line positions[a] (cm^{-1}) for the $\tilde{A}^2\Pi$-$\tilde{X}^2\Sigma^+$ $(010)^2\Delta_{3/2}$-$(010)^2\Pi$ sub-band of SrOH. The table shows $\bar{\nu}_{obs}$, the measured wavenumbers, and the residuals, $\bar{\nu}_{obs} - \bar{\nu}_{calc}$.

J	Q_{12ef}		Q_{12fe}		P_{12ee}		P_{12ff}	
3½	14558.684	0.007						
4½	14558.488	0.003						
5½	14558.283	-0.022	14558.295	-0.013	14555.499	0.010		
6½	14558.126	-0.010	14558.130	-0.015	14554.798	-0.009	14554.856	0.007
7½			14557.983	-0.013	14554.107	-0.028	14554.183	-0.012
8½							14553.558	0.003
.								
.								
12½	14557.286	-0.059						
13½	14557.232	-0.017						
14½	14557.146	-0.017						
15½								
16½	14557.030	0.011						
17½	14556.940	0.022						
18½								
19½			14557.158	-0.017				
20½			14557.161	-0.019				
21½			14557.218	0.022				

J	P_{1ee}		P_{1ff}		Q_{1ef}		Q_{1fe}	
3½					14560.647	-0.002		
4½	14558.684	0.018			14560.956	0.008		
5½	14558.488	0.016			14561.274	0.016		
6½	14558.283	-0.006	14558.295	0.002	14561.593	0.014	14561.638	0.011
7½	14558.126	0.008	14558.130	0.003			14562.010	0.032
8½			14557.983	0.008				
.								
.								
12½					14563.739	0.031		
13½	14557.286	-0.027			14564.122	0.027		
14½	14557.232	0.018			14564.543	0.052		
15½	14557.146	0.021			14564.926	0.029		
16½					14565.350	0.040		
17½	14557.030	0.053			14565.770	0.037		
18½	14556.940	0.023			14566.199	0.035		
19½					14566.604	0.001	14567.254	0.035
20½			14557.158	0.033			14567.761	0.027
21½			14557.161	0.033				
22½			14557.218	0.076				

TABLE 7.13 (continued)

J	R_{12ee}		R_{12ff}		R_{1ee}		R_{1ff}	
2½	14560.647	-0.010			14562.182	0.037		
3½	14560.956	-0.003			14562.988	0.044		
4½	14561.274	0.002			14563.762	0.007	14563.786	0.019
5½	14561.593	-0.002	14561.638	-0.005	14564.591	0.014	14564.607	0.011
6½			14562.010	0.014			14565.452	0.013
.								
.								
11½	14563.739	0.001			14569.718	-0.011		
12½	14564.122	-0.006			14570.615	-0.008		
13½	14564.543	0.016			14571.526	-0.001		
14½	14564.926	-0.008						
15½	14565.350	0.000			14573.403	0.040		
16½	14565.770	-0.005			14574.298	0.004		
17½	14566.199	-0.010			14575.278	0.042		
18½	14566.604	-0.047	14567.254	-0.012			14576.491	-0.026
19½			14567.761	-0.023			14577.470	-0.043

[a]Line positions have an assigned uncertainty of 0.03 cm^{-1}; blending of the $Q_{12} + P_1$ and $Q_1 + R_{12}$ branches was not resolved; since the splittings were within experimental uncertainty, the blended line measurements were assigned to both transitions.

TABLE 7.14: Line Positions[a] (cm^{-1}) for the $\tilde{A}^2\Pi$-$\tilde{X}^2\Sigma^+$ $(010)^2\Delta_{5/2}$-$(020)^2\Delta$ sub-band of SrOH. The table shows $\bar{\nu}_{obs}$, the measured wavenumbers, and the residuals, $\bar{\nu}_{obs} - \bar{\nu}_{calc}$.

J	R_2		Q_{21}		P_{21}		Q_2	
2½	14452.956	-0.023						
3½	14453.276	-0.002	14452.956	-0.015			14450.943	-0.055
4½	14453.634	0.047	14453.276	0.009	14450.943	-0.044	14450.766	-0.035
5½	14453.925	0.018	14453.634	0.060	14450.766	-0.021	14450.607	-0.007
6½			14453.925	0.034	14450.607	0.008	14450.403	-0.036
7½					14450.403	-0.018		
.								
.								
17½	14458.609	0.006						
18½	14459.072	0.006	14458.609	0.050			14449.170	-0.023
19½			14459.072	0.054	14449.170	0.024	14449.138	-0.023
20½					14449.138	0.027		
21½								
22½	14460.993	-0.031						
23½	14461.525	-0.015	14460.993	0.026			14449.062	-0.079
24½	14462.056	-0.012	14461.525	0.044	14449.062	-0.020	14449.109	-0.055
25½			14462.056	0.050	14449.109	0.007	14449.148	-0.049
26½					14449.148	0.015		

J	P_2	
19½	14439.363	0.075

[a]Line positions have an assigned uncertainty of 0.03 cm^{-1}; *e/f* parity splittings were not resolved; the P_2 and R_{21} branches, with one exception, were too weak to be observed; blending of the R_2 + Q_{21} and P_{21} + Q_2 branches was not resolved; since the splittings were within experimental uncertainty, the blended line measurements were assigned to both transitions.

TABLE 7.15: Line Positions[a] (cm^{-1}) for the $\tilde{A}^2\Pi$ - $\tilde{X}^2\Sigma^+$ $(010)^2\Delta_{5/2}$ - $(03^30)^2\Phi$ sub-band of SiOH. The table shows $\bar{\nu}_{obs}$, the measured wavenumbers, and the residuals, $\bar{\nu}_{obs} - \bar{\nu}_{calc}$.

J	R_2		Q_{21}		Q_2		P_{21}		P_2	
6½	14077.584	-0.002								
7½			14077.584	0.016	14073.581	-0.051				
8½	14078.297	-0.003					14073.581	-0.030	14069.213	0.031
9½			14078.297	0.020	14073.340	-0.017				
10½							14073.340	0.009	14067.968	0.049
11½	14079.443	-0.019								
12½	14079.825	-0.048	14079.443	0.011	14073.020	-0.016				
13½	14080.252	-0.044	14079.825	-0.015	14072.903	-0.050	14073.020	0.017	14066.064	-0.051
14½			14080.252	-0.009	14072.866	-0.016	14072.903	-0.015	14065.546	0.008
15½	14081.152	-0.027					14072.866	0.022	14064.962	-0.012
16½			14081.152	0.013	14072.798	0.021				
17½	14082.095	-0.014					14072.798	0.064	14063.889	0.008
18½	14082.592	0.000	14082.095	0.031	14072.730	0.010				
19½			14082.592	0.047	14072.744	0.035	14072.730	0.058	14062.871	0.034
20½							14072.744	0.084	14062.330	-0.003
21½										
22½										
23½										
24½										
25½	14086.275	-0.035								
26½	14086.824	-0.065	14086.275	0.029	14072.941	-0.034				
27½			14086.824	0.002	14073.005	-0.057	14072.941	0.033	14059.139	-0.009
28½							14073.005	0.013	14058.682	-0.060
29½										
30½										
31½	14089.891	-0.071								
32½			14089.891	0.008						
33½									14056.995	0.101

[a]Line positions have an assigned uncertainty of 0.03 cm^{-1}; the R_{21} branch was too weak to be observed; data for the rotational levels associated with the F_1 spin component of the $^2\Delta_{5/2}$ state were not obtained for this sub-band; blending of the R_2 + Q_{21} and Q_2 + P_{21} branches was not resolved; since the splittings were within experimental uncertainty, blended measurements were assigned to both transitions.

determined iteratively. This procedure involved using an estimate of ω_2 obtained by setting $x_{12} = x_{23} = 0$ and assuming a value of x_{22} for the $\tilde{A}^2\Pi$ state equal to that of the $\tilde{B}^2\Sigma^+$ state determined in ref. 8. Taking the value of $\epsilon\omega_2$ obtained from the least-squares fit of the $\kappa^2\Sigma^{(-)} \leftarrow {}^2\Sigma^+$ band to the expressions of eqs. 4.45-4.54, an initial estimate of ϵ was obtained. Subsequent fits of the entire data set provided more refined determinations of $\epsilon\omega_2$ which were used to obtain improved estimates of ϵ; convergence was reached after 3 iterations.

The deperturbed molecular constants obtained from the least-squares fit involving the $A(010)$ RT components are given in table 7.16. The variance of the final fit was 0.98, indicating that the estimated uncertainties in the measurements were reasonable. Although the fitted B values of the $\kappa^2\Sigma^{(-)}$, $\mu^2\Sigma^{(+)}$ and $^2\Delta$ components are very similar (within 0.00011 cm^{-1} of each other), the differences are nevertheless significant given the statistical uncertainties suggested by the least-squares fit. The agreement is comparable to that found in the deperturbation analysis of the $v_2 = 1$ level of BO_2[127]. Kawaguchi *et al.*[134,135] have shown that higher order vibration-rotation, Coriolis and Renner-Teller interactions with other vibrational levels within the $^2\Pi$ electronic state can introduce small contributions to the effective B values of the $\kappa^2\Sigma^{(-)}$ and $\mu^2\Sigma^{(+)}$ components. While the matrix model of table 7.16 succeeds in reducing the large apparent spin-rotation constants of the $^2\Sigma$ states, the fitted values of γ, 0.02070(6) and 0.02945(5) cm^{-1} for the $\mu^2\Sigma^{(+)}$ and $\kappa^2\Sigma^{(-)}$ states, respectively, are significantly different and are thus regarded as effective parameters. In recent work in this laboratory using isotope relations for CaOH and CaOD, Li and Coxon[131] have shown that the spin-rotation constants in table 7.16 are influenced by contributions from the RT effect. Specifically, it is shown that the effective parameters $\gamma^{\Sigma(-)}$ and

Table 7.16: Molecular constants for the SrOH molecule. All values are in cm^{-1} except ϵ (dimensionless); values in parentheses correspond to 1σ in units of the last significant figure; square brackets are used to indicate constants fixed in the least-squares fit; constants for $\tilde{X}(000)$ were held fixed to the values determined in ref. 37.

	$\tilde{A}(010)^a$			$\tilde{A}(000)^b$	
T^{Σ}	15055.694(1)	D^{Δ}	$2.186(4) \times 10^{-7}$	T_e	[14674.332]
ΔT^{Δ}	0.9672(14)	$D^{\Sigma(+)}$	$2.227(5) \times 10^{-7}$	A	[263.51741]
A	263.6728(26)	$D^{\Sigma(-)}$	$2.186(5) \times 10^{-7}$	A_D	$[7.0046 \times 10^{-5}]$
A_D	$4.0(16) \times 10^{-5}$	p^e	-0.1439(5)	B	[0.2538873]
$\epsilon\omega_2$	-30.716(6)	q^e	$-1.58(6) \times 10^{-4}$	D	$[2.1735 \times 10^{-7}]$
ϵ	[-0.0791]	q^v	$-3.64(12) \times 10^{-4}$	p^e	[-0.1432006]
B^{Δ}	0.253052(8)	$\gamma^{\Sigma(+)}$	0.02069(5)	q^e	$[-2.0000 \times 10^{-4}]$
$B^{\Sigma(+)}$	0.253155(24)	$\gamma^{\Sigma(-)}$	0.02945(5)		
$B^{\Sigma(-)}$	0.253046(8)	$\gamma_D^{\Sigma(+)}$	$2.87(27) \times 10^{-7}$		
		$\gamma_D^{\Sigma(-)}$	$2.49(34) \times 10^{-7}$		

	$\tilde{X}(010)\Pi^a$		$\tilde{X}(02^20)\Delta^a$		$\tilde{X}(03^30)^2\Phi^a$
T_{ev}	363.687(2)	T_{ev}	733.521(8)	T_{ev}	1111.438(9)
B	0.248549(4)	B	0.247833(19)	B	0.24728(2)
D	$2.175(7) \times 10^{-7}$	D	$[2.175 \times 10^{-7}]$	D	$[2.175 \times 10^{-7}]$
γ	0.002427(15)	γ	[0.002427]	γ	[0.0024275]
q	$-3.943(5) \times 10^{-4}$				

[a]Determined in this work.

[b]Determined from Ref. 33.

$\gamma^{\Sigma(+)}$ contain a factor $\epsilon\omega_2/\Delta E$, where ΔE is the spacing between the $\kappa^2\Sigma$ and $\mu^2\Sigma$ basis states.

The electronic parameters p^e and q^e determined from the deperturbation of the $v_2 = 1$ moiety are in excellent agreement with those for the $\tilde{A}(000)$[33] and $\tilde{A}(100)$ levels (see tables 7.3 and 7.16). Similarly, the spin-orbit coupling constant for the (010) level of 263.6728(25) cm^{-1} is very close to the (000) value of 263.51741(34) cm^{-1}[33]. Combined with the high quality of the least-squares fit, this establishes the credibility of the deperturbation model used in this work. While refinements to the model will no doubt lead to small improvements, the deperturbed nature of the molecular constants given in the table 7.16 is abundantly clear. The present work also provides much improved determinations of molecular constants for the $\tilde{X}^2\Sigma^+(010)$ and $\tilde{X}^2\Sigma^+(02^20)$ vibrational levels. Previous estimates[22,34] of these parameters obtained from the $\tilde{B}^2\Sigma^+$ - $\tilde{X}^2\Sigma^+$ system have been contaminated by perturbations in the $\tilde{B}^2\Sigma^+$ electronic state levels.

A plot of the reduced term values of the $\tilde{A}(010)$ Renner-Teller components as a function of J is given in figure 7.11. Clearly evident from this diagram is that the effects of the K-type resonance perturbations in the upper $\kappa^2\Sigma^{(-)}$ and $^2\Delta_{5/2}$ vibronic components are minimal: the most obvious manifestation is a small K-type doubling ($\approx$ 0.2 cm^{-1} at J = 50½) of the $^2\Delta_{5/2}$ sub-state rotational levels. The reasons for the weak nature of the $\kappa^2\Sigma^{(-)} \sim {}^2\Delta_{5/2}$ interaction is immediately apparent: not only is the energy separation much greater than for the $\mu^2\Sigma^{(+)}$ and $^2\Delta_{3/2}$ components, the interaction matrix element in table 7.6 is small, being a function of the ℓ-type doubling parameter q_v^v only. This can be contrasted to the $\mu^2\Sigma^{(+)} \sim {}^2\Delta_{3/2}$ off-diagonal matrix element which has terms containing both Λ- and ℓ-type doubling contributions. In addition to the observed term energies, fig. 7.11 shows the

Figure 7.11: Reduced term values for the observed (filled symbols) and deperturbed (open symbols) rotational levels of the vibronic components of SrOH $\tilde{A}^2\Pi(010)$. The deperturbed terms were obtained by setting the matrix elements off-diagonal between $^2\Delta$ and $^2\Sigma^+$ of the K-type resonance energy matrix (table 2) to zero. The reduced term energies are obtained by subtraction of $\bar{B}J(J + 1)$ with $\bar{B} = 0.253087$.

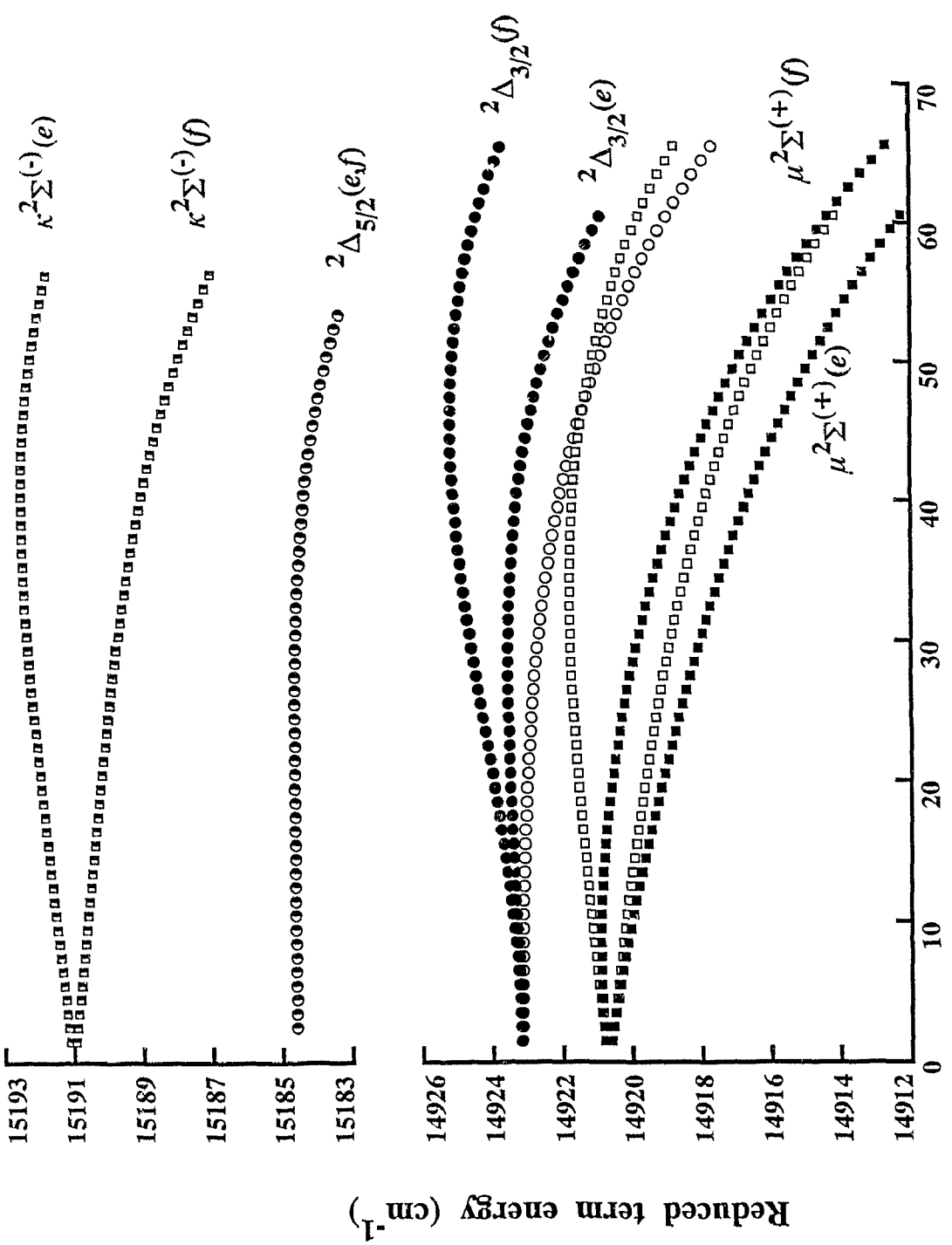
15193
15191
15189
15187
15185
15183
14926
14924
14922
14920
14918
14916
14914
14912
0
10
20
30
40
50
60
70
J
Reduced term energy (cm-1)
$\kappa^2\Sigma^{(-)}(e)$
$\kappa^2\Sigma^{(-)}(f)$
$^2\Delta_{5/2}(e,f)$
$^2\Delta_{3/2}(f)$
$^2\Delta_{3/2}(e)$
$\mu^2\Sigma^{(+)}(f)$
$\mu^2\Sigma^{(+)}(e)$

Figure 7.11

"unperturbed" energies obtained by setting the K-resonance matrix elements (specifically the upper right-hand 4 × 4 block in table 7.6) equal to zero. A K-resonance crossing in the f levels of the $\mu^2\Sigma^{(+)}$ and $^2\Delta_{3/2}$ components is observed at J = 46½. The effect of the level crossing in these lower spin-orbit components is obvious: a plot of the unperturbed reduced term values of the $\mu^2\Sigma^{(+)}$ and $^2\Delta_{3/2}$ levels are remarkably similar in appearance to the weakly perturbed $\kappa^2\Sigma^{(-)}$ and $^2\Delta_{5/2}$ levels, respectively. The strong K-resonance interaction leads to an anomalously large K-type doubling in the $^2\Delta_{3/2}$ component while simultaneously reducing the apparent spin-rotation splitting of the $\mu^2\Sigma^{(+)}$ sub-state. The unusually strong K-resonance interaction in the $\tilde{A}^2\Pi$ state of SrOH is at least in part due to the large value of the Λ-doubling parameter p^e which occurs on account of the second-order contributions arising from off-diagonal spin-orbit interactions with the nearby $\tilde{B}^2\Sigma^+$ state. The effects of K-type resonance in the v_2 = 1 level of SrOH are much larger than in previously studied examples[31,87,127,]; at J = 60½ the e and f levels of the lower spin-orbit components are displaced by approximately 3 and 6 cm^{-1}, respectively. In table 7.17, the mixing percentages of the eigenstates for particular J values are listed. Although mixing of the $\kappa^2\Sigma^{(-)}$ and $^2\Delta_{5/2}$ levels is minimal, the K-resonance perturbation leads to a strong mixing of the $\mu^2\Sigma^{(+)}$ and $^2\Delta_{3/2}$ states. As expected, the nominal character of the f parity wavefunctions changes over through the crossing region. However, because the K-resonance matrix element increases with J, strong mixing still occurs even for the highest observed J-values.

The present high resolution analysis of the RT components of the v_2 = 1 level of SrOH enables the determination of the g_K parameter introduced by Brown[85]. From the fourth order expressions of Brown and Jorgensen[84] where the anharmonic terms have been neglected

Table 7.17: Mixing percentages of the $v_2 = 1$ vibronic components of $\tilde{A}^2\Pi$ SrOH.

	e-levels				*f*-levels			
	$\mu^2\Sigma^{(+)}$	$^2\Delta_{3/2}$	$^2\Delta_{5/2}$	$\kappa^2\Sigma^{(-)}$	$(\mu^2\Sigma^{(+)})^a$	$(^2\Delta_{3/2})^a$	$^2\Delta_{5/2}$	$\kappa^2\Sigma^{(-)}$
$J = 2½$					14922.928	14925.297	15186.703	15193.011
$\|-1,1,1,½;J,½\rangle$	98.06	0.57	0.00	1.37	98.01	0.74	0.00	1.25
$\|1,1,1,½;J,3/2\rangle$	0.58	99.42	0.00	0.00	0.75	99.25	0.00	0.00
$\|1,1,1,½;J,5/2\rangle$	0.00	0.00	100.0	0.00	0.00	0.00	100.00	0.00
$\|1,1,-1,½;J,½\rangle$	1.36	0.01	0.00	98.63	1.24	0.01	0.00	98.75
$J = 20½$					15031.983	15035.467	15296.097	15301.620
$\|-1,1,1,½;J,½\rangle$	84.53	13.56	0.00	1.90	69.86	29.24	0.00	0.90
$\|1,1,1,½;J,3/2\rangle$	13.83	86.11	0.06	0.00	29.50	70.46	0.04	0.00
$\|1,1,1,½;J,5/2\rangle$	0.01	0.05	99.92	0.02	0.01	0.03	99.94	0.02
$\|1,1,-1,½;J,½\rangle$	1.63	0.27	0.02	98.08	0.63	0.27	0.74	99.08
$J = 46½$					15476.550	15484.110	15742.915	15747.358
$\|-1,1,1,½;J,½\rangle$	78.16	19.38	0.01	2.44	49.80	49.70	0.01	0.50
$\|1,1,1,½;J,3/2\rangle$	19.86	79.93	0.20	0.00	49.86	49.94	0.20	0.00
$\|1,1,1,½;J,5/2\rangle$	0.04	0.17	99.63	0.17	0.10	0.11	99.06	0.74
$\|1,1,-1,½;J,½\rangle$	1.93	0.52	0.16	97.39	0.25	0.25	0.74	98.76
$J = 70½$					16186.370	16198.455	16455.618	16459.418
$\|-1,1,1,½;J,½\rangle$					44.20	55.46	0.02	0.22
$\|1,1,1,½;J,3/2\rangle$					55.46	44.08	0.43	0.03
$\|1,1,1,½;J,5/2\rangle$					0.23	0.22	93.69	5.85
$\|1,1,-1,½;J,½\rangle$					0.10	0.13	5.86	93.90

[a]Mixing of basis functions renders these basis state labels inappropriate for all but the lowest J values.

$$\Delta T^{\Delta} = G_0(\Sigma) - G_0(\Delta) = \tfrac{1}{2}\,\epsilon^2\omega_2 + \tfrac{1}{4}\,\epsilon^4\omega_2 + \frac{\epsilon^2 A^2}{8\omega_2} - 2g_K\,. \qquad (7.5)$$

Using the constants of table 7.16 and an approximate value of ω_2, an estimate of $g_K = 0.196$ cm^{-1} is obtained. The magnitude of g_K provides a measure of the amount by which the Π electronic state is contaminated by Σ and Δ electronic states: mixing with Σ states results in positive contributions to g_K while Δ states give negative contributions[85]. Typically, the magnitude of the g_K term is on the order of a few cm^{-1}. The unusually small value of g_K in SrOH may be attributed to the near cancellation of $\tilde{B}^2\Sigma^+ \sim \tilde{A}^2\Pi$ and $\tilde{C}^2\Delta \sim \tilde{A}^2\Pi$ contributions. Some caution must be exercised in the interpretation of the significance of the g_K parameter, however, as both additional vibronic interactions and the neglect of anharmonicities in the bending potential may introduce sizable contributions. The estimates of ϵ, ω_2 and g_K along with a number of other fundamental vibrational and rotational molecular constants for the $\tilde{A}^2\Pi$ state of SrOH are given in table 7.18.

7.6 Discussion

The strong intensity anomalies observed in the branch structure in several bands observed in this work have been attributed to vibronic perturbations in the upper $\tilde{A}^2\Pi$ state. In the case of diatomic molecules, such interference effects occur when the perturbing state is of a different symmetry ($\Delta\Lambda = \pm 1$)[89]; for a triatomic molecule, however, given the presence of a vibrational angular momentum, the analogous symmetry requirement is $\Delta K = \pm 1$. A quantitative treatment of these intensity irregularities, which, because of the Renner-Teller and spin-orbit interactions involves numerous vibronic states, is not undertaken in the present work; instead, an effort is made to explain the origin of the vibronic perturbations in a manner which is consistent with experimental observations.

Table 7.18: Molecular constants of the $\tilde{A}^2\Pi$ fundamental bending mode of SrOH and CaOH. All values given in cm^{-1}; values in parentheses correspond to 1σ in units of the last significant digit.

	SrOH[a]	CaOH[b]
ν_2	381.362(1)[c]	361.346(1)
$\epsilon\omega_2$	-30.720(6)	-36.4040(7)
ϵ	-0.0791[d]	-0.100
ω_2	388.5[d]	365.825
g_K	0.196	
α_2	0.000803(10)[c]	0.001703

[a]Determined from this work.

[b]Determined in Ref. 29 and 30.

[c]Determined using an average value of B for the $\tilde{A}(010)$ level and the value of Ref. 33 for the $\tilde{A}(000)$ level.

[d]Estimated, see text.

The most compelling evidence for the existence of vibronic perturbations are the intensity irregularities observed in the dispersed fluorescence spectrum of the $\tilde{A}(000)^2\Pi_{3/2}$ - $\tilde{X}(010)^2\Pi$ sub-band. No such indications were evident in the high resolution investigation of the $\tilde{A}(000)$ - $\tilde{X}(000)$ band carried out by Brazier and Bernath[33] other than perhaps a missing R_2 branch. Rather surprisingly, the rotational levels of both spin-orbit components of the $\tilde{A}(000)^2\Pi$ levels were well described by the standard Hund's case (a) expressions indicating that the perturbation appears to be largely independent of J at least to within the precision of the data. The molecular constants for the $\tilde{A}(000)^2\Pi$ level may be compared to those obtained in the present work for the $\tilde{A}(100)^2\Pi$ level for which no indications of perturbations in the associated dispersed fluorescence spectra are found. The lambda-doubling parameters p^e and q^e are usually extremely sensitive to the presence of perturbations, yet, the $\tilde{A}(100)$ values of -0.14311(14) and -1.950(33) cm^{-1}, respectively, are very similar to the corresponding determinations of the $\tilde{A}(000)$ level given as -0.1432006(86) and -2.0000(133) cm^{-1} in ref. 33. It also should be noted that the spin-orbit constant determined by Brazier and Bernath[33] is only an effective parameter since the $\tilde{A}(000)$ level is a unique level in which the true spin-orbit parameter is slightly modified by the Renner-Teller effect. Using eq. 4.12, our determination of ϵ and the effective spin-rotation coupling constant $A_{eff}(000)$ = 263.51741 cm^{-1}[33], the true spin-orbit constant for the $\tilde{A}(000)$ level is 263.9303 cm^{-1}.

In the $\tilde{A}(010)$ Renner-Teller components, there was also evidence of vibronic perturbations which seemed to have little effect on the rotational energy level structure. In addition to the *P/R* intensity anomalies evident in the dispersed fluorescence spectra associated with the $^2\Delta_{5/2}$ vibronic component, it was found that the low J lines of the R_{21} and Q_1 branches of the

$(010)^2\Delta_{3/2} \leftarrow (000)^2\Sigma^+$ sub-band appear with about half the intensity of the adjacent R_2 lines of the $(010)\mu^2\Sigma^{(+)} \leftarrow (000)^2\Sigma^+$ band. Such a high intensity of the $(010)^2\Delta_{3/2} \leftarrow (000)^2\Sigma^+$ sub-band, particularly at low J, cannot be explained purely as a result of a rotationally induced K-type resonance. In the case of BO_2[127], the appearance of the forbidden $\Delta K = \pm 2$ K-resonance induced bands was fragmentary and transitions were observed only in the immediate vicinity of the crossings and beyond. In the present case, the matrix element between the $\mu^2\Sigma^{(+)}$ and $^2\Delta_{3/2}$ components results from a combination of Λ- and ℓ-type doubling where these effects lead to off-diagonal matrix elements that vary approximately as $[J(J+1)]^{1/2}$ and $J(J+1)$, respectively. At low J, not only are these K-type resonance matrix elements negligible, the $\mu^2\Sigma^{(+)}$ and $^2\Delta_{3/2}$ levels are separated by ≈ 2.6 cm^{-1}, so that mixing is insignificant (see table 7.17). Clearly there must be another mechanism in addition to K-type resonance to induce transition strength in the low J lines.

In view of the obvious vibronic perturbations observed in the $\tilde{A}^2\Pi$ state levels, it was of interest to consider possible terms of the effective Hamiltonian which may explain the origin of the vibronic perturbations. Recently, Northrup and Sears[83] have shown explicitly that vibronic mixing via second order $H_{HT} \times H_{SO}$ interactions may lead to significant vibronic perturbations of the excited bending levels of the $\tilde{X}^2\Pi$ state of NCS. By this mechanism, different vibronic levels of the $\tilde{A}^2\Pi$ state may interact through the $\tilde{B}^2\Sigma$ state vibrational levels. The dipolar term or Herzberg-Teller perturbation operator, given as[83,130]

$$H_{HT} = \tfrac{1}{2} V(q_+ L_- + q_- L_+) , \qquad (7.6)$$

connects basis functions with $\Delta v_2 = \pm 1$ and $\Delta\ell = -\Delta\Lambda = \pm 1$. Here, the ladder operators $q_\pm$ and $L_\pm$ act on the degenerate bending vibrational mode and

electronic orbital angular momenta, respectively, and V is a parameter defined previously by Bolman and Brown[130]. Using the following effective spin-orbit operator

$$H_{SO} = AL_zS_z + \tfrac{1}{2}A(L_+S_- + L_-S_+), \tag{7.7}$$

and H_{HT} of eq. 7.6, it is readily shown that second order $H_{HT} \times H_{SO}$ interactions have matrix elements within the $^2\Pi$ state that mix basis states with $\Delta v_2 = \pm 1$ and $\Delta P = 0$. This second order mechanism will introduce non-zero off-diagonal matrix elements that result in $\tilde{A}(010) \sim \tilde{A}(000)$ and $\tilde{A}(010) \sim \tilde{A}(020)$ mixing. As a result of the large spin-orbit splitting in the $\tilde{A}^2\Pi$ state, mixing via second order $H_{HT} \times H_{SO}$ will primarily mix the upper vibronic components of level (v_1, v_2, v_3) with the lower vibronic components of level $(v_1, v_2 + 1, v_3)$. For example, using the unsymmetrized parity basis of eq. 7.4, the $\tilde{A}(010)^2\Delta_{3/2} \sim \tilde{A}(000)^2\Pi_{3/2}$ interaction matrix element is of the form;

$$\frac{\langle 1,1,1,-\tfrac{1}{2};J,{}^3/_2|H_{SO}|0,1,1,\tfrac{1}{2};J,{}^3/_2\rangle\langle 0,1,1,\tfrac{1}{2};J,{}^3/_2|H_{HT}|1,0,0,\tfrac{1}{2};J,{}^3/_2\rangle}{E_{\Sigma-\Pi}} \tag{7.8}$$

where the term in the denominator is used to represent the separation of the $\tilde{B}^2\Sigma^+$ and $\tilde{A}^2\Pi$ states. A similar term arises between vibronic components of the (010) and (020) levels. It is to be expected that matrix elements of this type will be of a considerable magnitude in SrOH for two reasons. First, it is reasonable to conclude that the radial part of the off-diagonal spin-orbit interaction $\langle \tilde{A}^2\Pi \mid H_{SO} \mid \tilde{B}^2\Sigma^+ \rangle$ is significant and comparable in magnitude to the diagonal spin-orbit parameter of the $\tilde{A}^2\Pi$ state. This view is justified by recent ligand field calculations[43] which indicate that the fractional composition of the molecular wavefunctions of the $\tilde{A}^2\Pi$ and $\tilde{B}^2\Sigma^+$ states in terms

of atomic orbitals is similar. For the related alkaline earth halide CaI, the off-diagonal spin-orbit interaction has been determined[136] and is only slightly smaller than the diagonal spin-orbit parameter of the $\tilde{A}^2\Pi$ state. Second, the Herzberg-Teller perturbation operator can lead to significant mixing of electronic states especially when the energy separations are small. In NCS, the $\tilde{A}^2\Pi$ and $\tilde{B}^2\Sigma^+$ states are within 1000 cm^{-1} and mixing through H_{HT} is significant[79]: for SrOH, the $\tilde{A}^2\Pi$ and $\tilde{B}^2\Sigma^+$ states are separated by only about 1700 cm^{-1}.

The $H_{HT} \times H_{SO}$ matrix elements have no J dependence or parity dependence and, given that the interacting states are have very similar effective B values and are separated by $\approx$ 100 cm^{-1}, this explanation can account for the success in fitting the rotational levels of the $\tilde{A}(000)$ and $\tilde{A}(010)$ vibronic components without taking account explicitly of this interaction. In the $v_2 = 1$ moiety, this interaction results in a shift of the vibronic origins of the $^2\Delta$ components which is absorbed collectively by the A, v_2 and g_K terms.

Additional evidence for the presence of vibronic mixing in the $\tilde{A}^2\Pi$ state of SrOH is afforded by the permanent electric dipole determinations of Steimle *et al.*[3] Although the ground state experimental values of the electric dipole moment are in good agreement with the values predicted using the ligand-field[43] and semi-empirical electrostatic polarization[8] models, there is a large discrepancy between theory and experiment for the $\tilde{A}(000)^2\Pi_{1/2}$ and $\tilde{A}(000)^2\Pi_{3/2}$ values. Vibronic mixing has been invoked as a possible explanation for this poor agreement[3]. As indicated previously in the discussion concerning our determination of g_K, it is expected that mixing of the $\tilde{A}^2\Pi$ and $\tilde{C}^2\Delta$ states may also be appreciable. The $\tilde{C}^2\Delta$ state of SrOH has not yet been observed experimentally, but, theoretical calculations by Allouche *et al.*[43] have placed it at 20175 cm^{-1} , which is in reasonable agreement with

the prediction of 20221 cm^{-1} by Mestdagh and Visticot[8]. Certainly in the case of CaOH, the observation of the forbidden $\tilde{C}^2\Delta$ - $\tilde{X}^2\Sigma^+$ transition by Jarman and Bernath[35] provides strong experimental evidence for the existence of vibronic interactions among the low-lying $\tilde{A}^2\Pi$, $\tilde{B}^2\Sigma^+$ and $\tilde{C}^2\Delta$ electronic states.

The intensity measurements obtained in this work indicate that the nominally forbidden $\tilde{A}(010)\mu^2\Sigma^{(+)} \leftarrow \tilde{X}(000)^2\Sigma^+$ band, despite the poor Franck-Condon overlap, is only 40 - 50 times weaker than the allowed $\tilde{A}(000)^2\Pi_{3/2} \leftarrow \tilde{X}(000)^2\Sigma^+$ sub-band; in CaOH this factor is approximately 1000[31]. Bolman and Brown[130] have proposed a model to account for similarly forbidden vibronically induced parallel bands in the $\tilde{A}^2\Sigma$ - $\tilde{X}^2\Pi$ system of NCO[87]. In this three state model, all electronic states other than the $^2\Pi$ ground state and first excited $^2\Sigma^+$ electronic state are neglected. Limiting the multipole expansion of the perturbation operator in eq. 4.8 to the dipolar and quadrupolar terms, the transition strength is accounted for in terms of $^2\Pi \sim {}^2\Sigma^+$ vibronic mixing via the dipolar term. As indicated earlier, the dipolar (Herzberg-Teller) and quadrupolar (RT) terms, which have non-zero matrix elements subject to $\Delta\Lambda = \pm 1$ and $\Delta\Lambda = \pm 2$, respectively, may both contribute to the observed RT parameter ϵ. In the case of SrOH, it is expected that the evaluation of these individual contributions would enable the determination of the extent to which the $^2\Pi \sim {}^2\Sigma^+$ vibronic mixing through the mechanism proposed by Bolman and Brown influences the transition strength of the forbidden $\Delta v_2 = \pm 1$ bands. Gauyacq and Jungen[80] have shown that, within the three state approximation,

$$g_K = \frac{-\epsilon_1 \omega_2^2}{2\Delta E(1 + \epsilon_1)}, \tag{7.9}$$

where the ϵ_1 and ϵ_2 are dipolar and quadrupolar contributions, respectively, to the Renner-Teller parameter ϵ according to,

$$\epsilon = \frac{\epsilon_1 + \epsilon_2}{1 + \epsilon_1} . \qquad (7.10)$$

While the three state model enables the estimation of the ϵ_1 and ϵ_2 contributions from g_K for the 15 electron species NCO[85], NCS[83] and CO_2^+[80], the relative proximity of the $\tilde{C}^2\Delta$ state in SrOH precludes a similar determination in the present case. As a result, it is difficult to comment on the relative strength of the dipolar interaction in SrOH versus CaOH and thus it is not possible to conclusively demonstrate whether the mechanism of Bolman and Brown can account for the 20 - 25 fold increase in the relative strength of the $\Delta v_2 = 1$ bands of the $\tilde{A}^2\Pi$ - $\tilde{X}^2\Sigma^+$ system of SrOH with respect to CaOH. However, it is noteworthy that the determinations of the RT parameters ϵ and $\epsilon\omega_2$ for SrOH are comparable to those of CaOH[31] (see table 7.18). Moreover, the separations of the $\tilde{A}^2\Pi$ and $\tilde{B}^2\Sigma^+$ electronic states are similar, approximately 1700 cm^{-1} and 2000 cm^{-1} for SrOH and CaOH, respectively, suggesting that dipolar interactions should lead to comparable intensities for such bands.

An alternative explanation is afforded by the work of Brazier and Bernath[33], who noted the correlation between the magnitude of the spin-orbit coupling constant and the relative intensity of the $\Delta v_2 = \pm 1$ bands in the alkaline earth monohydroxides. These authors suggest a spin-orbit-vibronic interaction can account for the forbidden bands. Based on the present study, it is proposed that, more specifically, the transition strength may be acquired through vibronic mixing via a summation of second order $\boldsymbol{H}_{HT} \times \boldsymbol{H}_{SO}$ interactions of the kind alluded to earlier. Using a more general formulation of eq. 7.8, this may be represented as follows:

$$\{ \langle v_2, \tilde{A}^2\Pi | \, H_{HT} \, | v_2 \pm 1, \tilde{B}^2\Sigma^+ \rangle \langle v_2 \pm 1, \tilde{B}^2\Sigma^+ | \, H_{SO} \, | v_2 \pm 1, \tilde{A}^2\Pi \rangle$$

$$+ \langle v_2, \tilde{A}^2\Pi | H_{SO} | v_2, \tilde{B}^2\Sigma^+ \rangle \langle v_2, \tilde{B}^2\Sigma^+ | H_{HT} | v_2 \pm 1, \tilde{A}^2\Pi \rangle \} \; / \; E_{\Sigma-\Pi} \; . \quad (7.11)$$

While it is reasonable to conclude that both dipolar and second order $H_{HT} \times H_{SO}$ interactions may contribute to the intensity of the parallel bands in the $\tilde{A}^2\Pi$ - $\tilde{X}^2\Sigma^+$ system of SrOH, given the large spin-orbit interaction, the dominant mechanism more likely involves the $H_{HT} \times H_{SO}$ interaction.

In the broader context of the alkaline earth monohydroxides in general, the spectroscopy of the $\tilde{A}^2\Pi$ electronic state of SrOH is of particular interest in that it represents a degree of complexity that is intermediate between the relative simplicity of CaOH and the strongly perturbed BaOH. Recent studies in this laboratory[28,30,31,36,131] have resulted in considerable progress towards unraveling the rotational structure associated with the degenerate bending levels in the $\tilde{A}^2\Pi$ state of CaOH. High resolution investigations of the $v_2 = 1$ level[31,36] have indicated that the $\tilde{A}(010)^2\Delta_{3/2} \leftarrow \tilde{X}(000)^2\Sigma^+$ sub-band, with $\Delta K = 2$, does not occur with appreciable intensity. Moreover, the intensity interference effects observed in the present work on SrOH are similarly absent in CaOH[131]. As noted earlier, the $\tilde{A}^2\Pi$ states of SrOH and CaOH are similar in many respects, where the most striking difference is with respect to the magnitude of the spin-orbit coupling constant. It is therefore reasonable to conclude that much of the increased complexity observed in SrOH is directly related to the magnitude of the spin-orbit interaction. In contrast to the 4th and 5th row members of the alkaline earth monohydroxide series CaOH and SrOH, comparatively little is known of the $\tilde{A}^2\Pi$ state of BaOH, for which there have not been any high resolution investigations. Nevertheless, Fernando, Douay and Bernath[129] have tentatively located the $\tilde{A}^2\Pi(000)$ level at 11760 cm^{-1} and determined the spin-orbit coupling constant

as 570(5) cm^{-1}. Based on this work, it is expected that local perturbations in the $\tilde{A}^2\Pi$ state bending levels of BaOH due to *K*-resonance crossings will occur. Moreover, in view of the much larger spin-orbit constant in BaOH and the strong interference effects observed in the dispersed fluorescence spectra of SrOH, similar vibronic perturbations are expected in this heavier monohydroxide.

7.7 Conclusion

This work has resulted in the first determination of a number of fundamental electronic, vibrational and rotational constants for the first excited vibrational levels of the degenerate bending and M-O stretching modes in the $\tilde{A}^2\Pi$ electronic state of SrOH. The results include the first reliable determination of the Renner-Teller parameter (ϵ = -0.0791). The present example of a *K*-resonance crossing is unique in terms of the relatively large magnitude of the energy level shifts observed. The effects of vibronic perturbations have been observed in both the $\tilde{A}(010)^2\Pi$ level as well as the $\tilde{A}(000)^2\Pi$ vibrational level which was previously thought to be free of perturbations. A plausible mechanism to account for these perturbations has been presented. The rotational transitions of the $\tilde{A}(010)^2\Delta_{3/2} \leftarrow \tilde{X}(000)^2\Sigma^+$ sub-band given herein may provide a useful intermediate in future work employing stimulated emission pumping (SEP) by providing access to excited bending vibrational levels of the ground state with high vibrational angular momentum ($\ell \leq 3$).

BIBLIOGRAPHY

1. T. Tsuji, *Astron. Astrophys.* **23**, 411 (1973).
2. P. Pesch, *Astrophys. J.* **174**, L155 (1972).
3. T. C. Steimle, D. A. Fletcher, K. Y. Jung and C. T. Scurlock, *J. Chem. Phys.* **96**, 2556 (1992).
4. E. Murad, W. Swider and S. W. Benson, *Nature* **289**, 273 (1981).
5. S. C. Liu and G. C. Reid, *Geophys. Res. Lett.* **6**, 283 (1979).
6. E. S. Rittner, *J. Chem. Phys.* **19**, 1030 (1951).
7. S. F. Rice, H. Martin and R. W. Field, *J. Chem. Phys.* **83**, 5023 (1985).
8. J. M. Mestdagh and J. P. Visticot, *Chem. Phys.* **155**, 79 (1991).
9. B. S. Cheong and J. M. Parson, *J. Chem. Phys.* **100**, 1 (1994).
10. P. F. Bernath, *Science* **254**, 665 (1991).
11. J. F. W. Herschel, *Trans. Roy. Soc. Edinburgh* **9**, 445 (1823).
12. C. G. James and T. M. Sugden, *Nature (London)* **175**, 333 (1945).
13. A. Lagerqvist and L. Huldt, *Naturwissensch* **42**, 365 (1955).
14. A. G. Gaydon, *Proc. Roy. Soc. A* **231**, 437 (1955).
15. L. Huldt and A. Lagerqvist, *Ark. Fys.* **11**, 347 (1956).
16. J. Van der Hurk, Tj. Hollander, and C. Th. J. Alkemade, *J. Quant. Spectrosc. Radiat. Trans.* **13**, 273 (1974).
17. J. Van der Hurk, Thesis, *Rijksuniversitet Utrecht*, 1974.
18. J. Van der Hurk, Tj. Hollander and C. Th. J. Alkemade, *J. Quant. Spectrosc. Radiat. Trans.* **14**, 1167 (1974).
19. S. J. Weeks, H. Haraguchi and J. D. Winefordner, *Quant. Spectrosc. Radiat. Trans.* **19**, 633 (1978).
20. R. F. Wormsbecher, M. Trukula, C. Martner, R. E. Penn and D. O. Harris, *J. Molec. Spectrosc.* **97**, 29 (1983).

21. J. B. West, R. S. Bradford, J. D. Eversole and C. R. Jones, *Rev. Sci. Instrum.* **46**, 164 (1975).

22. J. Nakagawa, R. F. Wormsbecher and D. O. Harris, *J. Molec. Spectrosc.* **97**, 37 (1983).

23. R. C. Hilborn, Z. Qingshi and D. O. Harris, *J. Molec. Spectrosc.* **97**, 73 (1983).

24. P. F. Bernath and S. Kinsey-Nielsen, *Chem. Phys. Lett.* **105**, 663 (1984).

25. P. F. Bernath and C. R. Brazier, *Astrophys. J.* **288**, 373 (1984).

26. M. Li, Y. Zhang, C. Wang and Q. Zhu, *Appl. Laser* **4**, 149 (1984).

27. Q. Zhu, M. Li, Y. Zhang and C. Wang, *Acta Opt. Sin.* **5**, 765 (1985).

28. J. A. Coxon, M. Li and P. I. Presunka, *J. Molec. Spectrosc.* **150**, 23 (1991).

29. J. A. Coxon, M. Li and P. I. Presunka, *Molec. Phys.* **76**, 1463 (1992).

30. M. Li and J. A. Coxon, *J. Chem. Phys.* **97**, 8961 (1992).

31. J. A. Coxon, M. Li and P. I. Presunka, *J. Molec. Spectrosc.* **164**, 118 (1994).

32. R. A. Hailey, C. N. Jarman, W. T. M. L. Fernando and P. F. Bernath, *J. Molec. Spectrosc.* **147**, 40 (1991).

33. C. R. Brazier and P. F. Bernath, *J. Molec. Spectrosc.* **114**, 163 (1985).

34. P. I. Presunka and J. A. Coxon, *Can. J. Chem.* **71**, 1689 (1993).

35. C. N. Jarman and P. F. Bernath, *J. Chem. Phys.* **97**, 1711 (1992).

36. L. M. Ziurys, W. L. Barclay, Jr. and M. A. Anderson, *Astrophys. J.* **384**, L63 (1992).

37. M. A. Anderson, W. L. Barclay, Jr. and L. M. Ziurys, *Chem. Phys. Lett.* **196**, 166 (1992).

38. C. J. Whitman, B. Soep, J.P. Visticot and A. Keller, *J. Chem. Phys.* **93**, 991 (1990).

39. D. A. Fletcher, K. Y. Jung, C. T. Scurlock and T. C. Steimle, *J. Chem. Phys.* **98**, 1837 (1993).

40. C. T. Scurlock, D. A. Fletcher and T. C. Steimle, *J. Molec. Spectrosc.* **159**, 350 (1993).

41. C. W. Bauschlicher, Jr. and H. Partridge, *Chem. Phys. Lett.* **106**, 65 (1984).

42 C. W. Bauschlicher, Jr., S. R. Langhoff and H. Partridge, *J. Chem. Phys.* **84**, 901 (1986).

43. A. R. Allouche and M. Aubert-Frecon, *J. Molec. Spectrosc.* **163**, 599 (1994).

44. J. V. Ortiz, *J. Chem. Phys.* **92**, 6728 (1990).

45. C. W. Bauschlicher, Jr., S. R. Langhoff, T. C. Steimle and J. E. Shirley, *J. Chem. Phys.* **93**, 4179 (1990).

46. Z. J. Jakubek and R. W. Field, *J. Chem. Phys.* **98**, 6574 (1993).

47. W. E. Palke and B. Kirtman, *Chem. Phys. Lett.* **117**, 424 (1985).

48. W. L. Barclay, Jr., M. A. Anderson and L. M. Ziurys, *Chem. Phys. Lett.* **196**, 225 (1992).

49. N. H. Rosenbaum, J. C. Owrutsky, L. M. Tack, and R. J. Saykally, *J. Chem. Phys.* **84**, 5308 (1986).

50. P. J. Kalff and C. Th. J. Alkemade, *J. Chem. Phys.* **59**, 2572 (1973).

51. D. H. Cotton and D. R. Jenkins, *Trans. Farad. Soc.* **64**, 2988 (1968).

52. V. G. Ryabova, A. N. Khitrov, and L. V. Gurvich, *High Temp. (U. S. S. R.)* **10**, 669 (1972).

53. E. Murad, *J. Chem. Phys.* **75**, 4080 (1981).

54. J. Van der Hurk, Tj. Hollander and C. Th. J. Alkemade, *J. Quant. Spectrosc. Radiat. Trans.* **14**, 1167 (1974).

55. L. V. Gurvich, V. G. Ryabova, A. N. Khitrov and E. M. Starovoitov, *High*

Temp. (U. S. S. R.) **9**, 261 (1971).

56. P. J. Dagdigian, H. W. Cruse and R. N. Zare, *J. Chem. Phys.* **60**, 2330 (1974).
57. C. Matsumura and D. R. Lide, *J. Chem. Phys.* **50**, 71 (1969).
58. D. R. Lide and R. L. Kuczkowski, *J. Chem. Phys.* **46**, 4768 (1967).
59. D. E. Powers, S. G. Hansen, M. E. Geusic, A. C. Pulu, J. C. Hopkins, T. G. Dietz, M. A. Duncan, P. R. R. Langridge-Smith and R. E. Smalley, *J. Chem. Phys.* **86**, 2556 (1982).
60. K. Sakurai and H. P. Broida, *Chem. Phys. Lett.* **38**, 234 (1976); C. R. Vidal and J. Cooper *J. Appl. Phys.* **40**, 3370 (1969).
61. V. I. Srdanov and D. S. Pesic, *J. Molec. Spectrosc.* **90** , 27 (1981).
62. M. Trukula, D. O. Harris and R. C. Hilborn, *Chem. Phys. Lett.* **93**, 345 (1982).
63. A. S. C. Cheung, A. M. Lyra, A. J. Merer and A. W. Taylor, *J. Molec. Spectrosc.* **91**, 165 (1982).
64. W. Demtröder, *Laser Spectroscopy*, Springer-Verlag, Berlin (1982).
65. L. Ramaley, S. C. Foster and J. A. Coxon, *Chem., Biomed. and Environ. Instr.* **12**, 229 (1983).
66. P. I. Presunka and J. A. Coxon, *J. Chem. Phys.*, **100**, 1 (1994).
67. P. I. Presunka and J. A. Coxon, (submitted to *Chem. Phys.*).
68. S. C. Foster, Ph.D. Thesis, Dalhousie University, 1982.
69. B. A. Palmer, R. A. Keller, and R. Engleman Jr., *An Atlas of Uranium Emission Intensities in a Hollow Cathode Discharge*, Los Alamos Scientific Laboratory Report, LA-8251-MS.
70. J. A. Coxon and W. M Wickramaaratchi, *J. Molec. Spectrosc.* **79**, 380 (1980).
71. Coherent 699-29 Dye Laser Operating Manual.

72. S. Gerstenkorn and P. Luc, *Atlas du Spectre d'Absorption de la Molecule d'iode*, Centre Nationale de la Recherche Scientifique, Paris (1978).

73. S. Gerstenkorn and P. Luc, *Rev. Phys. Appl.* **14**, 791 (1979).

74. M. S. Shorem and A. L. Schawlow, *Opt. Commun.* **5**, 148 (1972).

75. J. T. Hougen, *J. Chem. Phys.* **36**, 519 (1962).

76. G. Herzberg, *Electronic Spectra of Polyatomic Molecules*, Van Nostrand Reinhold Company, New York, 1966.

77. G. Herzberg and E. Teller, *Z. Physik Chem.* **B21**, 410 (1933).

78. R. Renner, *Z. Physik* **92**, 172 (1934).

79. Ch. Jungen and A. J. Merer in *Molecular Spectroscopy: Modern Research*, vol. II, ed. K. N. Rao, Academic Press, New York (1976).

80. D. Gauyacq and Ch. Jungen, *Molec. Phys.* **41**, 383 (1980).

81. J. A. Pople, *Molec. Phys.* **3**, 16 (1960).

82. A. Carrington, A. R. Fabris, B. J. Howard and N. J. D. Lucas, *Molec. Phys.* **20**, 961 (1971).

83. F. J. Northrup and T. J. Sears, *Molec. Phys.* **71**, 45 (1990).

84. J. M. Brown and F. Jorgensen, *Adv. Chem. Phys.* **52**, 117 (1983).

85. J. M. Brown, *J. Molec. Spectrosc.* **68**, 412 (1977).

86. C. Devillers and D. A. Ramsay, *Canad. J. Phys.* **49**, 2839 (1971).

87. P. S. H. Bolman, J. M. Brown, A. Carrington, I. Kopp and D. A. Ramsay, *Proc. Roy. Soc. Ser A* **343**, 17 (1975).

88. G. Herzberg and D. N. Travis, *Can. J. Phys.* **42**, 1658 (1964).

89. H. Lefebvre-Brion and R. W. Field, *Perturbations in the Spectra of Diatomic Molecules*, Academic Press Inc., Orlando, Fla., (1986).

90. A. J. Merer and J. M. Allegretti, *Can. J. Phys.* **49**, 2859 (1971).

91. H. H. Nielsen, *Phys. Rev.* **77**, 132 (1950).

92. H. H. Nielsen, G. Amat and M. Goldsmith, *J. Chem. Phys.* **26**, 1060 (1957).

93. R. N. Dixon, *Phil. Trans. Roy. Soc.* **A252**, 165 (1960).

94. A. J. Kotlar, R. W. Field, J. A. Steinfield and J. A. Coxon, *J. Molec. Spectrosc.* **80**, 86 (1980).

95. E. Fermi, *Z. Physik* **71**, 250 (1931).

96. J. T. Hougen, *J. Chem. Phys.* **37**, 403 (1962).

97. D. R. Woodward, D. A. Fletcher and J. M. Brown *Molec. Phys.* **62**, 517 (1987); **68**, 261 (1989).

98. D. R. Lide and C. Matsumura, *J. Chem. Phys.* **50**, 3080 (1969).

99. B. P. Winnewisser in *Molecular Spectroscopy: Modern Research*, vol. III, Academic Press, New York (1980).

100. R. N. Dixon and D. A. Ramsay, *Can. J. Phys.* **46**, 2619 (1968).

101. D. C. Frost, S. T. Lee and C. A. McDowell, *Chem. Phys. Lett.* **23**, 472 (1973).

102. D. L. Albritton, A. L. Schmeltekopf and R. N. Zare, *Molecular Spectroscopy: Modern Research*, vol. 2 (Academic Press, New York, 1976).

103. J. Pliva, *Coll. Czech. Chem. Comm.* **23**, 1846 (1958).

104. G. Herzberg, *Infrared and Raman Spectra of Polyatomic Molecules*, D. Van Nostrand Company Inc., New York, 1945.

105. M. Larzilliere and Ch. Jungen, *Molec. Phys.* **67**, 807 (1987).

106. D. M. Jonas, X. Yang and A. M. Wodtke, *J. Chem. Phys.* **97**, 2284 (1992).

107. A. G. Maki, and D. R. Lide Jr., *J. Chem. Phys.* **47**, 3206 (1967).

108. B. Fabricant and J. S. Muenter, *J. Molec. Spectrosc.* **53**, 57 (1974).

109. M. Larzilliere, S. Abed, M. Carre, M. L. Gaillard, J. Lerme and M. Broyer, *Chem. Phys. Lett.* **119**, 55 (1985).

110. G. Amat and H. H. Nielsen, *J. Molec. Spectrosc.* **23**, 359 (1967).

111. C. H. Townes and A. L. Schawlow, *Microwave Spectroscopy*, McGraw-Hill Book Company Inc., New York (1955).

112. M. Larzilliere, K. Gragueb, J. Lerme and J. B. Koffend, *Chem. Phys. Lett.* **134**, 467 (1987).

113. J. A. Pople and H. C. Longuet-Higgins, *Molec. Phys.* **1**, 372 (1958).

114. H. C. Longuet-Higgins, *Adv. Spectosc.* **2**, 429 (1961).

115. R. F. Barrow, R. N. Dixon and G. Duxbury, *Molec. Phys.* **27**, 1217(1974).

116. G. Duxbury, *Molecular Spectroscopy*, Chemical Society Specialist Periodical Report, vol. 3, 1975, p. 497.

117. Ch. Jungen and A. J. Merer, *Molec. Phys.* **40**, 1 (1980).

118. Ch. Jungen, J. K-E. Hallin and A. J. Merer, *Molec. Phys.* **40**, 25 (1980).

119. Ch. Jungen, J. K-E. Hallin and A. J. Merer, *Molec. Phys.* **40**, 65 (1980).

120. Ch. Jungen and A. J. Merer, *Molec. Phys.* **40**, 95 (1980).

121. C. F. Chang and Y. N. Chiu, *J. Chem. Phys.* **53**, 2186 (1970).

122. J. F. M. Aarts, *Molec. Phys.* **35**, 1785 (1978).

123. A. J. Merer and D. N. Travis, *Can. J. Phys.* **43**, 1795 (1965).

124. J. T. Hougen and J. P. Jesson, *J. Chem. Phys.* **38**, 1524 (1963).

125. A. Chablo, *J. Molec. Struc.* **283**, 135 (1993).

126. K. Dressler and D. A. Ramsay, *J. Chem. Phys.* **27**, 971 (1957).

127. A. G. Adam, A. J. Merer, and D. M. Stuenenberg, *J. Chem. Phys.* **92**, 2848 (1990).

128. S. M. Kinsey-Nielsen, C. R. Brazier and P. F. Bernath, *J. Chem. Phys.* **84**, 698 (1986).

129. W. T. M. L. Fernando, M. Douay and P. F. Bernath, *J. Molec. Spectrosc.* **144**, 344 (1990).

130. P. S. H. Bolman and J. M. Brown, *Chem. Phys. Lett.* **21**, 213 (1973).

131. M. Li and J. A. Coxon, in preparation.

132. J. M. Brown, E. A. Colbourn, J. K. G. Watson and F. D. Wayne, *J. Molec. Spectrosc.* **74**, 294 (1979).

133. D. M. Stuenenberg, Thesis, University of British Columbia.

134. K. Kawaguchi, S. Saito and E. Hirota, *Molec. Phys.* **49**, 663 (1983).

135. K. Kawaguchi, E. Hirota and C. Yamada, *Molec. Phys.* **44**, 509 (1981).

136. D. E. Reisner, P. F. Bernath and R. W. Field, *J. Molec. Spectrosc.* **89**, 107 (1981).